Measurement of long-range correlations in small systems with the ATLAS detector

Xiao Tu

Submitted in partial fulfillment of the

requirements for the degree of

Doctor of Philosophy

under the Executive Committee

of the Graduate School of Arts and Sciences

COLUMBIA UNIVERSITY

2020

ABSTRACT

Measurement of long-range correlations in small systems with the ATLAS detector

Xiao Tu

Two-charged-particle correlations are measured as a function of pseudorapidity and azimuthal angle difference in pp collisions at $\sqrt{s}$ = 13, 2.76 and 5.02 TeV with the ATLAS detector at the Large Hadron Collider. A long-range structure in the two-dimensional function centered at $\Delta\phi = 0$ and extending over a large range of $\Delta\eta$ referred to as the "ridge" is seen in the three data sets. A template fitting method is implemented to extract the Fourier harmonics of the flow and gives the dependence of the harmonics on the charged-particle multiplicities. In this method a rescaled correlation function from peripheral events representing the recoil component plus a cosine modulation representing the ridge is used to describe the whole one-dimensional correlation function. Different multiplicity intervals for the peripheral events are used to extract the harmonics. The results presented show that $v_{\mathrm{n,n}}$ from correlation functions can be factorized into the products of single particle v_n. Significant contributions from v_2, v_3 and v_4 are obtained and their dependences on multiplicity and transverse momentum are studied. It is also shown that there is significant v_n even in the lowest multiplicity bins. In addition, the second harmonics v_2 in pp do not have a significant dependence on both the multiplicity and collision energy. Results of pp and pPb at the same energy are compared with each other in both multiplicity and p_{T} distributions.

Both $\mathrm{ch}^{\mathrm{trk}} - \mathrm{ch}^{\mathrm{trk}}$ and $\mathrm{ch}^{\mathrm{trk}}$-muon correlations are measured in pPb collisions at $\sqrt{s_{\mathrm{NN}}}$ = 8.16 TeV. Long-range correlations are studied through template fitting procedure. $\mathrm{ch}^{\mathrm{trk}}$-$v_2$ increases with $N_{\mathrm{ch}}^{\mathrm{rec}}$ at low multiplicity and saturates at high

multiplicity. Muon-v_2 is considerably smaller than $\mathrm{ch}^{\mathrm{trk}}$-$v_2$ and only has a weak dependence on event multiplicity. Factorization in both cases works pretty well.

Two-charged-particle correlation functions are also measured in Xe+Xe events at $\sqrt{s_{\mathrm{NN}}} = 5.44$ TeV. In the most central collisions direct Fourier decomposition is preferred to avoid negative recoil component that might appear in the template fitting method. v_n reaches its maximum value in the mid-centrality region and becomes smaller at both low and high centralities. Results are compared with Pb+Pb events at $\sqrt{s_{\mathrm{NN}}} = 5.02$ TeV showing that v_n obtained from these two systems have similar values and behaviors.

Contents

List of Figures

List of Tables

Acknowledgments

During my PhD program plenty of people have given me help and encouragement in different ways. Without them this thesis wouldn't be completed. First and foremost I need to give my gratitude to my PhD advisor Professor Brian Cole. He is well-known and experienced physicist who gave me the knowledge on heavy ion experiments. He is also a kind and caring research advisor who led me the way to the research in the ATLAS group. When I was doing my first analysis he discussed with me every afternoon in his office reviewing my results and giving advice on the next steps. Although I was new to experimental physics at that time, his careful consideration beyond his obligation always gave me great confidence and motivation. His enthusiasm about physics drives me into the study of different experiments and the physics behind these phenomena.

I would like to thank all the members from Columbia Heavy Ion Group. Professor William Zajc always gives me helpful insights and ideas during the group discussion. His profound knowledge in different areas of physics gave me a really deep impression. I am grateful to all the postdocs and graduate students from the group, Aaron Angerami, Soumya Mohapatra, Sarah Campbell, Martin Rybar, Tingting Wang, Felix Clark, Laura Havener and Yun Tian. They gave me a lot of helpful discussions and I learnt quite a lot from their work and experiences over these years. I would like to say special thanks to Soumya Mohapatra, a postdoc who has been working here from the first year I came into this group. He is a warm-hearted person and always eager to

helper others when someone has difficulties in their work. He gave me lots of advice on drawing plots for ATLAS notes and presenting slides in public meetings. He taught me how to use the Linux cluster and the ATLAS production and distributed analysis system (PanDA) from the very beginning. I also appreciate the consideration from Martin Rybar, with whom I first met at CERN. He cares much about the progress on my thesis project while I am working on it.

I need to say thanks to a couple of my friends at Columbia as well who stayed with me during all these years. Without their accompaniment my life as an international student wouldn't be so easy and comfortable. I also owe my gratitude to Professor Alberto Nicolis who led me to theoretical study on the effective field theory in fluid for one semester during my second year.

Last but not the least I must express my gratitude to my parents, who have brought me up and sent me to study in the United States. They have taught me lots of their life experience since I was a little child and given their unconditional love and care whenever I entered into difficulties in the real life. Without their support I wouldn't be here to pursue this degree.

For my parents Ling Chen and Jiuqing Tu

Chapter 1

Introduction

Quark-gluon plasma (QGP) is a special state of nuclear matter predicted by quantum chromodynamics (QCD), the theory that describes the strong interaction between quarks and gluons. At ordinary temperature and density, quarks and gluons are confined into hadrons with the result that the strong interaction is not noticeable at large distances. However at extreme high temperature and density, quarks and gluons are deconfined and form a strongly-coupled matter called quark-gluon plasma. Lattice QCD can be used to determine the properties of the phase transition between these two states [1, 2] . Figure 1.1 shows the QCD phase transition computed by lattice QCD at different temperatures and chemical potentials [3].

In the early 1970s, physicists proposed that quark-gluon plasma can be realized via ultra-relativistic heavy-ion collisions [4, 5]. By colliding heavy nuclei at very high speed, the energy density achieved after the collision can be comparable to the first few microseconds of the universe. QGP is formed under this extreme conditions for a very short period of time. Such experiments have been conducted in the Relativistic Heavy Ion Collider (RHIC) at Brookhaven National Laboratory and the Large Hadron Collider (LHC) at CERN via Au+Au or Pb+Pb collisions. Figure 1.2 shows the results from RHIC experiments. It is easy to see there is a significant elliptic flow v_2,

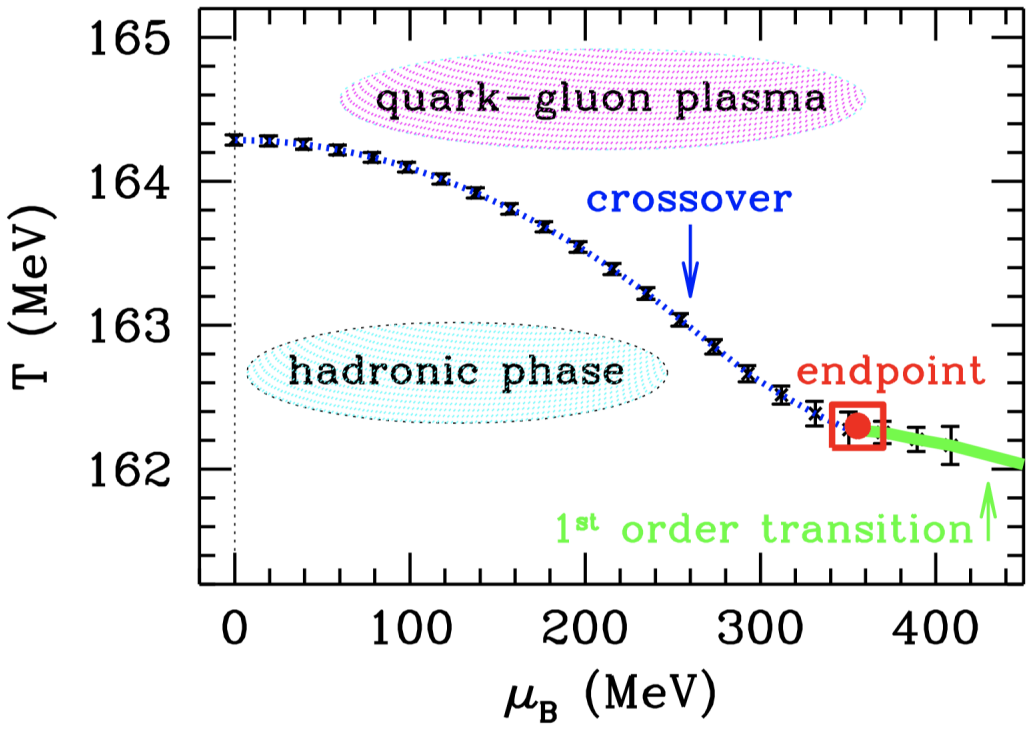

Figure 1.1: Phase diagram of QCD matter computed by lattice QCD with temperature and quark chemical potential as two axes.

which is consistent with the numerical simulation of hydrodynamics. This suggests the whole QGP medium is strongly-coupled by color forces between partons like the fluid and its evolution can be described by relativistic hydrodynamics presented in the next chapter. A direct evidence of this is the observation of azimuthal anisotropy of produced particles. Such significant azimuthal anisotropy can not be observed in a weakly coupled gas-like plasma, since it does not interact with partons passing through the medium.

One strong evidence of the existence of the QGP medium is the jet quenching effect in A+A collisions especially in the most central events. Since no jet quenching effect has been observed in small systems like p+A and pp even in high-multiplicity events, the production of QGP is not expected in small systems and thus hydrodynamics used to describe the collective behavior should not be valid in these events. However exper-

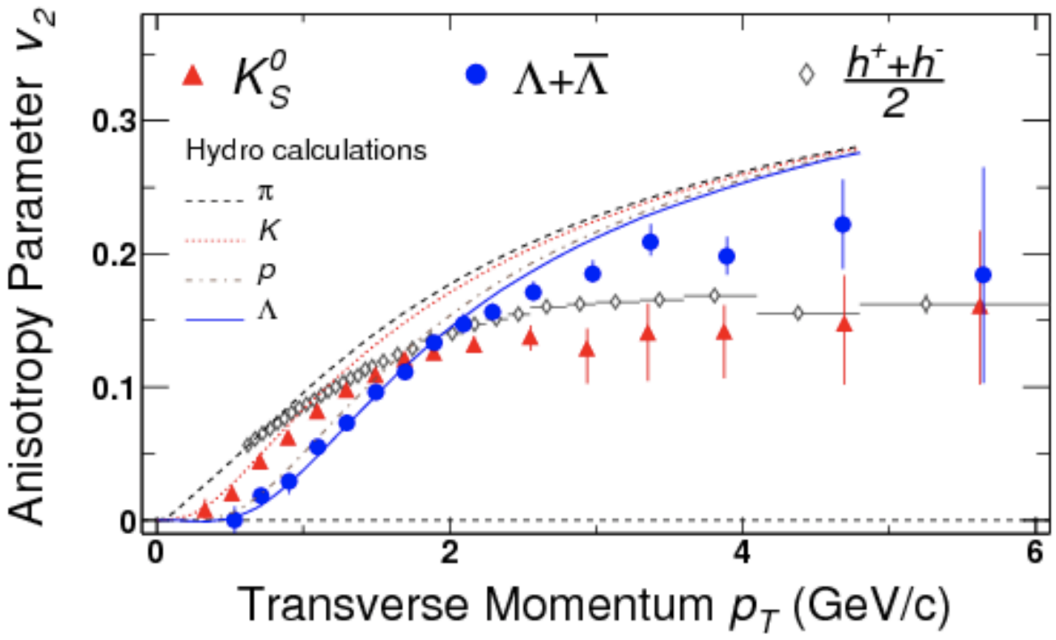

Figure 1.2: The figure shows the elliptic flow v_2 from minimum bias Au+Au collisions at RHIC for different identified hadrons. The hydrodynamic calculations are also plotted here for comparison [6].

iments have shown that azimuthal anisotropy of the producing particles, previously observed in A+A collisions and once thought to mainly result from jet quenching, is also observed in p+A and pp systems. It is still not clear whether the existence of QGP and the idea of collective behavior should be extended to such small systems [7]. How can such hot and dense medium exists while high p_{T} partons do not lose energy across the medium? Actually there are some alternative explanations such as saturation of the parton distributions or model calculations based on the initial state effects like color-glass condensate for the azimuthal anisotropy observation in small systems. However since results from experiments have shown too many similarities between the small system and A+A system, it is natural to assume that the azimuthal anisotropies of both systems should come from the same origin. The reason for the anisotropy flow in small systems still remains unanswered.

This thesis discusses the measurement of small system collectivity in heavy ion

physics. It introduces the two-particle correlation analysis that will be used later to extract the single particle Fourier harmonics. The nth order Fourier term of two-particle correlations is proportional to $v_n^2 \cos(n\Delta\phi)$. The jet contribution on the near side is eliminated. Only the distribution of long range particle pairs is considered. The dijet contribution on the away side is also removed using a peripheral template with only the soft correlation left which is the flow contribution. Different p_{T} bins are used to check for the factorization into single particle harmonics. The factorization relationship is correct if the long range correlation arises from the collective flow of single particles. Similar analysis is done for systems of different sizes. Results that will be presented later show that v_2 in pp collisions is a constant value within uncertainties at different multiplicities and energy levels [8, 9]. This means the flow-like collective behavior in pp collisions is more likely an intrinsic property of the system. While in the pPb system v_2 begins at some value close to the pp v_2 and increases with multiplicity. Finally it reaches some constant level at the central region [10, 11]. In order to further develop the features of azimuthal anisotropy in pPb systems, a correlation analysis of heavy flavor muons and charged particles is implemented [12, 13]. If QGP is produced in the pPb system, the thermalization of heavy flavor quarks is expected and the $\mathrm{ch}^{\mathrm{trk}}$-muon azimuthal correlation should also be observed. Another small system that will be studied in this thesis is the Xe+Xe system. Since it has larger event-by-event fluctuations compared to Pb+Pb system, it should produce higher eccentricities in the initial state. The Xe+Xe systems also have larger viscous effect during the hydrodynamic evolution than the Pb+Pb systems [14, 15].

The remainder of this thesis is organized as follows. Chapter 2 introduces the theoretical background of relevant heavy-ion physics including the basics of QCD, hydrodynamical description and the phenomenology of heavy-ion collisions. Chapter 3 discusses the first measurements of small system collectivity at RHIC and LHC as well as some theoretical calculation in order to explain the origin of this behavior.

Chapter 4 describes the experimental apparatus, the LHC, the ATLAS detector and also configuration and usage of its trigger system and sub-detectors. The charged-track and muon reconstruction methods used in ATLAS are also included. Chapter 5 focuses on several data sets used in the thesis as well as an introduction for two-particle correlation analysis and template fitting method that is used to extract the Fourier harmonics. Chapter 6 includes analysis on pp systems at different energy scales. The flow harmonics are compared with the pPb system at the same collision energy. In order to further investigate the p+Pb system, Chapter 7 extends the analysis to muon-hadron correlation after the heavy flavor decays. Besides the flow of charged tracks, muon elliptic flow is investigated in this chapter. Chapter 8 continues the analysis to Xe+Xe systems, where analysis from Pb+Pb and Xe+Xe are compared. Chapter 9 discusses similar measurements performed at CMS and ALICE and compares those results with the previous ATLAS measurement. Chapter 10 is the conclusion discussing all the results and their implications.

Chapter 2

Background of heavy ion physics

2.1 Quantum Chromodynamics

2.1.1 SU(3) group in QCD

Quantum chromodynamics is the theory to describe the strong interaction between quarks and gluons. It's a non-abelian gauge theory with symmetry group SU(3). Quarks have 6 flavors: up, down, strange, charm, bottom and top, $N_f = 6$. Each flavor has three colors: red, green and blue, $N_c = 3$. Gluons are the force carriers of the strong interaction, which have $N_c^2 - 1 = 8$ different color indices. Since quarks are fermions with spin $\frac{1}{2}$, the color space is a 3 dimensional complex space where each component is a Dirac spinor.

$$\psi = \begin{pmatrix} \psi_1 \\ \psi_2 \\ \psi_3 \end{pmatrix} \tag{2.1}$$

Transformations in SU(3) group satisfy

$$U^\dagger U = 1 \tag{2.2}$$

and

$$\det U = 1 \tag{2.3}$$

Since U is a 3×3 complex matrix, it has 18 real parameters. Considering the above 10 constraints in Eq. (2.2) and (2.3), only 8 of them are independent. Therefore any transformation in SU(3) group can be expressed in terms of 8 independent Hermitian matrices λ^a,

$$U = \mathrm{e}^{\mathrm{i}\theta_a \lambda^a/2}, \qquad a = 1, 2, \cdots, 8, \tag{2.4}$$

These traceless matrices are called Gell-Mann matrices. They are usually considered as the generalization of Pauli matrices in the case of SU(2).

$$\lambda^1 = \begin{pmatrix} 0 & 1 & 0 \\ 1 & 0 & 0 \\ 0 & 0 & 0 \end{pmatrix}, \quad \lambda^2 = \begin{pmatrix} 0 & -\mathrm{i} & 0 \\ \mathrm{i} & 0 & 0 \\ 0 & 0 & 0 \end{pmatrix}, \quad \lambda^3 = \begin{pmatrix} 1 & 0 & 0 \\ 0 & -1 & 0 \\ 0 & 0 & 0 \end{pmatrix},$$

$$\lambda^4 = \begin{pmatrix} 0 & 0 & 1 \\ 0 & 0 & 0 \\ 1 & 0 & 0 \end{pmatrix}, \quad \lambda^5 = \begin{pmatrix} 0 & 0 & -\mathrm{i} \\ 0 & 0 & 0 \\ \mathrm{i} & 0 & 0 \end{pmatrix}, \quad \lambda^6 = \begin{pmatrix} 0 & 0 & 0 \\ 0 & 0 & 1 \\ 0 & 1 & 0 \end{pmatrix},$$

$$\lambda^7 = \begin{pmatrix} 0 & 0 & 0 \\ 0 & 0 & -\mathrm{i} \\ 0 & \mathrm{i} & 0 \end{pmatrix}, \quad \lambda^8 = \frac{1}{\sqrt{3}} \begin{pmatrix} 1 & 0 & 0 \\ 0 & 1 & 0 \\ 0 & 0 & -2 \end{pmatrix},$$

The generators of SU(3) group are defined as

$$T^a = \frac{\lambda^a}{2} \tag{2.5}$$

satisfying

$$\mathrm{tr} T^a = 0, \qquad \mathrm{tr}(T^a T^b) = \frac{1}{2}\delta^{ab} \tag{2.6}$$

They also obey relations

$$[T_a, T_b] = \mathrm{i} f_{abc} T^c \tag{2.7}$$

where f_{abc} are called structure constants in SU(3) group, which are antisymmetric for all indices. The non-zero components are

$$f_{123} = 1, \tag{2.8}$$

$$f_{147} = -f_{156} = f_{246} = f_{257} = f_{345} = -f_{367} = \frac{1}{2} \tag{2.9}$$

$$f_{458} = f_{678} = \frac{\sqrt{3}}{2} \tag{2.10}$$

2.1.2 The QCD Lagrangian

Generally the Lagrangian density for free Dirac fields can be written as

$$\mathcal{L}_q = \bar{\psi}(\mathrm{i}\gamma^\mu \partial_\mu - m)\psi \tag{2.11}$$

where m represents the mass matrix, which only depends on the flavor indices. Since mass is independent of colors, the free Lagrangian is invariant under global gauge transformation in the color space,

$$\psi \to \psi' = U\psi = \mathrm{e}^{\mathrm{i}\theta_a T^a}\psi \tag{2.12}$$

Let's consider the local gauge transformation,

$$\psi \to \psi' = U\psi = \mathrm{e}^{\mathrm{i}\theta_a(x) T^a}\psi \tag{2.13}$$

In order for the Lagrangian to be invariant under the above transformation, the covariant derivative should be introduced in the kinetic term,

$$D_\mu = \partial_\mu + \mathrm{i} g A_\mu \tag{2.14}$$

where g is the coupling constant and A_μ is the gauge field. Since Lagrangian is invariant under the local gauge transformation, we require

$$D_\mu \to D'_\mu = U D_\mu U^\dagger \tag{2.15}$$

The above equation implies the following transformation of the gauge field,

$$A_\mu \to A'_\mu = U A_\mu U^\dagger - \frac{\mathrm{i}}{g} U \partial_\mu U^\dagger \tag{2.16}$$

Analogue of the case in electrodynamics, the gauge field tensor here is defined via

$$[D_\mu, D_\nu] = \mathrm{i} g F_{\mu\nu} \tag{2.17}$$

$F_{\mu\nu}$ is traceless, so we have $F_{\mu\nu} = F^a_{\mu\nu} T_a$. The Lagrangian density for the gauge field is therefore

$$\mathcal{L}_A = -\frac{1}{2}\mathrm{tr}(F_{\mu\nu}F^{\mu\nu}) = -\frac{1}{4}\mathrm{tr}(F^a_{\mu\nu}F^{\mu\nu}_a) \tag{2.18}$$

The full Lagrangian density is the Lagrangian of the quark field plus the Lagrangian of the gauge field,

$$\mathcal{L} = \mathcal{L}_\psi + \mathcal{L}_{\psi A} + \mathcal{L}_A = \bar{\psi}(\mathrm{i}\gamma^\mu D_\mu - m)\psi - -\frac{1}{4}\mathrm{tr}(F^a_{\mu\nu}F^{\mu\nu}_a) \tag{2.19}$$

where

$$\mathcal{L}_\psi = \bar{\psi}(\mathrm{i}\gamma^\mu \partial_\mu - m)\psi \tag{2.20}$$

$$\mathcal{L}_{\psi A} = g\bar{\psi} A_\mu \gamma^\mu \psi \tag{2.21}$$

$$\mathcal{L}_A = -\frac{1}{4}(\partial_\mu A_\nu \partial^\mu A^\nu - \partial_\mu A_\nu \partial^\nu A^\mu) \tag{2.22}$$

$$-g f_{abc} A^\mu_b A^\nu_c \partial^\mu A^\nu_a - \frac{g^2}{4} f_{abc} f_{cde} A_{a\mu} A_{b\nu} A^\mu_c A^\nu_d \tag{2.23}$$

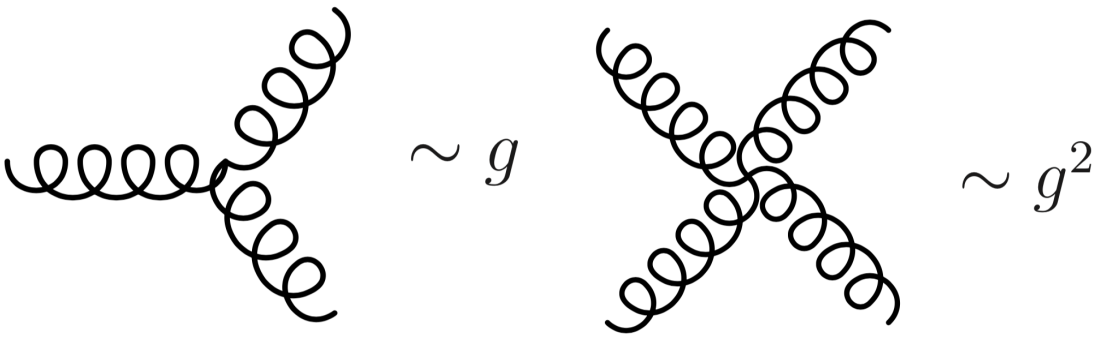

Figure 2.1: The left and right panels show the 3-gluon interaction and 4-gluon interaction respectively. Their corresponding Lagrangian terms are proportional to g and g^2.

$\mathcal{L}_\psi$ is the free Lagrangian for the quark field. $\mathcal{L}_{\psi A}$ gives the quark-gluon interaction representing the coupling between quark field and gauge field. The first term in $\mathcal{L}_A$ is the free propagator in the gluon field, while the second and the third terms are 3-gluon and 4-gluon self-interaction vertices, which are illustrated in Figure 2.1.

2.1.3 Running coupling constant and asymptotic freedom

When renormalization is introduced, the coupling constant g and Fermion mass both depend on the energy scale. Therefore they are often called running coupling constant and running mass. In the renormalizable QCD theory, the coefficient β is defined as

$$\beta(g) = \mu\frac{\partial g}{\partial \mu} = -(11 - \frac{2n_f}{3})\frac{g^3}{16\pi^2} = -\beta_0\frac{g^3}{16\pi^2} \tag{2.24}$$

where

$$\beta_0 = 11 - \frac{2n_f}{3} \tag{2.25}$$

The above expression only considers the leading order term. If $n_f \leq 16$, Eq. (2.24) gives $\beta_0 < 0$. In this case the coupling constant g increases as the energy scale μ decrease. When μ approaches infinity g decreases to 0. This is often called asymptotic

freedom. In the case of QED, since β is always positive, no asymptotic freedom is observed. Eq. (2.24) can be written as

$$\mu \frac{\partial \alpha_s}{\partial_\mu} = -\frac{\beta_0}{2\pi}\alpha_s^2 \tag{2.26}$$

which gives the result

$$\alpha_s(\mu) = \frac{g^2(\mu)}{4\pi} \approx \frac{4\pi}{\beta_0 \ln(\mu^2/\Lambda^2)} \tag{2.27}$$

If μ approaches Λ, QCD becomes strongly-coupled. Generally $\beta(g)$ can be expanded in terms of g^2 or α_s.

$$\frac{\mu}{\alpha_s}\frac{\partial \alpha_s}{\partial \mu} = \frac{2}{g}\beta(g) = -\beta_0(\frac{\alpha_s}{2\pi}) - \beta_1(\frac{\alpha_s}{2\pi})^2 - \beta_2(\frac{\alpha_s}{2\pi})^3 - \cdots \tag{2.28}$$

The next-to-leading order is calculated as

$$\beta_1 = 51 - \frac{19n_f}{3} \tag{2.29}$$

According to the renormalization theory, when the perturbative calculation includes the terms from all orders, values of physical observables should be irrelevant of the renormalization schemes. However when considering only finite number of terms, physical values generally depend on the renormalization scheme we use. In the case of $\beta(g)$ expansion, β_0 and β_1 do not depend on the renormalization scheme, while $\beta_n(n \geq 2)$ does. The way α_s varies with the energy scale Q is shown in Figure 2.2. From the value of α_s at a given energy scale μ_0, α_s at any other energy scale μ can be computed from Eq. (2.28). A common choice for the given energy scale is the mass of Z^0 boson. When $\mu_0 = m_Z = 91.19$ GeV, experimental measurements give the result

$$\alpha_s(m_Z) = 0.1181 \pm 0.0011 \tag{2.30}$$

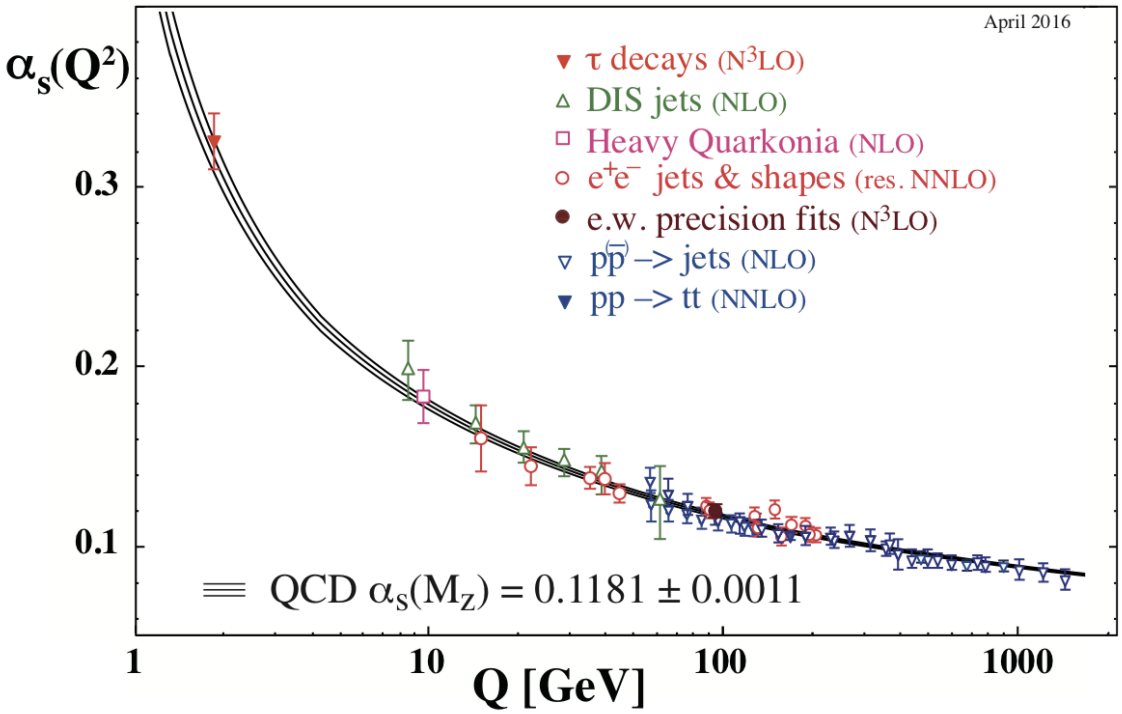

Figure 2.2: Coupling constant α_s as a function of energy scale Q. Different legends in the figure represent results from different measurements [16].

2.1.4 Color confinement

In the real world isolated quarks and gluons are not observed. Quarks and gluons are confined in hadrons that are color neutral. This means all particles that are observed in the experiments can not carry color charge. This phenomenon is called color confinement or quark confinement. Let's consider the system of a quarkonium composed of q and $\bar{q}$. It is a bound state where q and $\bar{q}$ interact through the exchange of gluons that carry color charge. The potential between quark and anti-quark can be estimated through the formula

$$V(r) = -\frac{4}{3}\frac{\alpha_s}{r} + F_0 r \tag{2.31}$$

When the separation is small, the first term of the above potential is dominant. The interaction between quark and anti-quark is Coulomb-like and much weaker than

that of a quarkonium with a larger separation. This is the phenomenon of asymptotic freedom discussed above. Since small distance leads to large energy scale, perturbative QCD can be used here. In order to describe the color confinement, a linear term is introduced in the above potential. When the separation is large, this second term is dominant. Perturbative QCD is no longer valid in the low energy scale. A new numerical method called lattice QCD is implemented to solve problems in the scale of large distance. In this method a grid with separation a between adjacent points in the space and time dimensions is introduced and after calculation the limit $a \to 0$ is taken to obtain the accurate result in the continuous theory of QCD. Figure 2.3 shows the potential in a quarkonium calculated in perturbative QCD in high energy scale and lattice QCD in low energy scale. When two quarks are pulled apart away from each other, the force between them is constant and results in a large value of potential. Eventually quarks from this pair will form new quarkonia with quarks from other pairs to minimize the potential of the whole system. Infinite amount of energy is required to pull single quark out of the quark anti-quark pair and thus isolated quarks with non-zero color charge cannot be found. A plot demonstrating how new quarkonium is formed is shown in Figure 2.4.

2.2 The Glauber model

The Glauber model, named after Roy Glauber, is a phenomenogical description of nucleus-nucleus collisions. During the collisions of two nuclei, the overlapping amount can be determined by the impact parameter b, which is the shortest transverse distance between the centers of two nuclei while they pass through each other. A collision with smaller impact parameter can produce denser medium and create more outgoing particles. Thus the impact parameter defines the centrality of the collision. Events with similar centralities are classified into the same group, since their resulting

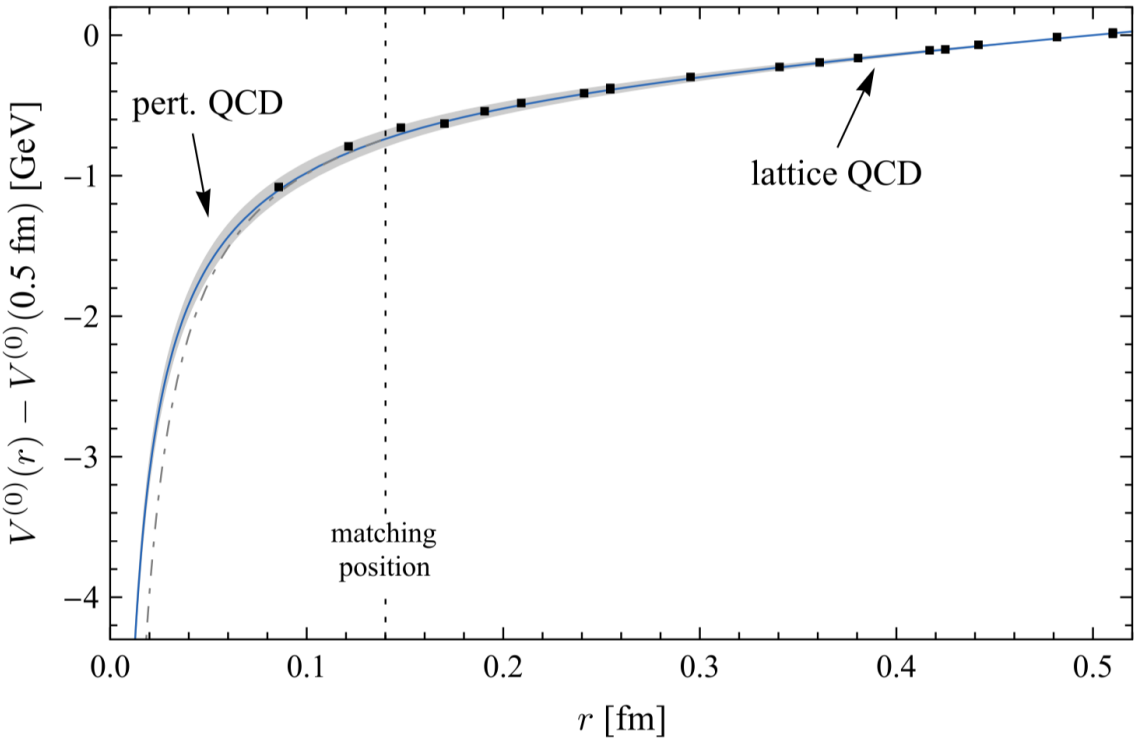

Figure 2.3: Potential between quark and antiquark calculated from perturbative QCD and lattice QCD. The two methods match at an intermediate distance. The dashed-dotted curve is the extrapolation using the Coulomb-plus-linear potential from the lattice QCD result [17].

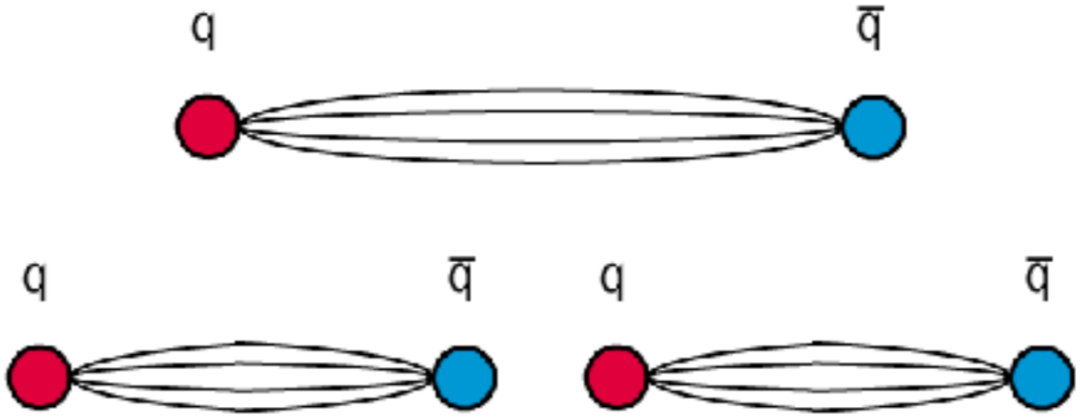

Figure 2.4: When quarks in the quarkonia are pulled apart. A new quark anti-quark pair is formed. No single isolated quark can be found.

particles usually have similar energy or momentum distributions.

However in experimental particle physics, it is impossible to measure the impact parameter b as well as the event centrality directly. We need to use phenomenogical models to describe the above collision process. By using the Glauber model, we make the following basic assumptions, which are usually referred to as "optical limit" [18].

- linear trajectory: Each nucleon is moving at a high speed and its trajectory can be approximately considered as a straight line and is not deflected by the Coulomb forces from other nucleons. This approximation is pretty good at high energies. At low energy there is a so-called Coulomb-modified Glauber model that can be applied [19].

- independent trajectory: The size of nucleus is assumed large compared to the nucleon-nucleon forces. This means each nucleon moves independently in the nucleus.

Under these assumptions the nucleus-nucleus interaction is decomposed into independent and individual nucleon-nucleon collisions. The overall nucleus-nucleus cross-section therefore can be computed in terms of nucleon-nucleon cross sections. The nuclear density is usually assumed to be a Fermi function called the Woods-Saxon distribution which is parametrized by three quantities [18],

$$\rho(r) = \rho_0 \frac{1 + \omega(r/R)^2}{1 + \exp(\frac{r-R}{a})} \tag{2.32}$$

where ρ_0 is the nucleon density in the center of the nucleus, a is called "skin depth", R is the nuclear radius and ω is determined by the shape of the nucleus. The density of Pb nucleus is illustrated in Figure 2.5. The inelastic nucleon-nucleon cross section $\sigma_{\text{inel}}^{\text{NN}}$ obtained from experiments is shown in Figure 2.6.

Figure 2.7 shows an example of nucleus-nucleus collisions. The projectile nucleus B is passing through the target nucleus A. Let's consider a small tube represented by

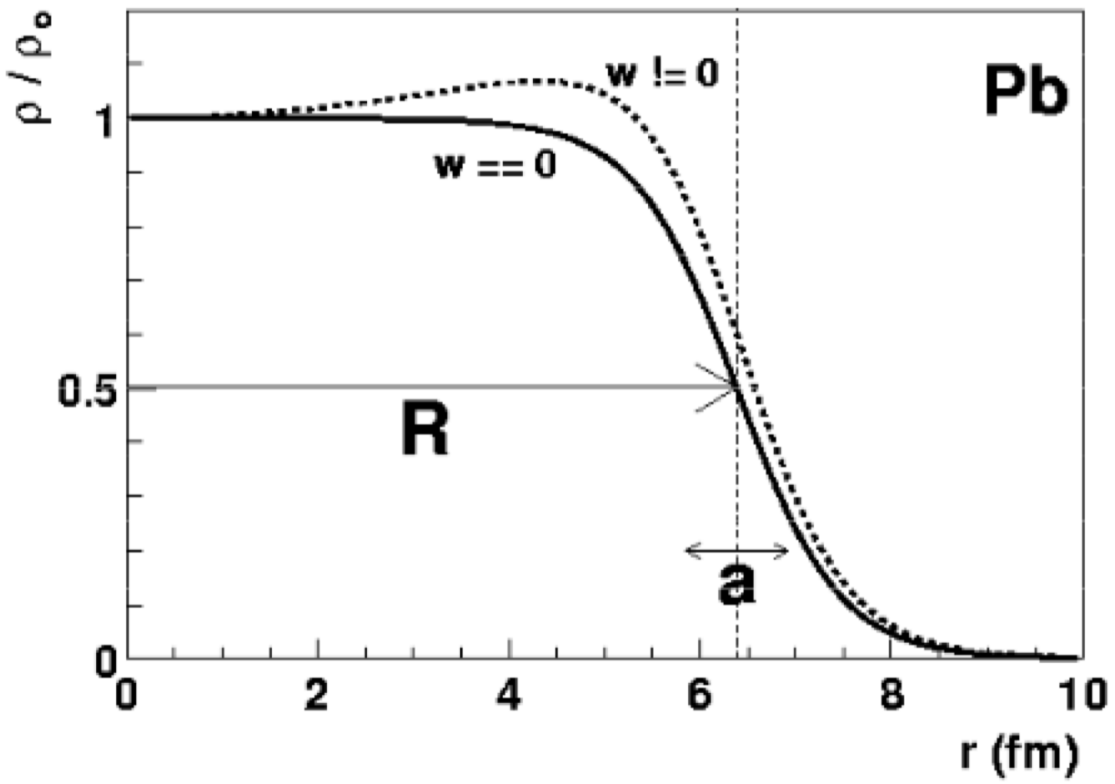

Figure 2.5: A figure showing the nucleon density of Pb determined by Woods-Saxon distribution as a function of r. The nuclear radius R is determined by the position where the nucleon density decreases to half of the density in the center.

a shaded square in the beam-line view of the figure. It has a displacement $\mathbf{s}$ relative to the center of nucleus A and $\mathbf{s} - \mathbf{b}$ relative to the center of nucleus B. The probability of finding a nucleon of A in this tube is

$$T_A(\mathbf{s}) = \int \rho_A(\mathbf{s}, z_A) dz_A \tag{2.33}$$

where $\rho_A(\mathbf{s}, z_A)$ is the probability to find a nucleon at $(\mathbf{s}, z_A)$. Then the probability for a nucleon-nucleon collision per unit transverse area is $T_A(\mathbf{s})\sigma_{\text{inel}}^{\text{NN}} T_B(\mathbf{s} - \mathbf{b})d\mathbf{s}$. The probability of one nucleon-nucleon interaction occurring is therefore

$$T_{AB}(\mathbf{b})\sigma_{\text{inel}}^{\text{NN}} = \int T_A(\mathbf{s})\sigma_{\text{inel}}^{\text{NN}} T_B(\mathbf{s} - \mathbf{b})d\mathbf{s} \tag{2.34}$$

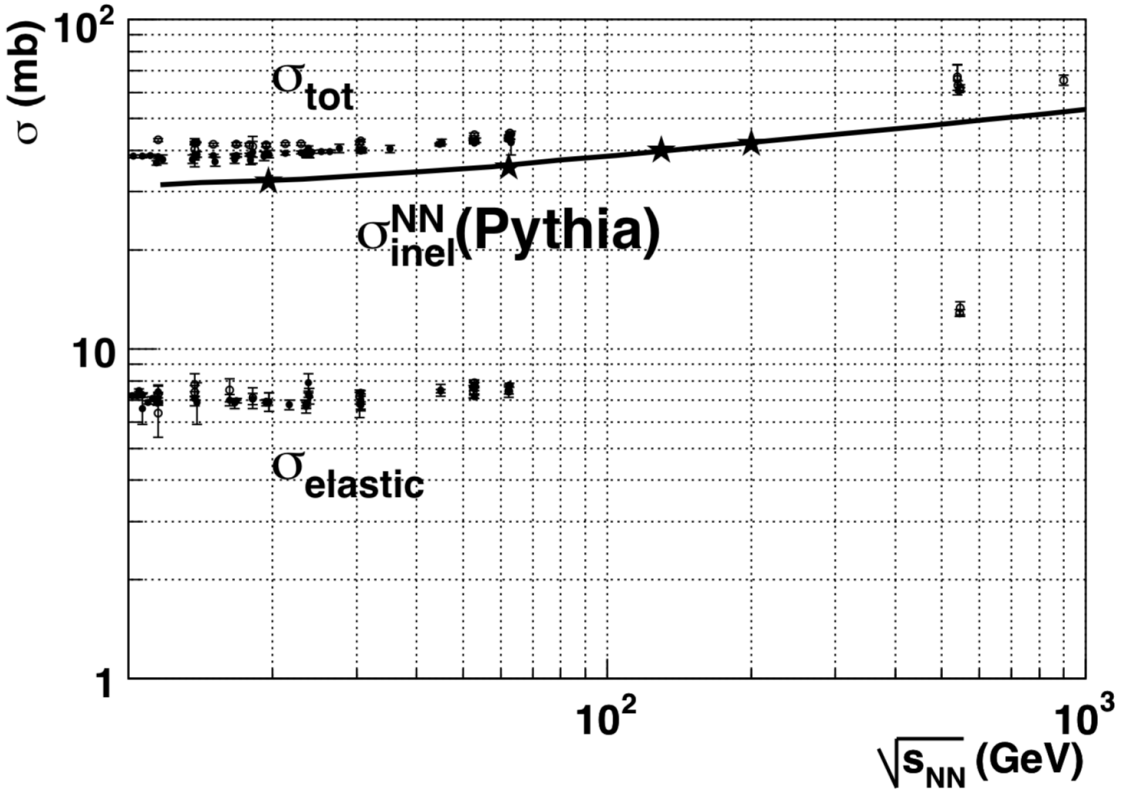

Figure 2.6: The solid line shows the inelastic cross section computed by the event generator Pythia. The upper points and lower points represents the total and elastic cross sections obtained from the experimental data [18].

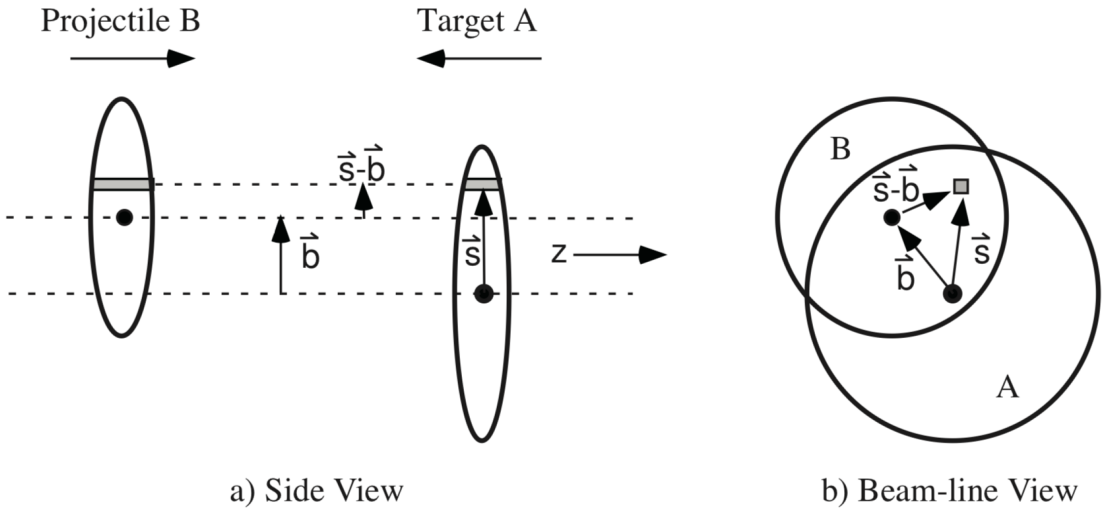

Figure 2.7: Side view and beam-line view of the nucleus-nucleus collisions. They are schematic representations for the Glauber model [18].

Using the knowledge of binomial distribution, the probability to find n such nucleon-nucleon interactions is

$$P(n,\mathbf{b}) = \left(\begin{array}{c} AB \\ n \end{array} \right) [T_{AB}(\mathbf{b})\sigma_{\rm inel}^{\rm NN}]^n [1 - T_{AB}(\mathbf{b})\sigma_{\rm inel}^{\rm NN}]^{AB-n} \tag{2.35}$$

The overall nucleus-nucleus cross section can be obtained as

$$\sigma_{\rm inel}^{\rm A+B} = \int_0^\infty 2\pi b db \; p_{\rm inel}^{\rm A+B}(b) = \int_0^\infty 2\pi b db \{1 - [1 - T_{AB}(b)\sigma_{\rm inel}^{\rm NN}]^{AB}\} \tag{2.36}$$

Especially when the target or the projectile nucleus is a single nucleon, the above equation gives the nucleus-nucleon cross section

$$\sigma_{\rm inel}^{\rm A(B)} = \int d\mathbf{s} \{1 - [1 - T_{A(B)}(\mathbf{s})\sigma_{\rm inel}^{\rm NN}]^{A(B)}\} \tag{2.37}$$

In a nucleus-nucleus collision, the total number of nucleons that participate in the nucleon interactions is called the "number of participants" or the "number of wounded nucleons" $N_{\rm part}$. From the above calculation, $N_{\rm part}$ is given by

$$\begin{aligned} N_{\rm part}(\mathbf{b}) &= A \int T_A(\mathbf{s}) \{1 - [1 - T_B(\mathbf{s} - \mathbf{b})\sigma_{\rm inel}^{\rm NN}]^B\} d\mathbf{s} + & (2.38) \\ & \quad B \int T_B(\mathbf{s} - \mathbf{b}) \{1 - [1 - T_A(\mathbf{s})\sigma_{\rm inel}^{\rm NN}]^A\} d\mathbf{s} & (2.39) \end{aligned}$$

The number of total nucleon-nucleon interactions can be estimated as

$$N_{\rm coll}(\mathbf{b}) = ABT_{AB}(\mathbf{b})\sigma_{\rm inel}^{\rm NN} \tag{2.40}$$

Glauber model can be implemented using Monte Carlo simulation as well [18]. The nucleons in the target and projectile nuclei are distributed according to some pre-determined density distribution. A random impact parameter is drawn and the nucleus-nucleus interaction is viewed as independent nucleon-nucleon collisions.

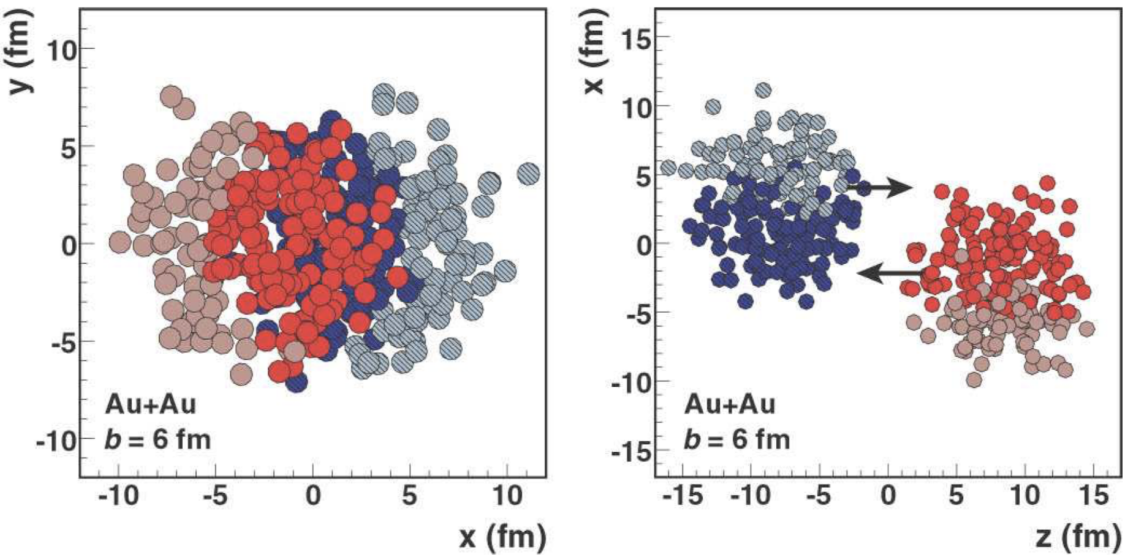

Figure 2.8: The figure shows Au+Au event at $\sqrt{s_{\rm NN}} = 200$ GeV simulated by Glauber Monte Carlo. The left and right panels illustrate the event along the beam line and from the transverse plane respectively. Each nucleon in the figure is drawn with a radius $\sqrt{\sigma_{\rm inel}^{\rm NN}/\pi}/2$. The nucleon with darker colors are participants [18].

The nucleon interaction occurs if the distance between two nucleons is smaller than $\sqrt{\sigma_{\rm inel}^{\rm NN}/\pi}$. Quantities like $N_{\rm coll}$, $N_{\rm part}$ and $\sigma_{\rm inel}^{\rm A+B}$ thus can be estimated.

2.3 Quark-gluon plasma

Quark-gluon plasma (QGP) is considered to exist in the early stage of the universe. Right after the Big Bang the universe expands exponentially. The inflation period lasts from 10^{-36} to 10^{-33} or 10^{-32} seconds. After this period the universe began to expand at a lower rate. Since the temperature and density is high at the beginning of the universe quarks and gluons are deconfined as quark-gluon plasma because of asymptotic freedom. About 10^{-6} seconds the universe began to cool down. Quarks and gluons were confined into color-neutral hadrons. Figure 2.9 shows the timeline of the universe from the Big Bang to today's world. Physicists proposed that quark-gluon plasma can be produced through heavy ion collisions. The physics right after

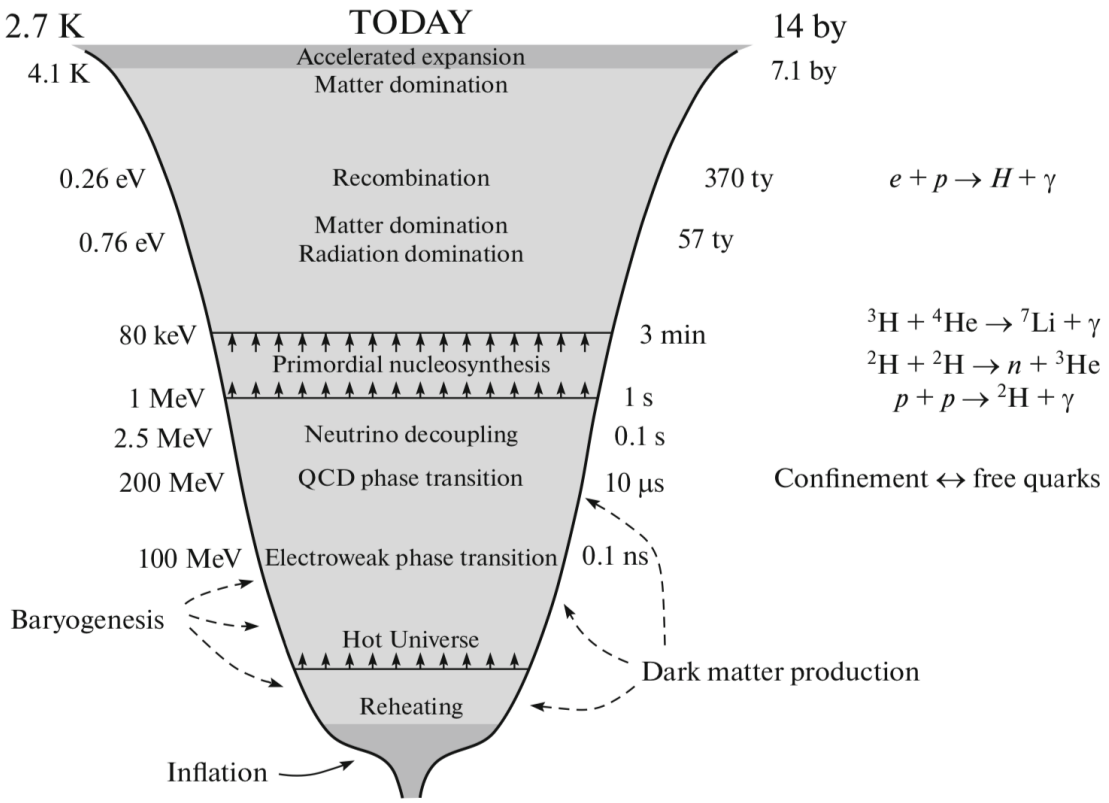

Figure 2.9: The evolution of the universe after the Big Bang is shown in the figure [20].

the collision is similar to what happened in the early of the universe.

Figure 2.10 shows the QCD phase diagram. There are mainly two phases of matter composed by quarks and gluons. When temperature and chemical potential (or the baryon density) are low, quarks and gluons are confined into the hadron phase. While temperature and chemical potential are high, they are deconfined into quark-gluon plasma that can be described by hydrodynamics. The transition between the two phases is proved to be the first-order phase transition. There is a smooth crossover indicated by the red dashed line to the left of the line representing the phase transition, which means there are no distinct differences between these two phases if the chemical potential is low. There must be a critical point between the smooth crossover and the phase transition. The study of this point is a fundamental

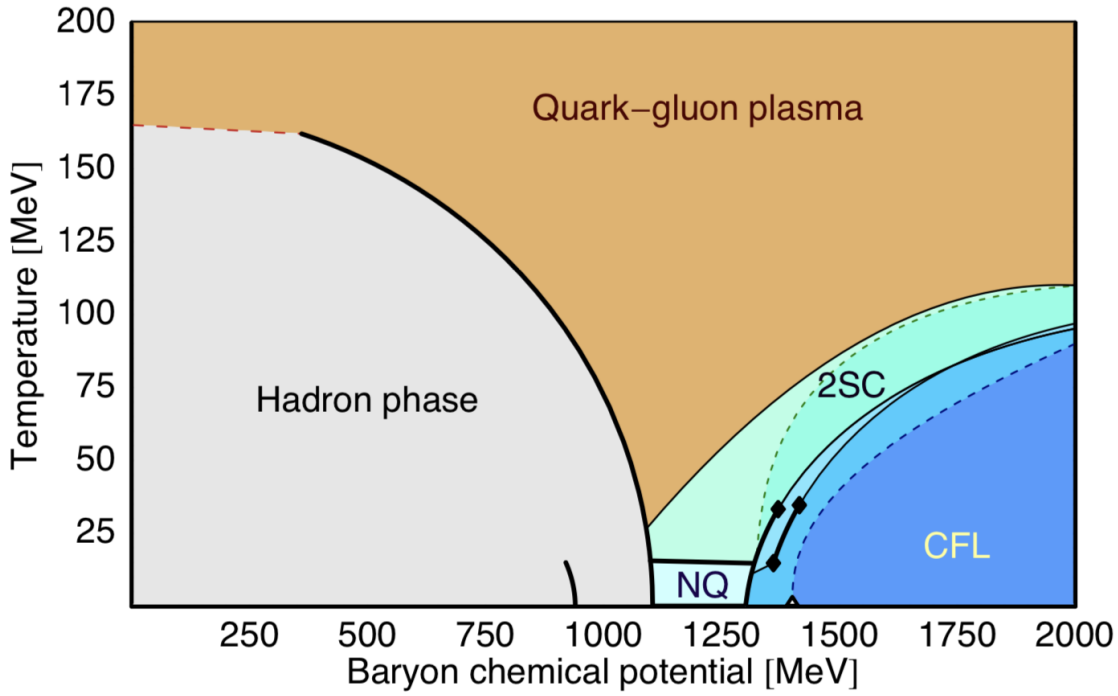

Figure 2.10: QCD phase diagram as a function of temperature and chemical potential.

issue in understanding the whole QCD matter. When chemical potential is zero the smooth crossover occurs at almost 170 MeV. This is the region where RHIC and LHC experiments are conducted.

2.4 Anisotropic flows

2.4.1 Single particle flows

The hot and dense medium called QGP is produced after heavy ion collisions. Due to the non-zero impact parameters in non-central events, the azimuthal distribution of the resulting particles in the transverse plane is not uniform. Their energies and momenta also vary with directions. This gives the direct evidence that QGP is a strong coupling matter and its collective expansion can be well described by hydrodynamics. To give a quantitative description, the distribution can be decomposed into Fourier expansions.

$$\frac{dN}{d\phi} \propto 1 + \sum_n 2v_n(p_{\mathrm{T}}) \cos(n(\phi - \Psi_{\mathrm{RP}})) \tag{2.41}$$

where

$$v_n = \langle \cos(n(\phi - \Psi_{\mathrm{RP}})) \rangle \quad \text{and} \quad \Psi_{\mathrm{RP}} = \frac{1}{n} \arctan \frac{\langle p_{\mathrm{T}} \sin(n\phi) \rangle}{\langle p_{\mathrm{T}} \cos(n\phi) \rangle} \tag{2.42}$$

where ϕ is the azimuthal angle, p_{T} is the transverse momentum and Ψ_{RP} is called the azimuthal angle of the reaction plane (RP). Reaction plane is the plane defined by the beam axis and the impact parameter vector, as is shown in Figure 2.11 [21]. At high p_{T}, anisotropy results from the energy loss of jets caused by the traversal in the medium. In the direction with the longest path length in the medium there are least number of particles emitted [22]. At low p_{T}, it results from the geometric anisotropy of the initial overlapping region in the transverse plane. Due to the anisotropy of the fluid pressure in the initial state, the medium expands in different directions with different accelerations and the direction with the largest gradient will have the most particles emitted. The anisotropic expansion due to pressure is sometimes referred to as "flow". The corresponding Fourier coefficients v_n are called "directed flow" (v_1), "elliptic flow" (v_2), "triangular flow" (v_3), "quadrangular flow" (v_4) and so on. The integrated directed flow over the whole p_{T} range should be zero due to the momentum conservation.

For non-central events, v_2 is dominant among all the flow harmonics due to the almond shape of the overlap region. This is especially true in the mid-central region since the eccentricity of the overlapping is usually very large. While in the most peripheral events flow harmonics are small in that the collective behavior is not obvious. In the most central region, since head-on collision occurs, the eccentricity of the overlapping is rather small and the elliptic flow now mainly comes from the initial state fluctuations of the nucleon positions. This is also considered as the main source for other v_n except the elliptic flow since the shape of the overlapping region

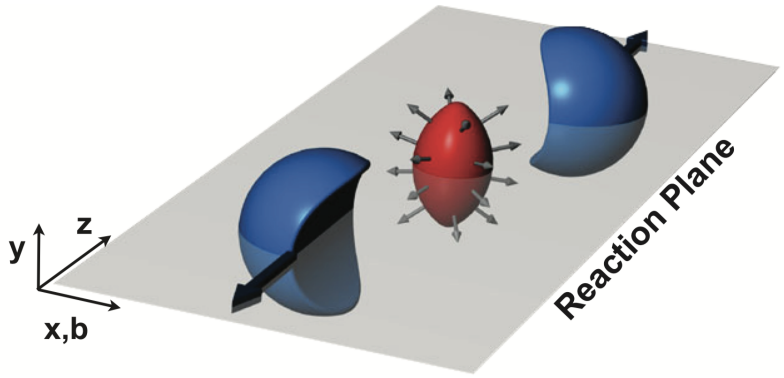

Figure 2.11: The figure shows a non-central collision. The red almond-shaped region is the overlap between two nuclei. It will expand into an anisotropic flow. The plane determined by x and z axes is the reaction plane.

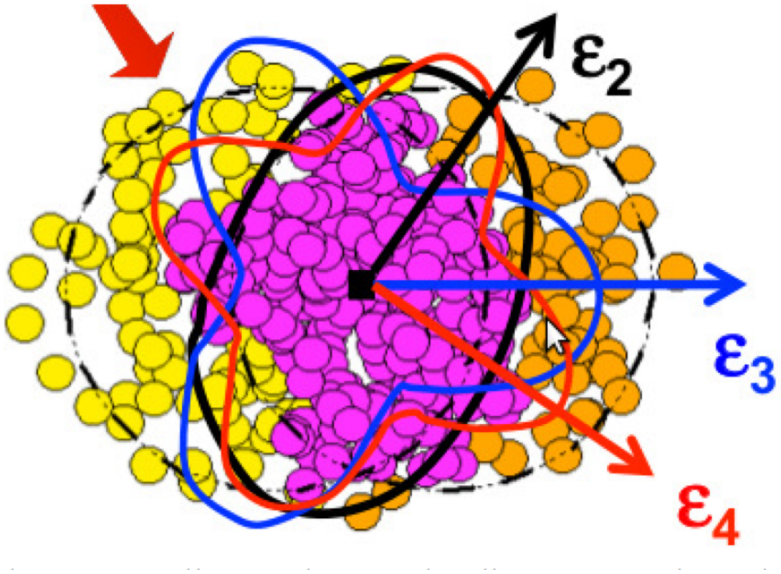

Figure 2.12: Plot of a heavy-ion collision showing the elliptic, triangular and quadrangular eccentricities in the initial state.

usually does not match the one that other flow requires. As a result, v_n ($n \geq 3$) is often considered to vary very weakly with centrality.

Besides the reaction plane, people sometimes also use the n-th order participant plane $\Psi_{\mathrm{PP,n}}$ for analysis [23]. For example the second-order participant plane is the plane aligned with the shorter axis of the region formed by participants, which is located very close to the reaction plane defined before. However reaction plane and

participant plane are both theoretical concepts. They are not observables in real experiments. During heavy ion runs, an experimental observable called event plane (EP) is used. It is typically determined by the energy deposited in the forward calorimeters. One way to obtain the flow harmonics is the event-averaged measurement, or event-plane method. This method has been widely used in the previous Pb+Pb events [24, 25]. In this method Fourier harmonics v_n can be expressed as

$$v_n \equiv \langle \cos(n(\phi - \Phi_n)) \rangle \tag{2.43}$$

where Φ_n is the event plane angle. This method averages the difference between the directions of single charged tracks and event plane. The angular brackets here are averaging over all charged particles in one event first and then over different events. Another way to measure the flow harmonics is to use a vector called per particle "flow vector" $\vec{v}_n = (v_n \cos n\Phi_n, v_n \sin n\Phi_n)$, where Φ_n is the event plane angle. When applying the event-by-event measurement, the distribution of $\vec{v}_n$ is usually assumed to be a two dimensional Gaussian function

$$p(\vec{v}_n) = \frac{1}{2\pi\delta_{v_n}^2} e^{(\vec{v}_n - \vec{v}_n^{\,\mathrm{RP}})^2/(2\delta_{v,n}^2)} \tag{2.44}$$

where $\vec{v}_n^{\,\mathrm{RP}}$ is the average of $\vec{v}_n$, i.e. $\langle \vec{v}_n \rangle$. By symmetry it is located in the reaction plane. The flow harmonics obtained from the previous event-plane method is $\langle v_n \rangle = \langle |\vec{v}_n| \rangle$. When $\delta_{v,n}$ is small, the relation between the results from these two methods is [26]

$$(\vec{v}_n^{\,\mathrm{RP}})^2 \approx \langle v_n \rangle^2 - \delta_{v,n}^2 \tag{2.45}$$

An alternative way to study the properties of v_n is through multi-particle cumulant analysis. Among all the cumulants two-particle correlations will be the main topic in this thesis and discussed throughout the following analysis chapters.

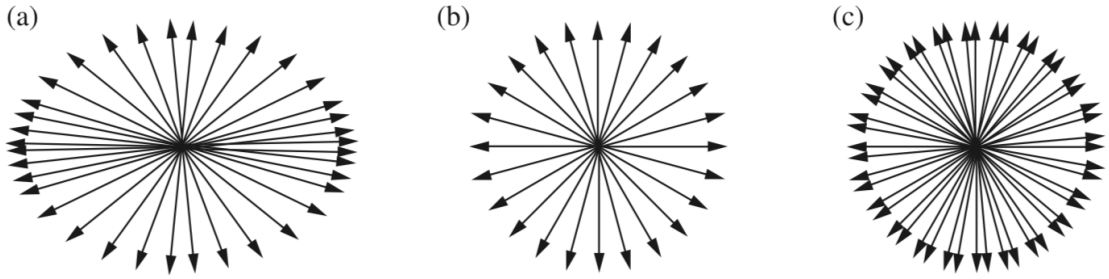

Figure 2.13: For (a), $v_2 > 0, v_2\{2\} > 0$. For (b), $v_2 = 0, v_2\{2\} = 0$. For (c), $v_2 = 0, v_2\{2\} > 0$.

2.4.2 Multi-particle cumulants

Although Eq.(2.41) gives a clear definition for single particle flows, the reaction plane angle can not be directly observed. In heavy ion experiments the direct observable quantity is the two-particle correlation which is given by

$$v_{n,n} = c_2\{2\} = \langle e^{i2(\phi_1-\phi_2)}\rangle \tag{2.46}$$

$$= \langle e^{i2(\phi_1-\psi_{RP}-(\phi_2-\psi_{RP}))}\rangle \tag{2.47}$$

$$= \langle\langle e^{i2(\phi_1-\psi_{RP})}\rangle\langle e^{-i2(\phi_2-\psi_{RP})}\rangle + \delta_2\rangle \tag{2.48}$$

$$= \langle v_2^2 + \delta_2\rangle \tag{2.49}$$

where $v_2 = \langle\cos(2\phi)\rangle$ and $v_2\{2\} = \sqrt{\langle\cos(2(\phi_1-\phi_2))\rangle}$. δ_2 refers to the non-flow correlations such as jet correlation and resonance decays. The second cumulant flow is defined as $v_2\{2\} = \sqrt{v_{n,n}}$. Figure 2.13 indicates how non-flow correlations contribute to $v_2\{2\}$.

If non-flow effects can be ignored, $v_2\{2\} = \sqrt{\langle v_2^2\rangle}$. Four-particle cumulants and six-particle cumulants are defined as the following:

$$c_n\{4\} = \langle v_n^4\rangle - 2\langle v_n^2\rangle^2 \tag{2.50}$$

$$c_n\{6\} = \langle v_n^6\rangle - 9\langle v_n^4\rangle\langle v_n^2\rangle + 12\langle v_n^2\rangle^3 \tag{2.51}$$

The corresponding second-order cumulant flows are then defined as

$$v_n\{4\} = \sqrt[4]{-c_n\{4\}} \tag{2.52}$$

$$v_n\{6\} = \sqrt[6]{\frac{1}{4}c_n\{6\}} \tag{2.53}$$

Generally a Gaussian distribution with a small variance σ is assumed for v_n. In this small variance Gaussian limit, the event-by-event fluctuation can be estimated by σ. Keeping only terms up to the order of σ^2, in the case of $n = 2$ we have

$$\langle v_2^2\rangle = \langle v_2\rangle^2 + \sigma^2, \qquad \langle v_2^4\rangle = \langle v_2\rangle^4 + 6\sigma^2\langle v_2\rangle^2, \qquad \langle v_2^6\rangle = \langle v_2\rangle^6 + 15\sigma^2\langle v_2\rangle^4 \tag{2.54}$$

Using the result $\langle (v_2 - \langle v_2\rangle)^n\rangle = 0$ and the induction method, we could easily obtain,

$$\langle v_2^n\rangle = \langle v_2\rangle^n + \frac{n(n-1)}{2}\sigma^2\langle v_2\rangle^{n-2} \tag{2.55}$$

Combining Eq.(2.52), Eq.(2.53) and Eq.(2.54), we could have,

$$v_2\{2\} = \langle v_2\rangle + \frac{1}{2}\frac{\sigma^2}{\langle v_2\rangle}, \qquad v_2\{4\} = \langle v_2\rangle - \frac{1}{2}\frac{\sigma^2}{\langle v_2\rangle}, \qquad v_2\{6\} = \langle v_2\rangle - \frac{1}{2}\frac{\sigma^2}{\langle v_2\rangle} \tag{2.56}$$

From the above results, we can see $v_2\{4\} \approx v_2\{6\} \approx \sqrt{\langle v_2\rangle^2 - \sigma^2}$, while $v_2\{2\} \approx \sqrt{\langle v_2\rangle^2 + \sigma^2}$. This means $v_2\{2\}$ should be larger than $v_2\{4\}$ and the difference between them is quite important. It represents the magnitude of event-by-event fluctuations plus also the non-flow correlation in the measurement. The ratio $v_2\{4\}/v_2\{2\}$ is usually used as an indication on the event-by-event flow fluctuations.

2.4.3 Collision geometry fluctuations and anisotropic flows

Glauber model uses two overlap Woods-Saxon distributions to generate the initial distribution of participants. The number of participants and their intial positions differ event by event. When two nuclei collide, the region defined by the participant interacting points may not be symmetric about the reaction plane due to fluctuations of the initial nucleon positions. This means the shorter axis of this region will not be alligned with the beam axis. The eccentricity and the triangularity defined within this region are called participant eccentricity and triangularity, which may not be the same as their reaction plane conterparts defined by the directions of beam axis. The participant eccentricity is given by

$$\epsilon_2 = \frac{\sqrt{(\sigma_y^2 - \sigma_x^2)^2 + 4(\sigma_{xy})^2}}{\sigma_y^2 + \sigma_x^2} \tag{2.57}$$

where σ_x^2, σ_y^2 and σ_{xy} are the variances and covariances of participant distributions along x and y directions among different events. If we assume the event-by-event average $\langle x \rangle = \langle y \rangle = 0$, this eccentricity can be written as

$$\epsilon_2 = \frac{\sqrt{\langle r^2 \cos(2\phi) \rangle^2 + \langle r^2 \sin(2\phi) \rangle^2}}{\langle r^2 \rangle} \tag{2.58}$$

$$= \frac{\langle r^2 \cos(2(\phi - \psi_2)) \rangle}{\langle r^2 \rangle} \tag{2.59}$$

where $\langle . \rangle$ first averages over all the participants and then averages over all the events, ψ_2 is the direction of the minor axis defined by the participant interacting region. This direction always has the largest pressure gradient. Single particle harmonic v_2 is defined as

$$v_2 = \langle \cos(2(\phi - \psi_2)) \rangle \tag{2.60}$$

Similarly for triangularity, we have,

$$\epsilon_3 = \frac{\sqrt{\langle r^2\cos(3\phi)\rangle^2 + \langle r^2\sin(3\phi)\rangle^2}}{\langle r^2\rangle} \quad (2.61)$$

$$= \frac{\langle r^2\cos(3(\phi-\psi_3))\rangle}{\langle r^2\rangle} \quad (2.62)$$

and

$$v_3 = \langle\cos(3(\phi-\psi_3))\rangle \quad (2.63)$$

Figure 2.14 shows the distributions of eccentricity and triangularity as a function of number of participants in $\sqrt{s_{\rm NN}}$ = 200 GeV Au+Au collisions from the Glauber Monte Carlo [27]. Both ϵ_2 and ϵ_3 decrease with the number of participants. This is expected since the geometric anisotrtopy of the overlap region should become smaller in central collisions. Figure 2.15 shows the relationship between collective flow harmonics v_2, v_3 and eccentricity, triangularity from a multi-phase transport (AMPT) model [27]. This suggests the anisotropy of the outgoing particle production is a lineaer response of the anisotropy of the initial geometry. This response is larger in v_2. And as the multiplicity increases, response in v_3 will also increase. Figure 2.16 shows the p_T dependence of v_2 and v_3 from AMPT model. Consistent with behavior of ϵ_2 and ϵ_3, v_2 and v_3 both decrease with the number of participants.

Collective flow harmonics can be measured in experiments through two particle correlation functions. An example of the two-particle correlation function in Au+Au is illustrated in Figure **??**. Only the first three harmonics are included in the fits. Higher order harmonics are included in the residuals. Besides the flow contribution, there are also non-flow contributions mainly from jets or resonance decays. Multiple analysis methods have been developed to extract the flow components. One of the most widely used method is called ZYAM method, which we will discuss in the following chapters. The structure of the correlation function in the long range can be decomposed into Fourier series as follows,

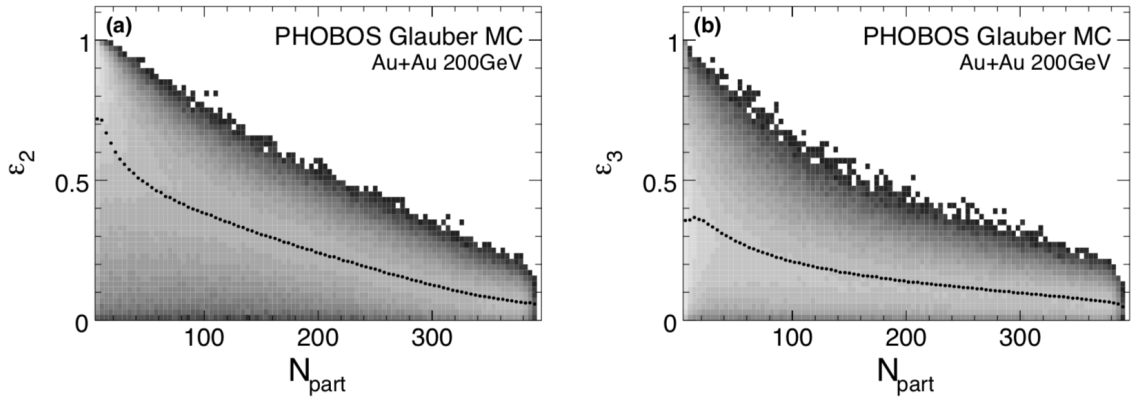

Figure 2.14: Distribution of eccentricity and triangularity as a function of number of participants in $\sqrt{(}s_{NN}) = 200$ GeV Au+Au collisions.

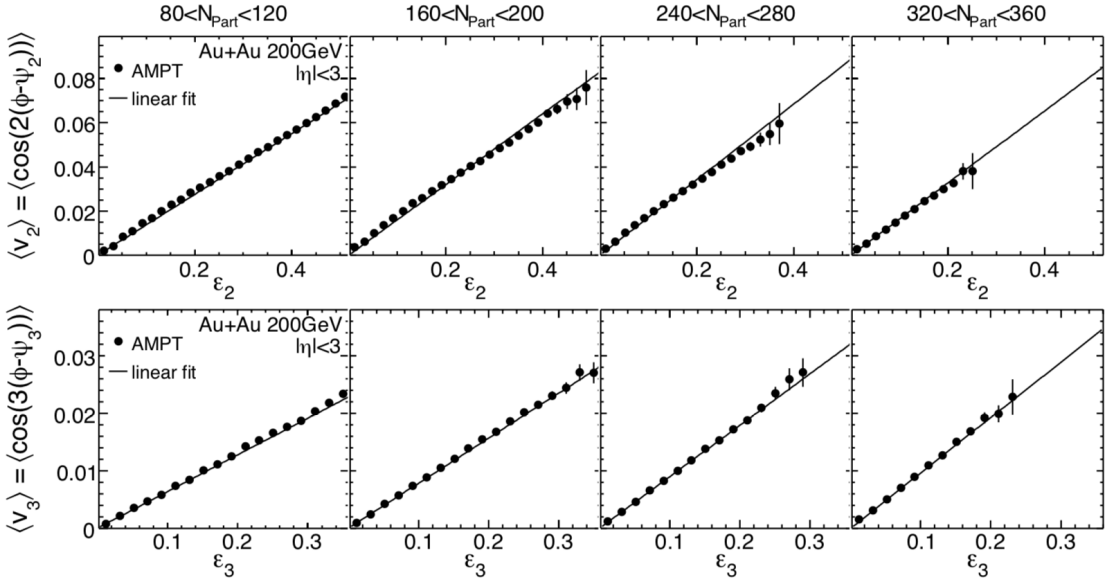

Figure 2.15: Elliptic flow and triangular flow as a function of eccentricity and triangularity respectively in $\sqrt{(}s_{NN}) = 200$ GeV Au+Au collisions using the AMPT model.

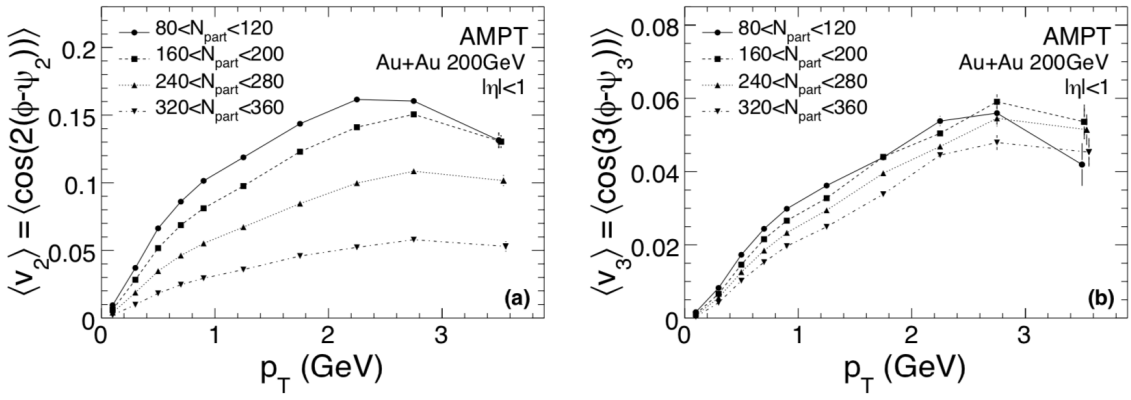

Figure 2.16: Elliptic flow and triangular flow as a function of transverse momentum in $\sqrt{s_{\rm NN}} = 200$ GeV Au+Au collisions using the AMPT model.

$$\frac{\mathrm{d}N^{\rm pairs}}{\mathrm{d}\Delta\phi} = \frac{N^{\rm pairs}}{2\pi}(1 + \sum_n 2V_{n\Delta}\cos(n\Delta\phi)) \tag{2.64}$$

In this section, we will use $V_{n\Delta}$ and $V_{n\Delta}^{\rm flow}$ to represent $v_{n,n}$ and $v_{n,n}^{\rm flow}$. According to the discussion in the previous section, the flow component $V_{n\Delta}^{\rm flow}$ is actually the flow part of the event-by-event average $\langle v_n \times v_n \rangle$. Thus it can be calculated as [27]

$$V_{n\Delta}^{\rm flow} = \frac{\langle \epsilon_n^2 \rangle}{\langle \epsilon_n \rangle^2} \frac{\int \frac{\mathrm{d}N}{\mathrm{d}\eta}(\eta_1)\frac{\mathrm{d}N}{\mathrm{d}\eta}(\eta_2)\,\langle v_n(\eta_1)\rangle\,\langle v_n(\eta_2)\rangle\,\mathrm{d}\eta_1\mathrm{d}\eta_2}{\int \frac{\mathrm{d}N}{\mathrm{d}\eta}(\eta_1)\frac{\mathrm{d}N}{\mathrm{d}\eta}(\eta_2)\mathrm{d}\eta_1\mathrm{d}\eta_2} \tag{2.65}$$

If we assume outgoing particles have a uniform distribution along the pseudorapidity direction and flow harmonics are independent of pseudorapidity, we will have $V_{n\Delta}^{\rm flow} = \langle v_n \times v_n \rangle$ from the above formula. Since v_n is proportional to ϵ_n, the factor $\frac{\langle \epsilon_n^2 \rangle}{\langle \epsilon_n \rangle^2}$ transforms $\langle v_n \rangle \times \langle v_n \rangle$ in the integral into $\langle v_n \times v_n \rangle$. This can avoid including non-flow correlations if we calculate $\langle v_n \times v_n \rangle$ directly. Figure 2.18 shows $V_{n\Delta}^{\rm flow}$ and $V_{n\Delta}$ as a function of $N_{\rm part}$. We can see the flow component is dominant in most cases.

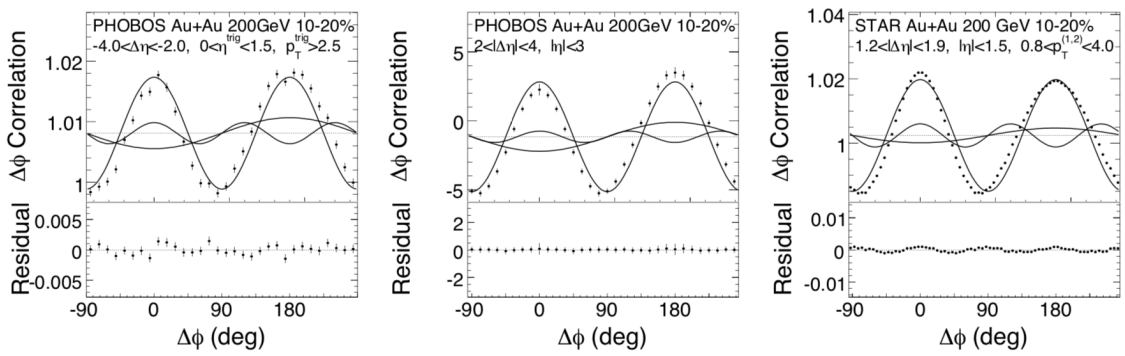

Figure 2.17: One dimensional two particle correlation functions with fits including only the first three harmonics in $\sqrt{(}s_{NN}) = 200$ GeV Au+Au collisions.

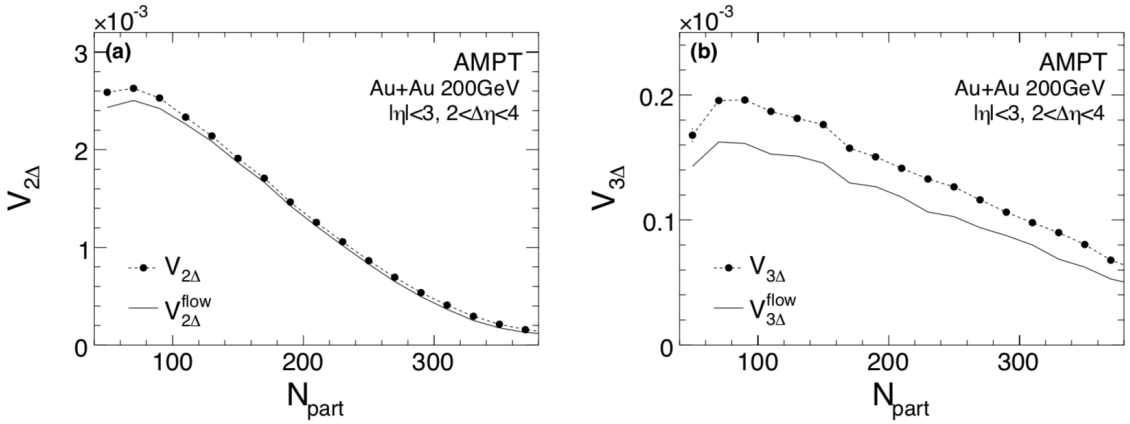

Figure 2.18: Distributions of $V_{2\Delta}$, $V_{2\Delta}^{\rm flow}$, $V_{3\Delta}$, $V_{3\Delta}^{\rm flow}$ as a function of $N_{\rm part}$ in $\sqrt{s_{\rm NN}} =$ 200 GeV Au+Au collisions using the AMPT model.

2.5 Relativistic hydrodynamics

2.5.1 Basic equations

In this section, we assume the metric tensor $g^{\mu\nu} = g_{\mu\nu} = diag\{+,-,-,-\}$. The basic equations in relativistic hydrodynamics are baryon density conservation and energy-momentum conservation.

$$\partial_\mu j^\mu = 0 \tag{2.66}$$

$$\partial_\nu T^{\mu\nu} = 0 \tag{2.67}$$

where j^μ is the baryon flux and $T^{\mu\nu}$ is the energy-momentum tensor. We can obtain the baryon density $n = u_\mu j^\mu$ and the energy density $\varepsilon = u_\mu u_\nu T^{\mu\nu}$ using the Lorentz four-velocity u_μ, which satisfies $u_\mu u^\mu = 1$. When there is an electromagnetic field, the second conservation law above can be written as

$$\partial_\nu T^{\mu\nu} = F^{\mu\nu} j_\nu \tag{2.68}$$

where $F^{\mu\nu}$ is the electromagnetic tensor. Since it is an antisymmetric tensor, we have $u_\mu u_\nu F^{\mu\nu} = 0$. The energy-momentum conservation is equivalent to,

$$u_\mu \partial_\nu T^{\mu\nu} = j_\nu E^\nu \tag{2.69}$$

$$\Delta^\alpha_\mu \partial_\nu T^{\mu\nu} = n E^\alpha \tag{2.70}$$

where $\Delta^{\mu\nu}$ is the spatial projection tensor orthogonal to u^μ.

Generally we can decompose j^μ and $T^{\mu\nu}$ using the metric tensor as follows,

$$j^\mu = g^{\mu\nu} j_\nu = (\Delta^{\mu\nu} + u^\mu u^\nu) j_\nu = n u^\mu + \Delta^{\mu\nu} j_\nu = n u^\mu + v^\mu \tag{2.71}$$

$$T^{\mu\nu} = g^{\mu\alpha} g^{\nu\beta} T_{\alpha\beta} = (\Delta^{\mu\alpha} + u^\mu u^\alpha)(\Delta^{\nu\beta} + u^\nu u^\beta) T_{\alpha\beta} = T_0^{\mu\nu} + T_1^{\mu\nu} \tag{2.72}$$

The first term nu^μ in the baryon flux decomposition represents the baryon flux in the perfect fluid. While the second term v^μ is related to the diffusion process. In the decomposition of energy-momentum tensor, $T_0^{\mu\nu}$ is the energy momentum tensor for the perfect fluid while $T_1^{\mu\nu}$ is the additional term arising from viscosity and dissipation. From the equations above, we have,

$$T_0^{\mu\nu} = \varepsilon u^\mu u^\nu - P\Delta^{\mu\nu} \tag{2.73}$$

$$T_1^{\mu\nu} = h^\mu u^\nu + h^\nu u^\mu - \Pi\Delta^{\mu\nu} + \pi^{\mu\nu} \tag{2.74}$$

where Π and $\pi^{\mu\nu}$ represent bulk and shear viscosity respectively.

$$h^\mu = \Delta^{\mu\nu} T_{\nu\alpha} u^\alpha \tag{2.75}$$

is associated with the heat flux satisfying $h^\mu u_\mu = 0$.

Plugging Eq. (2.71), (2.72), (2.73) and (2.74) into (2.66), (2.69) and (2.70), we obtain the basic equations in hydrodynamics,

$$0 = \partial_\mu j^\mu = \dot{n} + n\theta + \partial_\mu v^\mu \tag{2.76}$$

$$j_\nu E^\nu = u_\nu \partial_\mu T^{\mu\nu} = (\varepsilon + P + \Pi)\theta + \dot{\varepsilon} + \partial_\mu h^\mu - \dot{u}_\nu h^\nu - \pi^{\mu\nu}\partial_\mu u_\nu \tag{2.77}$$

$$nE_\alpha = \Delta_{\nu\alpha}\partial_\mu T^{\mu\nu} = (\varepsilon+P+\Pi)\dot{u}_\alpha - \partial_\mu(P+\Pi)\Delta^\mu_\alpha + h^\mu\partial_\mu u_\alpha + \dot{h^\nu}\Delta_{\nu\alpha} + h_\alpha\theta + \Delta_{\nu\alpha}\partial_\mu\pi^{\mu\nu} \tag{2.78}$$

where $\theta = \partial_\mu u^\mu$ and $\dot{a} = u^\mu\partial_\mu a$. The equations above are called continuity equation, energy equation and momentum equation respectively. In the case of perfect fluid, they have simple forms like,

$$0 = \dot{n} + n\theta \tag{2.79}$$

$$j_\nu E^\nu = (\varepsilon + P)\theta + \dot{\varepsilon} \tag{2.80}$$

$$nE_\alpha = (\varepsilon + P)\dot{u}_\alpha - \Delta^\mu_\alpha \partial_\mu P \tag{2.81}$$

Eq. (2.81) is called the Euler equation in relativistic hydrodynamics. In the non-relativistic limit, the thermal speed of microscopic particles is much smaller than the speed of light. Thus we could assume $P \ll \varepsilon$ and $\varepsilon \approx \rho$, where ρ is the mass density. The velocity of the macroscopic fluid motion is also small compared to the speed of light, which means $\gamma \approx 1$. Therefore, in the absence of the electromagnetic field, we obtain the Euler equation in the non-relativistic fluid dynamics.

$$\vec{a} = -\frac{1}{\rho}\nabla P \tag{2.82}$$

2.5.2 Navier-Stokes equations

From the knowledge of thermodynamics, we have

$$\varepsilon + P = Ts + \mu n \tag{2.83}$$

Thus we define the entropy flux in the equilibrium state as follows,

$$s^\mu_0 = su^\mu_0 = (\varepsilon + P)\beta^\mu - \alpha j^\mu_0 = P\beta^\mu + \beta_\lambda T^{\lambda\mu}_0 - \alpha j^\mu_0 \tag{2.84}$$

where $\beta_\mu = \beta u_\mu$. Through simple calculations, we also obtain the following relationship,

$$\begin{aligned}
d(P\beta^\mu) &= u^\mu d(P\beta) + P\beta du^\mu = u^\mu(nd\alpha - \varepsilon d\beta) - Pu^\mu d\beta + Pd\beta^\mu && (2.85)\\
&= nu^\mu d\alpha - (\varepsilon + P)u^\mu d\beta + Pd\beta^\mu && (2.86)\\
&= nu^\mu d\alpha - [(\varepsilon + P)u^\mu u^\lambda - Pg^{\mu\lambda}]d\beta^\lambda && (2.87)\\
&= j^\mu_0 d\alpha - T^{\lambda\mu}_0 d\beta_\lambda && (2.88)
\end{aligned}$$

Therefore,

$$ds_0^\mu = d(P\beta^\mu) + d(T_0^{\lambda\mu}\beta_\lambda) - d(\alpha j_0^\mu) = -\alpha dj_0^\mu + \beta_\lambda dT_0^{\lambda\mu} \tag{2.89}$$

From the last equation above, using the conservation laws of the baryon density and the four-momentum, it is easy to see that entropy is also conserved in the perfect fluid,

$$\partial_\mu s_0^\mu = 0 \tag{2.90}$$

Here we introduced a fundamental assumption that Eq. (2.89) is also valid for a small deviation from an equilibrium state to a neighbouring non-equilibrium state [28].

$$ds^\mu = -\alpha dj^\mu + \beta_\lambda dT^{\lambda\mu} \tag{2.91}$$

This means in a non-equilibrium state, entropy flux can be defined as

$$s^\mu = P\beta^\mu + \beta_\lambda T^{\lambda\mu} - \alpha j^\mu + \text{second order term} \tag{2.92}$$

Then consider the case of electromagnetic field, from Eq. (2.92), and ignore the second order corrections,

$$\begin{aligned}
\partial_\mu s^\mu &= \partial_\mu[P\beta^\mu + \beta_\lambda T^{\lambda\mu} - \alpha j^\mu] && (2.93)\\
&= j_0^\mu \partial_\mu \alpha - T_0^{\lambda\mu}\partial_\mu\beta_\lambda + \beta_\lambda \partial_\mu T^{\lambda\mu} + T^{\lambda\mu}\partial_\mu\beta_\lambda - \partial_\mu\alpha j^\mu - \alpha\partial_\mu j^\mu && (2.94)\\
&= -(j^\mu - j_0^\mu)(\partial_\mu\alpha + \frac{E_\mu}{T}) + (T^{\lambda\mu} - T_0^{\lambda\mu})\partial_\mu\beta_\lambda && (2.95)
\end{aligned}$$

where

$$\beta_\lambda \partial_\mu T^{\lambda\mu} = \beta_\lambda F^{\lambda\mu} j_\mu = -\nu_\mu \frac{E_\mu}{T} \tag{2.96}$$

Plugging Eq. (2.71), (2.72), (2.73) and (2.74) into (2.93), we can obtain

$$\partial_\mu s^\mu = -\nu^\mu(\partial_\mu\alpha + \frac{E_\mu}{T}) + h^\mu(\partial_\mu\beta + \beta\dot{u}_\mu) - \frac{\Pi}{T}\theta + \frac{\pi^{\mu\lambda}}{T}\partial_\mu u_\lambda \tag{2.97}$$

Recall in thermodynamics, we have formula

$$d\frac{P}{T} = nd\alpha - \varepsilon d\beta \tag{2.98}$$

This is equivalent to

$$\partial_\mu P = \frac{n}{\beta}\partial_\mu\alpha - \frac{\varepsilon + P}{\beta}\partial_\mu\beta \tag{2.99}$$

Combined with Eq. (2.81), we obtain the identity

$$\frac{n}{\varepsilon + P}(\partial_\mu\alpha + \frac{E_\mu}{T}) = \beta\dot{u}_\mu - u_\mu\dot{\beta} + \partial_\mu\beta \tag{2.100}$$

which can be rewritten as

$$\nu^\mu\frac{n}{\varepsilon + P}(\partial_\mu\alpha + \frac{E_\mu}{T}) = \nu^\mu(\beta\dot{u} + \partial_\mu\beta) \qquad h^\mu\frac{n}{\varepsilon + P}(\partial_\mu\alpha + \frac{E_\mu}{T}) = h^\mu(\beta\dot{u} + \partial_\mu\beta) \tag{2.101}$$

Using Eq. (2.101) in (2.97), we finally have

$$\partial_\mu s^\mu = q^\mu(\partial_\mu\beta + \beta\dot{u}_\mu) - \frac{\Pi}{T}\theta + \frac{\pi^{\mu\lambda}}{T}\partial_\mu u_\lambda \tag{2.102}$$

$$= q^\mu\frac{n}{\varepsilon + P}(\partial_\mu\alpha + \frac{E_\mu}{T}) - \frac{\Pi}{T}\theta + \frac{\pi^{\mu\lambda}}{T}\partial_\mu u_\lambda \tag{2.103}$$

where q^μ is a spatial vector representing the heat flux correctly to the first order.

$$q^\mu = h^\mu - \frac{\varepsilon + P}{n}\nu^\mu \tag{2.104}$$

From the principle of the entropy increase, non-equilibrium systems always evolve to maximize its entropy production. Therefore $\partial_\mu s^\mu \geq 0$ must be satisfied. Considering the isotropic properties of the fluid, the expression for q^μ, Π and $\pi^{\lambda\mu}$ can

be determined. For example, since q^μ is a spacial vector, from the requirement $q^\mu(\partial_\mu\beta + \beta\dot{u}_\mu) \geq 0$, q^μ must be proportional to $-\Delta^{\mu\nu}(\partial_\nu\beta + \beta\dot{u}_\nu)$. Therefore we have,

$$q^\mu = -\kappa T^2 \Delta^{\mu\nu}(\partial_\nu\beta + \beta\dot{u}_\nu) \tag{2.105}$$

or

$$q^\mu = -\kappa T^2 \Delta^{\mu\nu}\frac{n}{\varepsilon + P}(\partial_\nu\alpha + \frac{E_\nu}{T}) \tag{2.106}$$

where κ is called thermal conductivity, $\kappa > 0$. From this equation, we see the entropy increase originated from q^μ is caused by the dissipation of thermal and electrical conduction. The production rate of entropy due to this term in the particle rest frame is therefore

$$q^\mu(\partial_\mu\beta + \beta\dot{u}_\mu) = \kappa T^2(\nabla\frac{1}{T} + \frac{1}{T}\dot{\mathbf{v}})^2 \tag{2.107}$$

Using the logic above, from $-\Pi\theta \geq 0$, we have

$$\Pi = -\zeta\theta \tag{2.108}$$

where ζ is the bulk viscosity, $\zeta > 0$. Finally let's determine the form of $\pi^{\mu\nu}$. From the knowledge of tensor decomposition, we obtain

$$\partial_{(\mu}u_{\nu)} = \frac{1}{3}\theta\Delta_{\mu\nu} + \dot{u}_{(\mu}u_{\nu)} + \partial_{\langle\mu}u_{\nu\rangle} \tag{2.109}$$

where the parentheses in the lower indices indicate tensor symmetrization and the angular brackets in the lower indices mean the symmetric traceless part of the spatial projection. They are defined as

$$A^{(\mu\nu)} = \frac{1}{2}(A^{\mu\nu} + A^{\nu\mu}) \tag{2.110}$$

$$A_{\langle\lambda\mu\rangle} = (\Delta^{\alpha}_{(\lambda}\Delta^{\beta}_{\mu)} - \frac{1}{3}\Delta_{\lambda\mu}\Delta^{\alpha\beta})A_{\alpha\beta} \tag{2.111}$$

Therefore from the entropy principle

$$0 \leq \pi^{\mu\nu}\partial_{\mu}u_{\nu} = \pi^{\mu\nu}\partial_{(\mu}u_{\nu)} = \pi^{\mu\nu}\partial_{\langle\mu}u_{\nu\rangle} \tag{2.112}$$

we have

$$\pi^{\mu\nu} = 2\eta_S\partial^{\langle\mu}u^{\nu\rangle} \tag{2.113}$$

where η_S is the shear viscosity, $\eta_S > 0$.

There are two characteristic length widely used in hydrodynamics. One is the mean free path λ representing the microscopic length. The other one is used in macro scale and is usually chosen to be one spatial dimension of the system R. It can be estimated using the ratio of a macroscopic quantity, for example ε, to its gradient, $R \sim \varepsilon/|\partial\varepsilon|$, which means R^{-1} can be considered to be proportional to ∂_{μ}. The Knudsen number is introduced via $K \equiv \lambda/R$ [29]. Hydrodynamics can be applied if $\lambda \ll R$. Since Knudsen number is pretty small, we could expand the conserved current and energy-momentum tensor in terms of K, that is, in terms of $\lambda\partial_{\mu}$. This is called the gradient expansion. The zeroth order in the expansion corresponds to the theory of perfect fluid. The first order leads to Navier-Stokes equations. The phenomenological coefficients obtained above are called the first order transport coefficients. They are proportional to λ, making the corresponding dissipative term a first order quantity of K. For example.

$$\frac{\pi^{\mu\nu}}{\varepsilon} \sim \frac{\eta_S\partial\cdot u}{\varepsilon} \sim \frac{nm\lambda\partial\cdot u}{\varepsilon} \sim \lambda\partial_{\mu} \equiv K \tag{2.114}$$

$$\frac{q^{\mu}}{\varepsilon} \sim \frac{\kappa T\partial_{\mu}\alpha}{\varepsilon} \sim \frac{nm\lambda\partial_{\mu}\alpha}{\varepsilon} \sim \lambda\partial_{\mu} \equiv K \tag{2.115}$$

The second order theory of hydrodynamics have different descriptions. One of the most famous theories is Israel-Stewart (IS) equations. The complete IS equations are derived from kinetic theory and a technique called 14-moment approximation is used where 14 independent variables are introduced as functions of dissipative terms. The expressions for the second order transport coefficients can be derived from the differential equations that those independent variables satisfy [28].

2.6 Hydrodynamic evolution in heavy ion physics

The anisotropy of the final particle production can be used as a judgement on whether the interaction between high p_{T} partons after the heavy ion collision is strong or weak. If quarks and gluons form a weakly coupled gas-like medium, the outgoing particles can randomly choose the directions of their motion even in the anisotropic initial overlap region. This will result in a nearly isotropic distribution of final particles, which is indicated by the blue line in Figure 2.19 [30]. However if a strongly coupled fluid is formed, hydrodynamics becomes applicable which transforms the anisotropy in the initial coordinate space to anisotropy in the final momentum space, leading to the observable anisotropic flows in experiments. The measurement of anisotropic flows at LHC and RHIC are consistent with the hydrodynamic calculations suggesting QGP is a strongly-coupled medium.

The applicability of hydrodynamics suggests mean free path λ is much smaller than the spatial dimension of the system R,

$$\frac{\eta}{\rho R v} \approx \frac{\rho \lambda v}{\rho R v} \approx \frac{\lambda}{R} \ll 1 \tag{2.116}$$

where v is the microscopic velocity. This tells us the hydrodynamic limit leads to a very low shear viscosity. In hydrodynamics, the ratio η/s represents how far the momentum can be transferred to nearby fluid elements. For weak coupling,

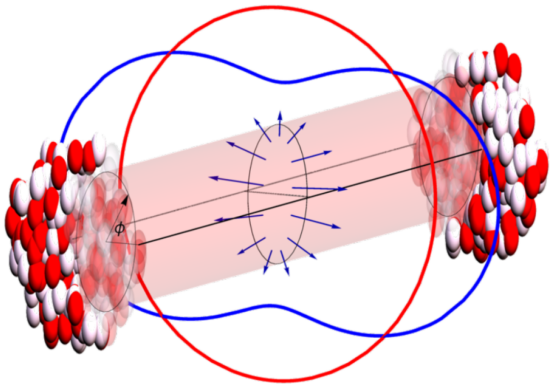

Figure 2.19: A sketch representing the expansion with weakly or strongly coupled interacting particles.

momentum can be transferred through a large distance due to lack of interactions. Shear viscosity can easily lead to large dissipative effect. In hydrodynamics $\eta/Ts = \eta/(\epsilon + p) \propto \lambda$, a sufficient large η/s ratio makes the mean free path λ larger than the de Broglie wavelength $1/T$. Therefore quasi-particles are well defined and a long distance for the momentum transfer is implied by the large mean free path. Whereas in strongly coupled systems, η/s ratio is small enough to make the mean free path computed by the above formula less than de Broglie wavelength $1/T$. Quasi-particles cannot be defined. The fluid is such a strongly-coupled medium that momentum cannot be transferred for a significant distance and shear viscosity can hardly be dissipated into heat. Besides hydrodynamics, other models used to describe the dynamics of the medium produced in heavy ion collisions should be consistent with this property. For example the AMPT model mentioned in the previous chapter implicitly assumes the mean free path of the producing particles is smaller than their de Broglie wavelength, which complies with a low viscous hydrodynamics.

The zeroth order hydrodynamics describe the dynamics of a perfect fluid. Higher order hydrodynamics allow for gradients that lead to small deviation from equilibrium states due to viscous effect. The hydrodynamic evolution is responsible for the time period after the collision and before hadronization. When the medium temperature decreases into the cross-over region T_c, the phase transition from QGP to the hadron

gas begins. This is called "freeze-out". The system is converted into a distribution of hadrons and its evolution is determined by the properties of the hadron gas.

In order to determine how the ratio η/s changes with temperature, we could match the theoretical calculation using the models based on different η/s functional forms to the observed data in experiments. A common measurement we could use is the distribution of the anisotropic flows v_n as a function of centrality. In addition to the η/s functional form, the model will also deal with initial state fluctuations in the overlap region of a collision to produce correct anisotropic flow values. During central collisions initial fluctuation is important to generate anisotropic flows, since ϵ_n becomes very small when there is only a small impact parameter. Moreover odd harmonics rely on the modeling of initial fluctuations to match the observed data. This is because by the symmetry of the collision geometry odd harmonics should always vanish, which contradicts the large v_3 observations during the measurement.

Figure 2.20 shows several different parametrization for the function $(\eta/s)(T)$ [31]. The blue line assumes a constant η/s value over the whole temperature interval. The other four parametrizations assume piece-wise linear distributions. This is the same as assuming a minimum value of η/s at $T = T_c$ somewhere in the cross-over phase transition region. While in the hadron resonance gas (HRG) and QGP phases, the ratio is linearly decreasing (increasing) with the temperature. The parametrization is required to match the measurement of the elliptic flow $v_2\{2\}$ in the mid-peripheral region at LHC. The measurement of flow coefficients as a function of centrality and its comparison with the results from the above five $(\eta/s)(T)$ parametrizations are shown in Figure 2.21. The left panel is for 2.76 TeV PbPb events at LHC, while the right panel is for 200 GeV AuAu events at RHIC. Curves from top to bottom are $v_2\{2\}$, $v_3\{2\}$ and $v_4\{2\}$ on the left and $v_2\{2\}$, $v_3\{2\}$ and $v_4\{3\}$ on the right. By construction all the parametrization results should match the $v_2\{2\}$ LHC mid-peripheral data. Differences begin to appear in the most peripheral region. $(\eta/s)(T)$ calculations

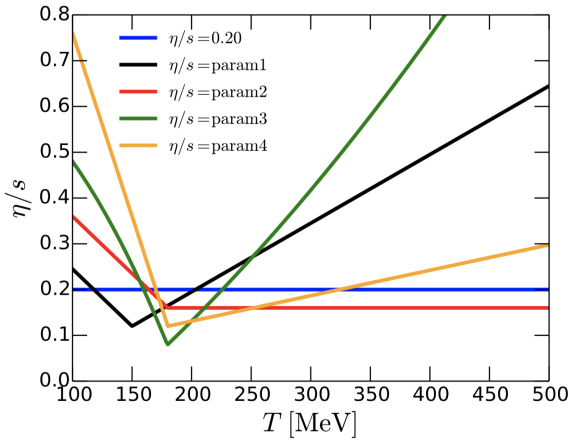

Figure 2.20: Different parametrization methods for $\eta/s(T)$ in order to match the elliptic flow measurement in the mid-peripheral collisions at LHC .

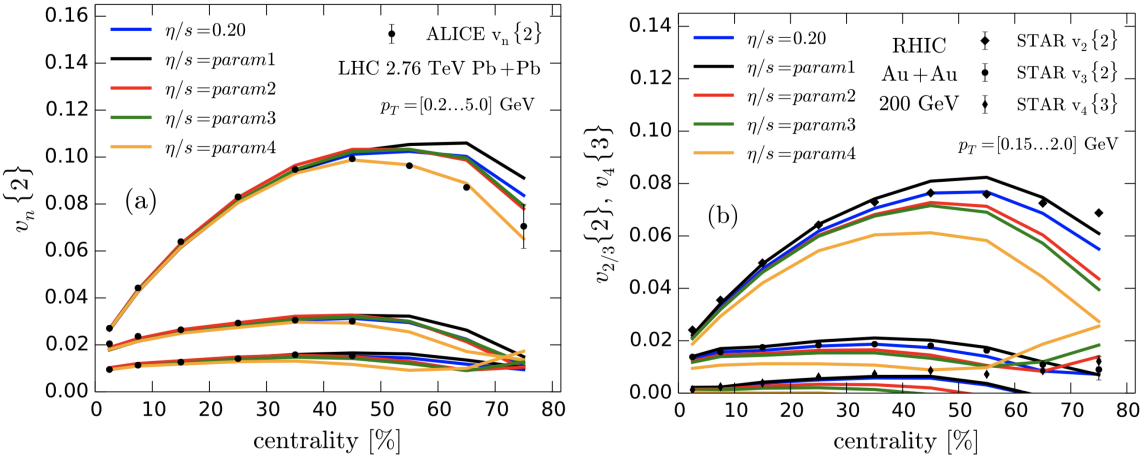

Figure 2.21: Centrality dependence of cumulant flow coefficients in 2.76 TeV PbPb events at LHC and 200 GeV AuAu events at RHIC, compared with results from different parametrization of $\eta/s(T)$.

and LHC measurement are consistent for higher order flows, which can not add any constraint on the functional form of $(\eta/s)(T)$. However in RHIC measurement it is easy to see that the blue curve and black curve give a better prediction for the data. The measurement shows $(\eta/s)_{\rm min}$ should vary between 0.08 to 0.2 at RHIC energies.

Another way to do this is to assume the ratio $(\eta/s)(T)$ has the following piece-wise linear functional form,

$$(\eta/s)(T) = \begin{cases} (\eta/s)_{\rm min} + (\eta/s)_{\rm slope}(T - T_c) & T > T_c \\ (\eta/s)_{\rm hrg} & T < T_c \end{cases} \tag{2.117}$$

Different from the previous case, here $(\eta/s)(T)$ in the HRG phase is assumed to be a constant value. Applying the Bayesian parameter estimation and fitting to the RHIC and LHC data [32] gives

$$(\eta/s)_{\rm min} \approx (0.07^{+0.05}_{-0.04}) \tag{2.118}$$

which is almost the same value as the lower limit of the η/s ratio given by quantum theories $\eta/s = 1/4\pi \approx 0.08$. All these results indicate that quark-gluon plasma has almost the smallest viscosity among all kinds of the fluids and is probably the most perfect liquid known in nature.

Chapter 3

Collectivity in small systems

3.1 Hydrodynamic calculation in small systems

Central pPb interaction has a similar multiplicity to peripheral PbPb one. We can assume the dependence of the final track multiplicity in central pPb on the number of participants is similar to that in peripheral PbPb. It is interesting to see whether hydrodynamic model is still applicable in these small systems. However it should be mentioned that as the impact parameter increases, the uncertainty from hydrodynamic calculation becomes important and should be taken into account. Actually few calculations for peripheral PbPb events at 2.76 TeV can match the experimental results very well. Hydrodynamics will be less applicable as the size of the system decreases. Such small systems are probably already at the limit of the hydrodynamic model.

In heavy ion physics the number of participants is closely related to the impact parameter. For small systems such as pPb, the distribution of number of participants as a function of impact parameter is shown in the left panel of Figure 3.1 [33]. In this calculation a Wood-Saxon distribution is assumed for the Pb nucleus. It is easy to see there are large fluctuations of $N_{\rm part}$ at a fixed impact parameter, which makes it

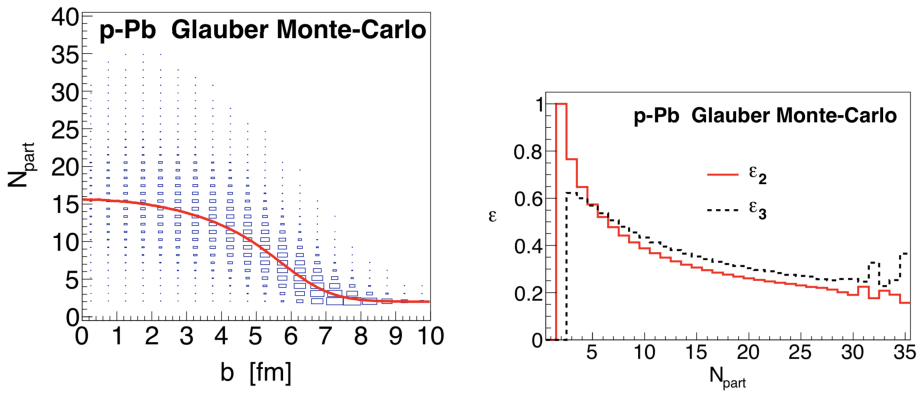

Figure 3.1: The left plot shows the distribution of number of participants as a function of the impact parameter in the pPb Glauber Monte Carlo. The right plot shows the distribution of eccentricity and triangularity as a function of the number of participants

impossible to use the impact parameter to determine centrality classes in pPb events. Intervals of number of participants can simply be used to represent centrality classes in pPb collisions. The right panel shows the distribution of ϵ_2 and ϵ_3 as a function of N_{part}. Similar to the previous AuAu events discussed in the last chapter, both eccentricity and triangularity decrease with centrality.

If a dense medium is produced in pPb, we could assume hydrodynamic model is still correct. In this case viscous hydrodynamic calculation can be applied to produce the final particle distributions. The initial entropy can be regarded as the sum of contributions from each nucleons. The contribution from each nucleon is a two dimensional Gaussian distribution in the transverse plane. The entropy density is adjusted to match the final particle multiplicity. The second order viscous hydrodynamics is used with shear and bulk viscosity terms to account for the deviation from the equilibrium states. The evolution will stop at the freeze-out temperature.

The results from this hydrodynamic calculation are shown in Figure 3.2 and Figure 3.3 [33]. In Figure 3.2, $v_2\{\Psi_2\}$ and $v_3\{\Psi_3\}$ are single particle elliptic and triangular flows $\langle v_2 \rangle$ and $\langle v_3 \rangle$ with respect to the event plane angles Ψ_2 and Ψ_3. $v_2\{2\}$ and $v_3\{2\}$ are the second and third flow coefficients obtained using two particle

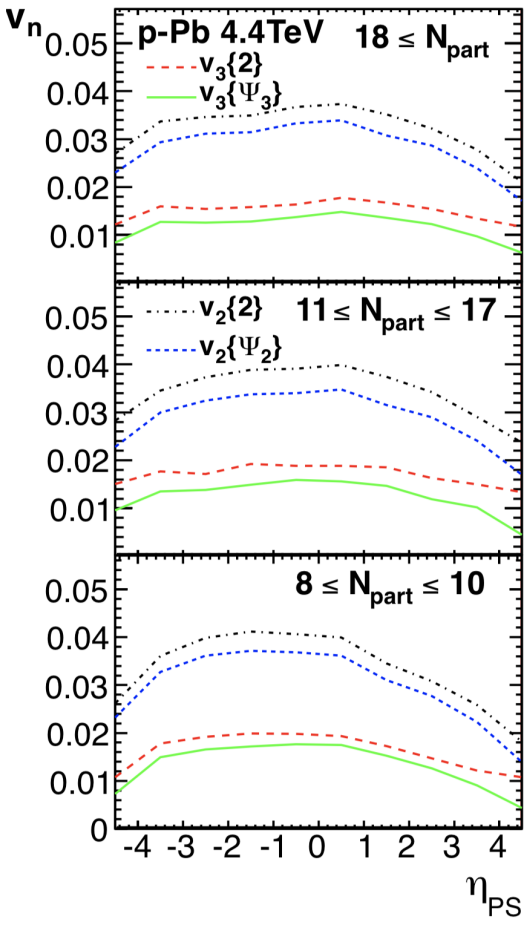

Figure 3.2: The distribution of v_2 and v_3 as a function of pseudorapidity in pPb 4.4 TeV from the viscous hydrodynamic calculation.

correlations, i.e. $v_n\{2\} = \sqrt{\langle v_n^2 \rangle}$. As discussed before, the difference between $v_n\{\Psi_n\}$ and $v_n\{2\}$ represents the event-by-event fluctuations. Both v_2 and v_3 do not show a significant dependence on centrality. Since eccentricity and triangularity decrease with centrality, the hydrodynamic responses v_2/ϵ_2 and v_3/ϵ_3 become larger in central events. In Figure 3.3, collective flows increase with transverse momentum below 2.5 GeV. In the low p_{T} region v_n do not vary with centrality dramatically, while in high p_{T} v_n decrease with centrality slightly.

The above calculation can also be applied to dAu events at RHIC. In the next section, we can see since dAu generally has a larger initial eccentricity than pPb, its

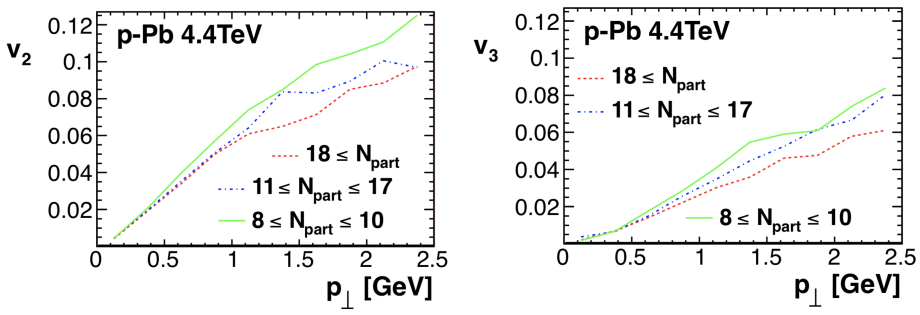

Figure 3.3: The distribution of v_2 and v_3 as a function of transverse momentum in pPb 4.4 TeV from the viscous hydrodynamic calculation.

measurement is quite consistent with the prediction given by hydrodynamics.

3.2 Observation of long-range correlations in pPb at $\sqrt{s_{\rm NN}} = 5.02$ TeV in LHC and dAu at $\sqrt{s_{\rm NN}} = 200$ GeV in RHIC

3.2.1 Peripheral subtraction

The collectivity in small systems was first studied in 5.02 TeV pPb events at ATLAS in LHC. Figure 3.4 shows the two dimensional two-particle correlation functions and their corresponding pre-trigger yields [34]. A detailed description on the construction of two-particle correlation functions and the definition of pre-trigger yields can be found in Chapter 5. Since non-flow contributions, such as high-$p_{\rm T}$ resonances and Bose-Einstein correlations, contribute only to the short range correlation, a large $|\Delta\eta|$ cut is implemented to remove the non-flow contribution from the correlation function. In these figures, the total transverse energy deposited in the forward calorimeters $\sum E_{\rm T}^{\rm Pb}$ are used to characterize the collision centrality. $\sum E_{\rm T}^{\rm Pb} < 20$ and $\sum E_{\rm T}^{\rm Pb} > 80$ represent the peripheral and central event classes respectively. The bottom left plot is the azimuthal dependence of the pre-trigger yields. The ZYAM procedure is

used to exclude the uncorrelated pairs from the correlation function. The pedestal representing uncorrelated pairs is determined by the minimum value of a second-order polynomial fit to $C(\Delta\phi)$. The near-side and away-side integrated yields in the bottom right panel are computed by the integration within $|\Delta\phi| < \pi/3$ and $|\Delta\phi| > 2\pi/3$ respectively. The red histogram represents the difference between the near-side and away-side yields. It varies very weakly with centrality suggesting the near-side and away-side enhancements have almost the same growth as the centrality increases.

Since the difference between the near-side and away-side yields mostly comes from the recoil component, this analysis assumes the recoil component on the away-side is centrality-independent. Figure 3.5 illustrates the difference between central and peripheral per-trigger yields $\Delta Y(\Delta\phi)$ in different p_{T} bins [34]. By subtracting peripheral $Y_p(\Delta\phi)$ from $Y_c(\Delta\phi)$, all the centrality independent correlations including the recoil component disappear with only the flow component left. $\Delta Y(\Delta\phi)$ can be decomposed into Fourier series to obtain the amplitude of the n-th flow,

$$a_n = \langle \Delta Y(\Delta\phi) \cos n\Delta\phi \rangle \tag{3.1}$$

The harmonics of the n-th flow for the flow correlation is thus given by

$$v_{n,n} = a_n/(b^{\mathrm{C}}_{\mathrm{ZYAM}} + a_0) \tag{3.2}$$

where $b^{\mathrm{C}}_{\mathrm{ZYAM}}$ is the ZYAM pedestal for the central event class. Factorization can be used to obtain single particle harmonics from $v_{n,n}$. Detailed descriptions about ZYAM procedure and factorization relationship can also be found in Chapter 5.

Similar analysis has also been applied to the 200 GeV dAu measurement at PHENIX in RHIC. Figure 3.6 demonstrates the central pre-trigger yield Y_c, peripheral per-trigger yield Y_p and their difference $\Delta Y(\Delta\phi) = Y_c - Y_p$ [35]. Different from the previous pPb case which relies on a second polynomial fit to find b_{ZYAM}, a

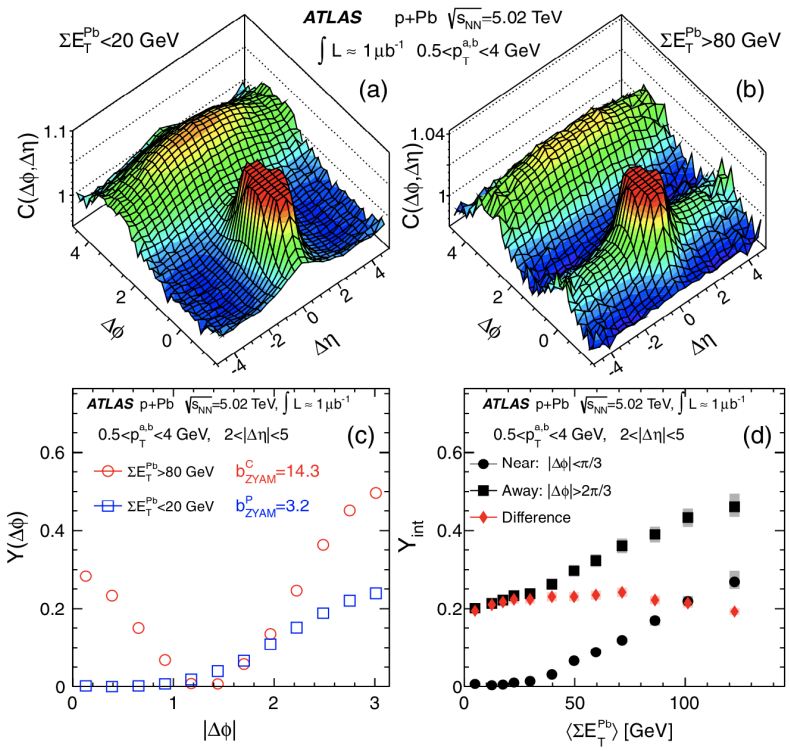

Figure 3.4: The upper two panels are 2D two particle correlation functions in central and peripheral regions. The bottom left is the azimuthal dependence of the per-trigger yield. The bottom right is the centrality dependence of the integrated yields on both the near side and away side as well as their difference.

functional form of a constant plus two Gaussians centered at $\Delta\phi = 0$ and π is used to determine b_{ZYAM} here. Since PHENIX does not have sufficiently large $|\Delta\eta|$ coverage to remove the whole short-range jet correlation, the major contribution of the systematic uncertainties in this measurement will come from the remaining part of this short-range correlation. Eq.(3.1) and Eq.(3.2) are also used to find single particle harmonics from long-range correlations.

Figure 3.7 shows the distributions of v_2 from both pPb and dAu measurement as a function of p_{T} [35]. The blue dashed line uses the hydrodynamic calculation similar to the one described in Section 3.1 but for dAu systems. The experimental data in dAu match the hydro calculation within uncertainties. The figure also compares the data with another hydro calculation indicated by the green dashed and solid lines. Figure 3.8 shows the distribution of the response v_2/ϵ_2 as a function of $\mathrm{d}N/\mathrm{d}\eta$ [35].

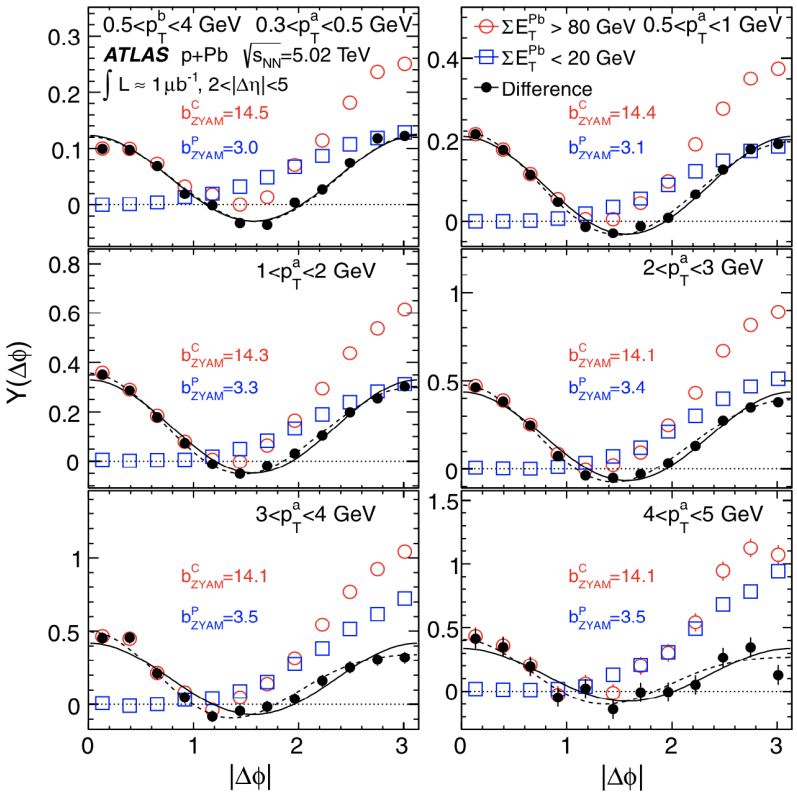

Figure 3.5: The pre-trigger yields of pPb at 5.02 TeV in different p_{T} bins. Both the yields in central and peripheral events as well as their difference are plotted. The yield difference is fitted to $a_0 + 2a_2\cos(2\Delta\phi)$ (solid line) and $a_0 + 2a_2\cos(2\Delta\phi) + 2a_3\cos(3\Delta\phi)$ (dashed line).

Results from pPb, PbPb at LHC and dAu, AuAu at RHIC are compared in the figure, where ϵ_2 is computed by the Glauber Monte-Carlo simulation. Three different nucleon representations in the Glauber Monte-Carlo are used for dAu and AuAu events: point-like centers, Gaussian smearing and uniform disks. dAu and AuAu events belong to the same charged-particle multiplicity range as pPb and PbPb events respectively. The eccentricity-rescaled v_2 for dAu and AuAu are also consistent with those in pPb and PbPb measurement although the initial eccentricity from dAu is expected larger than that in pPb. The dAu and pPb measurements in the figure can be considered as an extension of the AuAu and PbPb curves which can be explained by hydrodynamic flows. When divided by the initial eccentricity, v_2 in different systems at LHC or RHIC seem to follow the same trend. This not only suggests

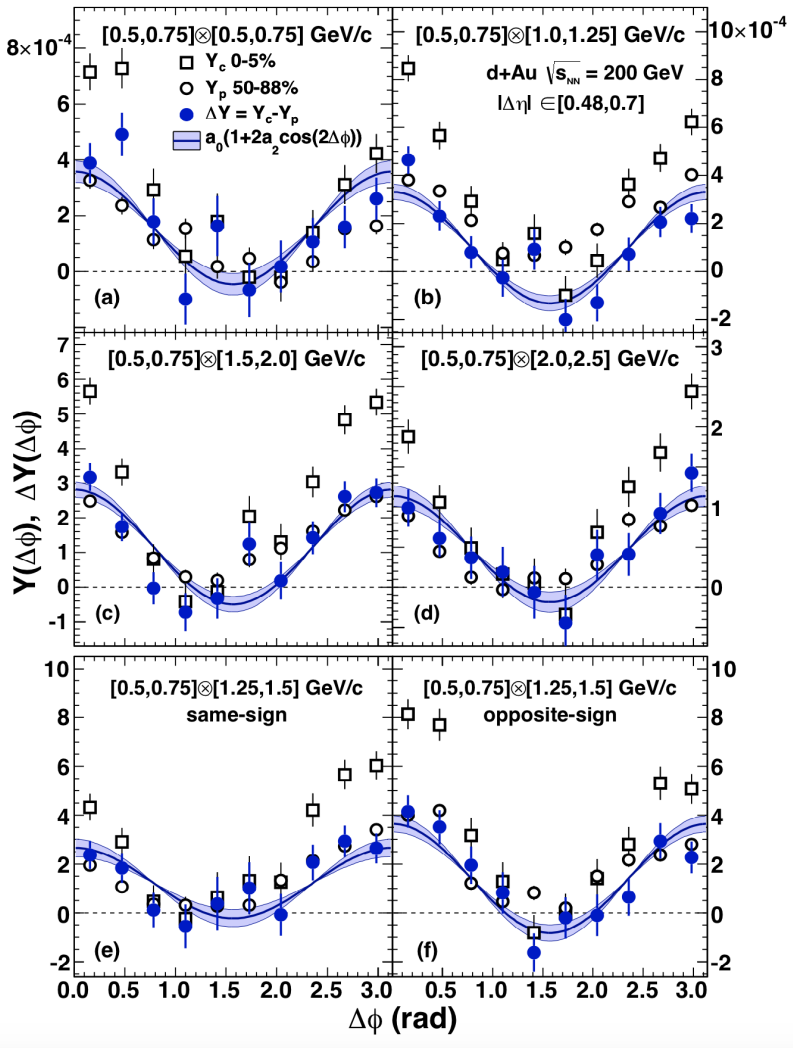

Figure 3.6: The pre-trigger yields of dAu at 200 GeV in different pseudorapidity regions. Both the yields in central and peripheral events as well as their difference are plotted. The yield difference is fitted to a $\cos(2\Delta\phi)$ modulation plus a constant.

the same physical mechanism underlying the collectivity for pPb and dAu, but also indicates the relationship between this physical mechanism and hydrodynamics.

3.2.2 Rescaled peripheral subtraction

Besides the peripheral subtraction used in the previous section, ATLAS has also adopted a modified version of this method [36]. In this method, a rescaled peripheral per-trigger yield is subtracted from the central event class. This scale factor is

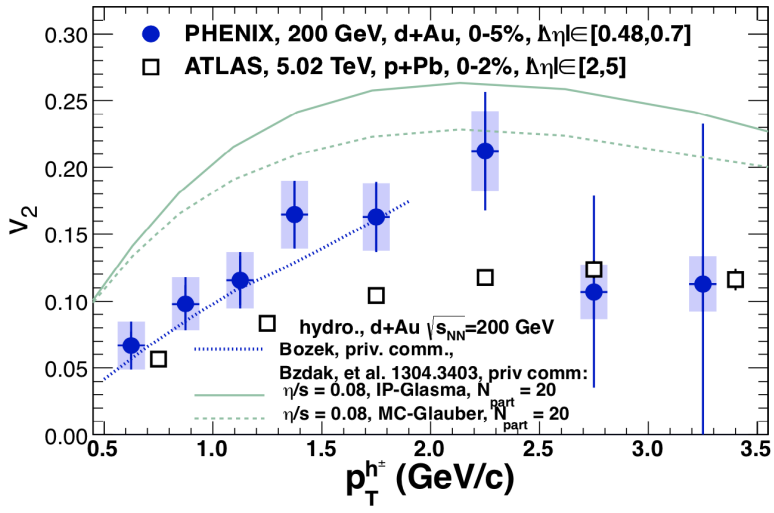

Figure 3.7: The distribution of v_2 as a function of p_{T} for both 200 GeV dAu events and 5.02 TeV pPb events. The experimental data are compared with two different kinds of hydrodynamic calculation. (One represented by the blue dashed line and the other represented by the green solid and dashed line.)

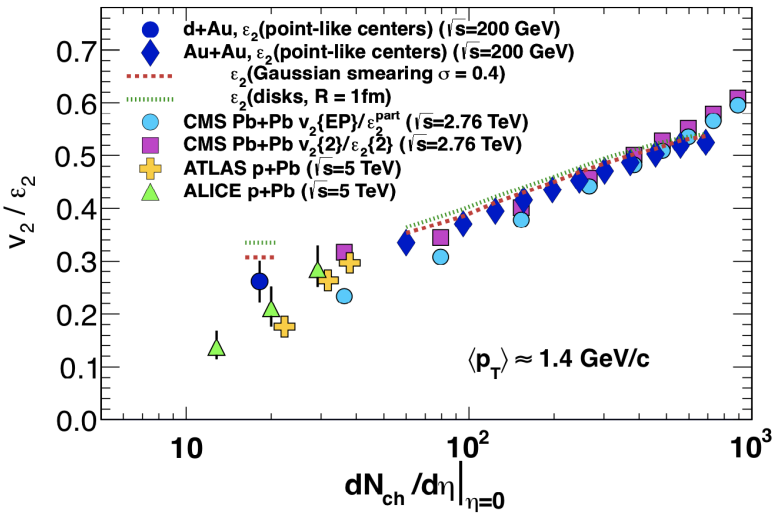

Figure 3.8: The distribution of v_2/ϵ_2 as a function of $\mathrm{d}N/\mathrm{d}\eta$ for pPb, PbPb at LHC and dAu, AuAu at RHIC. Three different nucleon representations are used for small systems.

determined by the ratio between the near-side short-range jet correlations in the peripheral and central event classes. The yield of near-side short-range jet correlation can be evaluated from

$$Y^{\mathrm{N-Peak}} = \int_{|\Delta\eta|<1} Y(\Delta\eta)d\Delta\eta - \frac{1}{5-2}\int_{2<|\Delta\eta|<5} Y(\Delta\eta)d\Delta\eta \tag{3.3}$$

where the long-range yield has been subtracted from the short-range yield to give the same jet correlation. The ratio α is therefore,

$$\alpha = \frac{Y^{\mathrm{N-Peak}}}{Y^{\mathrm{N-Peak}}_{\mathrm{peri}}} \tag{3.4}$$

In this analysis, $\Delta Y(\Delta\phi) = Y_c(\Delta\phi) - \alpha Y_p(\Delta\phi)$ is defined. Figure 3.9 shows the azimuthal dependence of per-trigger yields and their rescaled recoil components in different p_{T} bins for the most central events $N^{\mathrm{rec}}_{\mathrm{ch}} > 220$ [36]. The peripheral events here are defined by $\sum E^{\mathrm{Pb}}_{\mathrm{T}} < 10$ GeV. Figure 3.10 is the centrality dependence of the near-side and away-side integrated yields in the long range as well as their difference [36], which is similar to the bottom right panel of Figure 3.4. In this figure a blue solid line which is the rescaled peripheral integrated yield is compared with the difference. The fact that the near-side and away-side difference can be reproduced by the rescaled peripheral yield suggests the latter is a good estimation of the recoil component. In Figure 3.11, different harmonics are plotted as a function of transverse momentum. v_n^{unsub} and v_n are extracted from the per-trigger yields before and after the peripheral subtraction. No obvious difference is observed when $p_{\mathrm{T}} < 3$ GeV. The impact from the recoil becomes significant in large p_{T} regions. Since the recoil component is always peaked at $\Delta\phi = \pi$, it increases the values of v_2 and v_4 but decreases the values of v_3.

In addition to all these v_n extraction methods described above, a new method based on template fitting analysis will be introduced in Chapter 5. Most of the ATLAS results that will be presented in this thesis are extracted from the new method.

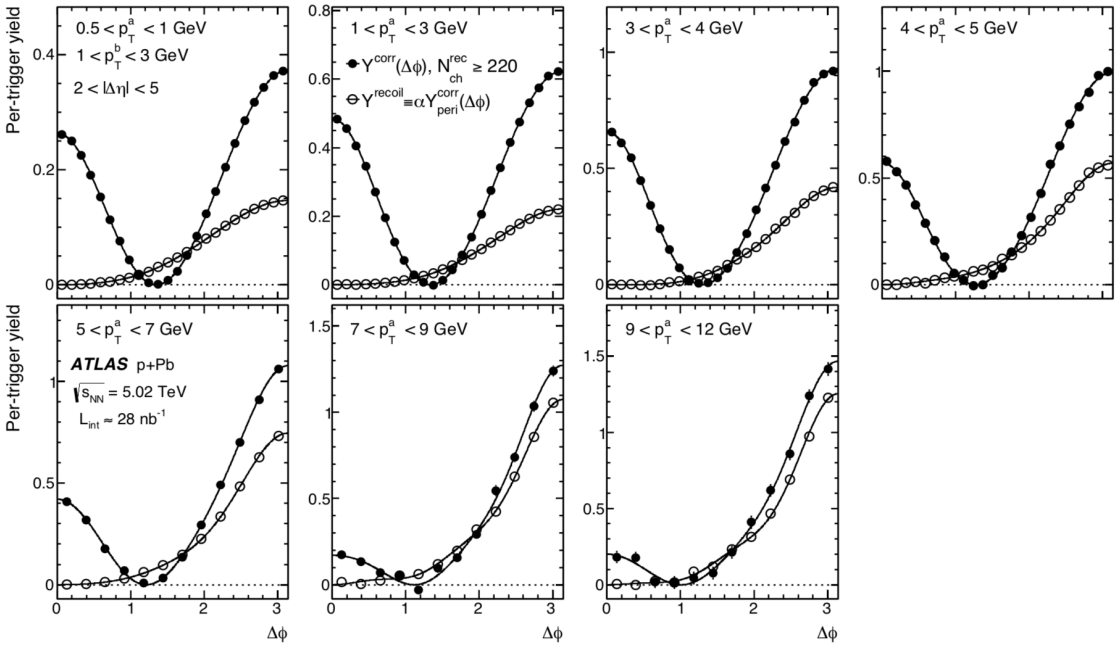

Figure 3.9: Per-trigger yields and rescaled recoil components in different p_{T} intervals for 5.02 TeV pPb events.

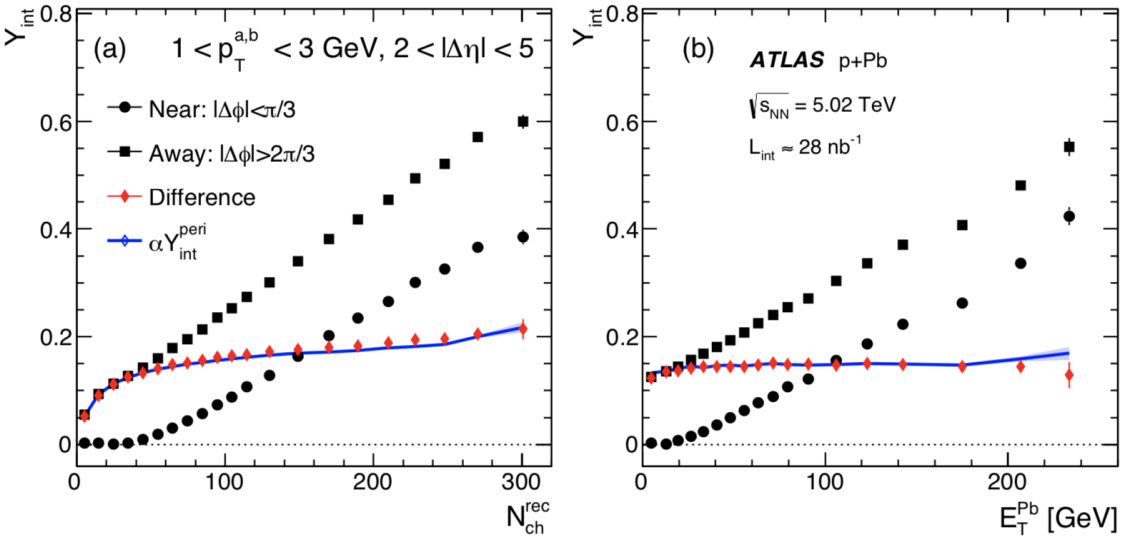

Figure 3.10: Centrality dependence of integrated yields for 5.02 TeV pPb events.

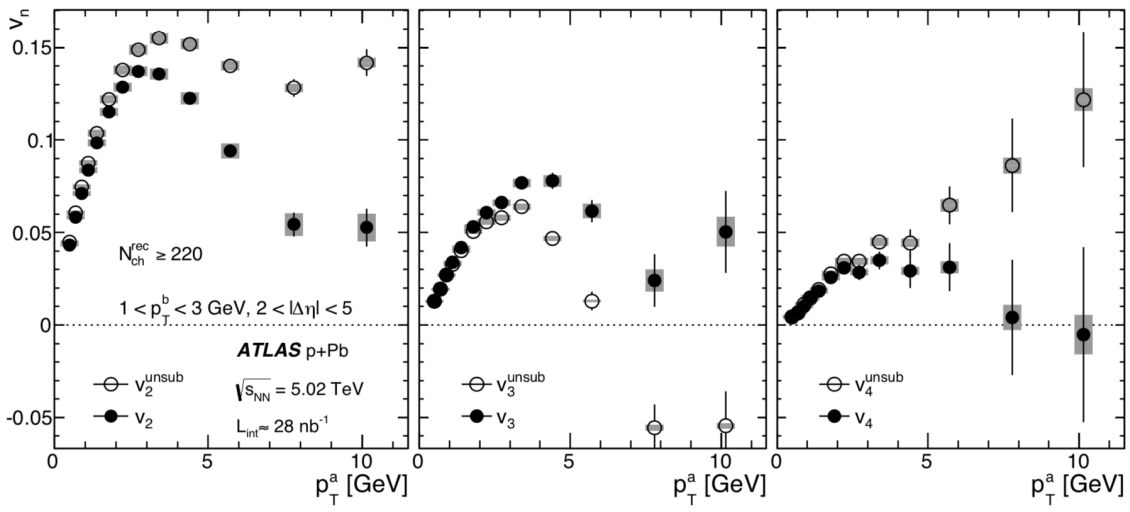

Figure 3.11: p_{T} dependence of flow harmonics before (v_n^{unsub}) and after (v_n) the recoil subtraction for 5.02 TeV pPb events.

3.3 Jet quenching calculation in small systems

Besides collective flows, another interesting topic in heavy ion physics lies in the jet analysis. The previous section discusses the hydrodynamic explanation for the collectivity in small systems. If the hydrodynamic calculation meets the experimental results, the existence of a hot and dense medium may be justified. However this is only the justification from the soft component. In order to further investigate whether the medium is formed during small system collisions, we can also concentrate on the hard component of the final particle production. The hard probe for the medium here refers to the jet-medium interaction. In this section the jet-medium interaction in small systems is calculated with the same procedure used in AA collisions and compared with data.

There are two aspects when we consider the jet-medium interactions. One is the nuclear modification factor R_{AA} measurement as a function of the transverse momentum. R_{AA} is defined as the ratio of the yield in AA collision to the yield in pp collision scaled up by the expected number of nucleon-nucleon interactions.

$$R_{\rm AA} = \frac{\frac{{\rm d}N^{\rm AA}}{{\rm d}p_{\rm T}}}{\langle N_{\rm coll}\rangle \frac{{\rm d}N^{\rm pp}}{{\rm d}p_{\rm T}}} \tag{3.5}$$

The other aspect is the azimuthal anisotropy resulting from jet energy loss due to different distances travelled by jets in different directions. This anisotropy for high energy partons is also highly correlated with the anisotropy in initial geometry. The anisotropic jet energy loss can be quantified by an angular dependence of $R_{\rm AA}(\phi)$. Similar to what we did in the collective flow, this angular dependence can be expanded into Fourier series,

$$R_{\rm AA}(\phi, p_t) = R_{\rm AA}(p_t) \times (1 + 2\sum_n v_n(p_t)\cos[n(\phi - \psi_n^J(p_t))]) \tag{3.6}$$

Figure 3.12 shows the $R_{\rm AA}$ results at RHIC and LHC in different centrality bins [37]. The red line is from the NTcE model calculation. The green and blue points are from experimental data. It is easy to see that at both the RHIC and LHC energy, the model calculation is consistent with the data. There is a huge suppression of $R_{\rm AA}$ values below 20 GeV in LHC. The data indicate a $R_{\rm AA}$ distribution with its values lower than 1. This is an obvious evidence of the jet quenching effect in heavy ion collisions. To generate the azimuthal dependence of the nuclear modification factor, a combination of Glauber Monte-Carlo used to simulate initial state fluctuations and the NTcE model for $R_{\rm AA}$ calculation needs to be implemented. Figure 3.13 shows the v_2 measurement from RHIC and LHC as well as its values from NTcE model through Eq.(3.6). There is typically an error coming from mismatching reference planes when we compare $R_{\rm AA}$ generated v_2 with the collective flow v_2. The difference can be accounted for by a scale factor equal to $\cos[n(\psi_n^J - \psi_n^{\rm EP})]$. Since in general these two reference planes may be highly correlated, we could directly compare results from jet quenching calculation with the experimental data illustrated in these figures. The jet quenching calculation from the model is mostly consistent with the data. It leads to a longer tail for v_2 at high $p_{\rm T}$ region. Since both the anisotropies of jet energy loss

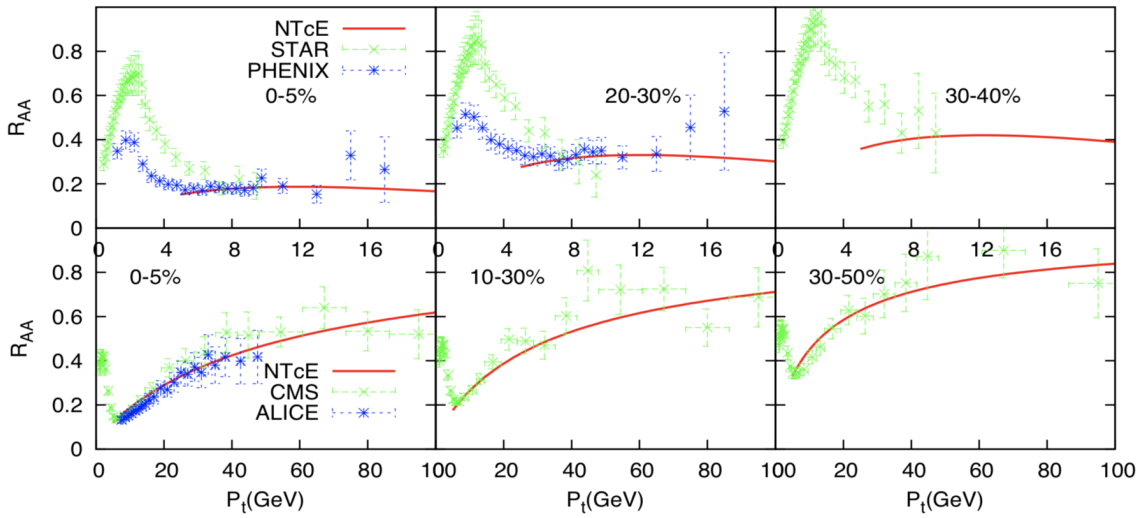

Figure 3.12: R_{AA} vs p_t in different centrality bins for AA collisions both at RHIC and LHC.

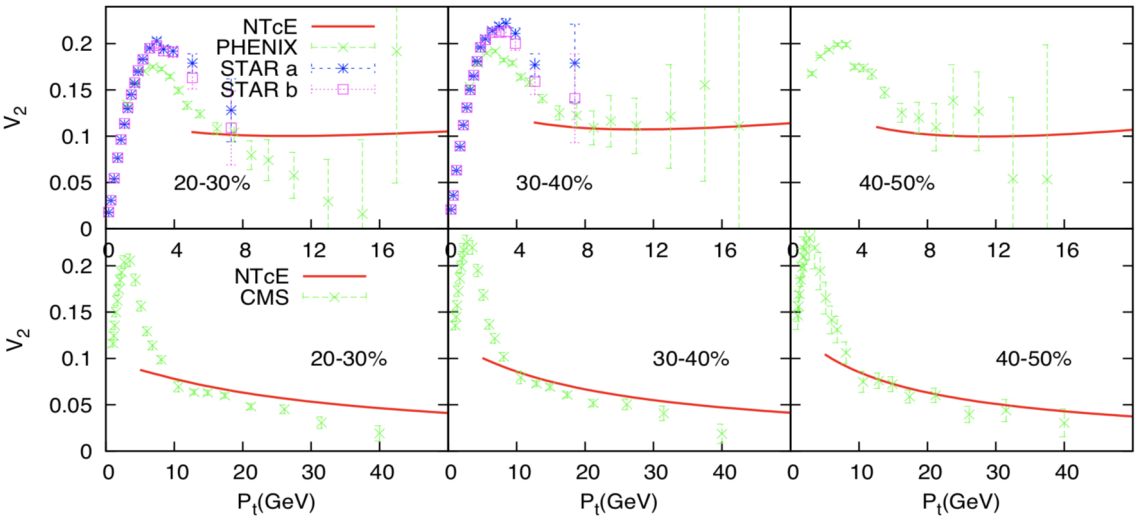

Figure 3.13: v_2 vs p_t in different centrality bins for AA collisions both at RHIC and LHC.

and collective flows are arising from the anisotropy of initial geometry, the correlation between hard particles and soft particles can also be expected.

As mentioned above, the same jet-medium calculation can also be applied in small systems such as high-multiplicity pA events. Two different methods are used to generate initial state in the Glauber Monte-Carlo simulation. In Figure 3.14,

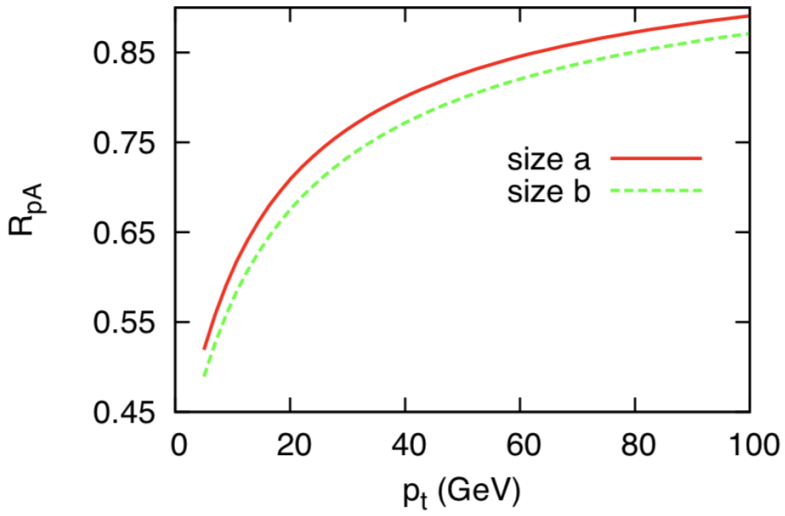

Figure 3.14: R_{AA} vs p_t in central pPb collisions both at RHIC and LHC.

"size a" uses a linear relationship between initial entropy density and participant density. While "size b" assumes a linear relationship between initial entropy density and collision density [37]. It is easy to notice that R_{pA} in central pA events has almost the same dependence on p_{T} as R_{AA} in peripheral AA events. There is also a significant suppression below 20 GeV in Figure 3.14 suggesting jet quenching effect should exit in central pPb if this calculation is applicable in small systems. However recent measurement in LHC shows that the suppression of nuclear modification factor in pPb events is not observed. Figure 3.15 illustrates this measurement from CMS [38]. Different from the PbPb R_{AA} curve, pPb R_{pA} values are very close to 1 across the high p_{T} interval. How can such a hot and dense medium exist while high p_{T} partons do not lose energy across the medium? This surprising result puts the origin of the collectivity in small systems still in question.

Another interesting measurement that might give some insights on this topic is the v_n distribution in high p_{T} interval. Figure 3.16 shows the results from jet quenching model [37]. From left to right v_1, v_2 and v_3 distributions are illustrated. Although they all exhibit long tails up to 80 GeV, v_2 is dominant among the three. The

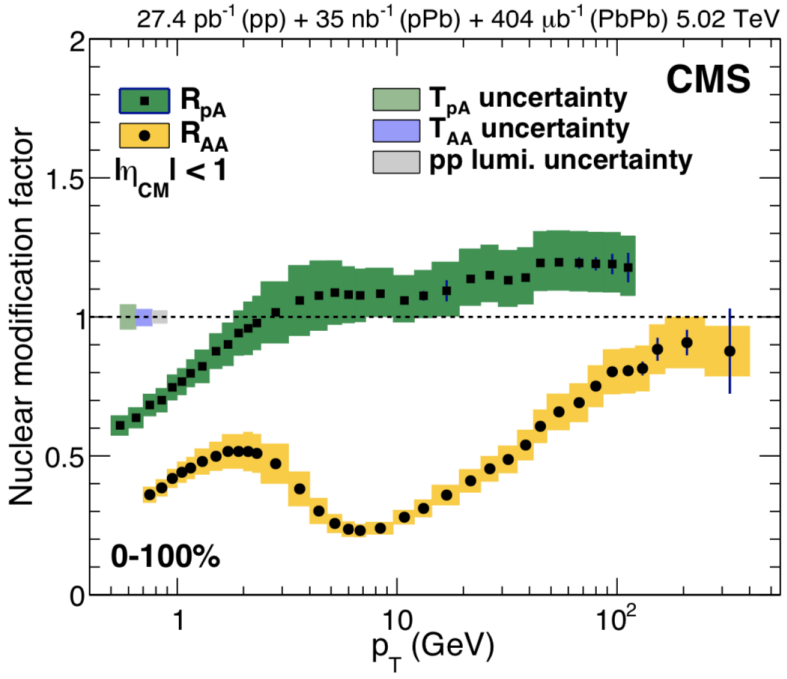

Figure 3.15: Measurements of R_{pA} and R_{AA} at CMS.

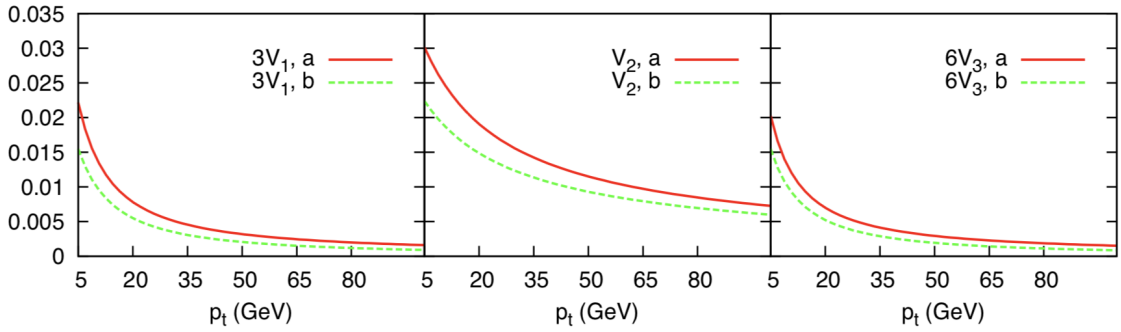

Figure 3.16: v_n vs p_t in central pPb collisions both at RHIC and LHC.

difference between ψ_n^J and ψ_n^{EP} has already been taken into account in this figure. If the measurement of flow harmonics at LHC can be extended to 10 GeV level, a direct comparison between this measurement and the above calculation can be used as an indicator whether the dense medium is formed and jet-medium interaction really exists in such small systems.

All the above discussion in this chapter concentrates on pA or dA systems. For smaller systems such as pp, the physical picture for the collision might be

quite different. Although some experimental results suggest some properties of the collective behavior in pp systems, there is no global agreement on whether a hot and dense medium is produced in pp events. Questions like whether hydrodynamics is still useful or collective flows exist in pp still need to be answered.

Chapter 4

Experimental setup

4.1 The Large Hadron Collider

The Large Hadron Collider (LHC) is located in the European Organization of Nuclear Research (CERN) near Geneva, at the border of Switzerland and France. It is the largest and highest-energy particle collider in the world. The collider lies in a circular tunnel 50 to 175 m deep under the ground with a circumference of 26.7 km. LHC is mainly designed for proton-proton collisions. It can also be used for lead-lead and proton-lead collisions. Two beams moving in the opposite directions intersect at four different points along the LHC accelerator ring where head-on collisions take place and detectors are constructed for experimental purposes. The location of the LHC main ring and some detectors are shown in Figure 4.1.

The way that protons and lead ions are accelerated in the LHC is illustrated in Figure 4.2. Before accelerated in the main ring, particles are first injected into a few preaccelerators to increase their energy. Protons are prepared by ionizing the hydrogen gas and then injected into a linear particle accelerator called LINAC 2 where the proton beam will be accelerated to a energy of 50 MeV. Then the accelerated beams are transferred into the Proton Synchrotron Booster (PSB) and their energy

will reach a level of 1.4 GeV. After the PSB acceleration, beams are injected into the Proton Synchrotron (PS) and accelerated to 26 GeV. Finally they reach the Super Proton Synchrotron (SPS) where they obtain a energy up to 450 GeV. At last the SPS injects protons into the LHC main ring in two opposite directions. Each beam will be accelerated to their peak energy around 7 TeV. Unlike proton beams, lead ions are first accelerated by another linear accelerator called LINAC 3 where they will be further injected into the Low Energy Ion Ring (LEIR). After that they will be transferred into the PS and SPS before finally injected into the LHC main ring where ions can be accelerated up to a few TeV per nucleon.

1232 dipole magnets are installed along the LHC ring to guarantee the accelerated beams to move on its circular path. They can generate a magnetic field up to 8 T. In order to keep the curvature of the beam trajectory unchanged, the magnetic field should increase proportionally with the beam energy. For example, as the protons are accelerated from 450 GeV to 6.5 TeV, the dipole field should increase from 0.54 to 7.7 T. In addition, 392 quadrupole magnets are also used to keep the beam focused in both the horizontal and vertical directions. This quadrupole field will direct beams to collide at the intersection points where the field becomes stronger to increase the chances of beam interactions.

There are seven particle detectors constructed along the LHC ring. ATLAS (A Toroidal LHC Apparatus) and CMS (Compact Muon Solenoid) are constructed for a wide range of physics including the search for the Higgs boson. ALICE (A Large Ion Collider Experiment) is designed for the studies of quark-gluon plasma through heavy-ion collisions. LHCb (LHC-beauty) focuses on the measurement of products related to b-quarks. The other three detectors, TOTEM (Total Cross Section, Elastic Scattering and Diffraction Dissociation), LHCf (LHC-forward) and MoEDAL (Monopole and Exotics Detector At the LHC) are relatively small and designed for other specialized experiments.

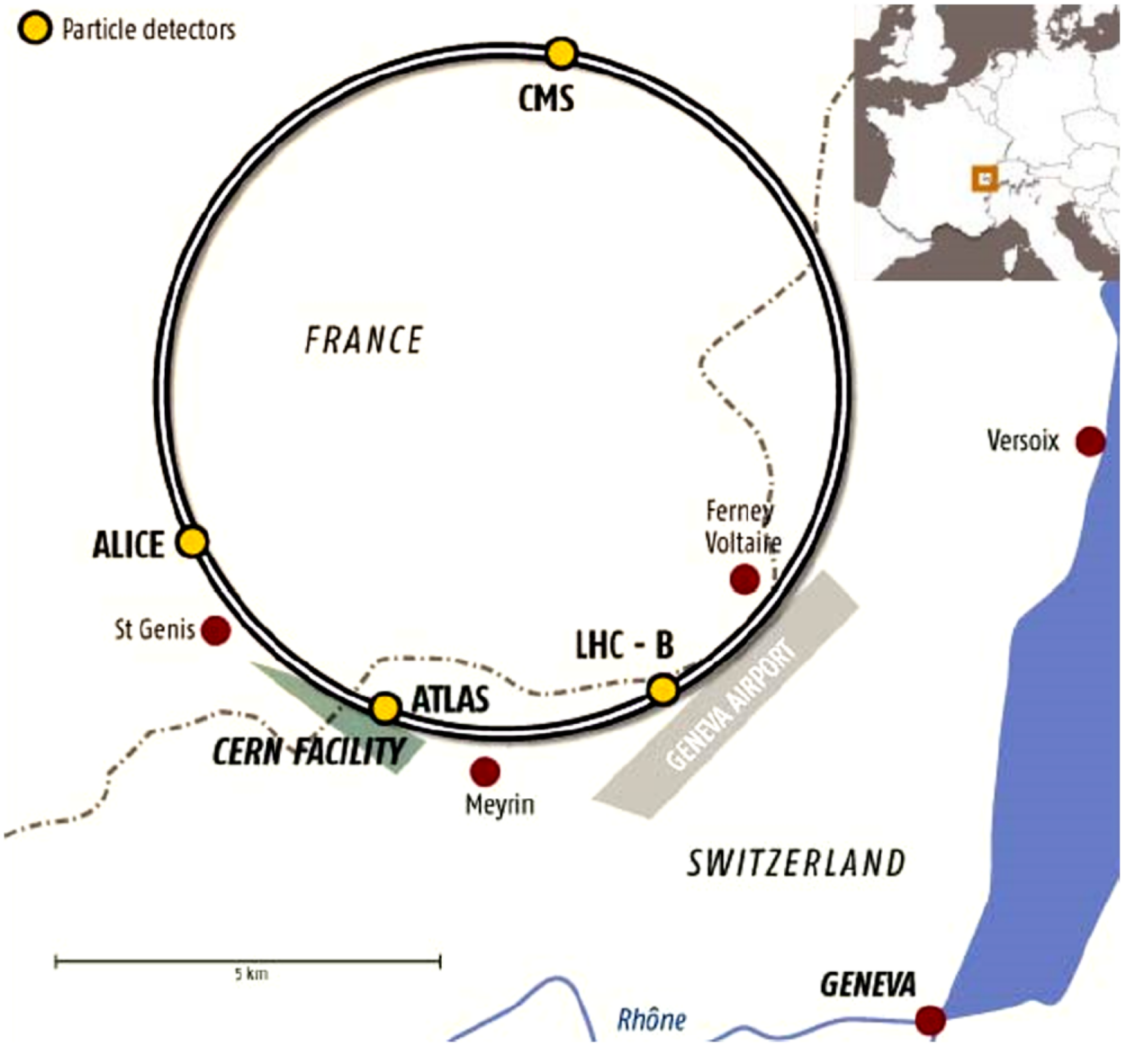

Figure 4.1: The location of the LHC ring as well as four primary particle detectors are shown in the figure.

4.2 Luminosity

In particle collider physics, the total number of events N in a specific time period is proportional to the cross section σ of the corresponding interaction. The proportionality factor is defined as the integrated luminosity L_{int} in this time interval.

$$N = \sigma L_{\text{int}} \tag{4.1}$$

Thus the event rate dN/dt can be obtained,

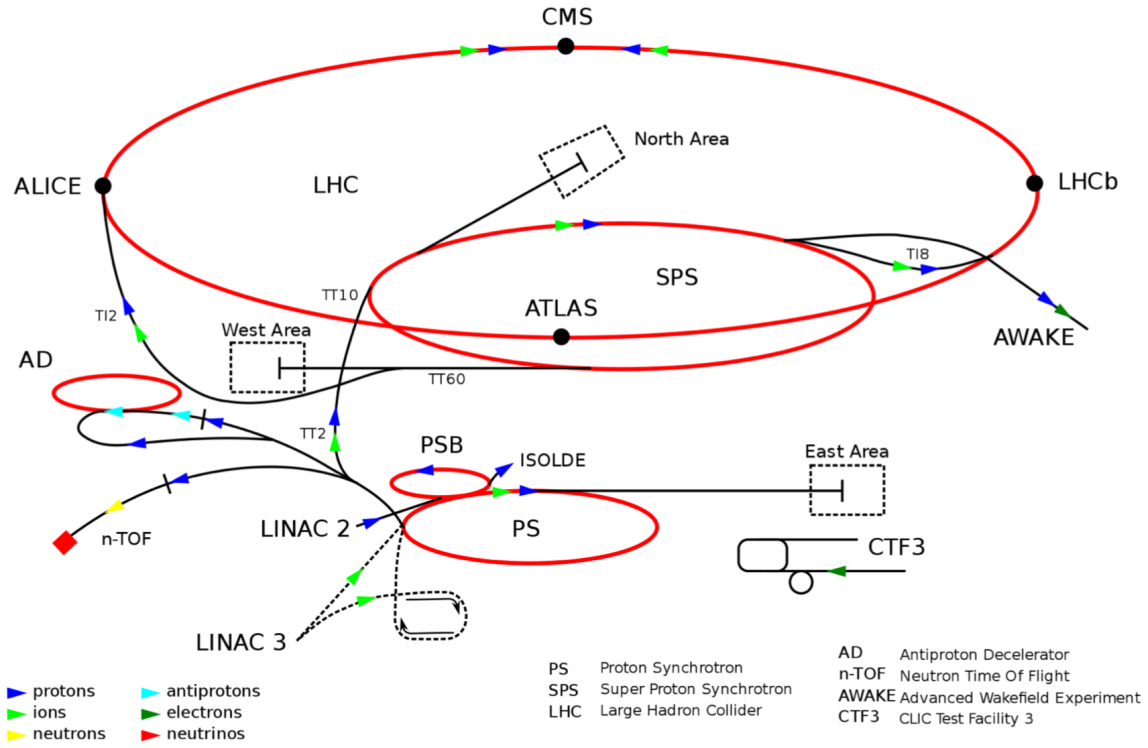

Figure 4.2: A figure showing the configuration of LHC accelerators. The accelerations of different particles are illustrated using arrows of different colors. Preaccelerators as well as the LHC main ring are represented by the red line.

$$\frac{dN}{dt} = \sigma L \tag{4.2}$$

where $L = dL_{\text{int}}/dt$ is the instantaneous luminosity. From the definition above, L can be regarded as the number of collisions per unit time per unit area during the interaction. Therefore it can also be calculated using beam parameters [39, 40],

$$L = \frac{n_b f_r n_1 n_2}{2\pi \Sigma_x \Sigma_y} \tag{4.3}$$

where n_b is the number of colliding bunches. f_r is the beam revolution frequency in LHC. Here it is used as the colliding frequency for each bunch. n_1 and n_2 are the number of particles per bunch. Σ_x, Σ_y are the transverse sizes of the beam in horizontal and vertical directions. The bunch current n_1 and n_2 can be measured using the Direct Current Current Transformers (DCCT) and Fast Beam Current

Transformers (FBCT). However there are "ghost" charges and "satellite" charges that need to be removed from the measurement of the above transformers. "Ghost" charges appear when charges occupy empty bunches and "satellite" charges are charges outside the RF buckets. The transverse profiles Σ_x and Σ_y are obtained in the van der Meer (vdM) scans, which will be described in the following sections. This expression can be used to calculate luminosity. The result is used to calibrate the response of luminosity detectors.

The number of collisions per bunch crossing is defined as follows

$$\mu = \frac{1}{n_b f_r}\frac{dN}{dt} = \frac{L\sigma}{n_b f_r} \tag{4.4}$$

In practice, not all events can be "seen" by the detector. Only part of the cross section is "visible". For a detector with an efficiency ϵ, only $\mu_{\text{vis}} = \epsilon\mu$ and $\sigma_{\text{vis}} = \epsilon\sigma$ can be measured. Thus,

$$\mu_{\text{vis}} = \frac{L\sigma_{\text{vis}}}{n_b f_r} \tag{4.5}$$

σ_{vis} can be obtained through the measurement of μ_{vis} and the calculation of L from Eq. (4.3). During an experiment μ_{vis} is measured by the luminosity detector using some specific counting algorithm. Two primary luminosity detectors are used in ATLAS: LUCID and BCM. These detectors count the number of bunch crossings that satisfy the criteria in the counting method. There are two kinds of event counting algorithms: EventOR (inclusive counting) and EventAND (coincidence counting). The EventOR algorithm requires a bunch crossing to have at least one hit in the detector. Whereas the EventAND algorithm counts the number of bunch crossings that have at least one hit on both sides of the detector. Based on which detector and algorithm are used, the measurement can be labeled as `LucidEventOR`, `LucidEventAND`, `BCMHEventOr`, `BCMTEventOr` etc. Generally the number of collisions in one bunch crossing is assumed

to follow a Poisson process, therefore the fraction of the bunch crossings that contain at least one collision is

$$P_{\text{event}} = \frac{N_{\text{count}}}{N_{\text{BC}}} = 1 - e^{-\mu_{\text{vis}}} \tag{4.6}$$

The time period of each counting measurement is the duration of a luminosity block (LB) Δt_{LB}. It is chosen to be the unit of time in the above equation. N is the number of counts. $N_{\text{BC}} = f_r \Delta t_{\text{LB}}$ is the number of total bunch crossings in one LB. Thus we obtain

$$\mu_{\text{vis}} = -\ln\left(1 - \frac{N_{\text{count}}}{N_{\text{BC}}}\right) \tag{4.7}$$

In reality, there can be background that may also produce an event contributing to the total counts. If we denote the fractions from real particle collisions and from background as P_{coll} and P_{bkgd} respectively, we will have

$$1 - P_{\text{event}} = (1 - P_{\text{coll}})(1 - P_{\text{bkgd}}) \tag{4.8}$$

Therefore,

$$\mu_{\text{vis}} = -\ln\left(1 - P_{\text{coll}}\right) = -\ln\left(\frac{1 - P_{\text{event}}}{1 - P_{\text{bkgd}}}\right) \tag{4.9}$$

If the visible interaction rate is very small $\mu_{\text{vis}} \ll 1$, we can approximate,

$$\mu_{\text{vis}} \approx -\ln\left(1 - (P_{\text{event}} - P_{\text{bkgd}})\right) \approx P_{\text{event}} - P_{\text{bkgd}} \tag{4.10}$$

This means the interaction rate μ_{vis} is approximately a linear function of the counts of bunch crossings, which is expected since there can hardly be more than one event within one bunch crossing if μ_{vis} is small. There are two main sources of the background contribution: after-glow and beam-gas. After-glow results from the time-delayed particles hitting the detector. Beam-gas refers to the interactions

between particles from the beam and the residual gas. A estimate of the background contribution can be written as

$$P_{\rm bkgd} = P_{\rm AG} + P_{\rm BG} \tag{4.11}$$

In the analysis the collision rate is defined from $\mu_{\rm vis}$,

$$R_{\rm sp} = \mu_{\rm vis} \frac{n_1 n_2|_{ref}}{n_1 n_2} \tag{4.12}$$

During vdM scans the collision rate $R_{\rm sp}$ is measured at different beam separations. The reference bunch currents in the above equation are chosen to be the ones at the central position of the horizontal measurement. Thus we can express $R_{\rm sp}$ as a function of the horizontal and vertical beam separations, δ_x and δ_y. vdM analysis assumes this function can be factorized into the products of two functions depending only on δ_x or δ_y,

$$R_{\rm sp}(\delta_x, \delta_y) = R f_x(\delta_x) f_y(\delta_y) \tag{4.13}$$

Typically $f_x(\delta_x)$ and $f_y(\delta_y)$ are assumed to have a maximum of 1 at $\delta_x = 0$ and $\delta_y = 0$. Function parameters are obtained by fitting the curves of collision rates from the horizontal and vertical vdM scans, which are performed at $\delta_y = 0$ and $\delta_x = 0$ respectively. Then the transverse sizes of the beam can be calculated as follows

$$\Sigma_x = \frac{1}{\sqrt{2\pi}} \frac{\int d\delta_x R(\delta_x, 0)}{R f_y(0)} = \frac{1}{\sqrt{2\pi}} \int d\delta_x f_x(\delta_x) \tag{4.14}$$

$$\Sigma_y = \frac{1}{\sqrt{2\pi}} \frac{\int d\delta_y R(0, \delta_y)}{R f_x(0)} = \frac{1}{\sqrt{2\pi}} \int d\delta_y f_y(\delta_y) \tag{4.15}$$

One simple functional form for f_x, f_y is the Gaussian distribution,

$$f_{x,y}(\delta_{x,y}) = e^{-(\delta_{x,y} - x_0, y_0)^2 / 2\Sigma_{x,y}^2} \tag{4.16}$$

Here we assume the maximum collision rates in the horizontal and vertical directions are not at 0, but at x_0 and y_0 respectively. There are also other functional forms that are widely used, especially `Gaussian Times Polynomial` and `Double Gaussian`. Figure 4.3 illustrates the fitting results using different forms of f_x and f_y from algorithm `BCMVEvtOr`.

There are still two problems remaining in the above discussion. First the functional form of $R_{\rm sp}$ may not be factorized as described. In this case, some non-factorized functions, such as two coupled-Gaussian function, will be used. Second there are other effects such as beam-beam displacement, dynamic beta correction and orbit drift that need to be taken into account in the analysis. Beam-beam displacement results from the electromagnetic force between the two beams. This force can deflect beams causing the actual separation of the two colliding bunches different from the one we use in the measurement. The interaction between the beams will also squeeze the bunches in the transverse plane changing the β^* in the collision, which leads to a dynamic beta correction. The orbit drift is the drift of the beam due to the change of the magnetic field in LHC. All these effects need to be properly considered in order to obtain the correct result.

4.3 The ATLAS detector

The conventional coordinate system used in the particle collider physics is briefly introduced here. The interaction point is defined to be the origin of the system with the z-axis extending along the beam direction. The x-y plane is therefore perpendicular to the beam direction through the interaction point. The azimuthal angle ϕ is measured around the beam axis while the polar angle θ is the angle between the beam axis and particle direction. The transverse momentum p_T and transverse energy E_T are the projections of total momentum and energy onto the x-y plane.

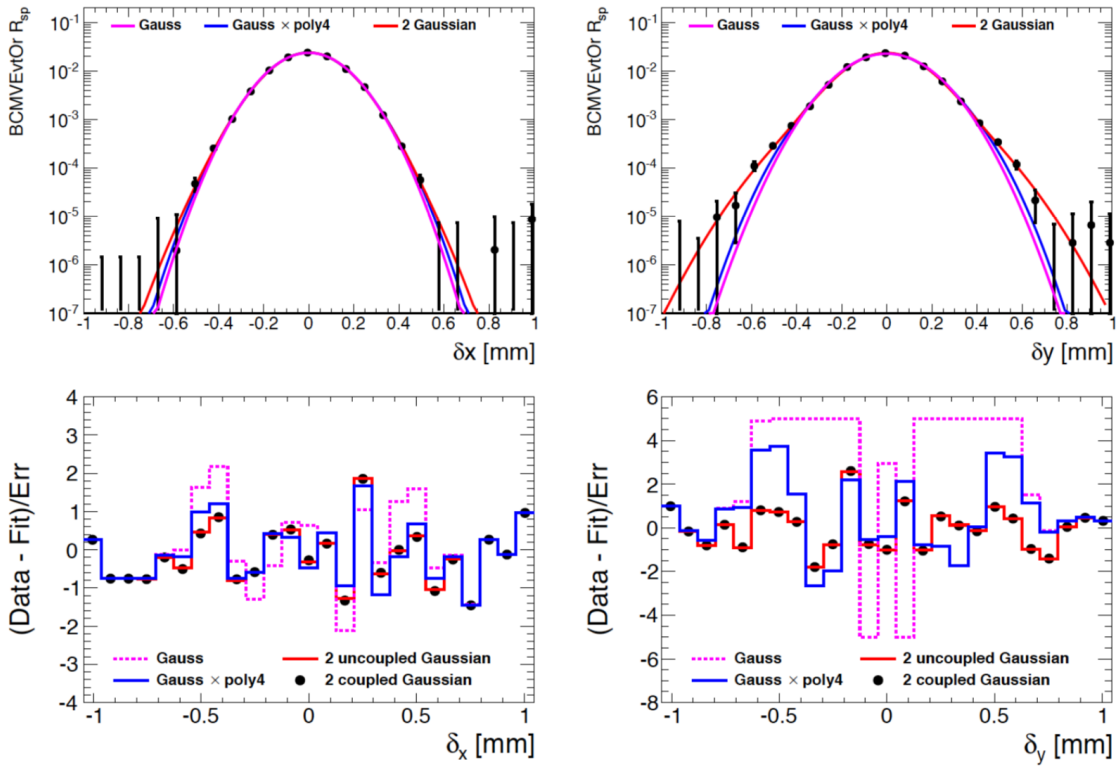

Figure 4.3: Fits for the collision rates R_{sp} using different functional forms during the horizontal and vertical *vdM* scans are shown in the top panels. Gaussian, Gaussian times 4th order polynomial, two uncoupled Gaussian and two coupled Gaussian are used for comparing. The quality of these fits is shown in the bottom. It can be seen that two coupled Gaussian and two uncoupled Gaussian give completely the same results [39].

The rapidity is defined as

$$y = \frac{1}{2} \ln \frac{E + p_z}{E - p_z} \tag{4.17}$$

In the ultra-relativistic limit, $E \approx |\vec{p}|$, we obtain the pseudo rapidity

$$\eta = \frac{1}{2} \ln \frac{|\vec{p}| + p_z}{|\vec{p}| - p_z} = -\ln \tan \frac{\theta}{2} \tag{4.18}$$

Pseudo rapidity η only depends on the polar angle of the trajectory of the particle. "Forward" and "backward" directions mainly mean the large $|\eta|$ region close to the

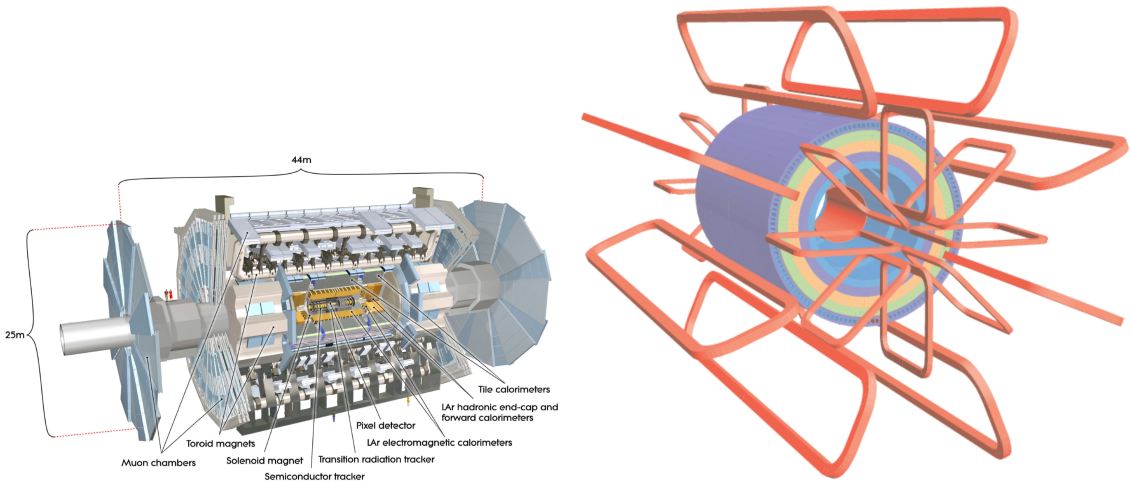

Figure 4.4: The left panel shows the structure of the ATLAS detector. The inner detector, calorimeter and muon chambers are illustrated in this figure. The magnet systems are used to generate magnetic fields for the inner detector and muon spectrometer. The right panel is a brief view for the ATLAS magnetic system. The solenoid in the center is placed surrounding the inner detector. The eight toroid coils as well as end-cap coils lie around the calorimeters.

beam axis. The former has positive η while the latter has negative η. The separation in the $\eta - \phi$ space is defined as

$$\Delta R = \sqrt{(\Delta\eta)^2 + (\Delta\phi)^2} \tag{4.19}$$

An overview of the ATLAS detector is shown in Figure 4.4. It has a length of 44 m and a diameter of 25 m. From the innermost to the outermost the detector is comprised of the inner detector, calorimeter and muon spectrometer [41]. ATLAS detector is used to conduct experiments at different energy levels and collect data from various proton-proton, proton-nucleus and nucleus-nucleus collisions.

The ATLAS magnetic system consists of three superconducting magnets: a central solenoid, a barrel toroid and two end-cap toroids which are shown in the left panel of Figure 4.4. The central solenoid is placed around the inner-detector cavity and produces a 2 T magnetic field for the inner detector. The barrel and two end-cap toroids are placed surrounding the calorimeters. They produce a 0.5 T and 1 T magnetic

field respectively in the barrel and end-cap regions of the muon spectrometer. The arrangement of the magnetic coils are shown in the right panel of Figure 4.4.

4.3.1 Inner detector

The ATLAS inner detector (ID) is immersed in a 2T magnetic field produced by the central solenoid. It performs the measurement of the transverse momentum of charged particles using their bending trajectories in the magnetic field. It also can provide information about primary and secondary vertices. Tracks reconstructed in the ID are usually above a p_T threshold 0.4 GeV. The detector covers a pseudorapidity range $-2.5 < \eta < 2.5$ and the full 2π azimuthal angle. It has three sub-detectors: pixel detectors, silicon microstrip detectors (SCT) and transition radiation trackers (TRT) placed from the innermost to the outermost. The construction of these three parts can be found in Figure 4.5. The ID is contained in an envelope with $|z| < 3512$ mm and $R < 1150$ mm.

The pixel detector has three barrel layers and two end-caps. Each end-cap consists of three disk layers. There are totally 1744 identical modules in the pixel detector. The three barrel layers, which are called Layer-0,1 and 2, have a radius 50.5, 88.5 and 122.5 mm respectively. In the end-cap region the three disks are placed 495, 580 and 650 mm away from the interaction point. Every disk has 8 sectors, so there are 48 end-cap sectors from both sides. The pixel detector is contained in an envelope of $45.5 < R < 242$ mm and $|z| < 3092$ mm.

The SCT consists of four barrel layers and two end-caps. Each end-cap has nine disk layers. There are 4088 modules in SCT. The four barrel layers, which are called Layer-3,4,5 and 6, have a radius 299, 371 443 and 514 mm respectively. The nine disks are placed away from the interaction point from $|z| = 853$ mm to $|z| = 2720$ mm. The envelope used for the SCT barrel has a size of $|z| < 805$ mm and $255 < R < 549$ mm, whereas the one used for the SCT end-cap has the size of $810 < |z| < 2797$ mm

and $251 < R < 610$ mm.

The TRT contains 73 layers in the barrel and 160 layers in each end-cap. The barrel layers are made of straws with fibers inside covering a radial distance from 554 to 1082 mm. The end-cap layers are straws with foil inside placed at the region $|z| = 848 \sim 2710$ mm. The TRT barrel has 96 modules while each TRT end-cap has only 20 modules. Except in the region between the barrel and end-cap any charged track with $p_T > 0.5$ GeV and $|\eta| < 2.0$ is likely to have at least 36 hits on the straws when crossing the TRT modules. The size of the TRT barrel envelope is $|z| < 780$ mm and $554 < R < 1082$ mm, whereas the size of TRT end-cap envelope is $827 < |z| < 2744$ mm and $617 < R < 1106$ mm.

Figure (4.6) illustrates how charged tracks emitting from the interaction point interact with ID. The track at $\eta = 1.4$ traverses three pixel barrel layers and four SCT end-cap disks producing approximately 40 hits on the straws contained in the TRT end-cap. In contrast the track at $\eta = 2.2$ traverses only one pixel layer in the barrel and two pixel disks in the end-cap. It crosses the last four disks of the SCT end-cap and leaves the inner-detector cavity. Since TRT barrel only covers the pseudo rapidity range $|\eta| < 2$, it does not hit any straws in the TRT layers.

4.3.2 Calorimeter

The structure of the ATLAS calorimeter is illustrated in Figure 4.7. It consists of the electromagnetic calorimeter, hadronic calorimeter and forward calorimeter. The electromagnetic calorimeter uses lead as the absorber plates and liquid argon as the active medium. It is divided into a barrel part and two end-caps at each side. The electromagnetic barrel covers a pseudorapidity range $|\eta| < 1.475$, whereas the electromagnetic end-cap (EMEC) locating just behind the central solenoid has a pseudorapidity coverage $1.375 < |\eta| < 3.2$. Electrons and photons passing through the EM calorimeter will induce electromagnetic showers with the energies of the

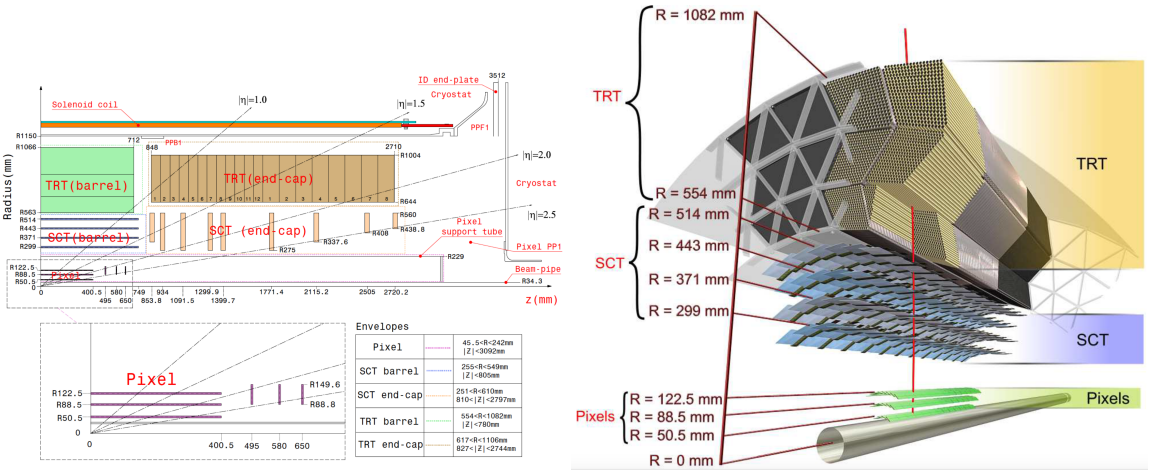

Figure 4.5: The left panel shows the structure of ATLAS inner detector. From innermost to outermost are pixel detector, SCT and TRT. The charged-particle tracks with different $|\Delta\eta|$ are illustrated. The detailed view of pixels is drawn in the bottom. Different R and $|z|$ ranges for the barrel and end-cap of each sub-detectors are shown in the bottom right table. The right panel shows the structure of ATLAS inner detector from a different direction. Only the barrel parts of Pixels, SCT and TRT are drawn here. Each layer is specified with their R values. The red line represents a track with $\eta = 0.3$.

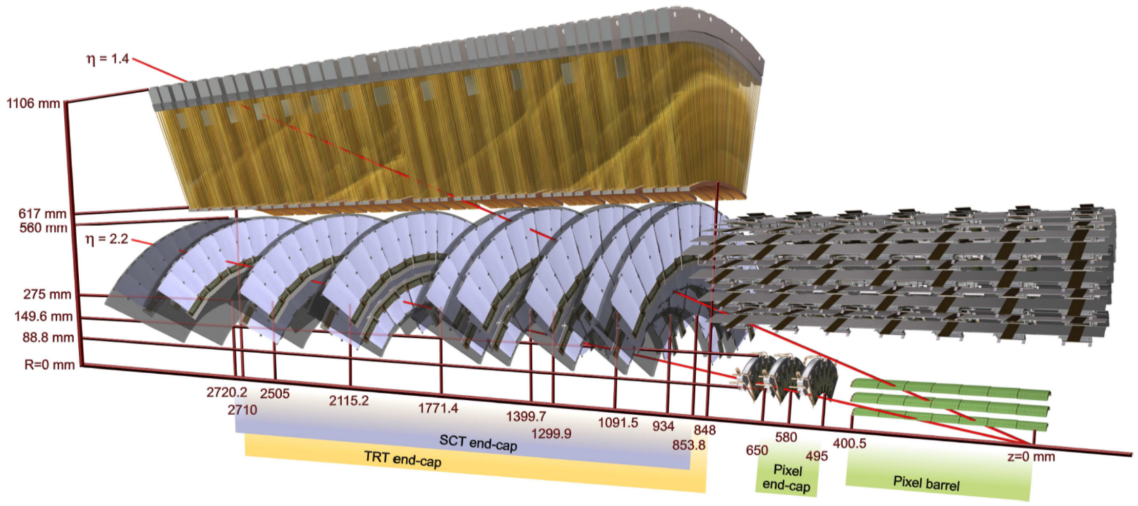

Figure 4.6: Cut-away view of the inner detector. Pixel barrel, pixel end-cap, SCT end-cap and TRT end-cap are shown in this figure. Two charged tracks with p_T at 10 GeV and η at 1.4 and 2.2 respectively are illustrated by the red line.

secondary particles deposited in the detector material.

The hadronic calorimeter has two components: the hadronic end-cap calorimeter and scintillator tile calorimeter. The hadronic end-cap (HEC) has copper as the absorber and liquid argon as the active medium. It is made of four layers and has a pseudorapidity coverage $1.5 < |\eta| < 3.2$ lying just behind the electromagnetic end-cap. The HEC is designed to overlap with the pseudorapidity coverage of the tile calorimeter and forward calorimeter to reduce the drop in material density at the transition region. The outer hadronic calorimeter, which is also called the tile calorimeter, is placed directly outside the EM barrel. It has an inner radius of 2.28 m and an outer radius of 4.25 m. The central tile barrel covers the region $|\eta| < 1.0$, whereas two extended tile barrels cover $0.8 < |\eta| < 1.7$ at each side. Both the central barrel and extended barrel have three layers. They use steel as the absorber and scintillating tiles as the active medium. Hadrons passing through the hadronic calorimeter will induce hadronic showers producing large numbers of secondary particles depositing their energies in the detector material.

The forward calorimeter (FCal) is placed in the center of each end-cap cryostat to cover the region closest to the beam axis. It has three layers covering the forward region $3.1 < |\eta| < 4.9$. The first layer is for electromagnetic measurement. Copper is used as the absorber in this layer. The other two layers are for hadronic measurement and tungsten is used as the absorber. Like the electromagnetic calorimeter and HEC liquid argon is used as the active medium in the FCal . In nucleus-nucleus analysis the energy deposited in FCal can be used to determine the centrality of the events.

4.3.3 Muon spectrometer

Muon spectrometer is used to perform the measurement of muon momentum by bending the muons in the magnetic field. It is a circular field around the beam axis perpendicular to the trajectories of muons exiting the calorimeter. As discussed

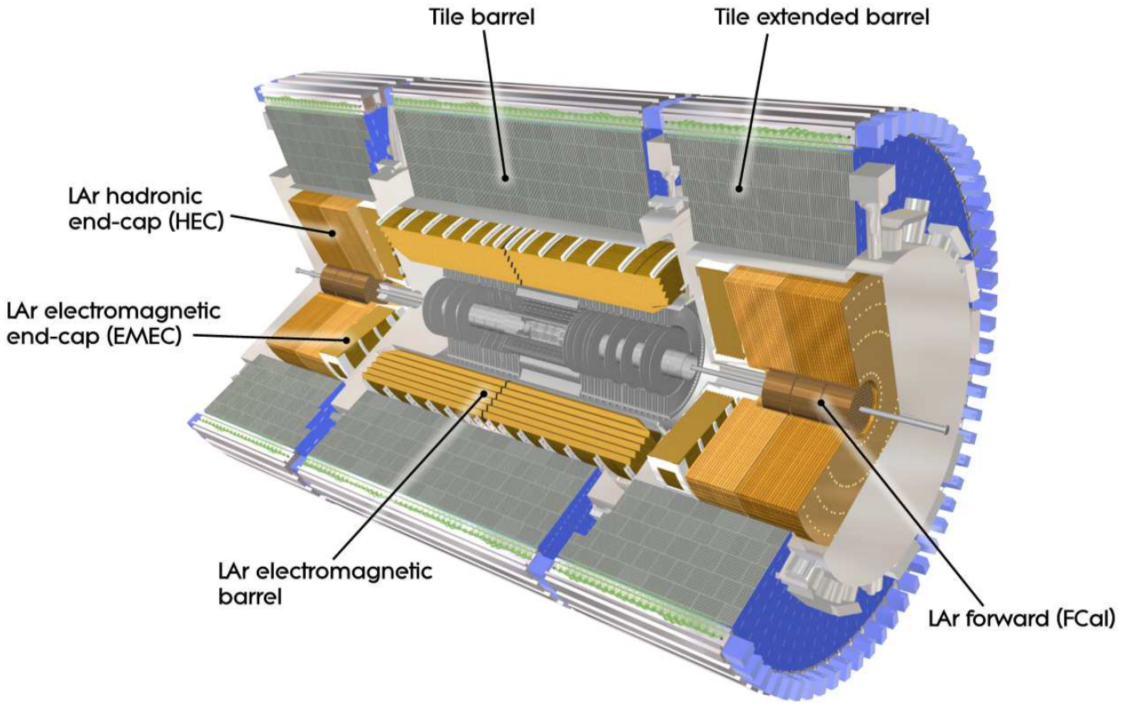

Figure 4.7: Cut-away view of the ATLAS calorimeter. Electromagnetic calorimeter, hadronic calorimeter and forward calorimeter are illustrated in the figure.

above, this magnetic field is produced by three large superconducting toroids. Two end-cap toroids are inserted at each end of a barrel toroid with the same axis. There are eight coils in each toroid. The end-cap toroid is rotated by $\pi/8$ with respect to the barrel toroid. The layout of these three coils is illustrated in the right panel of Figure 4.4. The barrel toroid generates field over the pseudorapidity range $|\eta| < 1.4$, whereas the end-cap toroids generate field for $1.6 < |\eta| < 2.7$. At the transition region $1.4 < |\eta| < 1.6$ magnetic field provided by both the barrel and end-cap toroids might be weak.

4.3.4 Trigger

The frequency of bunch crossings and the total interaction rates in LHC are usually too large to be fully recorded. Due to limitations of processing speed and storage of the system, only part of the event data can be used by the detector. Trigger system is

then used to select a certain amount of events that are relevant to our analysis while neglecting the remaining majority irrelevant interactions. Its job is to decide whether the data from a certain event needs to be recorded or not. ATLAS trigger system consists of three different levels: Level 1 (L1), Level 2 (L2) and the event filter. L2 and event filter combined together are also called High Level Trigger (HLT).

L1 trigger selection is based on the measurement from muon spectrometer and calorimeters. The L1 muon trigger uses the information from muon trigger chambers. Resistive Plate Chambers (RPC) are used in the barrel part and Thin-Gap Chambers (TGC) are used in the end-cap regions. It searches the hits that are compatible with high p_{T} muons from the interaction point. The calorimeter trigger makes decisions using the information from all calorimeters including hadronic, electromagnetic and forward calorimeter from barrel parts to end-cap regions. It can be used to identify objects with high transverse energy, such as electrons, photons, τ-leptons, jets as well as events with large total E_{T}. Trigger information such as multiplicities of electrons, photons, muons and flags indicating which threshold is passed are transferred to the Central Trigger Processor (CTP), which makes the final decision at L1 whether the event will be accepted or not. L1 trigger makes decision within 2.5 μs after each bunch crossing, reducing the event rates down to 75kHz.

For every selected event, L1 trigger system sends information about the regions of detectors that identified the trigger objects (for example, electrons or photons), to L2 trigger. This information is called Regions-of-Interest (RoI), which will be used later as seeds for the selection performed by HLT. L2 trigger processes events within the time of 40 ms. It reduces event rates to a level of 3.5 kHz. Finally the event filter uses the offline analysis procedure to further select events down to a rate of 200 Hz. The processing time per event at event filter is about 4 second. HLT selections use the information from the entire calorimeter, muon spectrometer as well as the inner detector. This gives better knowledge about the energy deposition and track

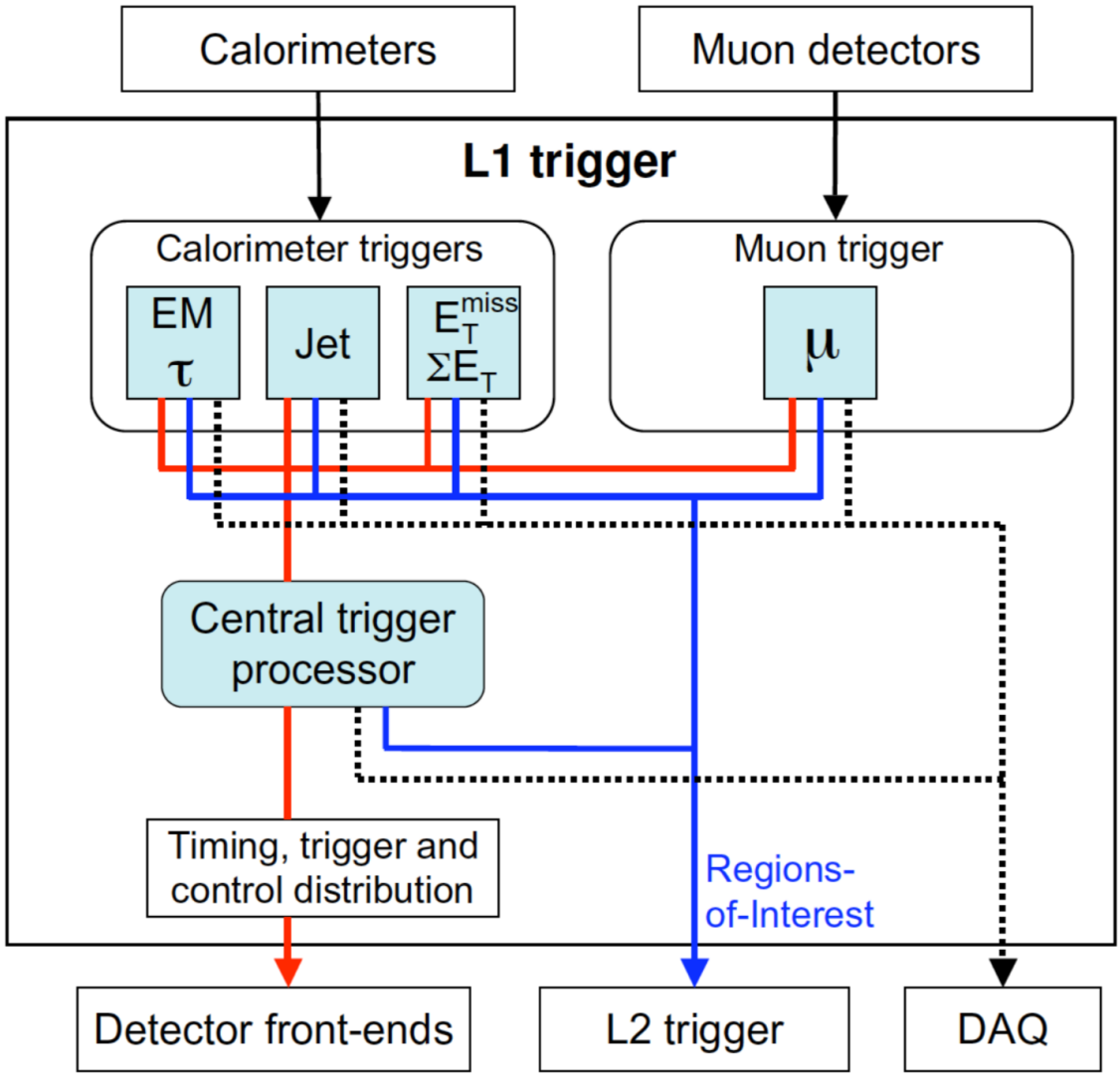

Figure 4.8: A simple diagram showing how L1 trigger system works. Information from calorimeters and muon spectrometer is sent to calorimeter and muon triggers. Decision on whether this event will be accepted or not is made at CTP. Information about RoI is sent to L2 trigger at the same time, which is used as seeds for HLT selections.

reconstruction in an event, which can improve the threshold cuts and enhance the particle identification.

4.4 ATLAS track reconstruction

4.4.1 Track candidates

The algorithm that is widely used to reconstruct charged-particle tracks in the ATLAS inner detector is called the inside-out algorithm. It starts from the construction of track seeds using three different space points in the silicon detectors. A charged particle follows a helical path in a uniform magnetic field which can be determined from the three points in a track seed. Track momentum and the impact parameter with respect to the beam line can then be estimated from this helical trajectory. According to which subdetector recorded these space points, track seeds can be classified into pixel-only, SCT-only and mixed-detector seeds [42]. A combinatorial Kalman filter is used to add new hits from the other pixel and SCT layers and then track candidates can be built from these seeds. These newly added hits are required to follow the same helical direction of the previous track seed. Of course there can be numbers of track candidates from the same seed. To tell which candidate a particular hit belongs to, a procedure called ambiguity solving is implemented.

4.4.2 Ambiguity solving

There can be many fake tracks among the above track candidates and also different candidates may share the same space points from the outer layers of the silicon detectors. The procedure of ambiguity solving is implemented to give each track candidate a score based on the number of hits, holes and χ^2 of the fit. Hits on a track will always increase the score. This suggests long trajectories are always preferred rather than short tracks. If a hit is expected at the intersection of a trajectory with

an active sensor but it is not found, this intersection is counted a hole. Intersections with an inactive sensor are not included in holes. Instead it is often regarded as hits during the track selection (see the next chapter). The appearance of holes on a track will decrease the score. The goodness of the fit can also influence the track score [42]. A large χ^2 in the fit can reduce the score dramatically. The score depends on the precision of the measurement as well [43]. If a space point is measured by a preciser subdetector, the procedure tends to give the score a higher weight. On the contrary if it is from a poor measurement, it receives a lower weight to the score. When a candidate has a high score, it is more likely to represent the trajectory of a real particle. Because of this if there are hits shared by more than one candidates, they are always assigned to the track which will have the highest score after adding them. Only scores above a certain value will be accepted by the ambiguity solver. An example of ambiguity solving procedure is shown in the left panel of Figure 4.9.

4.4.3 TRT track extension

Tracks that have been accepted by the ambiguity solver will be extrapolated into TRT. Hits in TRT will be added if they are compatible with the directions of the these tracks. Track candidates in the TRT extension are formed using these extrapolated track trajectories. To decide which candidate is a good reconstructed track, a procedure similar to ambiguity solving is implemented [43]. A score is given to each of track candidates extended in TRT. If the new score is higher than the old one, the extended track candidate will be accepted. Otherwise we will still use the old track. The final collection of track candidates from this step gives the output of the inside-out algorithm.

4.4.4 The outside-in algorithm

Different from the inside-out algorithm that begins with the reconstruction in the silicon detector, the outside-in algorithm reverses the direction of track reconstruction. It starts from the outer parts of the inner detector and extends into silicon detectors. This algorithm can not find particles with low momentum, since trajectories of these particles usually exhibit a large curvature and thus cannot intersect with the TRT region. The outside-in algorithm is mainly used to reconstruct secondary particles since they are often kept away from the central beam line and may not have sufficient hits in the silicon detector to survive the ambiguity solving procedure.

There are also some other situations that tracks cannot be reconstructed using the inside-out procedure. Ambiguous hits can exist in the silicon detector. It decreases the score of the track candidate and thus makes the candidate rejected by the ambiguity solver. In addition when there is a significant energy loss near the outer endpoint of the silicon-detector track, the extrapolation from the silicon detectors may indicate the wrong direction of the real trajectory [43]. In these cases TRT extensions cannot be found using the original inside-out algorithm and the outside-in algorithm is therefore needed. Tracks that only have TRT segments without segments in the silicon detectors are called TRT-standalone tracks [44]. An example of the TRT extension in the inside-out reconstruction and TRT-standalone tracks in the outside-in algorithm is illustrated in the right panel of Figure 4.9.

The outside-in algorithm can be implemented after the inside-out reconstruction. TRT hits that have already matched the extension of inside-out tracks will no longer be used in the outside-in procedure. The unused silicon hits after the outside-in reconstruction usually come from low p_{T} particles. Tracks from low p_{T} particles usually have very small radius and thus can not survive the ambiguity solving.

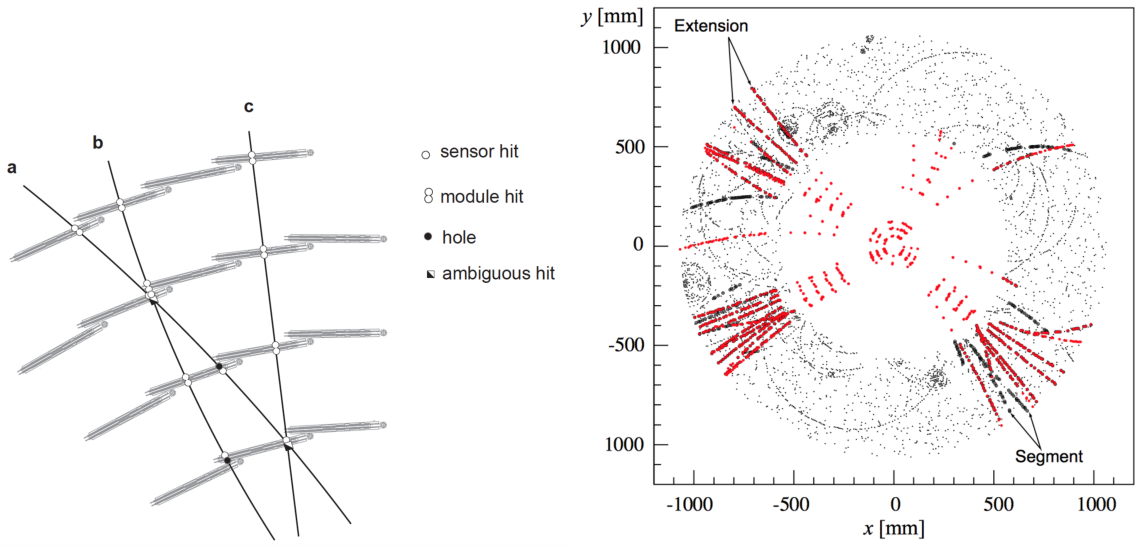

Figure 4.9: The left panel shows the process of ambiguity solving. Three tracks are illustrated in the figure. A module hit representing the measurement on both sides of the SCT layers produces higher scores than two independent sensor hits. Therefore track b has the highest score among the three. The right panel is a sample of $t\bar{t}$ event. The bright lines represent the TRT extensions from the silicon detector. The black lines are TRT-standalone tracks in the outside-in algorithm [43].

4.5 Muon reconstruction and identification

4.5.1 Muon reconstruction

Muons are reconstructed at ATLAS using the combined information from ID, MS as well as calorimeters. They are usually reconstructed independently in ID and MS first. In the ID muons are reconstructed using the same way as other charged particles described above. In the MS muon reconstruction begins with the building of track segments in the Monitored Drift Tube chambers (MDT) and Cathode Strip Chambers (CSC). Different chambers use different reconstruction algorithms to find its own segment. Muon track candidates are formed by putting these segments together. Generally two compatible track segments are needed to obtain one candidate. Whereas sometimes in the transition region between the barrel and end-cap only one track segment is needed [45]. A fit is performed in MS including all the hits that are

assigned to a certain candidate. The fits are made iteratively by adding new hits that are compatible with the direction of the trajectory or removing bad hits that are far away from the trajectory until a better χ^2 value can be obtained. The muon track candidate will pass the selection criteria if its χ^2 is small enough. According to how muon tracks are reconstructed in ATLAS, there can be four kinds of reconstructed muons, each of which is illustrated in Figure 4.10.

1. Combined muons: Nearly 96% of the reconstructed muons are Combined muons [46]. They are reconstructed by a combined fit from hits in both ID and MS. Most Combined muons are reconstructed using the outside-in algorithm. Muon trajectories are first reconstructed in MS and then extrapolated into the inner detector. The inside-out algorithm is also sometimes used as an alternative approach where tracks are extrapolated from ID to MS [45]. Fits may be performed iteratively in MS with new hits added or bad hits removed in order to obtain a better χ^2.

2. Segment-tagged muons: When muons have relative low p_{T}, only a small part of MS is crossed. It is impossible to form a complete MS muon track candidate when there are not enough MS hits. In this case a ID track is considered to be a muon when there is at least one track segment in MS compatible with extrapolation of the ID track. These are called Segment-tagged muons.

3. Calorimeter-tagged muons: A ID track can also be identified as a muon when it has a deposited energy in the calorimeter compatible with a minimum ionizing particle. This kind of identification is used in the region $|\eta| < 0.1$ where MS is not fully covered.

4. Stand-alone muons(or Extrapolated muons): When MS muon candidate appears in the region $|\eta| > 2.5$ outside the pseudorapidity coverage of ID, Standalone muon reconstruction is implemented. Trajectories of such muons are

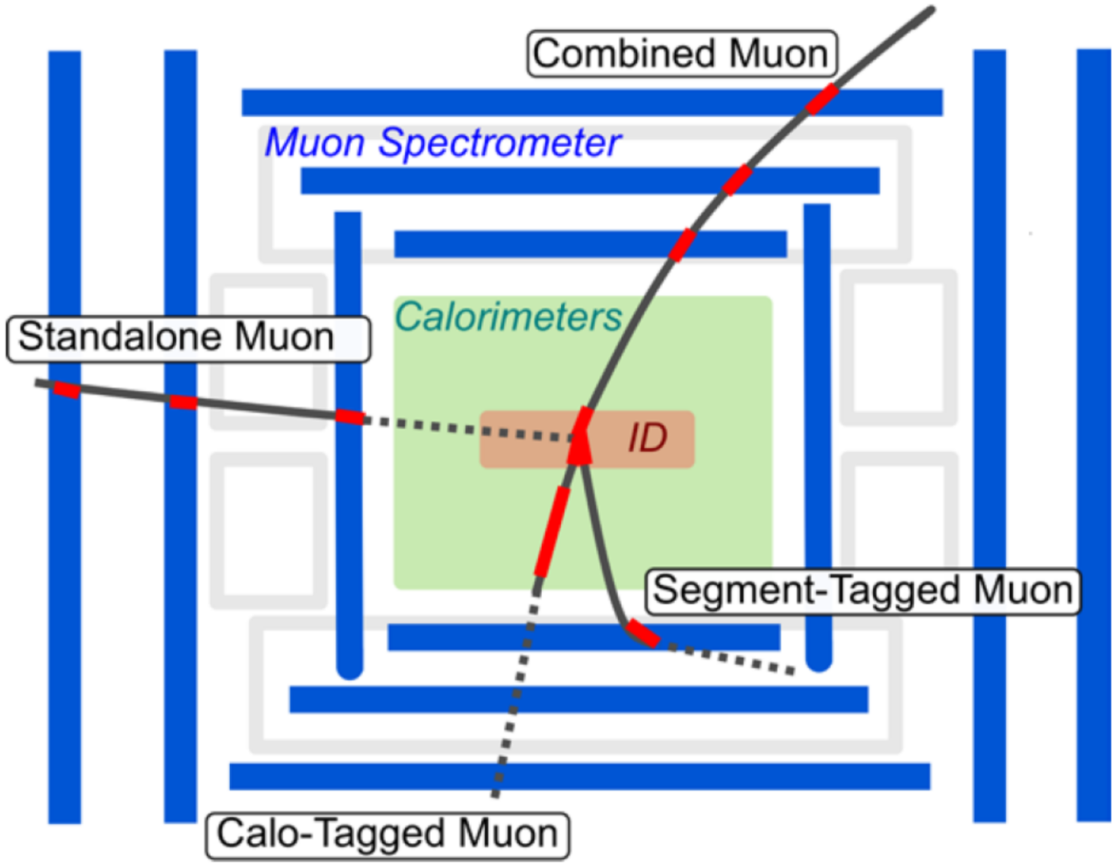

Figure 4.10: A sketch showing the four types of reconstruction muons. The red segments represent the interactions between muon tracks and the corresponding detectors. Combined muons use the combined track candidates obtained from both ID and MS. Segment-Tagged muons are reconstructed mainly in ID and extrapolate to a single segment in MS. Calorimeter-Tagged muons use the energy deposit in the calorimeter and Standalone muons are reconstructed only in the MS [47].

reconstructed using only MS tracks. Since there are no corresponding track segments in ID, muon track candidates in MS are extrapolated to the beam line accounting for the estimated energy loss in the calorimeter in order to give a better measurement of track parameters.

4.5.2 Muon identification

The procedure of muon identification is to apply different quality cuts on the muon track candidates. There are four muon identification categories: Tight, Medium, Loose and High-p_{T} muons. They are inclusive identifications where the category with tighter cuts is always included in the category with looser ones. The Medium, Tight and Loose muon criteria are listed as follows:

1. Medium muons: Medium criteria are the default muon selection used in ATLAS. Only Combined and Stand-alone muons can be selected by these criteria.

   - For Combined muons:

     a) The muon candidate is required to have hits ≥ 3 in at least 2 MS layers. For region $|\eta| < 0.1$, only hits in one layer is needed, but there should be no more than 1 hole.

     b) qOverP significance < 7, which is defined as the absolute difference between the ratios of charge to momentum in ID and MS divided by the quadrature summation of their uncertainties.

   - For Stand-alone muons:

     a) The candidate is required to have hits in at least 3 MS layers.

     b) $2.5 < |\eta| < 2.7$

2. Tight muons: A tighter cut is introduced to reject fake muons. Only Combined muons satisfying the following cuts are included:

   a) The candidate is required to have hits in at least 2 MS layers.

   b) χ^2 of the combined track fit < 8

   c) An additional cut on the qOverP significance and a certain momentum imbalance is implemented to guarantee the compatibility between momenta

measurement in ID and MS. The momentum imbalance used here is defined as the ratio of absolute difference between p_{T} measured in ID and MS to the p_{T} of the combined track.

3. Loose muons: All muon categories can be classified as loose muons.

   - Combined and Stand-alone muons are required to pass the Medium criteria.
   - Calorimeter-tagged and Segment-tagged muons should be in the range $|\eta| < 0.1$.

Chapter 5

Data sets and data analysis

5.1 Data sets

5.1.1 2015 pp data at $\sqrt{s} = 13$ and 5.02 TeV

The 13 TeV pp data in 2015 were taken in two periods, a few low-luminosity runs recorded during June with the number of collisions per bunch crossing, $\mu \approx 0.002 \sim 0.04$ plus a few intermediate-luminosity runs in August with $\mu \approx 0.05 \sim 0.6$. It has an integrated luminosity of 75nb^{-1}. The 5.02 pp data were taken in November. It includes a few intermediate-luminosity runs with $\mu \approx 1.5$, which has an integrated luminosity of 26pb^{-1}.

The configurations of minimum-bias (MB) triggers are different for these data sets. At 13 TeV MB events were collected using a L1 trigger requiring at least one hit in the MBTS. Whereas at 5.02 TeV MB events can either produce at least one hit in the MBTS using a L1 trigger or contain at least one reconstructed track on HLT. In order to obtain events with higher multiplicity, high-multiplicity (HMT) triggers are also implemented. The configuration of these triggers are shown in Table 5.1. Each trigger is a combination of a requirement on L1 E_{T} (only one trigger for the 13 TeV pp data uses the requirement of hits on MBTS) and a requirement on the

number of reconstructed tracks on HLT. Events used in the analysis are required to have one good reconstructed vertex. To reject pileup events only tracks associated with the reconstructed vertex having the largest Σp_{T}^2 are used. If there is a pileup vertex very close to this primary vertex, such events can be suppressed by excluding events with more than one good vertex. The tracking selection cuts used for pp data are sometimes called the pp-MinBias cuts:

- $|\eta| < 2.5$
- $p_{\mathrm{T}} > 0.4$ GeV
- To reject fake tracks, at least one pixel hit and six SCT hits are required
- A hit in the innermost layer of pixel detectors, i.e. the insertable B-Layer (IBL), is expected; if a hit is not expected in the IBL, a hit in the next pixel layer is required if such a hit is expected
- $|d_0| < 1.5$ mm, where d_0 is the impact parameter with respect to the beam line
- $|z_0 \sin\theta| < 1.5$ mm, $z_0 \sin\theta$ is the longitudinal distance between the primary vertex and the position where d_0 is measured
- The track fit probability $\chi^2 > 0.01$ for tracks with $p_{\mathrm{T}} > 10$ GeV. This is to remove the tracks with mis-measured p_T due to interactions with the detector material

5.1.2 2013 pPb data at $\sqrt{s_{\mathrm{NN}}} = 5.02$ TeV

The 2013 pPb data were collected during run 1 with an integrated luminosity of 28nb^{-1}. It consists of a Pb (Z= 82, A =208) beam and a 4 TeV proton beam. Since the Pb beam was circulating with the same radius as the proton beam, the corresponding Pb nucleon has an energy of $4 \times Z/A = 4 \times 82/208 = 1.57$ TeV.

Therefore the center-of-mass frame of the two colliding nucleons has a longitudinal rapidity shift of $\Delta Y = -0.465$ relative to the ATLAS rest frame in the direction of the proton beam, resulting a center-of-mass energy of 5.02 TeV per nucleon pair. The data were collected in two periods. Period A is from January 21st to February 2nd. Run numbers from 217946 to 218589 belong to this period. In these runs Pb was circulating in beam 2, moving into the positive η region, which is called "Pb going side". Meanwhile protons was circulating in beam 1 and detected in the negative η region. This is "proton going side". Runs from 218677 to 219114 belong to period B from February 2nd to 10th. In this period Pb and proton beams are reversed so that Pb was moving into the negative η region and protons are going into the positive η region with their energies remaining unchanged.

The Minbias trigger requires at least one hit on each side of the MBTS. The time difference between hits on two sides needs to satisfy $|\Delta t_{\mathrm{AC}}| < 10$ ns. A few HMT triggers are also implemented, which is illustrated in Table 5.1. Each event is required to have one good reconstructed vertex. Events with more than one primary vertex are excluded. The tracking selection is typically the same as the previous pp data with an additional requirement that $|d_0|/\sigma_{d_0} < 3$ and $|z_0 \sin\theta|/\sigma_{z_0 \sin\theta} < 3$, where σ_{d_0} and $\sigma_{z_0 \sin\theta}$ are uncertainties as d_0 and $z_0 \sin\theta$ respectively.

pp and pPb events can be characterized by the number of reconstructed charged tracks, $N_{\mathrm{trk}}^{\mathrm{rec}}$. These tracks are required to satisfy s set of selection criteria during the track reconstruction process. Figure 5.1 shows the event multiplicity distributions of these data sets. The peaks exhibited in the histograms arise from different thresholds of HMT triggers used in the analysis.

5.1.3 2016 pPb data at $\sqrt{s_{\mathrm{NN}}} = 8.16$TeV

The 8.16 TeV pPb data were taken from November to December 2016 during run 2 with an integrated luminosity of 171nb^{-1}. The proton has an energy of 6.5 TeV and

pp 13 TeV		pp 5.02 TeV		pPb 5.02 TeV	
L1	HLT	L1	HLT	L1	HLT
MBTS	$N_{\mathrm{trk}}^{\mathrm{HLT}} \geq 60$	$E_{\mathrm{T}}^{\mathrm{L1}} > 5$ GeV	$N_{\mathrm{trk}}^{\mathrm{HLT}} \geq 60$	$E_{\mathrm{T}}^{\mathrm{L1,FCal}} > 10$ GeV	$N_{\mathrm{trk}}^{\mathrm{HLT}} \geq 100$
$E_{\mathrm{T}}^{\mathrm{L1}} > 10$ GeV	$N_{\mathrm{trk}}^{\mathrm{HLT}} \geq 90$	$E_{\mathrm{T}}^{\mathrm{L1}} > 10$ GeV	$N_{\mathrm{trk}}^{\mathrm{HLT}} \geq 90$	$E_{\mathrm{T}}^{\mathrm{L1,FCal}} > 10$ GeV	$N_{\mathrm{trk}}^{\mathrm{HLT}} \geq 130$
		$E_{\mathrm{T}}^{\mathrm{L1}} > 20$ GeV	$N_{\mathrm{trk}}^{\mathrm{HLT}} \geq 90$	$E_{\mathrm{T}}^{\mathrm{L1,FCal}} > 50$ GeV	$N_{\mathrm{trk}}^{\mathrm{HLT}} \geq 150$
				$E_{\mathrm{T}}^{\mathrm{L1,FCal}} > 50$ GeV	$N_{\mathrm{trk}}^{\mathrm{HLT}} \geq 180$
				$E_{\mathrm{T}}^{\mathrm{L1,FCal}} > 65$ GeV	$N_{\mathrm{trk}}^{\mathrm{HLT}} \geq 200$
				$E_{\mathrm{T}}^{\mathrm{L1,FCal}} > 65$ GeV	$N_{\mathrm{trk}}^{\mathrm{HLT}} \geq 225$

Table 5.1: Configurations of HMT triggers used in the analysis of pp data and 5.02 TeV pPb data. Each HMT trigger is a combination of a requirement on L1 E_{T} or hits on MBTS and a requirement on the number of HLT-reconstructed tracks. $E_{\mathrm{T}}^{\mathrm{L1}}$ refers to the transverse energy over the entire ATLAS calorimeters, while $E_{\mathrm{T}}^{\mathrm{L1,FCal}}$ refers to the transverse energy only deposited in FCal. $N_{\mathrm{trk}}^{\mathrm{HLT}}$ is evaluated using charged tracks with $p_{\mathrm{T}} > 0.4$ GeV.

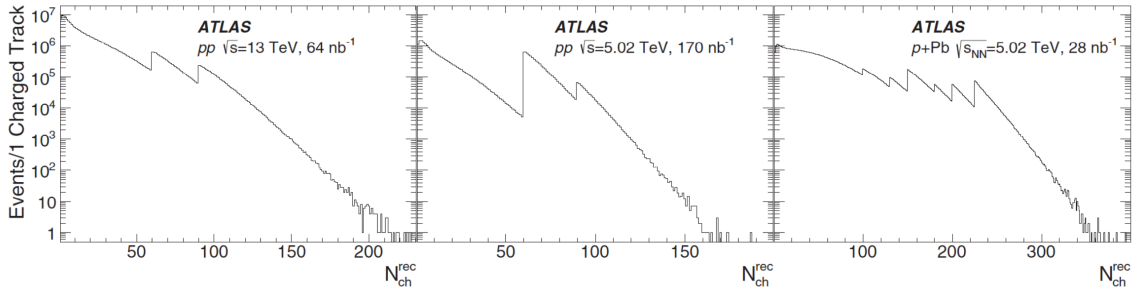

Figure 5.1: Multiplicity distributions for different data sets. All reconstructed tracks are required to have $p_{\mathrm{T}} > 0.4$ GeV. Peaks exhibited in these distributions come from events selected by HMT triggers with different thresholds. Typically HMT triggers can not record the entire luminosity. Only part of the interactions can be recorded by the HMT trigger with the highest thresholds. For pp data with 13 TeV and 5.02 TeV, luminosities of only 64 nb^{-1} and 170 nb^{-1} were recorded. While for 5.02 TeV pPb data, the full luminosity 28nb^{-1} can be recorded.

L1	HLT	L1	HLT	L1	HLT
$E_{\mathrm{T}}^{\mathrm{L1}} > 20GeV$	$N_{\mathrm{trk}}^{\mathrm{HLT}} \geq 120$	$E_{\mathrm{T}}^{\mathrm{L1}} > 90$ GeV	$N_{\mathrm{trk}}^{\mathrm{HLT}} \geq 200$	$E_{\mathrm{T}}^{\mathrm{L1}} > 160$ GeV	$N_{\mathrm{trk}}^{\mathrm{HLT}} \geq 260$
$E_{\mathrm{T}}^{\mathrm{L1}} > 20$ GeV	$N_{\mathrm{trk}}^{\mathrm{HLT}} \geq 140$	$E_{\mathrm{T}}^{\mathrm{L1}} > 120$ GeV	$N_{\mathrm{trk}}^{\mathrm{HLT}} \geq 200$	$E_{\mathrm{T}}^{\mathrm{L1}} > 200$ GeV	$N_{\mathrm{trk}}^{\mathrm{HLT}} \geq 260$
$E_{\mathrm{T}}^{\mathrm{L1}} > 50$ GeV	$N_{\mathrm{trk}}^{\mathrm{HLT}} \geq 140$	$E_{\mathrm{T}}^{\mathrm{L1}} > 120$ GeV	$N_{\mathrm{trk}}^{\mathrm{HLT}} \geq 220$	$E_{\mathrm{T}}^{\mathrm{L1}} > 160$ GeV	$N_{\mathrm{trk}}^{\mathrm{HLT}} \geq 280$
$E_{\mathrm{T}}^{\mathrm{L1}} > 50$ GeV	$N_{\mathrm{trk}}^{\mathrm{HLT}} \geq 160$	$E_{\mathrm{T}}^{\mathrm{L1}} > 160$ GeV	$N_{\mathrm{trk}}^{\mathrm{HLT}} \geq 240$	$E_{\mathrm{T}}^{\mathrm{L1}} > 200$ GeV	$N_{\mathrm{trk}}^{\mathrm{HLT}} \geq 280$
$E_{\mathrm{T}}^{\mathrm{L1}} > 90$ GeV	$N_{\mathrm{trk}}^{\mathrm{HLT}} \geq 180$	$E_{\mathrm{T}}^{\mathrm{L1}} > 200$ GeV	$N_{\mathrm{trk}}^{\mathrm{HLT}} \geq 240$		

Table 5.2: Configurations of HMT triggers used in the pPb data at 8.16 TeV. Each HMT trigger is a combination of a requirement on L1-E_{T} and a requirement on the number of HLT-reconstructed tracks. HLT-reconstructed tracks are required to have $p_{\mathrm{T}} > 0.4$ GeV.

the corresponding Pb nucleus has an energy of $6.5 \times Z/A = 6.5 \times 82/208 = 2.56$ TeV per nucleon, resulting a center-of-mass energy of 8.16 TeV. As described above, the center-of-mass frame of pPb system has a longitudinal boost of 0.465 relative to the lab frame in the proton-going direction. The data were also taken in two periods. The directions of proton and Pb beams were reversed in the second period. From run 313062 to 313435, Pb was circulating in beam 2 coming from negative η region. From run 313572 to 314170, Pb was circulating in beam 1 coming from positive η region. There are 30 runs passing the Good Run List selection.

In the hadron-hadron analysis, minimum-bias events are required to have at least one hit in MBTS at L1 plus at least one reconstructed track at HLT. The HMT trigger each has a requirement on L1-E_{T} and a requirement on the multiplicity of HLT-reconstructed tracks. The configuration of total fourteen HMT triggers are shown in Table 5.2.

In order to sample enough events with prompt muons for hadron-muon analysis, some high-multiplicity triggers are redefined by additionally requiring a L1 muon with $p_{\mathrm{T}} > 4$ GeV and a HLT muon with $p_{\mathrm{T}} > 4$ GeV as well. Each of them has a different L1-E_{T} or HLT-multiplicity threshold. These triggers will be called "μ4" triggers later in this thesis. Therefore events selected are required to pass any of the following trigger requirements:

1. A trigger that requires one reconstructed muon with $p_{\mathrm{T}} > 4$ GeV at HLT.

2. Triggers requiring a reconstructed muon with $p_{\mathrm{T}} > 4$ GeV both at L1 and at HLT level. There is also an additional requirement on the event multiplicity $N_{\mathrm{trk}}^{\mathrm{rec}} > X$. We will simply refer these triggers as Trk$X$_L1MU4. The following are the triggers used in this analysis:

   a) Trk60_L1MU4

   b) Trk80_L1MU4

   c) Trk100_L1MU4

   d) Trk120_L1MU4

3. Triggers requiring a reconstructed muon with $p_{\mathrm{T}} > 4$ GeV both at L1 and at HLT level. Additional requirements are implemented on transverse energy deposited in the entire calorimeter $\Sigma E_{\mathrm{T}} > T$ GeV at L1 level and the event multiplicity $N_{\mathrm{trk}}^{\mathrm{rec}} > X$. These triggers will be referred to as Trk$X$_L1MU4_TET.

   a) Trk100_L1MU4_TE50

   b) Trk120_L1MU4_TE50

   c) Trk140_L1MU4_TE50

   d) Trk140_L1MU4_TE70

   e) Trk140_L1MU4_TE90

   f) Trk160_L1MU4_TE50

   g) Trk160_L1MU4_TE70

   h) Trk180_L1MU4_TE70

   i) Trk180_L1MU4_TE90

   j) Trk180_L1MU4_TE120

k) Trk200_L1MU4_TE90

l) Trk200_L1MU4_TE120

m) Trk200_L1MU4_TE160

n) Trk240_L1MU4_TE120

o) Trk240_L1MU4_TE160

4. The same definition with the above triggers but the the calorimeter used at L1 level is restricted to the range $|\eta| < 2.4$. These triggers will be called as Trk$X$_L1MU4_TET_ETA24.

a) Trk60_L1MU4_TE10_ETA24

b) Trk60_L1MU4_TE15_ETA24

c) Trk60_L1MU4_TE20_ETA24

d) Trk80_L1MU4_TE15_ETA24

e) Trk80_L1MU4_TE20_ETA24

f) Trk80_L1MU4_TE25_ETA24

g) Trk100_L1MU4_TE15_ETA24

h) Trk100_L1MU4_TE20_ETA24

i) Trk100_L1MU4_TE25_ETA24

j) Trk120_L1MU4_TE15_ETA24

k) Trk120_L1MU4_TE20_ETA24

l) Trk160_L1MU4_TE25_ETA24

m) Trk160_L1MU4_TE20_ETA24

n) Trk160_L1MU4_TE25_ETA24

o) Trk160_L1MU4_TE30_ETA24

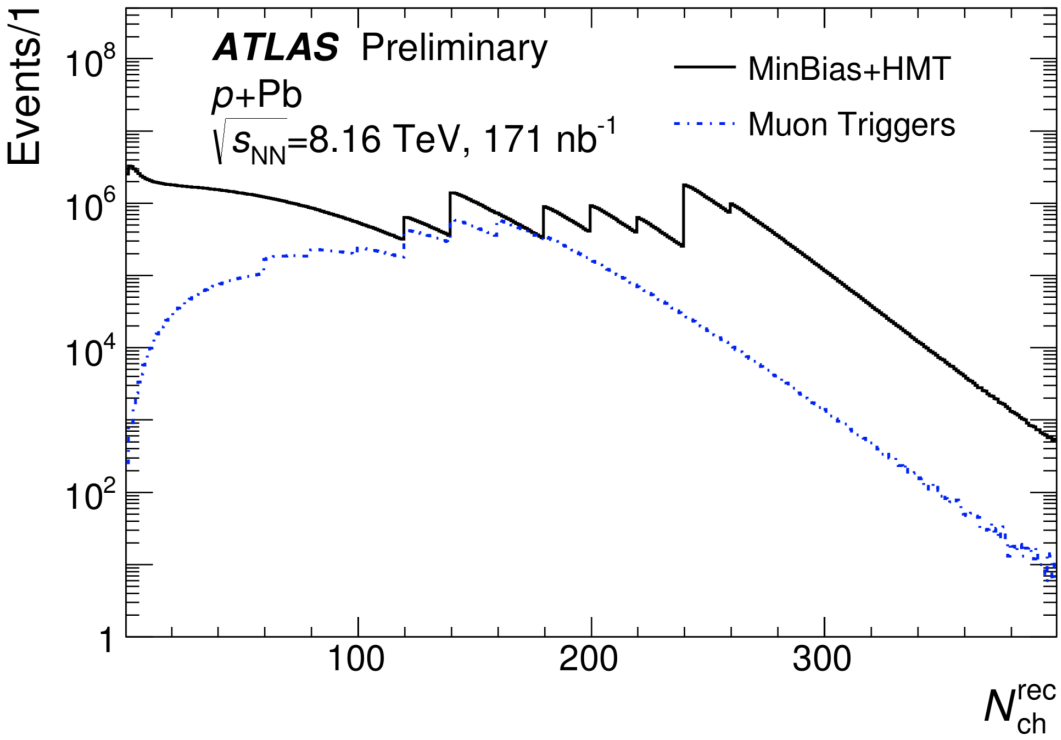

Figure 5.2: Multiplicity distributions for events selected by MinBias plus HMT triggers or μ4 triggers. All reconstructed tracks are required to have $p_{\mathrm{T}} > 0.4$ GeV. The HMT and μ4 triggers with the highest thresholds record the full 171nb^{-1} luminosity.

p) Trk220_L1MU4_TE30_ETA24

q) Trk220_L1MU4_TE35_ETA24

r) Trk220_L1MU4_TE40_ETA24

Like the previous pp data, tracks only associated with the vertex with the largest Σp_{T}^2 are used to suppress pileup events. Tracking selection cuts are generally the same as the ones used for the previous pp analysis. Event activity is shown in Figure 5.2, where only tracks with $p_{\mathrm{T}} > 0.4$ GeV are included.

The muon selection criteria used in this analysis are as follows:

1. It should be a Combined muon.

2. It passes the Tight muon or Medium muon quality cuts.

3. Muon $p_{\mathrm{T}} > 4$ GeV

4. It must match any of the $\mu 4$ triggers defined above

To further suppress the background contributions from in-flight koan or pion decays, a discriminant is implemented using the momentum imbalance distribution of the reconstructed muons [48]. The momentum imbalance can be used to describe the incompatibility of muon momentum measurement in ID and MS. It is defined as:

$$\frac{\Delta p}{p_{\mathrm{ID}}} = \frac{p_{\mathrm{ID}} - p_{\mathrm{MS}} - p_{\mathrm{param}}(p_{\mathrm{MS}}, \eta, \phi)}{p_{\mathrm{ID}}} \tag{5.1}$$

where p_{ID} is the track momentum measured in ID. p_{MS} is the track segment momentum measured by MS. $p_{\mathrm{param}}(p_{\mathrm{MS}}, \eta.\phi)$ is the parametrized estimation of the average muon energy loss when crossing the calorimeter. It is determined from the MC simulation as a function of p_{MS}, η and ϕ. Prompt muons from heavy flavor decays should have a momentum imbalance distribution with a mean of 0. However muons from pion or kaon decays only takes a small part of the energy from pions or kaons. Thus energy measured in MS would be quite smaller than energy measured in ID, which shifts its mean to the positive region. Figure 5.3 shows the distribution of momentum imbalance obtained from 13 TeV pp MC simulations. The black histogram represents the primary stable prompt muons. The background distribution typically has a broader shape than signal muons and is always peaked at some positive mean value. In this analysis, a cut $\Delta p/p_{\mathrm{ID}} < 0$ is implemented to reduce such background. In this way majority of the non-prompt muons will be rejected and a clean sample of prompt muons can be obtained.

5.1.4 2017 XeXe data at $\sqrt{s_{\mathrm{NN}}} = 5.44$ TeV

The 5.44 TeV XeXe data were taken in October 2017. It has only one run 338037 with stable beams. The total luminosity is $3\mu\mathrm{b}^{-1}$ with a peak μ about 0.00019. The

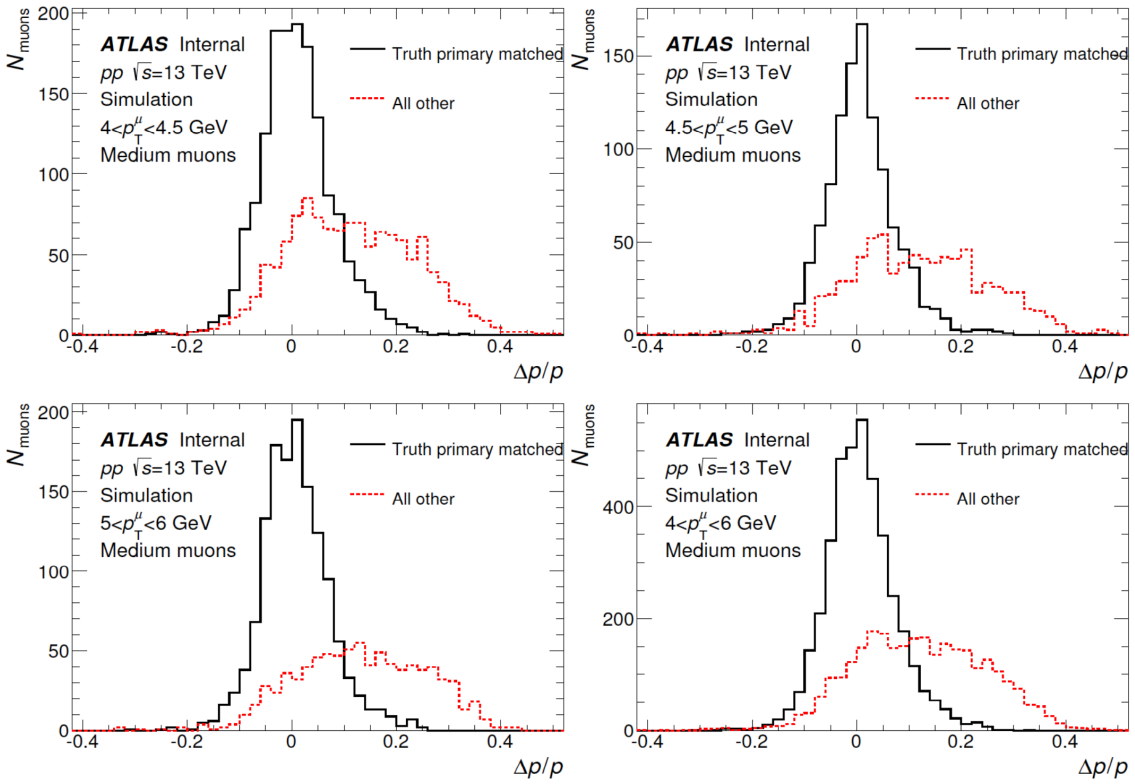

Figure 5.3: Momentum imbalance distributions of prompt and non-prompt muons from MC simulations at different muon p_{T} level. The medium muon selection cuts are used.

analysis presented here only uses MinBias stream from this run. Only one trigger is used to select events from this data set. It requires the total transverse energy deposited in the calorimeter at L1 above 4 GeV. The pileup rejection is implemented using the tight correlation between the $E_{\mathrm{T}}^{\mathrm{FCal}}$ and N_{trk}, which is illustrated in Figure 5.4. Events with single vertex are included in the narrow band that is located between the two red lines. However for pileup events since N_{trk} is calculated only with tracks from the primary vertex while $E_{\mathrm{T}}^{\mathrm{FCal}}$ also includes contributions from pileup vertex, such events will be located outside the tight correlation band with a larger $E_{\mathrm{T}}^{\mathrm{FCal}}$ value compared to the corresponding non-pileup events. Events that are not within the spaces between the two red lines will be excluded from the analysis.

In heavy ion collisions events can be classified using centrality percentiles based on

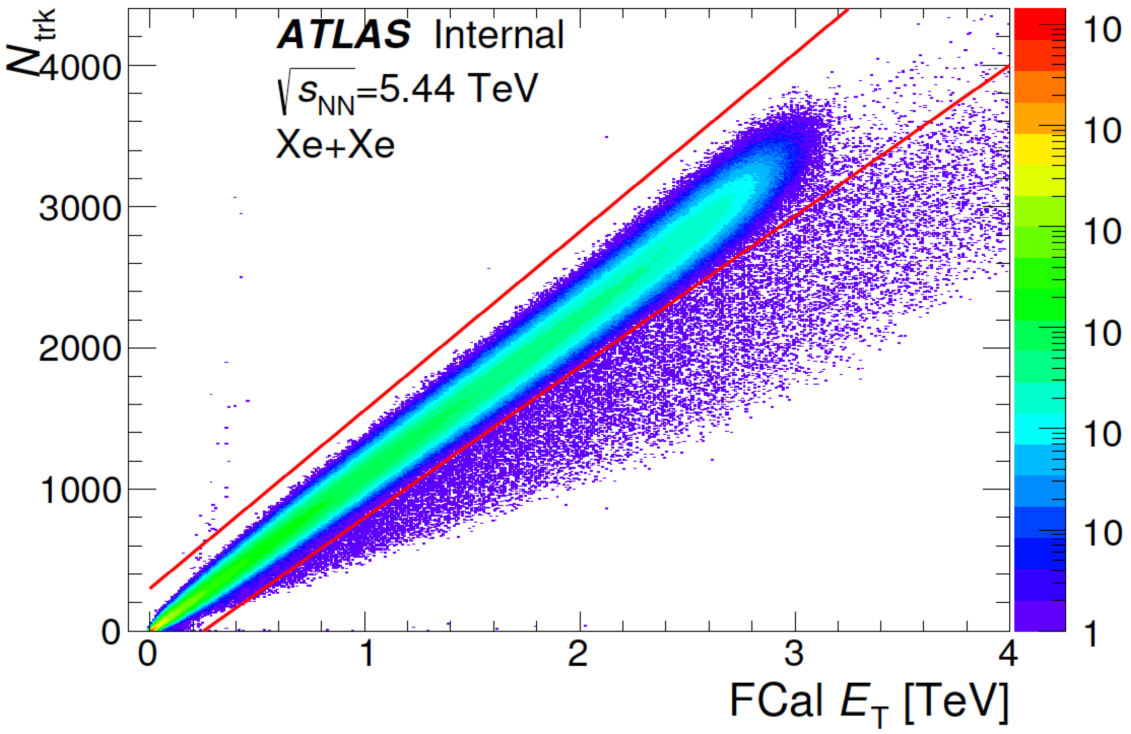

Figure 5.4: The correlation between $E_{\mathrm{T}}^{\mathrm{FCal}}$ and N_{trk} is shown in this figure. Red lines represent cuts used to reject pileup and other bad events.

$E_{\mathrm{T}}^{\mathrm{FCal}}$. Figure 5.5 shows the centrality distribution of XeXe data and its comparison to the 5.02 TeV PbPb data. PbPb E_{T} distribution in the right panel is scaled by a factor of 0.65 to match the XeXe distribution. It can be seen that centrality distributions from XeXe and PbPb events have almost identical shapes.

Different from the previous *pp* MinBias cuts, the so-called Heavy Ion Tight cuts are used for the track selection here:

- $|\eta| < 2.5$
- $p_{\mathrm{T}} > 0.5$ GeV
- To reject fake tracks, at least 2 pixel hits and 8 SCT hits are required
- There can be 1 SCT hole at most

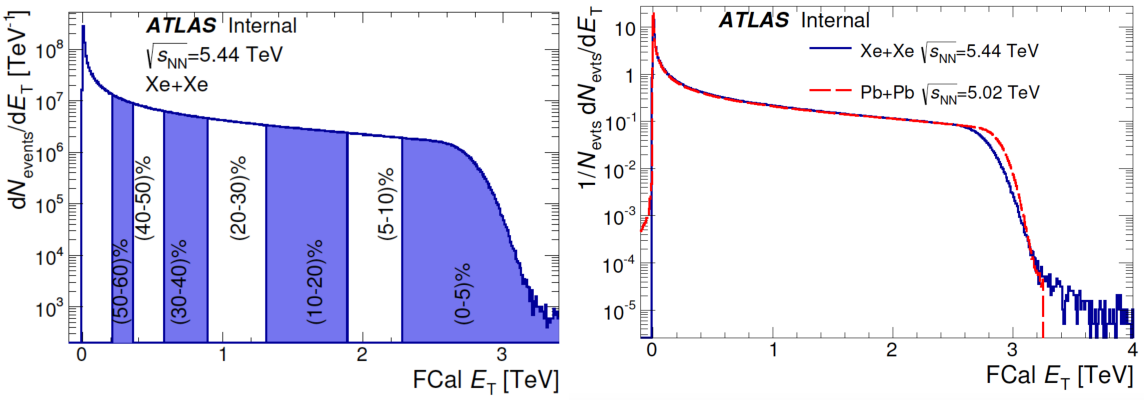

Figure 5.5: Figures that illustrate the centrality distribution of XeXe events and its comparison to the 5.02 TeV PbPb data. Different centrality bands are drawn in the left panel. The distribution is shown over the 0-80% centrality range. PbPb distribution in the right panel is scaled up by 0.65 to match the XeXe distribution.

- A hit in the IBL is expected; if a hit is not expected in the IBL, a hit in the next pixel layer is required if such a hit is expected
- $|d_0| < 1.0$ mm
- $|z_0 \sin\theta| < 1.0$ mm
- The track fit probability $\chi^2 > 0.01$ for tracks with $p_{\mathrm{T}} > 10$ GeV.
- $\chi^2/n.d.f < 6$

5.2 Data analysis

5.2.1 2-D two-particle correlations

Two-particle correlation functions are measured as a function of relative pseudo rapidity $\Delta\eta = \eta_a - \eta_b$ and relative azimuthal angle $\Delta\phi = \phi_a - \phi_b$ of two charged particles. Particle a is called "trigger" particle and particle b is called "associated" particle. In this analysis, the "trigger" particle is always a reconstructed charged track, while the "associated" particle can be either a reconstructed charged track or

a reconstructed muon. Since η is covered from -2.5 to 2.5 in ID, we have $|\Delta\eta| < 5$ in the analysis. The correlation function $C(\Delta\eta, \Delta\phi)$ is defined as the foreground distribution $S(\Delta\eta, \Delta\phi)$ divided by the background distribution $B(\Delta\eta, \Delta\phi)$.

$$C(\Delta\eta, \Delta\phi) = \frac{S(\Delta\eta, \Delta\phi)}{B(\Delta\eta, \Delta\phi)} \tag{5.2}$$

Foreground distribution is the $\Delta\eta, \Delta\phi$ distribution of two particles from the same event. Since the distribution of charged particles does not have a big dependence on the pseudo rapidity within the region $-2.5 < \eta < 2.5$, the distribution should have a peak for pairs with $|\Delta\eta| = 0$ and decline to zero for pairs with $|\Delta\eta| = 5$. Therefore $S(\Delta\eta, \Delta\phi)$ has a large triangular shape in the direction of $\Delta\eta$ axis. Besides the triangular distribution, it also includes physical correlations of two particles as well as the detector acceptance which arises from holes and dead modules in the ID. Background distribution $B(\Delta\eta, \Delta\phi)$ is the distribution of two particles from mixed events. Since two particles come from different events, the physical correlation no longer exits. It has a similar shape as the foreground distribution but only with the detector acceptance effect. In this thesis, we require the two events used in the mixing should satisfy $|\Delta N_{\mathrm{ch}}^{\mathrm{rec}}| < 10$ and $|\Delta z_{\mathrm{vtx}}| < 10$ mm. This means each pair of the mixed events are guaranteed to have similar multiplicities and primary vertex positions to properly reflect the acceptance effect. By taking the ratio in Eq. (5.2), the detector acceptance can be cancelled out. The sign of $\Delta\phi$ of each pair is flipped randomly when filling into histograms, therefore $S(\Delta\eta, \Delta\phi)$ and $B(\Delta\eta, \Delta\phi)$ are symmetric around $\Delta\phi = 0$ by construction. So is the correlation function $C(\Delta\eta, \Delta\phi)$.

Figure 5.6 is an example of two-dimensional two-particle correlation functions for *pp* events at 13 TeV. Both the "trigger" and "associated" particles are in the p_{T} range $0.5 \sim 5$ GeV. The left panel is for peripheral events with $0 < N_{\mathrm{ch}}^{\mathrm{rec}} < 20$ while the right panel is for central events with $N_{\mathrm{ch}}^{\mathrm{rec}} > 120$. These functions are plotted over the region $-\pi/2 < \Delta\phi < 3\pi/4$ and $|\Delta\eta| < 4.6$. In both panels, the peak centered

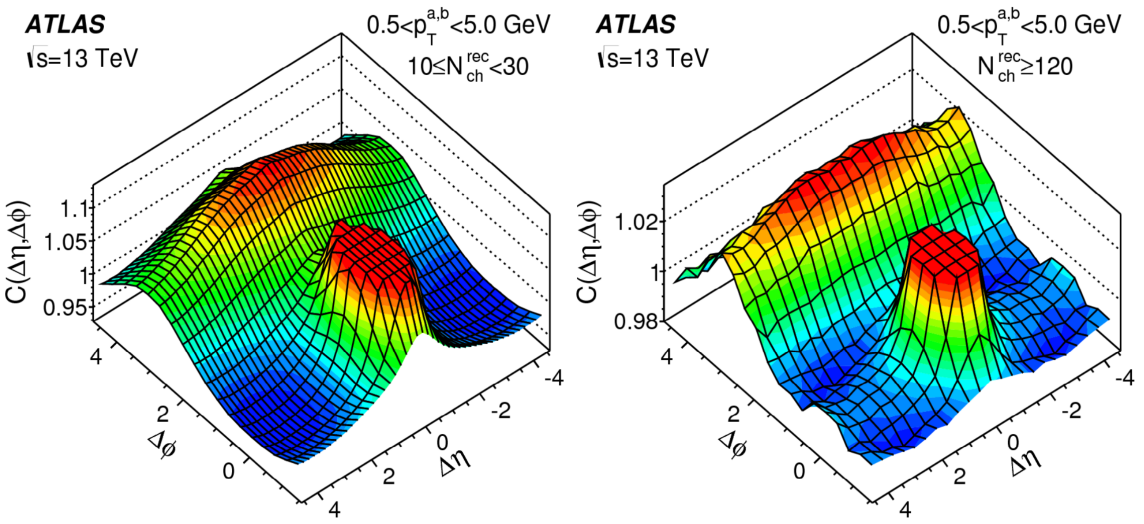

Figure 5.6: Two-particle correlation functions in pp events at 13 TeV. The left panel is for peripheral events with $0 < N_{ch}^{rec} < 20$.The right panel is for central events with $N_{\mathrm{ch}}^{\mathrm{rec}} > 120$. The peak at $\Delta\eta, \Delta\phi = 0$ is truncated in both panels.

at $\Delta\eta, \Delta\phi = 0$ is the jet contribution. The enhancement at $\Delta\phi = \pi$ along the $\Delta\eta$ axis mainly comes from the dijet component. In addition, there is a small ridge that can be seen clearly in the central events at $\Delta\phi = 0$ extending over large $|\Delta\eta|$ region. This is the near-side long-range correlations.

5.2.2 Per trigger yields

To extract the long-range correlations, a 1D two-particle correlation, which is only a function of $\Delta\phi$, is needed. It is defined as the ratio of the foreground distribution integrated over large $|\Delta\eta|$ region to the background distribution integrated over the same $|\Delta\eta|$ region. As is shown in Eq. (5.3). Usually the long range $|\Delta\eta|$ region in the integration is chosen to be $2 < |\Delta\eta| < 5$, while in the 8.16 TeV pPb analysis we integrate over $1 < |\Delta\eta| < 5$. Since in that case the jet component already disappears when $|\Delta\eta|$ goes above 1. By integrating over only large $|\Delta\eta|$ region, the jet peak centered at $\Delta\eta, \Delta\phi = 0$ is excluded and only the long range part is included in near side.

$$C(\Delta\phi) = \frac{S(\Delta\phi)}{B(\Delta\phi)} = \frac{\int_{2<|\Delta\eta|<5} d\Delta\eta\ S(\Delta\eta, \Delta\phi)}{\int_{2<|\Delta\eta|<5} d\Delta\eta\ B(\Delta\eta, \Delta\phi)} \tag{5.3}$$

From the 1D correlation function defined above, the "per-trigger-particle" yield $Y(\Delta\phi)$ is obtained.

$$Y(\Delta\phi) = \frac{1}{N^a} \frac{\int d\Delta\phi\ B(\Delta\phi)}{\int d\Delta\phi} C(\Delta\phi) \tag{5.4}$$

It is defined as the long range correlation per trigger particle. N^a is the number of "trigger" particles in the corresponding multiplicity and transverse momentum bin. Since $B(\Delta\phi)$ only represents the detector acceptance, it is a good idea to normalize it when we calculate per trigger yield. This is why the factor in the middle of the right hand side in Eq. (5.4) comes. It is a normalization factor for the background distribution appearing in the denominator of $C(\Delta\phi)$. Actually there is also another way to normalize the background distribution. That is to require $C(\Delta\phi)$ and $S(\Delta\phi)$ give the same integral over the 2π $\Delta\phi$ region. In this thesis, however, we will stick to Eq. (5.4). From this equation we can see $Y(\Delta\phi)$ has an identical shape as $C(\Delta\phi)$ and has an integral approximately equal to the integral of $S(\Delta\phi)$ divided by N^a.

5.2.3 Template fitting method

As we have discussed so far, the per trigger yield consists of the long range correlations on the near side, which is referred to as the "ridge" structure, and the dijet peak on the away side. There is also a large pedestal under the ridge and away-side peak which represents the uncorrelated pairs in $\Delta\phi$. To extract the long range correlation, a template fitting procedure is implemented in this analysis. The fitting function is assumed to be the sum of a hard component, which represents the dijet contribution, and a cosine modulation, which is the "ridge" correlation.

$$Y^{\text{templ}}(\Delta\phi) = Y^{\text{templ}}_{\text{hard}}(\Delta\phi) + Y^{\text{templ}}_{\text{ridge}}(\Delta\phi) \tag{5.5}$$

where

$$Y_{\text{ridge}}^{\text{templ}}(\Delta\phi) = G^{\text{templ}}(1 + \sum_{n=2}^{\infty} 2v_{n,n}\cos(n\Delta\phi)) \tag{5.6}$$

To estimate $Y^{\text{hard}}(\Delta\phi)$ in eq (5.5), a further assumption needs to be made: The away-side dijet components in the per-trigger yields have identical shapes in different multiplicity bins. This is the key assumption underlying the long-range correlation analysis throughout this thesis. This means we could use the per-trigger yields from a different multiplicity bin, usually a peripheral bin, as a reference to estimate the $Y^{\text{hard}}(\Delta\phi)$ in a higher multiplicity bin we are now considering. We will refer to this higher multiplicity bin we are considering as the central sample and the reference bin as the peripheral sample.

ZYAM-based template fitting procedure

One way to use the peripheral reference to estimate $Y^{\text{hard}}(\Delta\phi)$ is called "zero-yield at minimum"(ZYAM) method. This assumes there are no long range correlations in ultra-peripheral events. Thus if we remove all the uncorrelated pairs from the per-trigger yield, the distribution left is the hard component we need to estimate. For peripheral bins, the minimum is typically at $\Delta\phi = 0$. So we have,

$$Y^{\text{peri}}(\Delta\phi) = Y_{\text{hard}}^{\text{peri}}(\Delta\phi) + Y^{\text{peri}}(0) \tag{5.7}$$

Since the hard component has identical shape in different multiplicity regions. We use a scale factor F to match them between peripheral and central samples.

$$Y_{\text{hard}}^{\text{templ}}(\Delta\phi) = FY_{\text{hard}}^{\text{peri}}(\Delta\phi) \tag{5.8}$$

Therefore the fitting function we have is

$$Y^{\text{templ}}(\Delta\phi) = F(Y^{\text{peri}}(\Delta\phi) - Y^{\text{peri}}(0)) + G^{\text{templ}}(1 + \sum_{n=2}^{\infty} 2v_{n,n}\cos(n\Delta\phi)) \tag{5.9}$$

F and $v_{n,n}$ are fitting parameters. G is determined by requiring $Y^{\text{templ}}(\Delta\phi)$ gives the same integral as $Y(\Delta\phi)$ over the 2π $\Delta\phi$ region. This is similar to the peripheral subtraction method used in the previous pPb analysis before [36]. In that method, a scale factor similar to F is determined by matching the near-side jet peaks between peripheral and central events. In the template fitting method, we don't need any information about the short range distributions any more.

Improved template fitting procedure

Another way to estimate $Y^{\text{hard}}(\Delta\phi)$ is to assume the ridge correlation in peripheral events have the same shape as in central events $v_{n,n}^{\text{peri}} = v_{n,n}$. That is to say, the ridge Fourier coefficient $v_{n,n}$ is independent of multiplicity. Instead of Eq. (5.7) and (5.9) above, we have

$$Y^{\text{peri}}(\Delta\phi) = Y_{\text{hard}}^{\text{peri}}(\Delta\phi) + G^{\text{peri}}(1 + \sum_{n=2}^{\infty} 2v_{n,n}\cos(n\Delta\phi)) \tag{5.10}$$

and

$$Y^{\text{templ}}(\Delta\phi) = FY^{\text{peri}}(\Delta\phi) + G(1 + \sum_{n=2}^{\infty} 2v_{n,n}\cos(n\Delta\phi)) \tag{5.11}$$

where

$$G = G^{\text{templ}} - FG^{\text{peri}} \tag{5.12}$$

Again F and $v_{n,n}$ are fitting parameters. G is determined by requiring $Y^{\text{templ}}(\Delta\phi)$ and $Y(\Delta\phi)$ have the same integral. An example of improved template fitting procedure is shown in Figure 5.7. The transverse momenta of both "trigger" and "associated" particles are between $0.5 \sim 5$ GeV. The left and right panels are for

13 TeV pp data and 5.02 TeV pp data respectively. From top to bottom panels the multiplicity bins that are used are $30 < N_{\rm ch}^{\rm rec} < 40$, $60 < N_{\rm ch}^{\rm rec} < 70$ and $N_{\rm ch}^{\rm rec} > 120$. In each figure, the black dots are the per trigger yield from the experimental data. The red line is the fitting function. The black open circles indicate the scaled peripheral correlation, which is $FY^{\rm peri}(\Delta\phi)$, shifted up by an amount of G. Both the dijet component in the central events and the long range correlation in the peripheral events are included in the scaled peripheral correlation. The blue dashed line is a ridge component represents the difference between the ridge correlations of central and peripheral events. This ridge component is also shifted up by $FY^{\rm peri}(0)$ for presentation. It is easy to see that the enhancement on the near side $\Delta\phi = 0$ as well as the ridge component increases with multiplicity.

Comparison of ZYAM-based and improved template fitting procedures

Since foreground and background distributions are symmetric around $\Delta\phi = 0$ by construction, per trigger yields in central and peripheral events can be decomposed to Fourier cosine expansions as follows:

$$Y(\Delta\phi) = \sum_{n=0}^{\infty} a_n \cos(n\Delta\phi) \tag{5.13}$$

and

$$Y^{\rm peri}(\Delta\phi) = \sum_{n=0}^{\infty} a_n^{\rm peri} \cos(n\Delta\phi) \tag{5.14}$$

From Eq. (5.5) and (5.6), we can see there is no $\cos(\Delta\phi)$ term in $Y_{\rm ridge}^{\rm templ}(\Delta\phi)$. This means all the $\cos(\Delta\phi)$ term in the Fourier expansion of $Y(\Delta\phi)$ should be absorbed into $Y_{\rm hard}^{\rm templ}(\Delta\phi)$. Similar statement is also true for the hard component in $Y^{\rm peri}(\Delta\phi)$. Therefore hard components in the template fitting model are always proportional to the first-order Fourier coefficients. Matching the hard components in the central

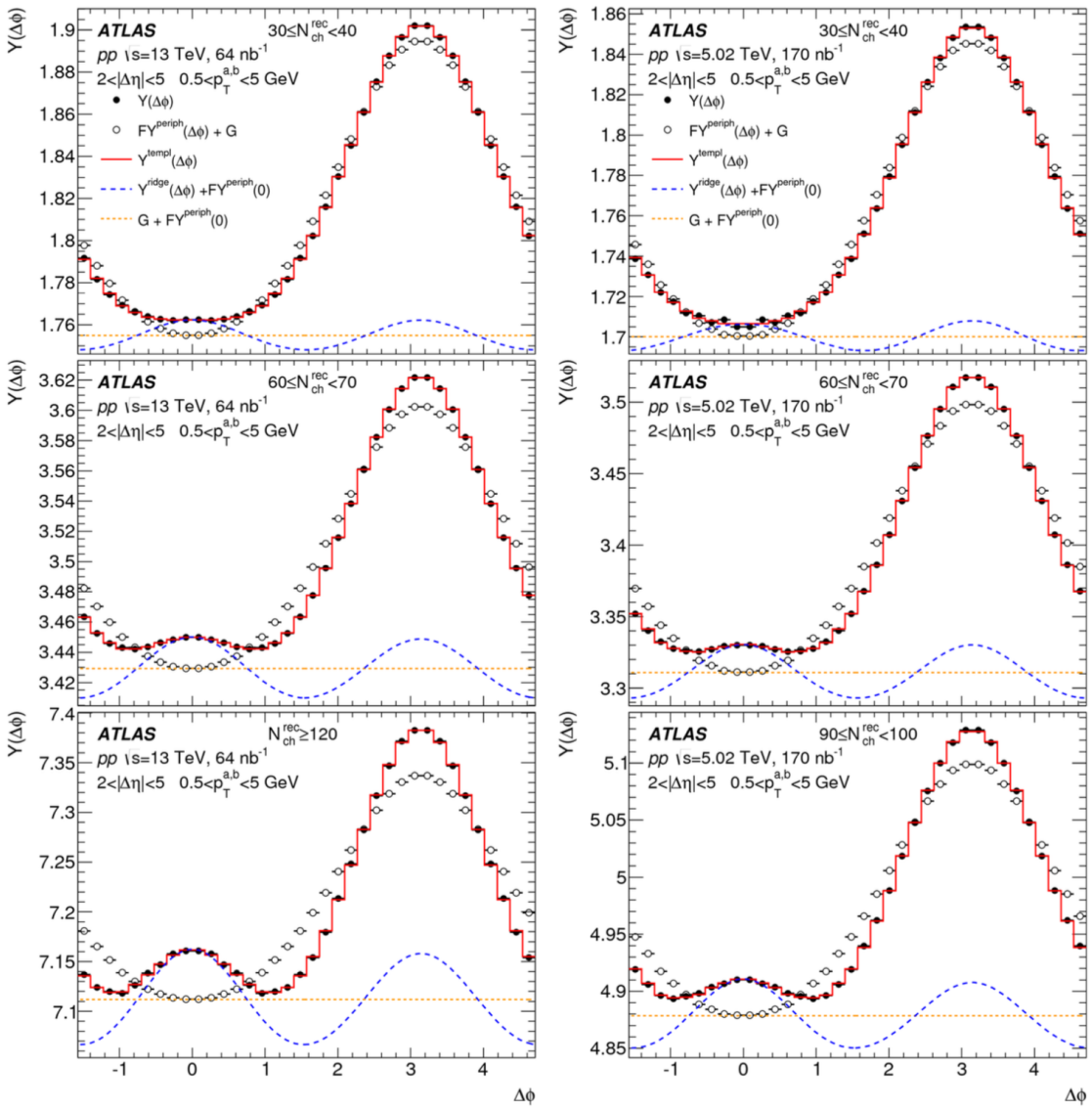

Figure 5.7: Improved template fitting method is implemented on the per trigger yields of 13 TeV and 5.02 TeV *pp* data. The fitting includes the second, third and fourth order harmonics. Both particles have transverse momenta $0.5 < p_{\mathrm{T}} < 5$ GeV. From top to bottom panels different multiplicity bins are used.

and peripheral events is actually matching their first-order Fourier coefficients. If we assume $Y^{\text{templ}}(\Delta\phi) \approx Y(\Delta\phi)$, we will have

$$F \approx \frac{a_1}{a_1^{\text{peri}}} \tag{5.15}$$

Eq. (5.15) is true for both ZYAM-based and improved template fitting method. Furthermore for ZYAM-based template fitting method, we obtain

$$v_{n,n} \approx \frac{1}{2} \frac{a_n - F a_n^{\text{peri}}}{a_0 - F a_0^{\text{peri}} + F Y^{\text{peri}}(0)} \tag{5.16}$$

From the equation above, we can see when the multiplicity of the central sample approaches the multiplicity of the peripheral reference, all $v_{n,n}$ become 0. For improved template fitting method, we have

$$v_{n,n} \approx \frac{1}{2} \frac{a_n - F a_n^{\text{peri}}}{a_0 - F a_0^{\text{peri}}} \tag{5.17}$$

Such values can be used as the initial values for the fitting parameters during the template fitting procedure. Since collective flow increases with multiplicity, we could expect $0 \leq v_{n,n}^{\text{peri}} \leq v_{n,n}$. The assumptions used in ZYAM-based and improved template fitting method are actually requiring $v_{n,n}^{\text{peri}}$ equal to its lower and upper bounds. It can be proved that by using the lower and upper bounds of $v_{n,n}^{\text{peri}}$, ZYAM-based and improved template fitting procedures produce the lower and upper bounds for $v_{n,n}$ in the central sample. The true value of $v_{n,n}$ should lie somewhere between these two bounds.

In the real analysis, the improved template fitting procedure should always be preferred, since it gives more accurate results than the ZYAM-based one. One way to see this is to look at the Fourier coefficients a_n in Eq. (5.13). These coefficients usually don't have a big dependence on the event multiplicity. Since we have assumed the hard components have identical shapes among different multiplicity bins, the Fourier coefficients $v_{n,n}$ in the ridge component should also not highly multiplicity-dependent.

Another way to see this is to compare the values of $v_{n,n}$ obtained using different peripheral references. The multiplicity dependence of $v_{n,n}$ reflects the azimuthal anisotropy in the central sample and should not depend on the peripheral reference we choose. The ZYAM-based results are more sensitive to which peripheral bin we use in the fitting especially in low multiplicity regions. However results from the improved fitting method are more stable when we change peripheral references. This means the assumption made in the improved fitting method may be more reasonable. Unless otherwise specified, when saying template fitting method, we will always mean the improved template fitting procedure in this thesis.

5.2.4 Single-particle harmonics and factorization

If the long range correlation arises from the single-particle modulations, the per trigger yield can be regarded as the convolution of the two single-particle azimuthal distributions. This means the Fourier coefficient of the two-particle correlation is equal to the product of the corresponding single-particle azimuthal harmonics.

$$v_{n,n}(p_{\mathrm{T}}^a, p_{\mathrm{T}}^b) = v_n(p_{\mathrm{T}}^a) v_n(p_{\mathrm{T}}^b) \tag{5.18}$$

Thus single particle harmonics can be obtained from $v_{n,n}$ given by the template fitting method

$$v_n(p_{\mathrm{T}}^b) = \frac{v_{n,n}(p_{\mathrm{T}}^a, p_{\mathrm{T}}^b)}{v_n(p_{\mathrm{T}}^a)} = \frac{v_{n,n}(p_{\mathrm{T}}^a, p_{\mathrm{T}}^b)}{\sqrt{v_{n,n}(p_{\mathrm{T}}^a, p_{\mathrm{T}}^a)}} \tag{5.19}$$

To check whether Eq. (5.18) holds, we can calculate $v_n(p_{\mathrm{T}}^b)$ through Eq. (5.19) using different p_{T}^a values. The result should be independent of p_{T}^a we choose. In the hadron-muon analysis, muon is always the "associated" particle. Eq. (5.19) becomes

$$v_n^{\mu}(p_{\mathrm{T}}^b) = \frac{v_{n,n}^{h-\mu}(p_{\mathrm{T}}^a, p_{\mathrm{T}}^b)}{v_n^h(p_{\mathrm{T}}^a)} = \frac{v_{n,n}^{h-\mu}(p_{\mathrm{T}}^a, p_{\mathrm{T}}^b)}{\sqrt{v_{n,n}^{h-h}(p_{\mathrm{T}}^a, p_{\mathrm{T}}^a)}} \tag{5.20}$$

Chapter 6

Results of proton-proton events at $\sqrt{s} = 5.02$ and 13 TeV

6.1 Measurement of pp collisions at $\sqrt{s} = 13$ TeV

6.1.1 Yield measurement

Figure 6.1 shows the two-particle correlation (2PC) functions constructed from 13 TeV pp data. The p_{T} ranges for both trigger and associated particles are chosen to be (0.5,5) GeV. From top left to bottom right panels event multiplicity increases from 0 to above 120. The top left one indicates the most peripheral collision, while the bottom right one represents the most central collision. The statistical fluctuation in the central-collision plots is due to insufficient statistics at high multiplicity in pp collisions. For all cases there is a peak centered at $\Delta\phi = \Delta\eta = 0$. It is the jet correlation where both particles in the pair are from the same jet. Since we are not interested in the near side jet correlation, this peak is truncated at some small value above 1 in order to observe other components in 2PC more clearly. The away side peak at $\Delta\phi = \pi$ arises from the pair where two particles come from different jets. By momentum conservation the two jets should always be back-to-back in $\Delta\phi$, but

not necessarily back-to-back in $\Delta\eta$. That's why this enhancement on the away side is along the full $\Delta\eta$ range. In central collisions, especially for events with $N_{\rm ch}^{\rm rec} > 90$, a small ridge structure can be observed at $\Delta\phi = 0$ along $\Delta\eta$ direction. This ridge correlation becomes obvious as the event multiplicity increases.

Figure 6.2 shows the 1D two particle correlation functions corresponding to the previous two dimensional plots. It is the projection of 2D correlation function onto $\Delta\phi$ axis at large $|\Delta\eta|$ values. Usually a cut $|\Delta\eta| > 2$ is chosen for the analysis. The correlations have been normalized to a mean value of 1. Multiplicity range changes from the top left panel to the bottom right panel. The away-side jet peaks have almost identical shapes across different multiplicity bins. On the near side the yellow dashed line represents the minimum value of the correlation and different structure is observed at $\Delta\phi = 0$. Low-multiplicity events have a concave-up structure which has its minimum at $\Delta\phi = 0$. Events with an intermediate multiplicity show an almost flat correlation. While events with a high multiplicity produce a small peak above the yellow line. It should be mentioned that even in the most peripheral collision the ridge correlation still exists. It is already included in the concave-up structure and is difficult to observe just from figures.

Figure 6.3 shows the average yield of associated particles for each trigger particle. The bottom panels are showing $Y^{\rm corr}$. This is the yield after the subtraction of the pedestal, i.e. after the ZYAM procedure. The integration of Y above the yellow line, or the integration of $Y^{\rm corr}$ is called $Y_{\rm int}$. Plots that represent the variation of $Y_{\rm int}$ as a function of event multiplicity are showing in Figure 6.4. There are two ways to calculate $Y_{\rm int}$. One is from the histogram. The other is from the Fourier fits of the histogram which are represented by the red line. Both ways are illustrated in the left panel of Figure 6.4. $Y_{\rm int}$ stays at zero until $N_{\rm ch}^{\rm rec}$ equal to 50 and then it increases linearly with event multiplicity. This is because the near side correlation has the concave-up or flat structure when $N_{\rm ch}^{\rm rec} < 50$. When $N_{\rm ch}^{\rm rec} > 50$ the peak at

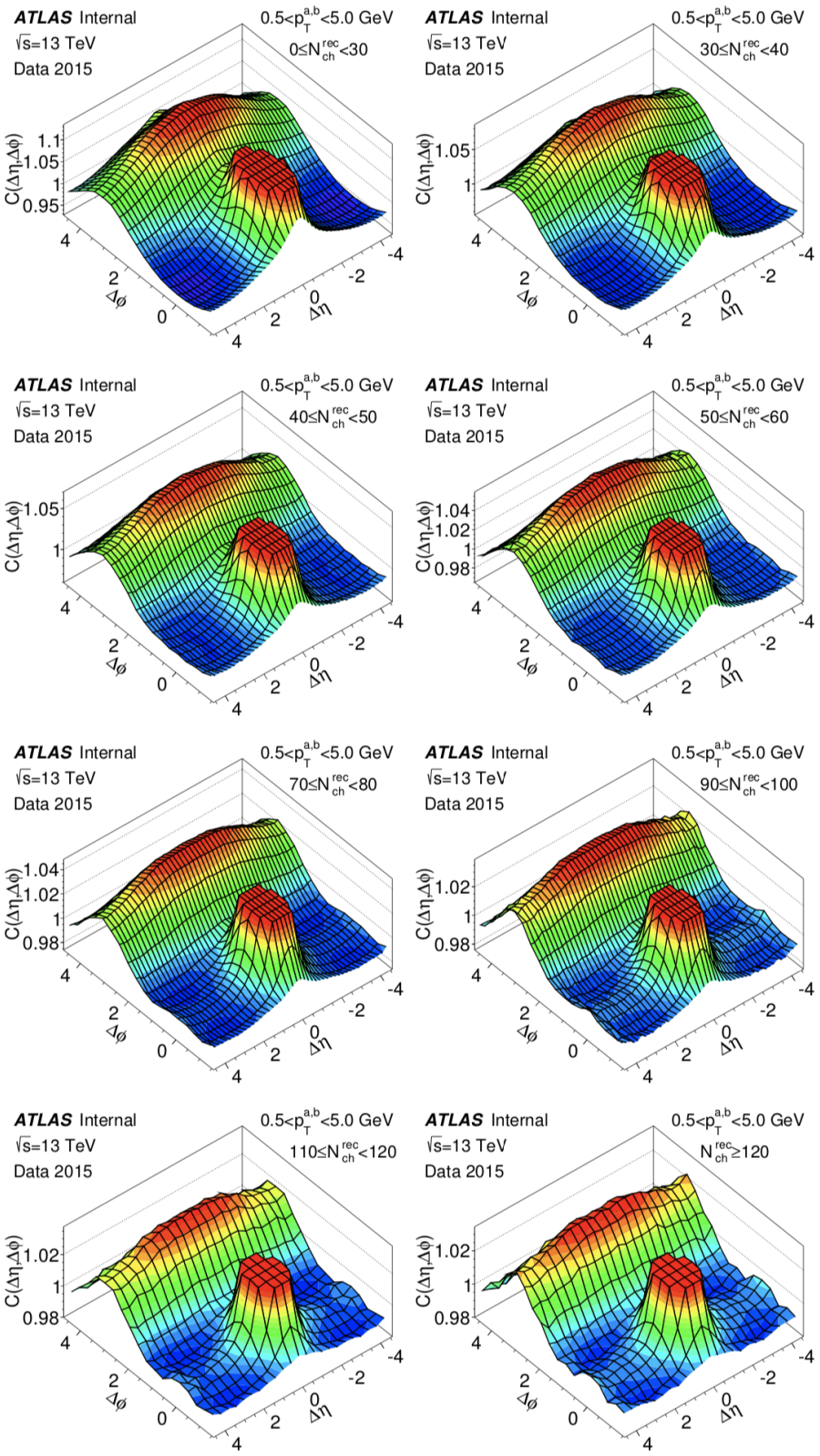

Figure 6.1: Two-particle correlation functions in *pp* events at 13 TeV. From top left to bottom right panels event multiplicity increases from 0 to above 120.

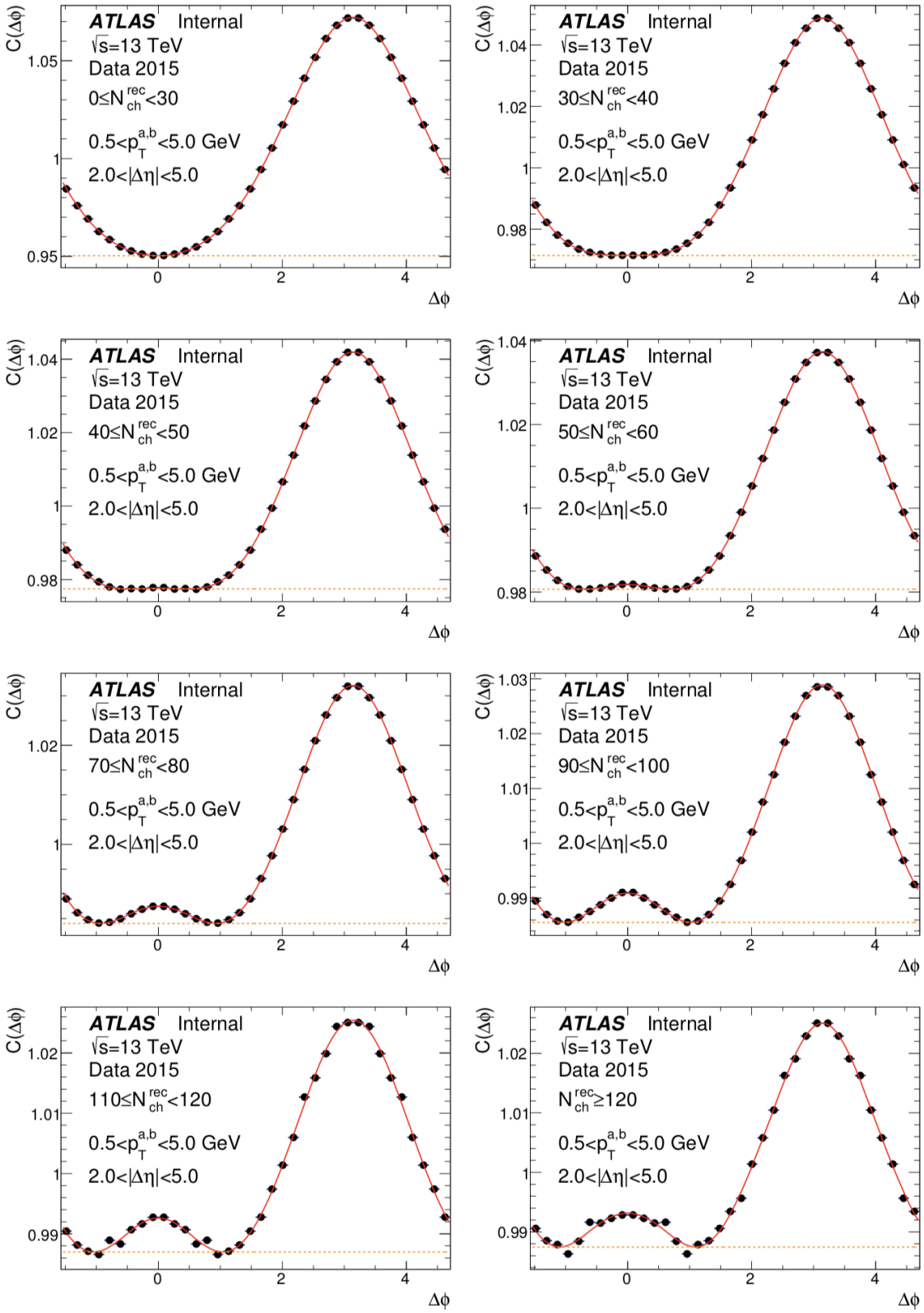

Figure 6.2: One-dimensional two-particle correlation function in pp events at 13 TeV for $|\Delta\eta| > 2$. Each panel is for a different multiplicity bin. The red line represents the Fourier fits up to the 5th order harmonics.

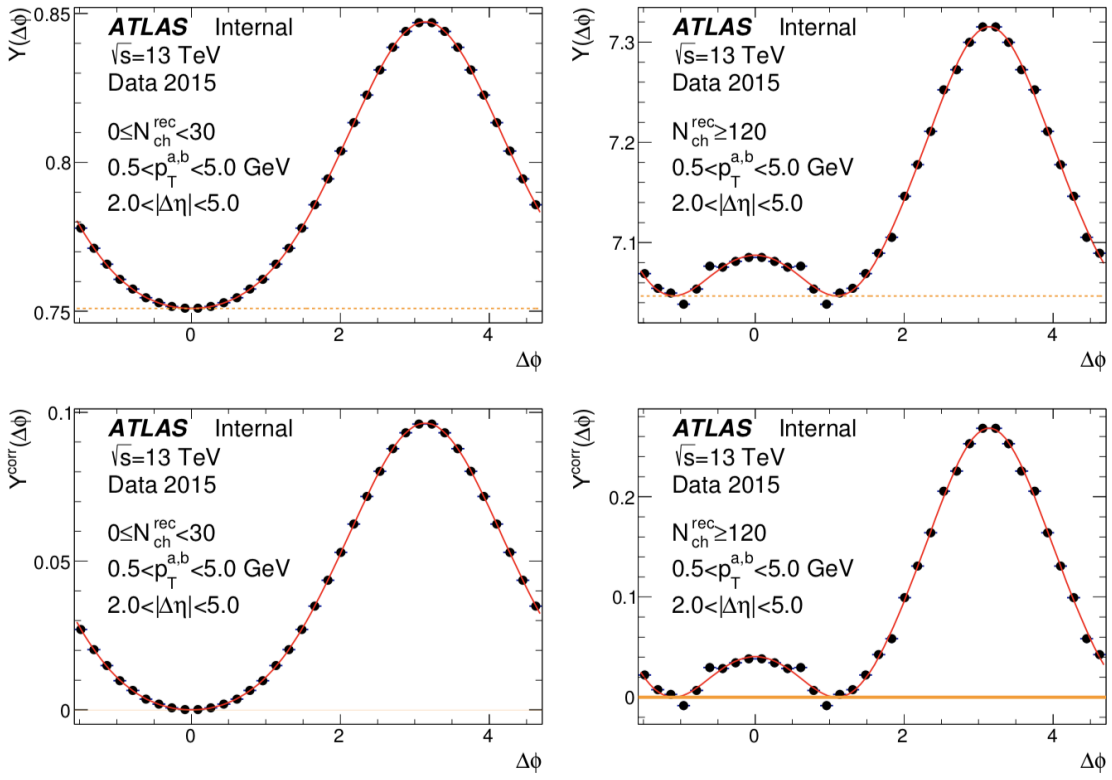

Figure 6.3: Per-trigger yields in *pp* events at 13 TeV. The bottom panels show the yields after the ZYAM procedure. They represent the correlation after the subtraction of the pedestal.

near side begin to appear. In the right panel correlations from opposite charge pairs and the same charge pairs are studied. Only the systematic variation between the two results is observed. Figure 6.5 shows the p_{T} dependence of the integrated yield. Y_{int} increases with the transverse momentum of the trigger particle until it reaches its maximum at $2 \sim 3$ GeV and then decreases.

6.1.2 ZYAM-based template fitting measurement

Figure 6.6 represents the old template fits where the ZYAM procedure is implemented for the above per-trigger yields. The black circle is the peripheral correlation after the subtraction of the pedestal. It is used as the estimate of the dijet contribution. The parameter B in these figures is the scale factor for the peripheral correlation in

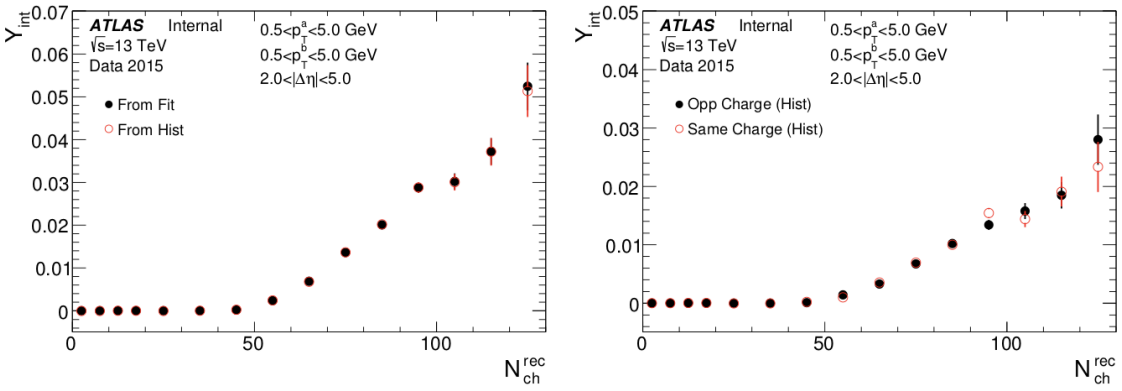

Figure 6.4: Plots show the integrated yields as a function of event multiplicity. The left panel includes the results from histograms and fits. While the right panel includes the results from opposite charge and same charge pairs.

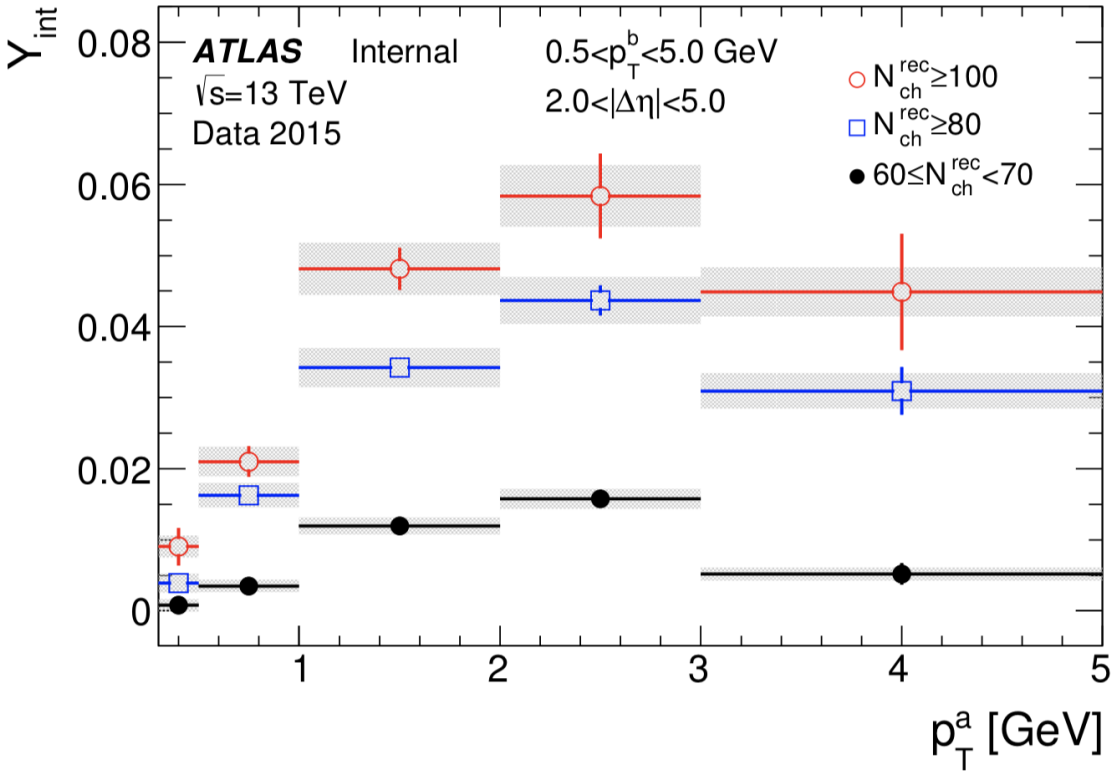

Figure 6.5: Plots show the integrated yields as a function of transverse momentum of the trigger particle.

the ZYAM-based template fitting method. The blue dashed line demonstrates the ridge correlation. The second harmonic term dominates in the ridge modulation. Its amplitude is $2Cv_{2.2}$, twice of the value indicated in the right parts of each panel. By default the peripheral bin used in the analysis is $0 < N_{\rm ch}^{\rm rec} < 20$ and the transverse momentum ranges used for both particles are (0.5, 5) GeV. Even in the panel with the concave-up structure there is a ridge correlation contributing to the near side. This gives the reason that $Y_{\rm int}$ is always zero below a multiplicity of 50. The ridge correlation that hides below the concave-up structure is not included in $Y_{\rm int}$. Thus the ZYAM procedure used in the previous yield analysis does not give the full long-range correlation in the peripheral reference.

$v_{2,2}$ in the long-range correlation from the ZYAM-based fits are shown in Figure 6.7. It increases with multiplicity in low multiplicity region and saturates at high multiplicity region. Different peripheral references are chosen for this analysis. Results from the reference with lower multiplicity give larger values than that with higher multiplicity. The difference due to the choice of peripheral references is larger in low multiplicity region and smaller in high multiplicity region. All choices of peripheral references should asymptotically give the same results at large $N_{\rm ch}^{\rm rec}$. As discussed above by construction $v_{n,n}$ extracted from the ZYAM-based templates decline to 0 at the most peripheral collisions. Although this is true regardless of the peripheral reference used, using the reference with the highest multiplicity bin gives the most rapid decline in the ultra-peripheral region. This is because ZYAM-based template fits assume there is no long-range correlation in the peripheral reference, therefore no v_n values either. $v_{n,n}$ should be close to 0 when the multiplicity bin of the data is approximately the same as that of the peripheral reference. The right panel shows the distribution of the single particle azimuthal harmonics which are the square root of the values in the left panel.

In order to check the factorization relationship, different bins for $p_{\rm T}^{\rm b}$ are used

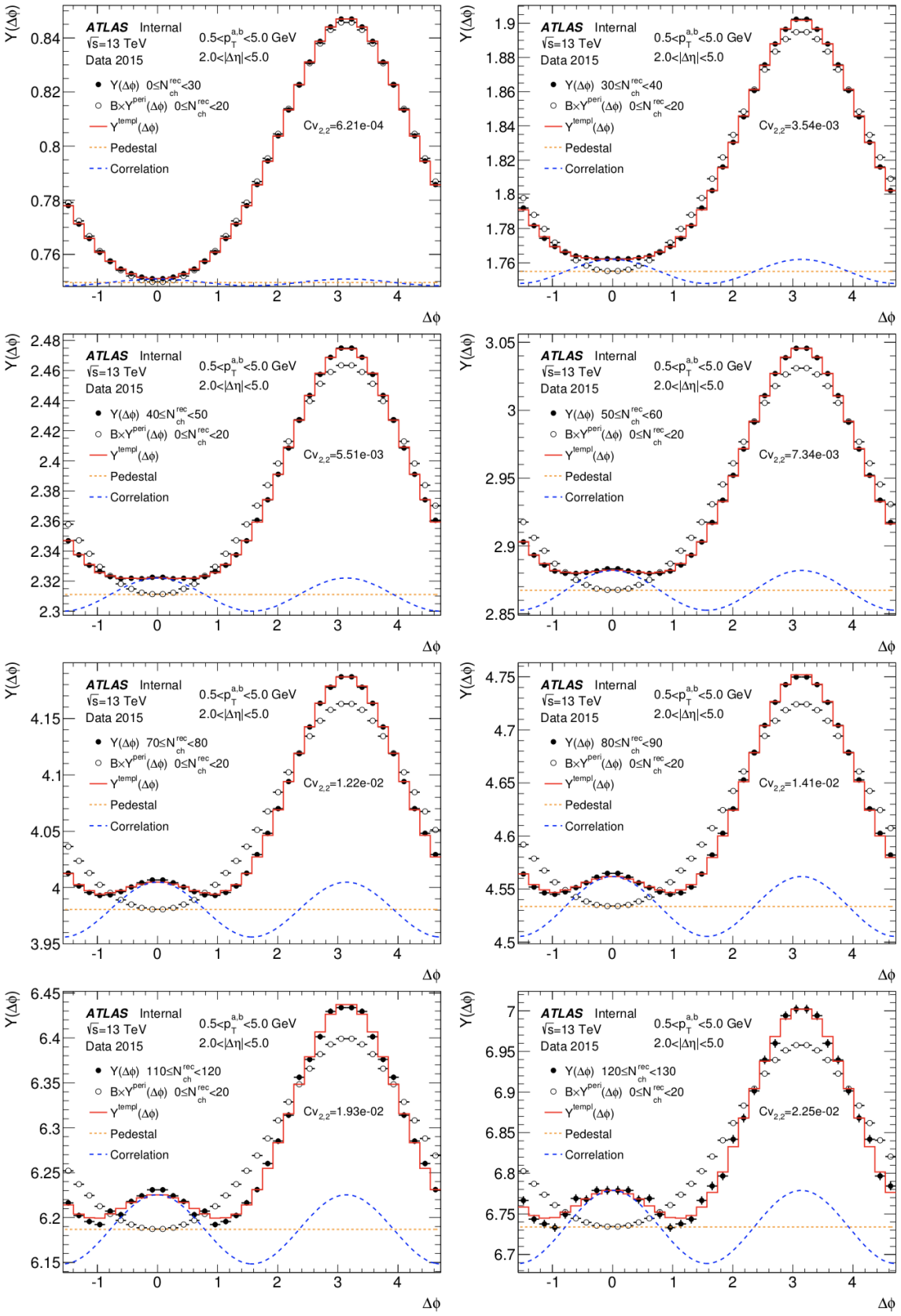

Figure 6.6: ZAYM-based template fitting method for pp events at 13 TeV. Each panel is for a certain multiplicity bin. The p_{T} ranges for both particles are chosen to be (0.5, 5) GeV. $|\Delta\eta|$ is required above 2.

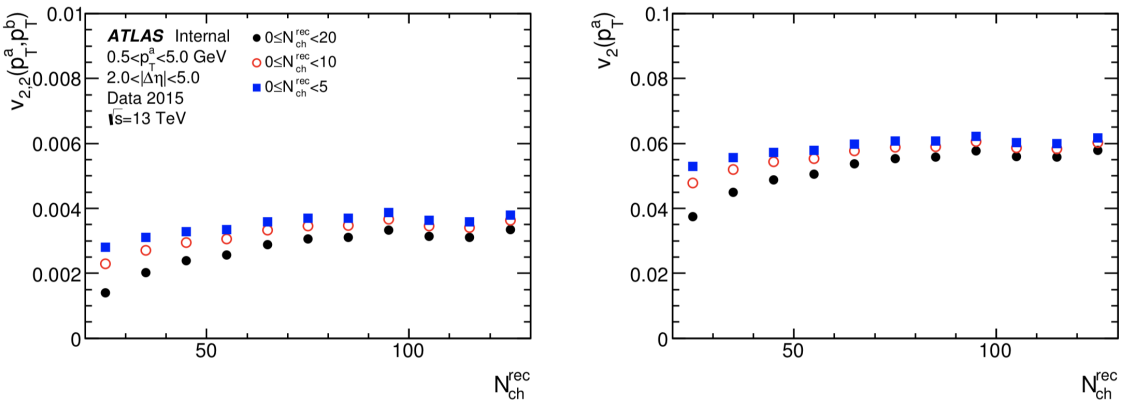

Figure 6.7: The second harmonics $v_{2,2}$ for pp events at 13 TeV extracted from ZYAM-based template fits are shown in the left panel. Different peripheral references are used for comparison. Three multiplicity bins for peripheral events are used: $0 < N_{\mathrm{ch}}^{\mathrm{rec}} < 5$, $0 < N_{\mathrm{ch}}^{\mathrm{rec}} < 10$ and $0 < N_{\mathrm{ch}}^{\mathrm{rec}} < 20$. The right panel shows the corresponding v_2.

to extract the values of $v_{2,2}$ for the same multiplicity range. This is shown in the left panels in Figure 6.8. It is clear to see that $v_{2,2}$ increases with the transverse momentum of the associated particle while the p_{T} range for the trigger particle is fixed. The right panels show $v_2(p_{\mathrm{T}}^{\mathrm{a}})$ obtained from dividing $v_{2,2}(p_{\mathrm{T}}^{\mathrm{a}}, p_{\mathrm{T}}^{\mathrm{b}})$ by $v_2(p_{\mathrm{T}}^{\mathrm{b}})$. Almost identical results of v_2 as a function of $N_{\mathrm{ch}}^{\mathrm{rec}}$ are obtained. This means the factorization relationship holds pretty well in this full multiplicity range.

6.1.3 Improved template fitting measurement

In the improved template fits instead of using the peripheral reference with the ZYAM procedure we use the full peripheral correlation as the estimate of the away-side jet correlation. The template fitting plots are shown in Figure 6.9. Since the majority of the pedestal in $Y(\Delta\phi)$ is included in the peripheral reference, the fitting parameter C, which also has the name "Pedestal" in the panels, lies far below the yield histogram, indicated by the yellow dashed line. For easy comparison in the later analysis we will shift this pedestal (C) and the ridge correlation (blue dashed curve) up by the value of the scaled peripheral reference at $\Delta\phi = 0$ in improved template fits. In that case

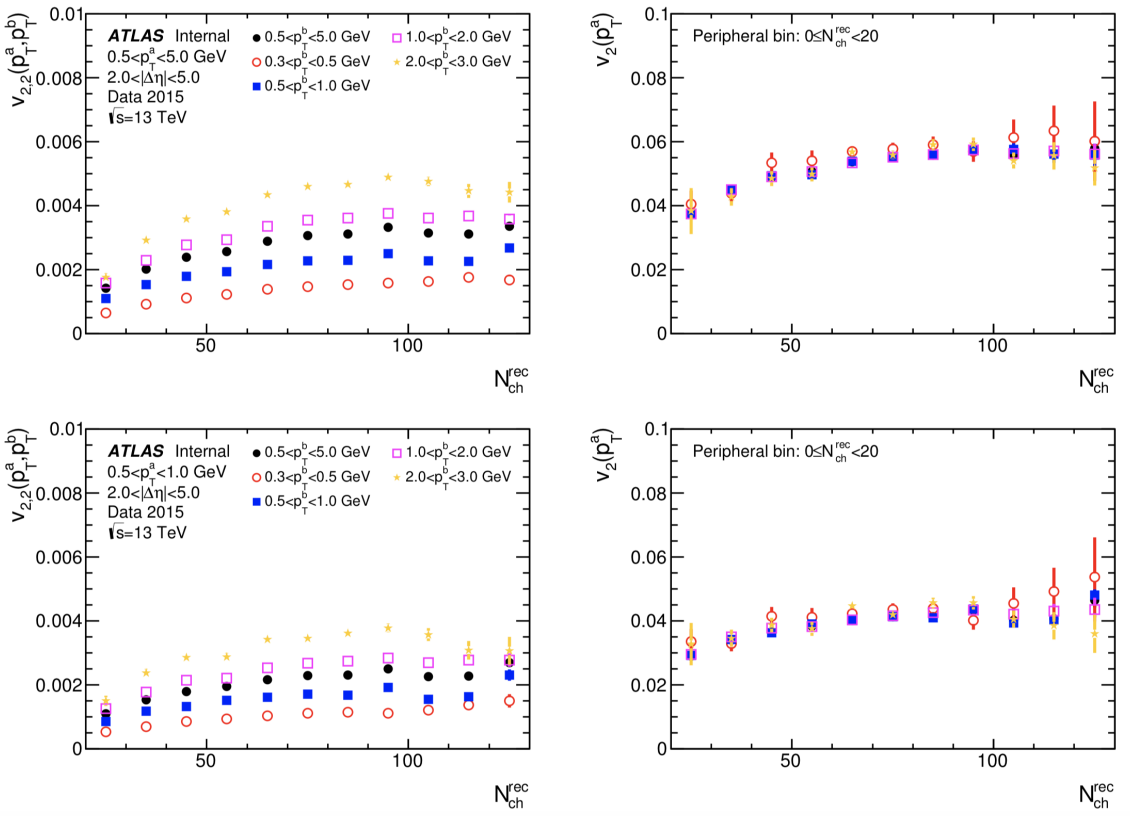

Figure 6.8: Factorization relationship for pp events at 13 TeV is checked as a function of event multiplicity. $v_{2,2}$ is calculated using different bins for $p_{\mathrm{T}}^{\mathrm{b}}$ while $p_{\mathrm{T}}^{\mathrm{a}}$ is fixed. Five bins of $p_{\mathrm{T}}^{\mathrm{b}}$ are used: $0.5 < p_{\mathrm{T}}^{\mathrm{b}} < 5$ GeV, $0.3 < p_{\mathrm{T}}^{\mathrm{b}} < 0.5$ GeV, $0.5 < p_{\mathrm{T}}^{\mathrm{b}} < 1.0$ GeV, $1.0 < p_{\mathrm{T}}^{\mathrm{b}} < 2.0$ GeV and $2.0 < p_{\mathrm{T}}^{\mathrm{b}} < 3.0$ GeV. The right panel shows the corresponding v_2.

only a small part of y axis will be used and fits will look similar to the ZYAM-based ones even if ZYAM procedure is not used here. Values of B and $Cv_{2,2}$ are the same for ZYAM-based and improved template fits. Since C is much smaller in the improved fitting method, $v_{2,2}$ becomes much larger compared to the ZYAM-based results.

Different from the old template fits, the improved template fitting procedure assumes that peripheral reference has the same Fourier harmonics of the long-range correlation in $Y(\Delta\phi)$ or $C(\Delta\phi)$ as the data. The $v_{2.2}$ results are illustrated in Figure 6.10. The upper plots illustrate results with different peripheral references. All histograms do not decline to zero in the peripheral region and by construction they show a very weak dependence on multiplicity. The difference between them

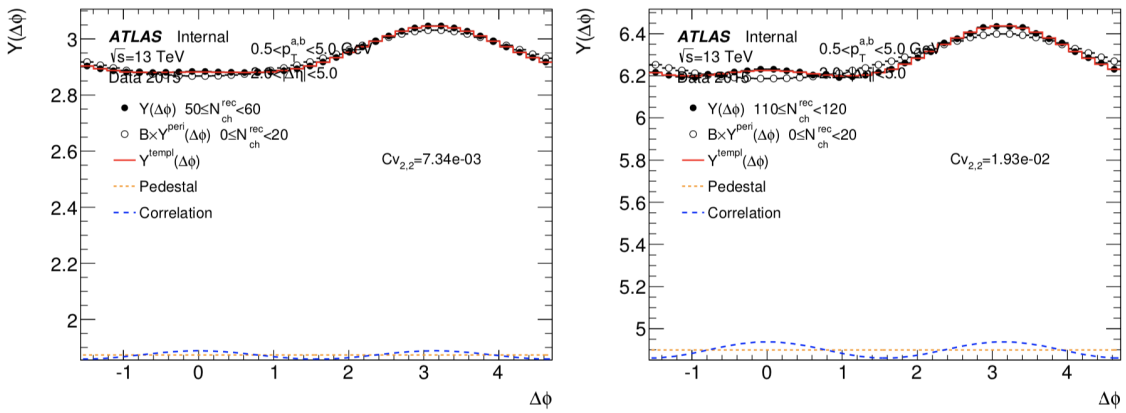

Figure 6.9: Improved template fitting method for pp events at 13 TeV. Each panel is for a certain multiplicity bin. The p_{T} ranges for both particles are chosen to be (0.5, 5) GeV. $|\Delta\eta|$ is required above 2.

is pretty small compared to the ZYAM-based cases, which means the assumptions underlying the improved template fitting method may be more reasonable. The improved template-fit results should be closer to their actual physical values since single particle harmonics should not depend on the peripheral references used in the template fitting analysis. The bottom panels illustrate the ratios of these results. The default reference $0 < N_{\mathrm{ch}}^{\mathrm{rec}} < 20$ is used as the denominator.

Factorization relationship is checked both as a function of event multiplicity and the transverse momentum of the trigger particle. Figure 6.11 demonstrates the multiplicity dependence of $v_{2,2}$ using different $p_{\mathrm{T}}^{\mathrm{b}}$ intervals. $v_{2,2}$ values increase with $p_{\mathrm{T}}^{\mathrm{b}}$ for fixed $p_{\mathrm{T}}^{\mathrm{a}}$. From the right panels we see factorization holds quite well, especially in the low and intermediate multiplicity range. Figure 6.12 checks the factorization of $v_{2,2}$ as a function of $p_{\mathrm{T}}^{\mathrm{a}}$. From the right panels we see factorization holds true for low and intermediate p_{T} but breaks at high p_{T}. This might result from the large systematic errors due to the multiplicity-dependent change in the shapes of the away-side jet correlation at high p_{T} values. With the increase of the multiplicity, factorization will hold for higher p_{T} intervals. Figure 6.13 also includes similar analysis for $v_{3,3}$.

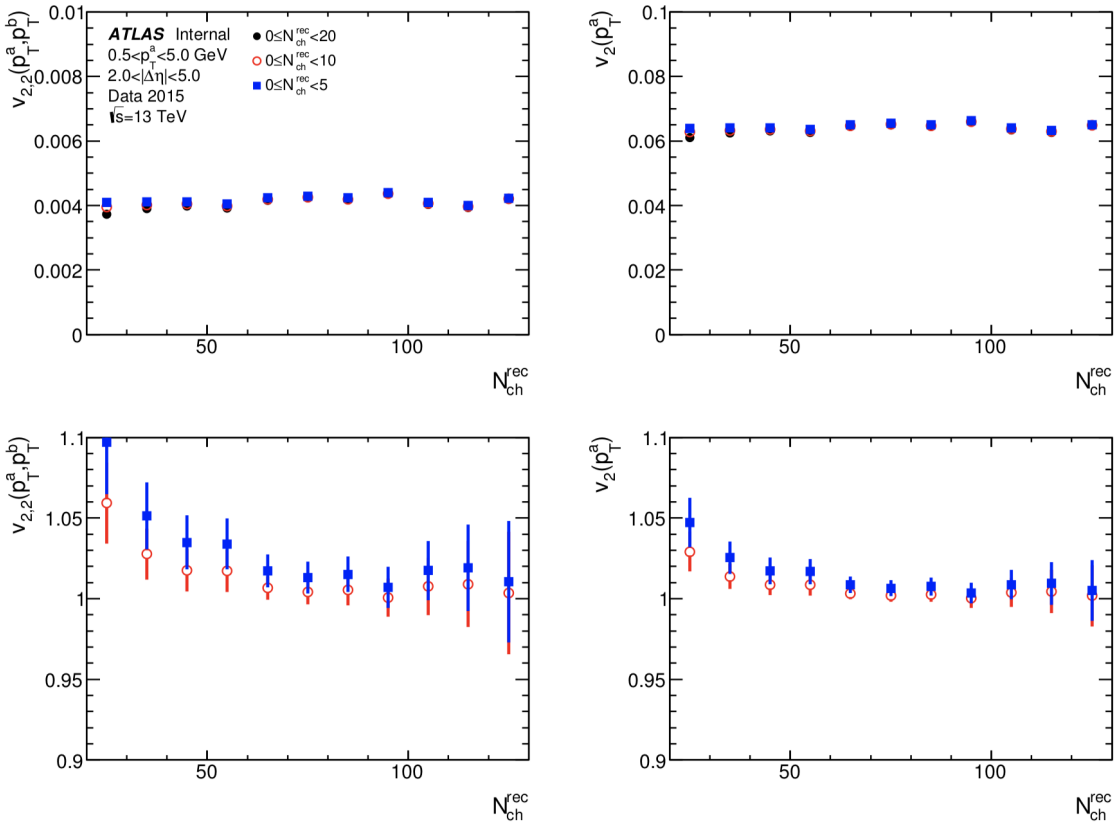

Figure 6.10: The second harmonics $v_{2,2}$ for pp events at 13 TeV extracted from improved template fits are shown in the left panel. Different peripheral references are used for comparison. Three multiplicity bins for peripheral events are used: $0 < N_{\mathrm{ch}}^{\mathrm{rec}} < 5$, $0 < N_{\mathrm{ch}}^{\mathrm{rec}} < 10$ and $0 < N_{\mathrm{ch}}^{\mathrm{rec}} < 20$. The upper right panel shows the corresponding v_2. The bottom panels illustrate the ratios between results from different peripheral references.

As a cross check, the dependence of the long-range correlation on the relative charge of the particles is also studied. We constructed 2PC using the same-charge pairs and opposite-charge pairs and implemented the improved template fits. Results are shown in Figure 6.14. No systematic difference is observed in the figure. It comes to the conclusion that the long-range correlation is not charge dependent.

Figure 6.15 shows the comparison of results obtained from direct Fourier decomposition, ZYAM-based template fits and improved template fits. Values of $v_{2,2}$, $v_{3,3}$ and $v_{4,4}$ are illustrated from top to bottom panels. Error bars represent statistical uncertainties only. Without the removal of the hard contribution, i.e. the away-side

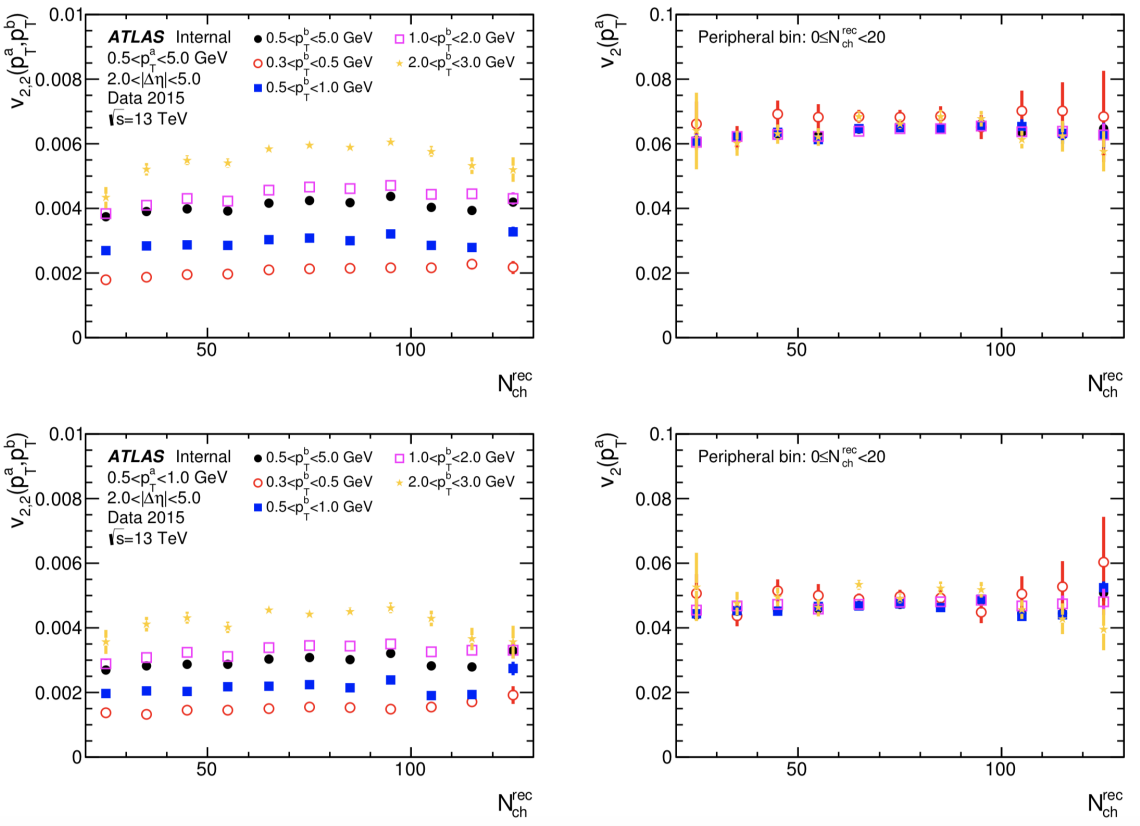

Figure 6.11: Factorization relationship for pp events at 13 TeV is checked as a function of event multiplicity. $v_{2,2}$ is calculated using different bins for $p_{\mathrm{T}}^{\mathrm{b}}$ while $p_{\mathrm{T}}^{\mathrm{a}}$ is fixed. Five bins of $p_{\mathrm{T}}^{\mathrm{b}}$ are used: $0.5 < p_{\mathrm{T}}^{\mathrm{b}} < 5$ GeV, $0.3 < p_{\mathrm{T}}^{\mathrm{b}} < 0.5$ GeV, $0.5 < p_{\mathrm{T}}^{\mathrm{b}} < 1.0$ GeV, $1.0 < p_{\mathrm{T}}^{\mathrm{b}} < 2.0$ GeV and $2.0 < p_{\mathrm{T}}^{\mathrm{b}} < 3.0$ GeV. The right panel shows the corresponding v_2.

jet correlation, the resulting Fourier harmonics are different from those obtained in the template fitting method. As we can see v_2 from direct Fourier decomposition is always larger than that from the other two methods. While v_3 from Fourier transform always gives smaller values. This is because the hard component always gives positive v_2 and negative v_3 (This is obvious since the hard component is peaked at $\Delta\phi = \pi$). Those differences are larger in low multiplicity events and gradually decreases to 0 at high multiplicity since in central events 2PC is dominated by the soft contribution. The fraction of the jet correlation becomes smaller due to the large underlying event. ZYAM-based template fits give smaller results than improved ones which is expected. The right panels are drawn as a function of $E_{\mathrm{T}}^{\mathrm{FCal}}$. Different from the multiplicity

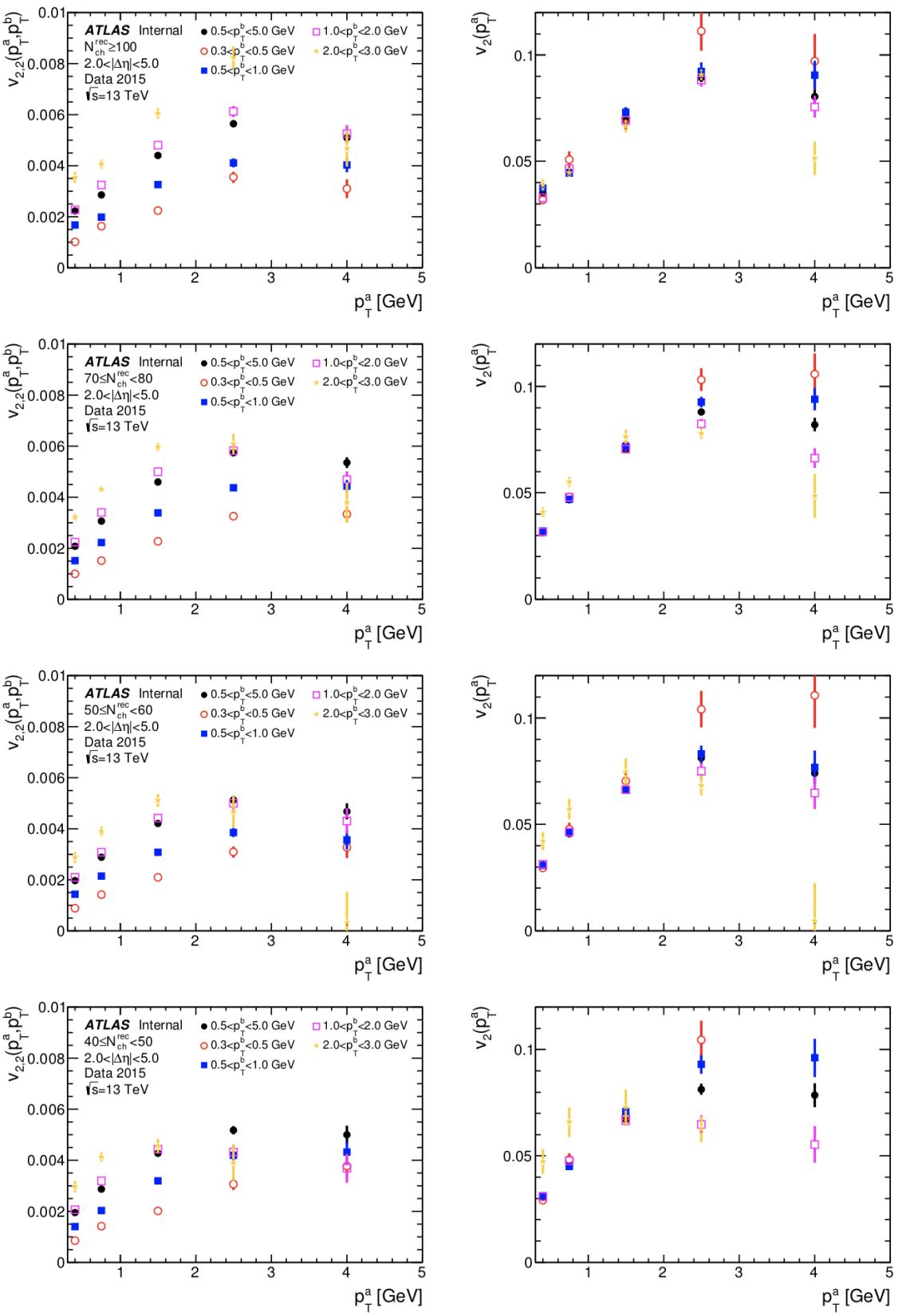

Figure 6.12: Factorization relationship for pp events at 13 TeV is checked as a function of $p_{\mathrm{T}}^{\mathrm{a}}$. $v_{2,2}$ is calculated using different bins for $p_{\mathrm{T}}^{\mathrm{b}}$ while $p_{\mathrm{T}}^{\mathrm{a}}$ is fixed. The right panel shows the corresponding v_2.

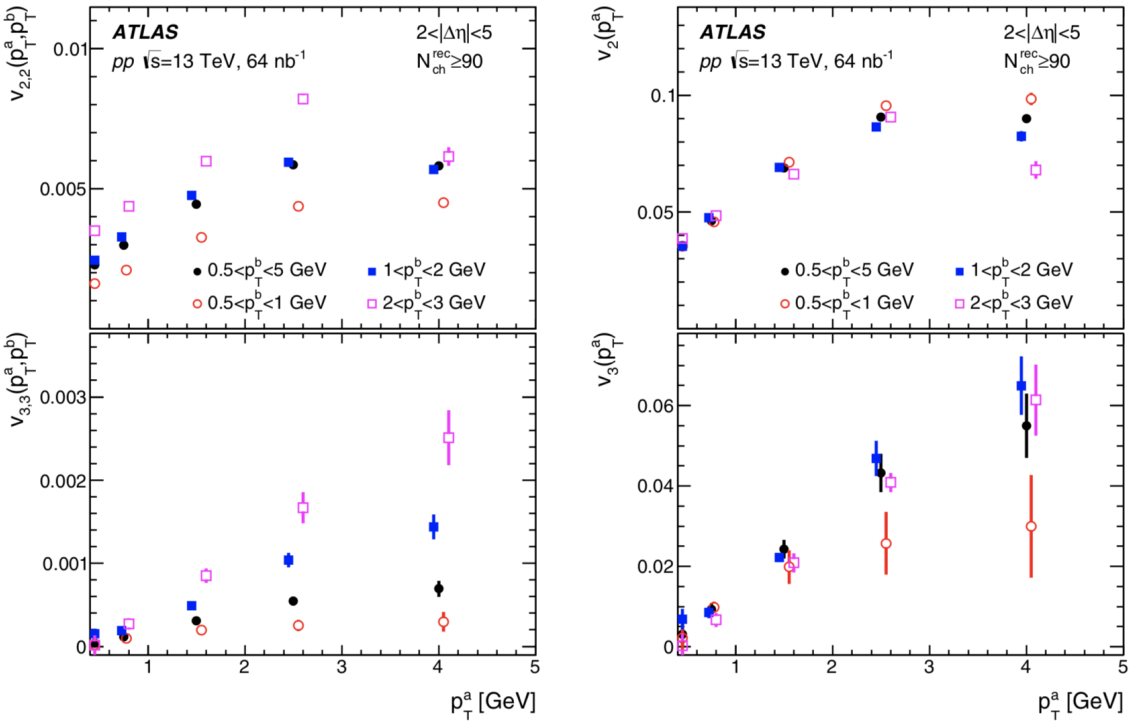

Figure 6.13: Factorization relationship for pp events at 13 TeV of both $v_{2,2}$ and $v_{3,3}$ is checked as a function of $p_{\mathrm{T}}^{\mathrm{a}}$. Different bins for $p_{\mathrm{T}}^{\mathrm{b}}$ are used.

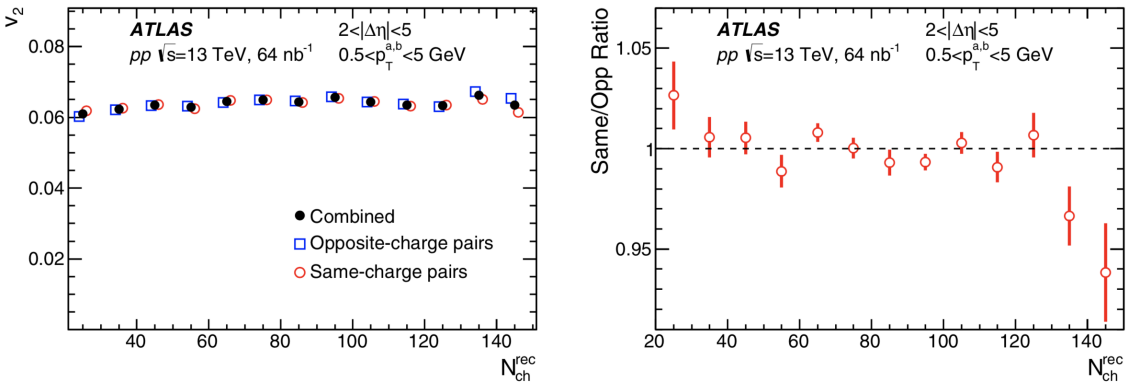

Figure 6.14: Multiplicity dependence of v_2 is checked for opposite-charge pairs and same-charge pairs for pp events at 13 TeV. The right panel shows the ratio of the two.

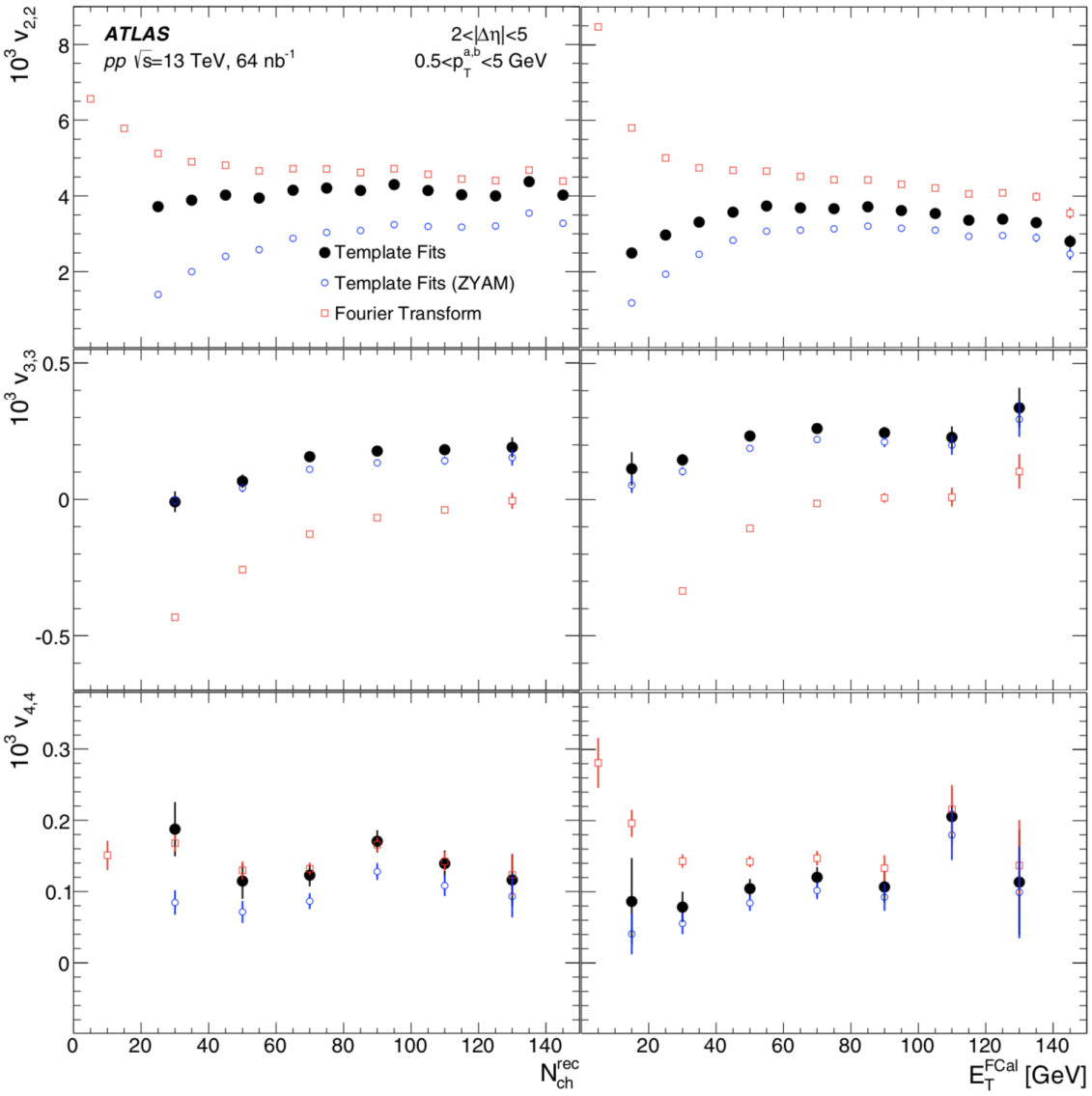

Figure 6.15: From top to bottom panels $v_{2,2}$, $v_{3,3}$ and $v_{4,4}$ values are shown as a function of $N_{\mathrm{ch}}^{\mathrm{rec}}$ in the left panels and a function of $E_{\mathrm{T}}^{\mathrm{FCal}}$ in the right panels for pp events at 13 TeV. Three different methods: template fits, template fits (ZYAM) and Fourier transform are used to extract harmonics of the correlation function.

dependence there is a decline in the v_2 distribution at low $E_{\mathrm{T}}^{\mathrm{FCal}}$.

Values of $v_{2,2}$, $v_{3,3}$ and $v_{4,4}$ obtained from direct Fourier decomposition, ZYAM-based template fits and improved template fits are also shown as a function of $|\Delta\eta|$ in Figure 6.16. Region of $|\Delta\eta| < 1$ is excluded to suppress the near side jet correlation at $\Delta\phi = 0$. v_n from template fits are distributed more stable than from

Fourier transform. Especially v_2 from template fits shows a very weak dependence on $|\Delta\eta|$ when $|\Delta\eta| > 1.5$ since near side jet correlation is diminished at large pseudorapidity separation. This means harmonics extracted from the template fits can represent the true long-range correlation which should not significantly depend on the pseudorapidity separation. Meanwhile v_n from Fourier transform usually have a strong dependence on $|\Delta\eta|$ due to the change in the shape of the away-side dijet component in different $|\Delta\eta|$ intervals. $v_{2,2}$ from Fourier transform decreases with $|\Delta\eta|$ and $v_{3,3}$ obtained from Fourier transform might have negative values.

6.2 Measurement of pp collisions at $\sqrt{s} = 2.76$ TeV

Figure 6.17 shows the per-trigger yields for pp events at 2.76 TeV as well as their improved template fitting results. The pedestal indicated by the yellow dashed line and ridge correlation indicated by the blue dashed line are shifted up for easy comparison. Each panel corresponds to a specific multiplicity bin. The black circle represents the rescaled peripheral reference $0 < N_{\rm ch}^{\rm rec} < 20$, which represents the away-side jet correlation. Both particles are chosen from (0.5, 5) GeV $p_{\rm T}$ interval.

Figure 6.18 shows the multiplicity dependence of $v_{2,2}$ using different peripheral references. Values from different graphs are consistent with each other. There is a small dip of $v_{2,2}$ at large multiplicity which is understood due to pileup. Since a portion of high multiplicity pp events are actually pile-up events, the true multiplicity in such events is much smaller than the measured one resulting in a small $v_{2,2}$ than expected. Figure 6.19 checks the factorization using different bins for $p_{\rm T}^{\rm b}$. $v_{2,2}$ increases with $p_{\rm T}^{\rm b}$ for the the given $p_{\rm T}^{\rm a}$. It is obvious that factorization works pretty well even at 2.76 TeV. The left panels of Figure 6.20 show the $p_{\rm T}$ dependence of $v_{2,2}$. $v_{2,2}$ increases with $p_{\rm T}$ at low $p_{\rm T}$ range, reaches its maximum between $2 \sim 3$ GeV and

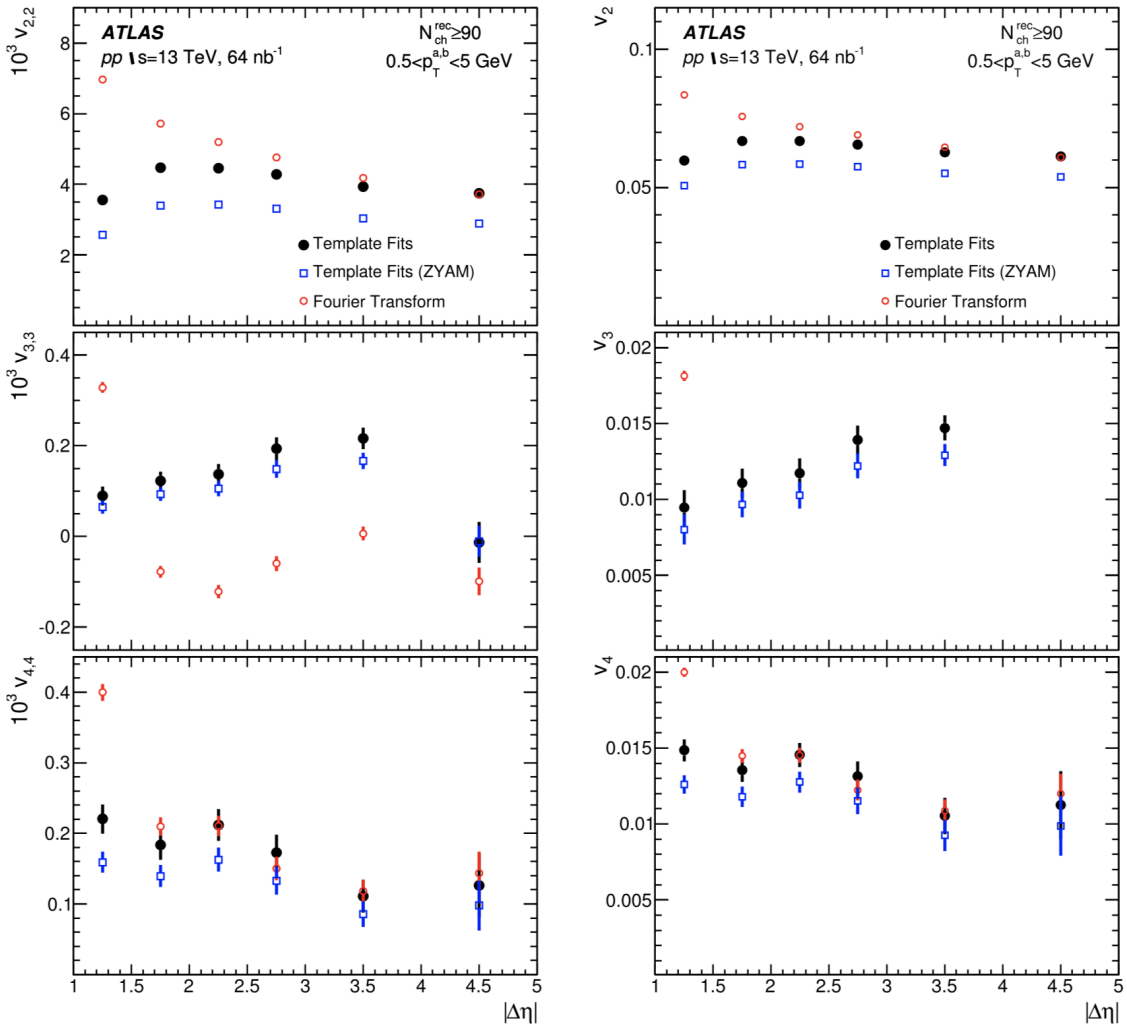

Figure 6.16: From top to bottom $v_{2,2}$, $v_{3,3}$ and $v_{4,4}$ values are shown as a function of $|\Delta\eta|$ in the left panels for pp events at 13 TeV. The right panels show the corresponding v_n values. Three different methods: template fits, template fits (ZYAM) and Fourier transform are used to extract harmonics of the correlation function.

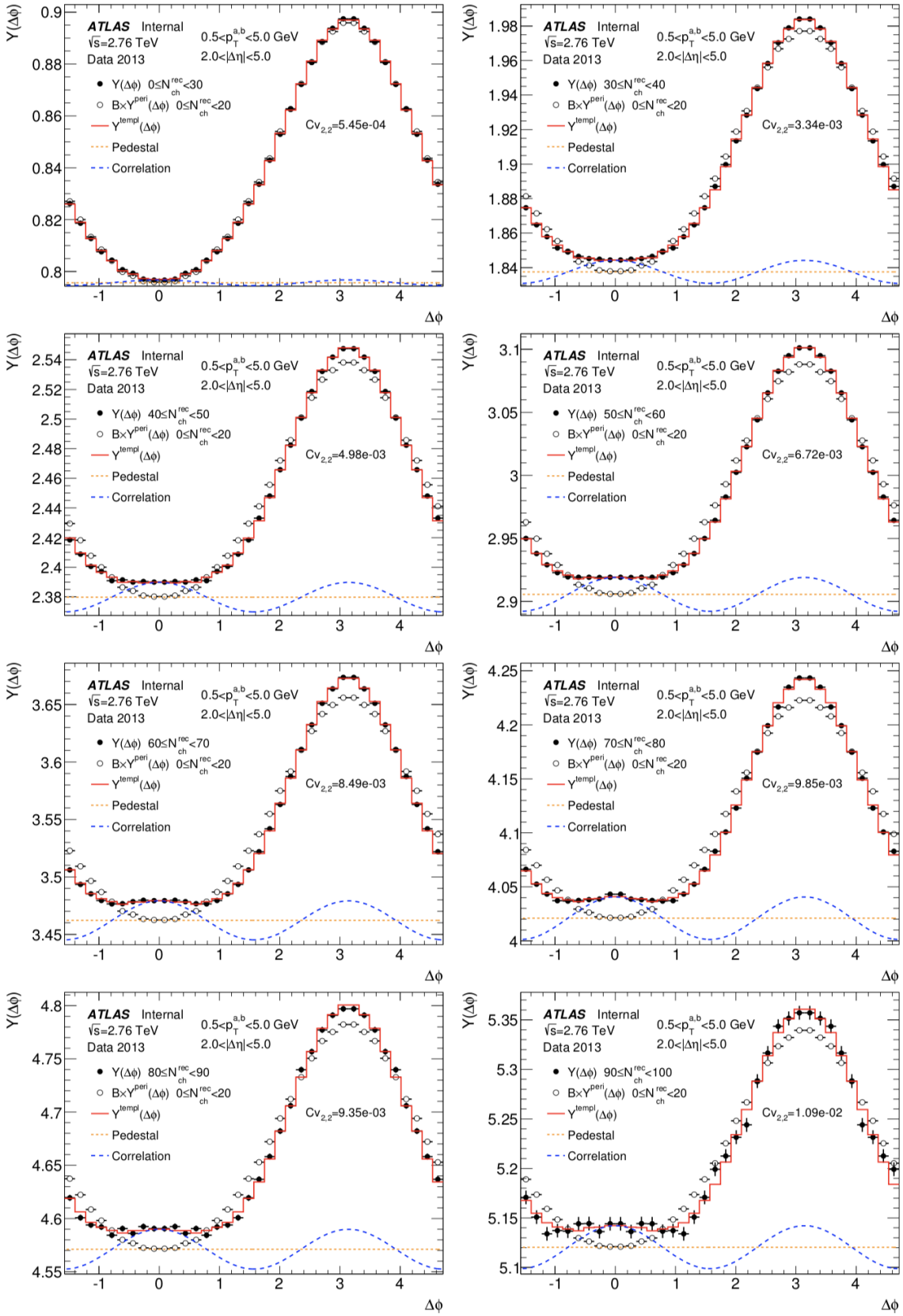

Figure 6.17: Improved template fitting method for *pp* events at 2.76 TeV. Each panel is for a certain multiplicity bin. The p_{T} ranges for both particles are chosen to be (0.5, 5) GeV. $|\Delta\eta|$ is required above 2.

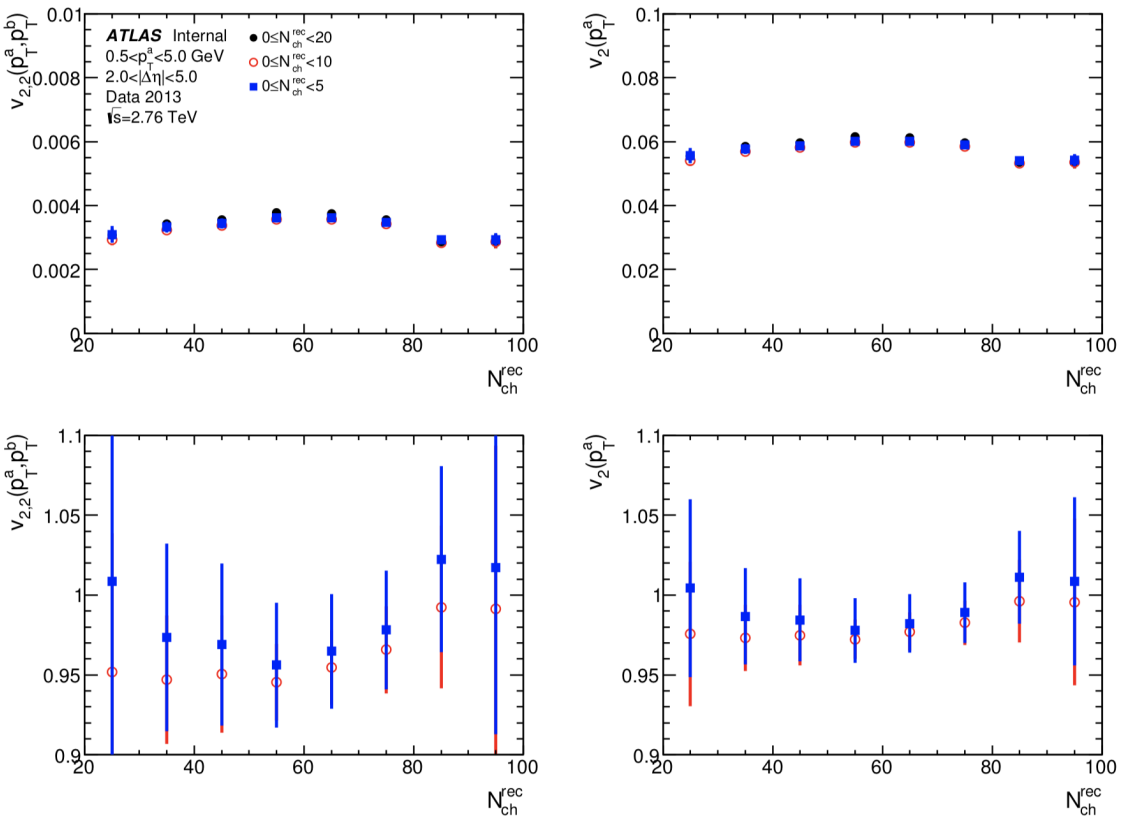

Figure 6.18: The second harmonics $v_{2,2}$ for pp events at 2.76 TeV extracted from improved template fits are shown in the left panel. Different peripheral references are used for comparison. Three multiplicity bins for peripheral events are used: $0 < N_{\mathrm{ch}}^{\mathrm{rec}} < 5$, $0 < N_{\mathrm{ch}}^{\mathrm{rec}} < 10$ and $0 < N_{\mathrm{ch}}^{\mathrm{rec}} < 20$. The upper right panel shows the corresponding v_2. The bottom panels illustrate the ratios between results from different peripheral references.

then decreases. The right panels illustrate the dependence of single particle v_2 on the bins used for $p_{\mathrm{T}}^{\mathrm{b}}$. Factorization works well at low and intermediate p_{T} but may break at high p_{T} values due to the above-mentioned multiplicity-dependent distortions of the shape in the dijet correlation. Factorization at high p_{T} works better for large multiplicity events.

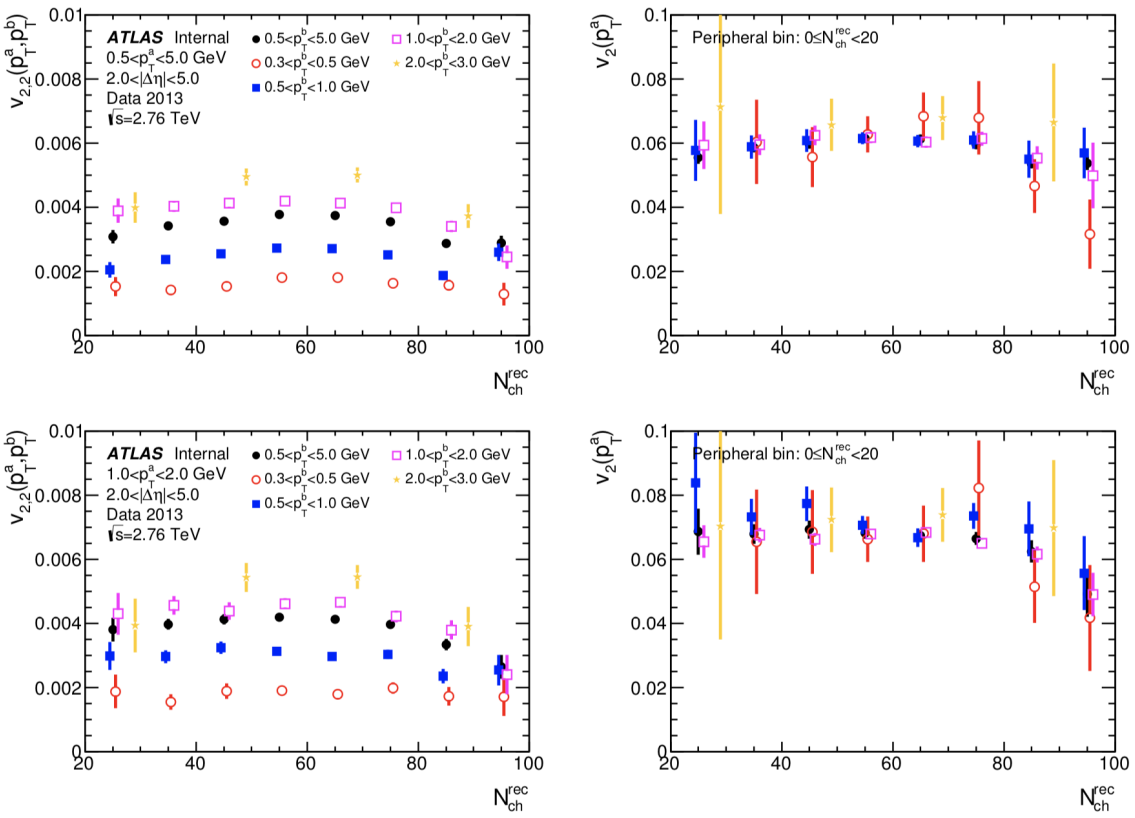

Figure 6.19: Factorization relationship for pp events at 2.76 TeV is checked as a function of event multiplicity. $v_{2,2}$ is calculated using different bins for $p_{\mathrm{T}}^{\mathrm{b}}$ while $p_{\mathrm{T}}^{\mathrm{a}}$ is fixed. The right panel shows the corresponding v_2 values.

6.3 Measurement of pp collisions at $\sqrt{s} = 5.02$ TeV

6.3.1 Results of pp events at $\sqrt{s} = 5.02$ TeV

Figure 6.21 illustrates the 2D two particle correlation functions for pp events at 5.02 TeV. $\Delta\eta$ axis is truncated at ± 4 since statistics are insufficient in $4 < |\Delta\eta| < 5$. The jet correlation at $\Delta\eta = \Delta\phi = 0$ is suppressed in order to demonstrate the structure of the correlation function in detail. Four different multiplicity bins are used. Long-range correlation can be observed in high-multiplicity events along the $|\Delta\eta|$ axis. Figure 6.22 shows (improved) template fits with each panel corresponding

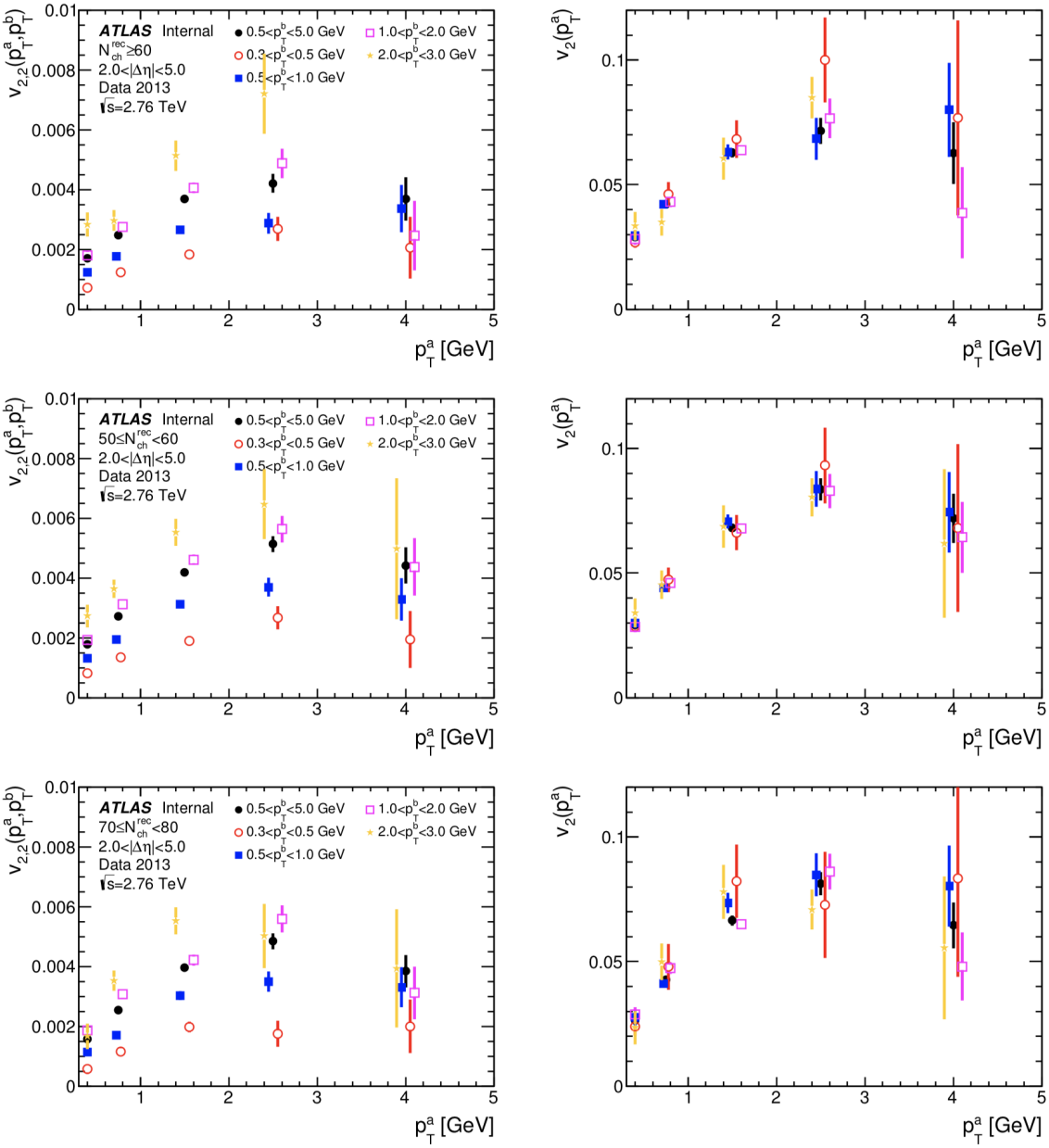

Figure 6.20: Factorization relationship for pp events at 2.76 TeV is checked as a function of $p_{\mathrm{T}}^{\mathrm{a}}$. $v_{2,2}$ is calculated using different bins for $p_{\mathrm{T}}^{\mathrm{b}}$ while $p_{\mathrm{T}}^{\mathrm{a}}$ is fixed. The right panel shows the corresponding v_2 values.

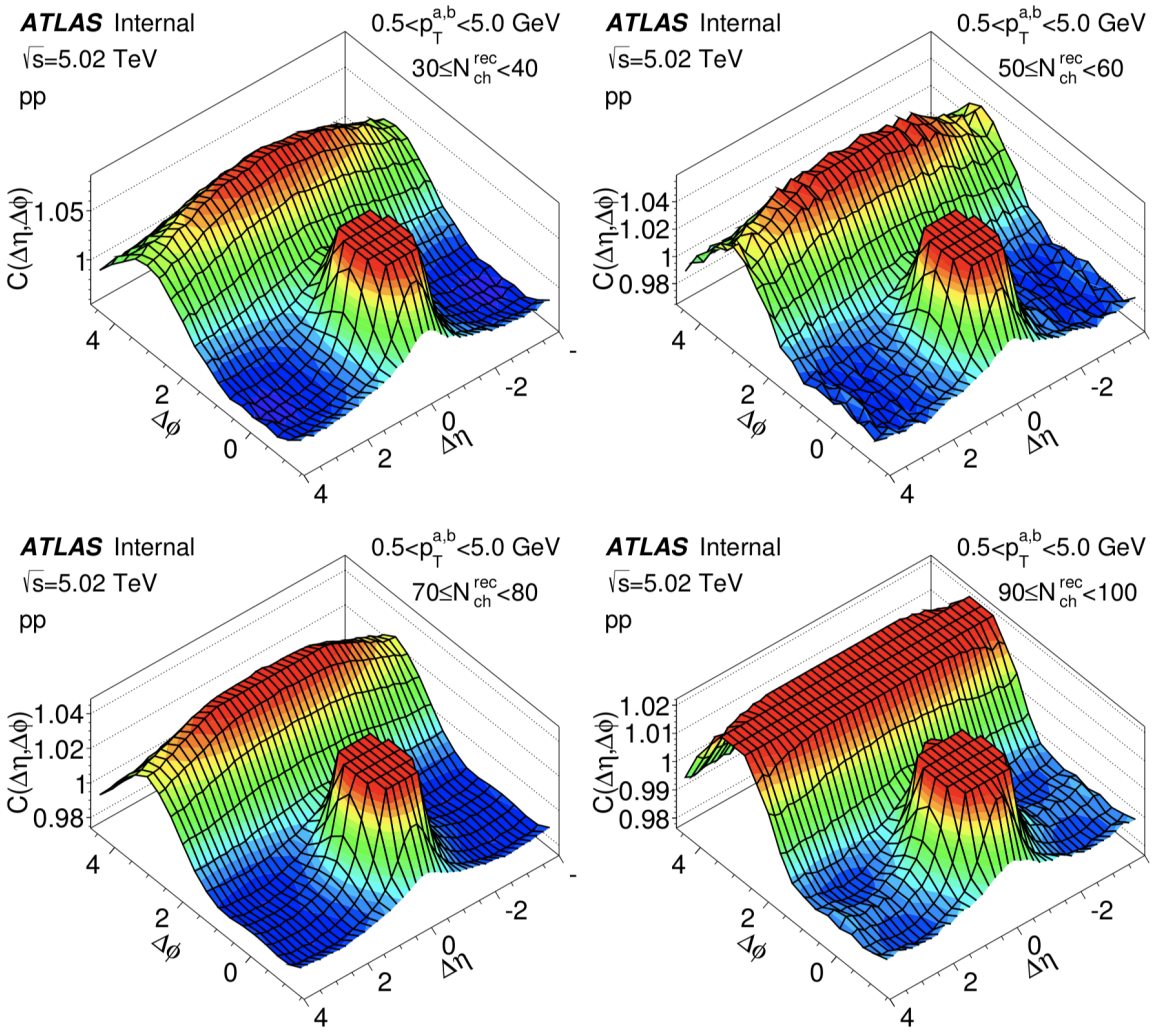

Figure 6.21: Two dimensional two-particle correlation functions for *pp* events at 5.02 TeV. Both particles are chosen in (0.5,5) GeV. Each panel corresponds to a different multiplicity bin.

to a different multiplicity bin. The default reference bin $0 < N_{\mathrm{ch}}^{\mathrm{rec}} < 20$ is used. Pedestal and ridge correlation have been shifted up for easy comparison with the away-side jet correlation estimated from a peripheral reference. It is easy to see that the amplitude of the long-range modulation increases with multiplicity. The near-side correlation changes from a concave-up structure to a small peak.

Figure 6.23 shows $v_{2,2}$, $v_{3,3}$ and $v_{4,4}$ as a function of multiplicity. The p_{T} intervals here for both particles are (1,5) GeV. Three methods are used to extract these Fourier harmonics for comparison. The black dots and blue circles represent improved and

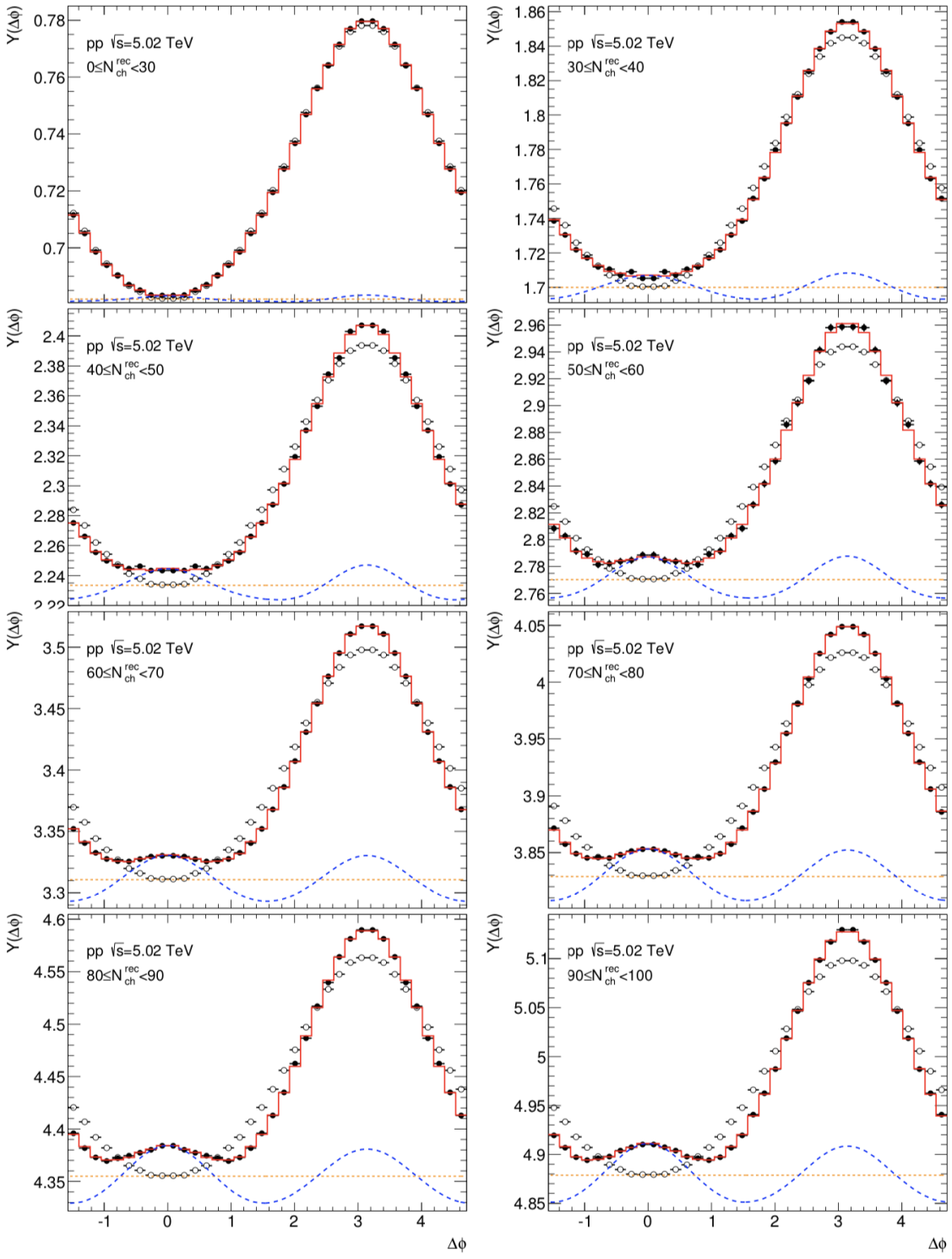

Figure 6.22: (Improved) template fits for *pp* events at 5.02 TeV. Both particles are chosen in (0.5,5) GeV. Each panel corresponds to a different multiplicity bin. The peripheral reference is $0 < N_{\mathrm{ch}}^{\mathrm{rec}} < 20$.

ZYAM-based template fits respectively. Both of them give smaller results than the red squares from direct Fourier transform. The difference between them comes from the away-side jet correlation which always contributes to a positive $v_{2,2}$ and a negative $v_{3,3}$. Results from template fits (both improved and ZYAM-based) show very weak dependence on the event multiplicity while results from Fourier transform show a large dependence especially in low multiplicity events. This is because although the shape of the hard component is assumed to be the same for different $N_{\mathrm{ch}}^{\mathrm{rec}}$ regions, the magnitude of the pedestal arising from uncorrelated pairs is not the same. This makes the contribution from dijet correlation large in low multiplicity events and small in high multiplicity events. It is also observed that the long-range correlation is dominated by $v_{2,2}$ while values of $v_{3,3}$ and $v_{4,4}$, which are comparable to each other, are much smaller.

Figure 6.24 shows values of $v_{2,2}$ for different $p_{\mathrm{T}}^{\mathrm{b}}$ at fixed $p_{\mathrm{T}}^{\mathrm{a}}$. Factorization of $v_{2,2}$ works pretty well at 5 TeV. $v_{3,3}$ and $v_{4,4}$ are not shown here since there are not enough statistics to study the factorization of higher order harmonics as a function of multiplicity. A solution to this is to study the dependence of $p_{\mathrm{T}}^{\mathrm{a}}$ and make broader bins to increase the statistics. This is illustrated in Figure 6.25. Factorization of $v_{2,2}$ and $v_{3,3}$ holds up to 3 GeV except for the last bin. However factorization of $v_{4,4}$ does not work well even with intermediate values of $p_{\mathrm{T}}^{\mathrm{a}}$.

6.3.2 Comparison with pPb collisions at $\sqrt{s_{\mathrm{NN}}} = 5.02$ TeV

In some previous papers single particle flow harmonics in pPb systems are calculated through cumulant method [40] or two particle correlation method with peripheral subtraction procedure [36]. The above template fitting method in two particle correlation analysis, however, can also be used in pPb systems. In order to compare the physics from systems with different sizes, our analysis focuses on pPb systems at the same collision energy as the previous pp one. Two dimensional two-particle correlation

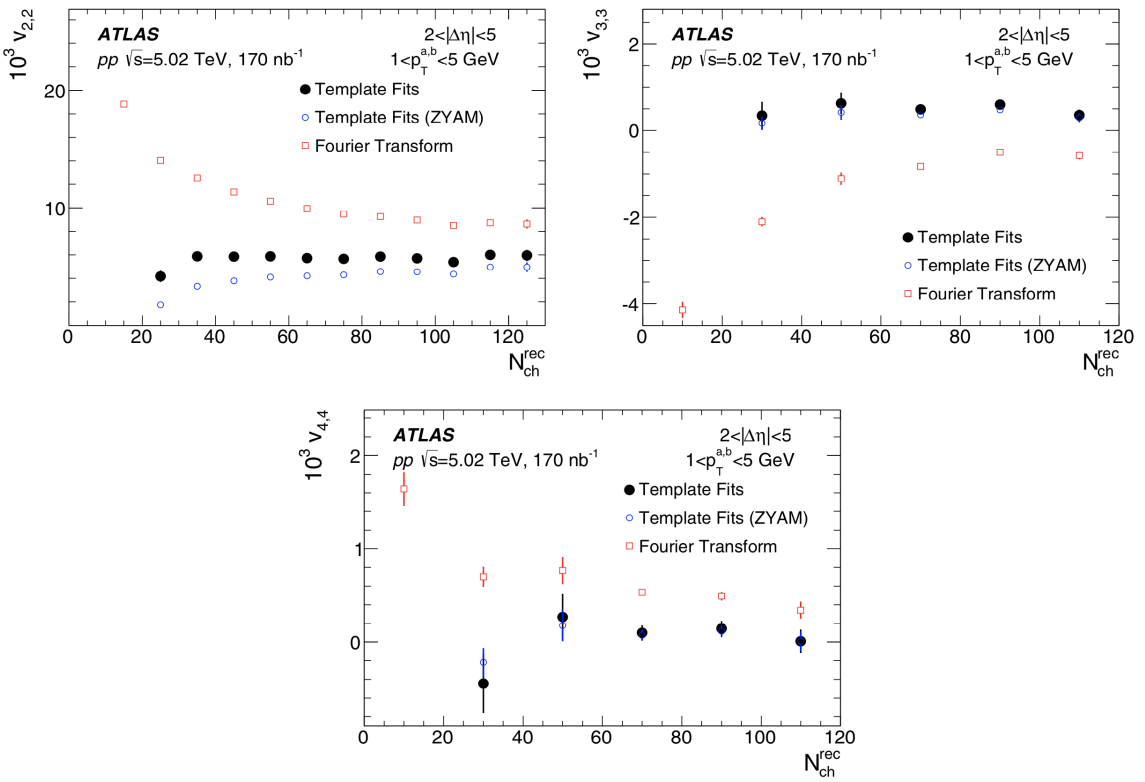

Figure 6.23: Measurement of $v_{2,2}$, $v_{3,3}$ and $v_{4,4}$ from (improved) template fits, template fits (ZYAM) and Fourier transform as a function of event multiplicity. Both particles are chosen in (1,5) GeV.

functions are shown in Figure 6.26. The ridge structure is already observable when $N_{\mathrm{ch}}^{\mathrm{rec}} < 80$. As the multiplicity increases the structure of the long-range correlation becomes prominent and there is a clearly high ridge on the near side. It is known that the single particle azimuthal anisotropy or the long range correlation of pPb events arises from the initial geometry and collective expansion. The collective behavior in pPb systems is much larger than that in pp. Similar features that were observed in pp systems can also be observed here. Figure 6.27 illustrates the improved template fits for pPb systems. Event multiplicity increases from top to bottom and from left to right panels. The ridge structure on the near side becomes a high peak whose size is already comparable to the away-side dijet correlation when $N_{\mathrm{ch}}^{\mathrm{rec}}$ reaches 200. The long-range modulation that is indicated by the blue dashed line is therefore much

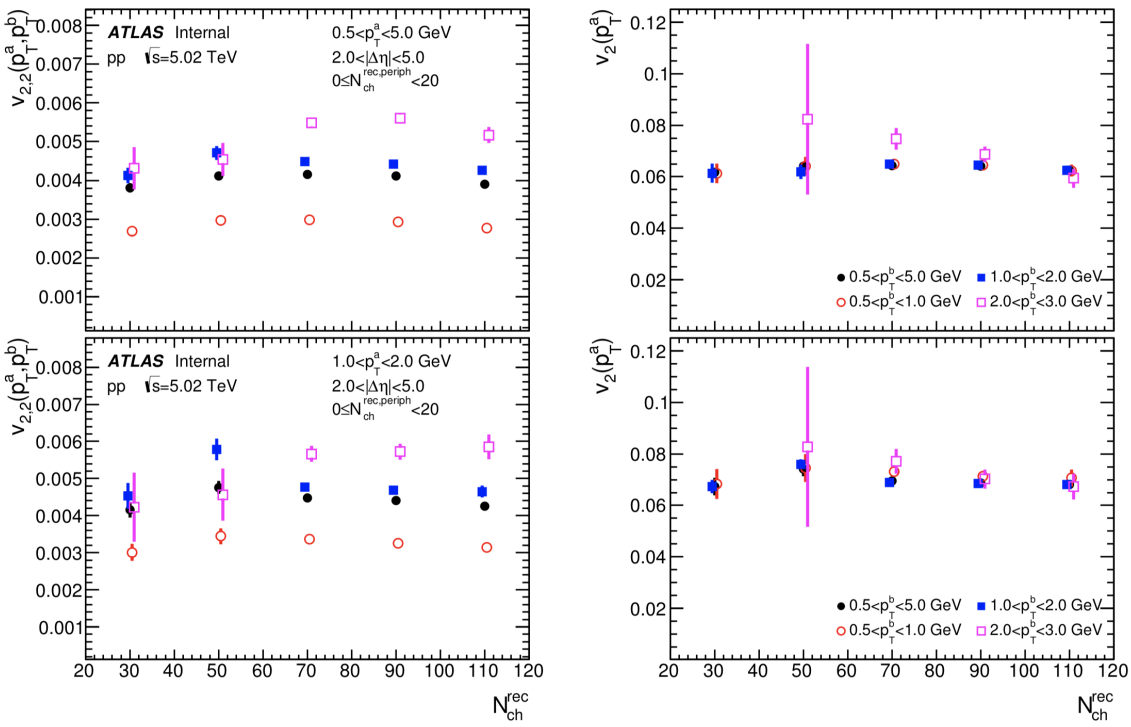

Figure 6.24: Factorization relationship for pp events at 5.02 TeV is checked as a function of $N_{\mathrm{ch}}^{\mathrm{rec}}$. Only results for $v_{2,2}$ is included since there are no enough statistics for $v_{3,3}$ and $v_{4,4}$. Different graphs in one panel represent different bins used for $p_{\mathrm{T}}^{\mathrm{b}}$.

larger than pp systems.

Figure 6.28 illustrates the values of $v_{2,2}$, $v_{3,3}$ and $v_{4,4}$ as a function of $N_{\mathrm{ch}}^{\mathrm{rec}}$ on its left panels and Pb-going side FCal-Et $E_{\mathrm{T}}^{\mathrm{FCal,Pb}}$ on its right panels. In each panel four different ways are used to obtain these Fourier coefficients: (improved) template fits, template fits (ZYAM), Fourier transform and peripheral subtraction. The last method, peripheral subtraction procedure, refers to the analysis method used in the previous ATLAS pPb long-range paper. It is similar to the ZYAM-based template fitting procedure, where the scale factor of the peripheral reference is not determined by fitting (or by matching the away-side jet correlation) but by matching the near-side jet peak within $|\Delta\eta| < 1, |\Delta\phi| < 1$. From Figure 6.28 we can see template fits (ZYAM) and peripheral subtraction give nearly identical values from $v_{2,2}$ to $v_{4,4}$. Scale factors obtained from template fits are almost the same as the

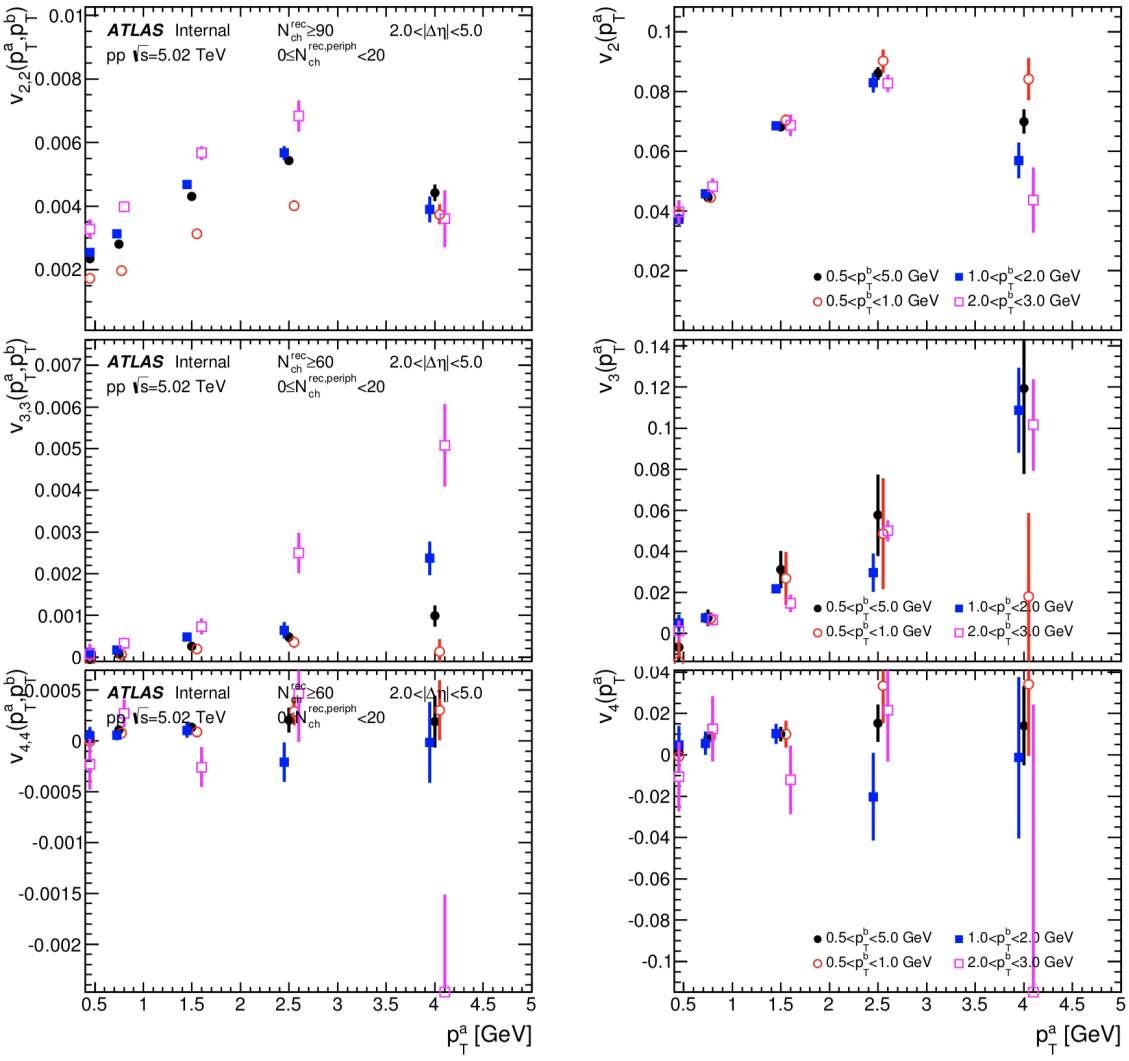

Figure 6.25: Factorization relationship for pp events at 5.02 TeV is checked as a function of $p_{\mathrm{T}}^{\mathrm{a}}$. From top to bottom, results for $v_{2,2}$, $v_{3,3}$ and $v_{4,4}$ are plotted in each row. Different graphs in one panel represent different bins used for $p_{\mathrm{T}}^{\mathrm{b}}$.

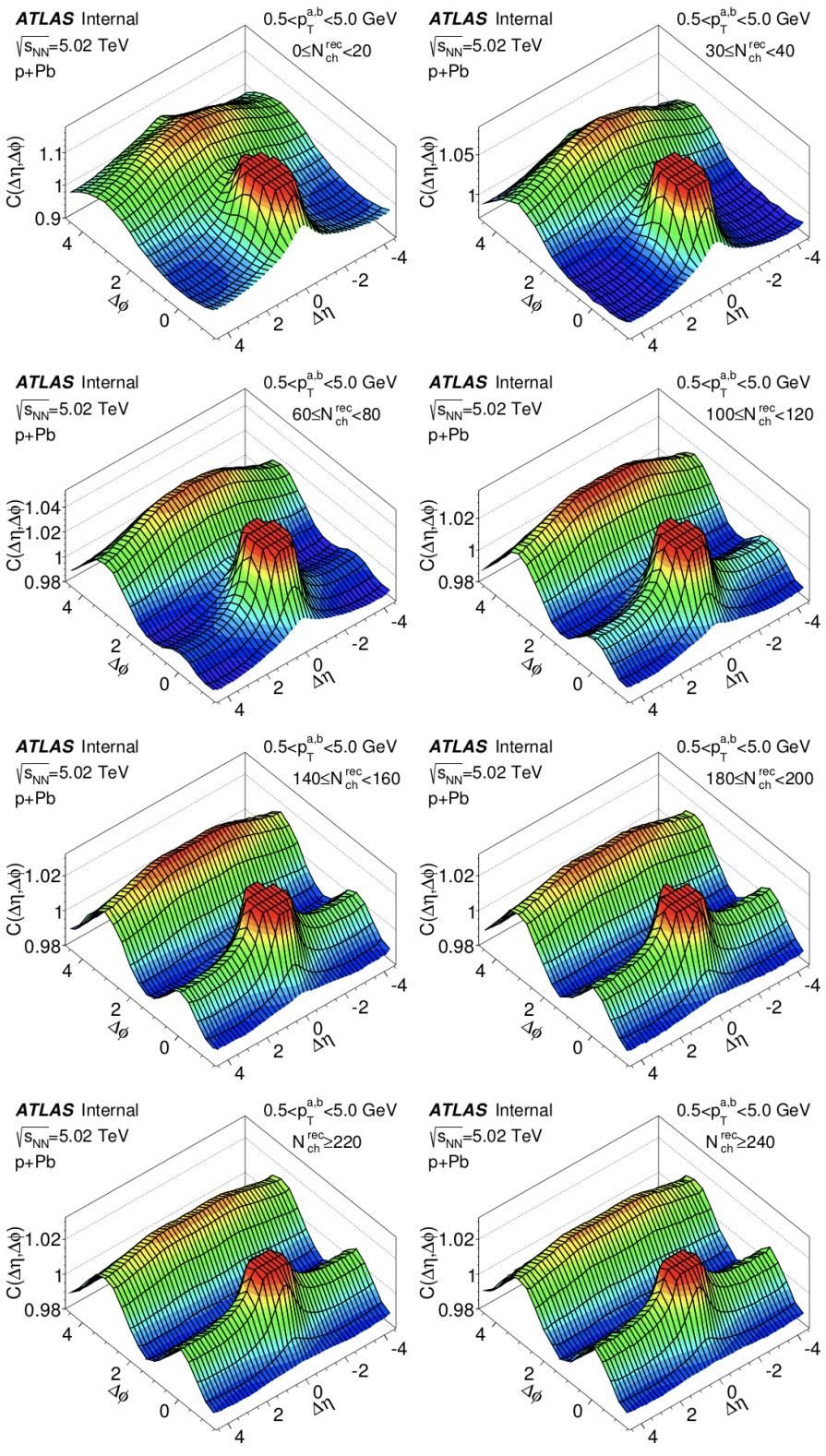

Figure 6.26: Two dimensional two-particle correlation functions for pPb events at 5.02 TeV. Both particles are chosen in (0.5,5) GeV. Each panel corresponds to a different multiplicity bin.

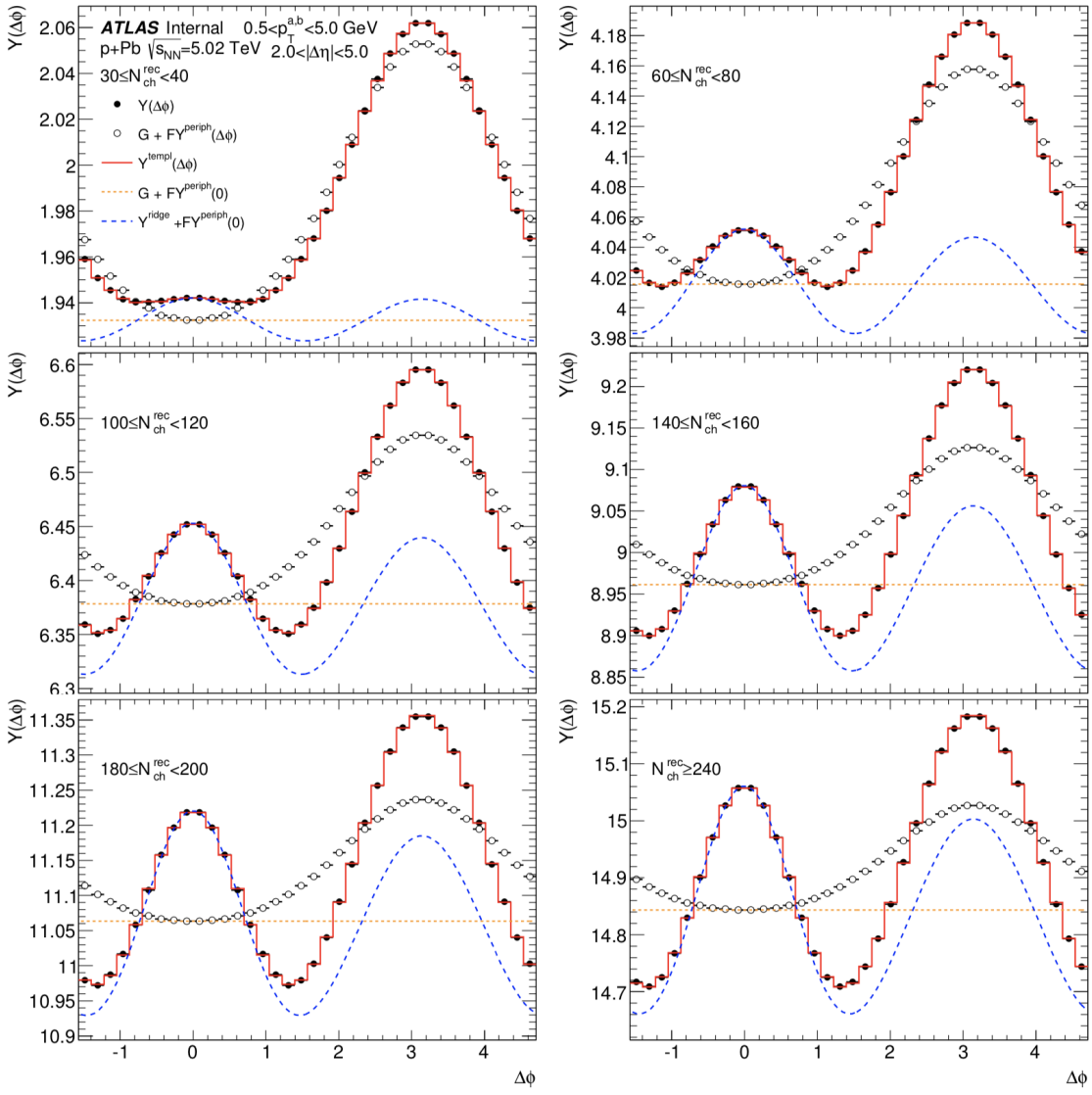

Figure 6.27: (Improved) template fits for pPb events at 5.02 TeV. Both particles are chosen in (0.5,5) GeV. Each panel corresponds to a different multiplicity bin. The peripheral reference is $0 < N_{\mathrm{ch}}^{\mathrm{rec}} < 20$.

one from matching the near side jet peak, which justifies the assumption underlying the template fitting method that the away-side jet correlation has identical shapes across different multiplicity bins. Different from the case in pp, improved template fits and Fourier transform lead to close values in $v_{2,2}$. Since pPb events produce large collective flow compared to pp, the fraction of the hard contribution in 2PC of pPb is much smaller than that in pp. However for $v_{3,3}$ template fits systematically give larger values than Fourier transform. Another interesting behavior we could notice is that $v_{n,n}$ from pPb are no longer a constant value or show only weak dependence on the event multiplicity. $v_{2,2}$ increases with both $N_{\rm ch}^{\rm rec}$ and $E_{\rm T}^{\rm FCal,Pb}$ at low and intermediate multiplicity and saturates when $N_{\rm ch}^{\rm rec}$ is above 150. This phenomenon is usually considered to result from the initial geometry of pPb collisions. When the impact parameter is large, proton trajectory crosses the edge of the lead ion. This is the peripheral collision. When the impact parameter decreases, the intersection of the proton trajectory with the lead ion moves closer to its center. At some point the impact parameter no longer has much effect on the collision geometry and multiplicity saturates. $v_{3,3}$ and $v_{4,4}$ also show a significant dependence on $N_{\rm ch}^{\rm rec}$. This seems to suggest that another basic assumption underlying the improved template fitting method, $v_{n,n}$ in the peripheral reference is the same as that in $Y(\Delta\phi)$ or $C(\Delta\phi)$ of central events, is not correct. However further analysis has shown that, like the case in pp, our pPb template fitting results do not highly depend on the peripheral references. This means even $v_{n,n}$ is not a constant as a function of multiplicity, template fitting procedure is still valid and can give highly-accurate results.

Factorization of $v_{2,2}$ and $v_{3,3}$ is checked as a function of event multiplicity in Figure 6.29. With different bins for $p_{\rm T}^{\rm b}$ $v_{2,2}$ can change by a factor of 3. On the right panel factorization works well except for $2 < p_{\rm T}^{\rm b} < 3$ GeV and $N_{\rm ch}^{\rm rec}$ below 50. $v_{3,3}$ can change by a factor of 2 with varied bins for $p_{\rm T}^{\rm b}$. Factorization holds true for each $p_{\rm T}^{\rm b}$ bin across the whole $N_{\rm ch}^{\rm rec}$ range. Figure 6.30 checks its factorization relationship

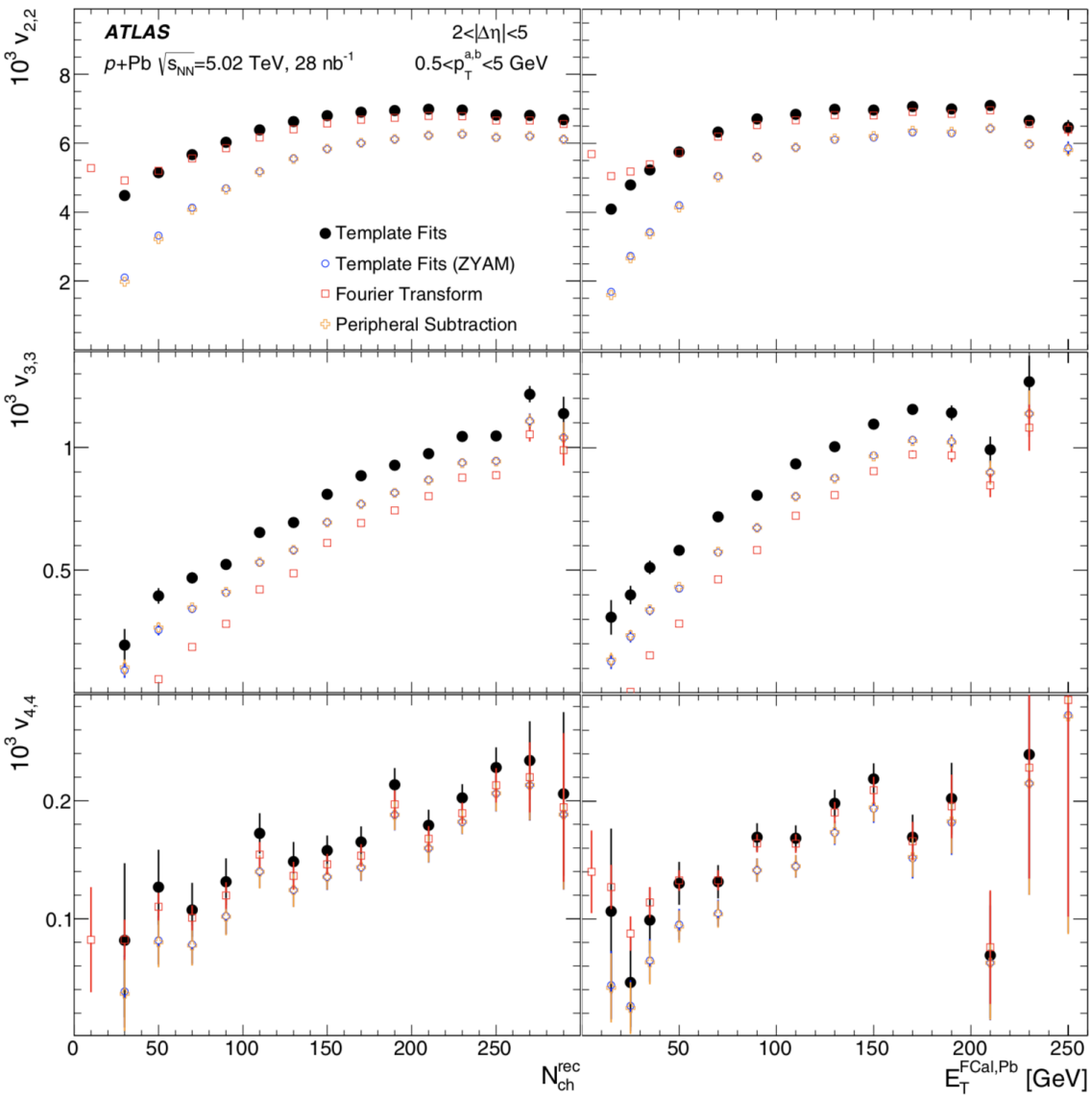

Figure 6.28: Measurement of $v_{2,2}$, $v_{3,3}$ and $v_{4,4}$ from (improved) template fits, template fits (ZYAM), Fourier transform and peripheral subtraction for pPb events at 5.02 TeV. Graphs in the left panels are plotted as a function of event multiplicity, while in the right panels graphs are plotted as a function of FCal Et on the Pb going side. Both particles are chosen in (0.5,5) GeV.

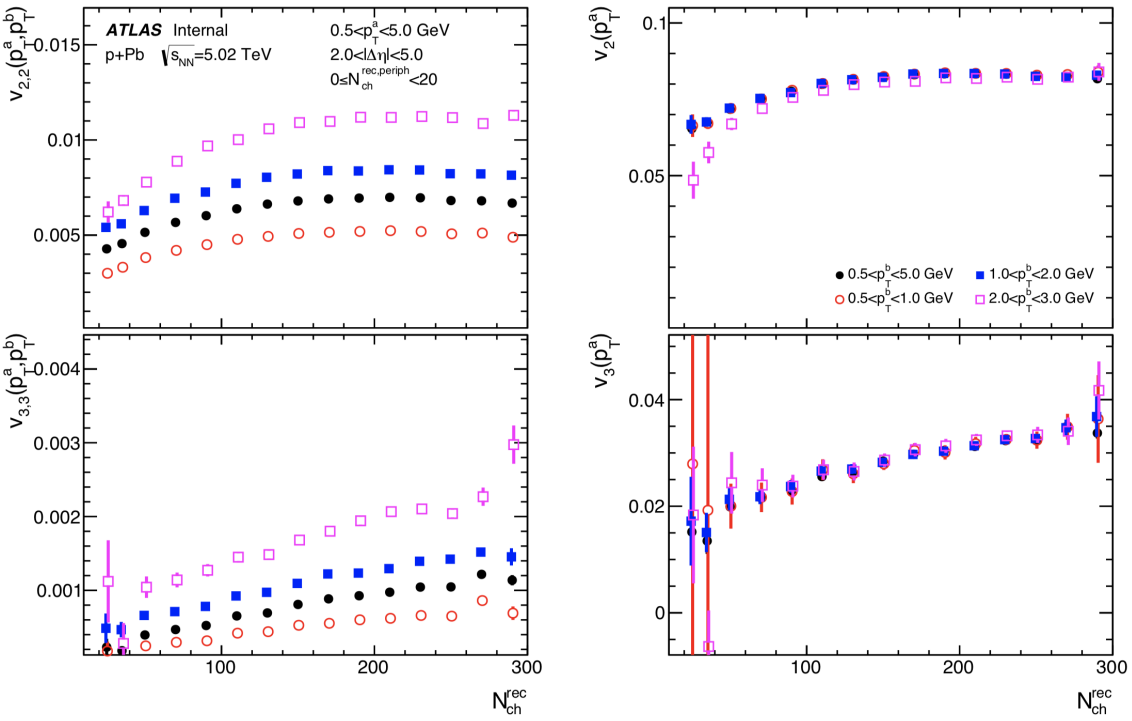

Figure 6.29: Factorization relationship for pPb events at 5.02 TeV is checked as a function of $N_{\mathrm{ch}}^{\mathrm{rec}}$. $v_{n,n}$ is calculated using different bins for $p_{\mathrm{T}}^{\mathrm{b}}$ for a fixed $p_{\mathrm{T}}^{\mathrm{a}}$. The right panel shows the corresponding v_n values.

using the dependence on p_{T}. $v_{2,2}$ shows a weak decline after its maximum at $2 \sim 3$ GeV. While $v_{3,3}$ and $v_{4,4}$ increases with p_{T} until 5 GeV. Up to 5 GeV all harmonics can be factorized to single particle distributions very well.

6.3.3 Comparison between energies

In this section results from events at different collision energies are compared. Figure 6.31 demonstrates the dependence of v_2 on $N_{\mathrm{ch}}^{\mathrm{rec}}$. Each row corresponds to a different kind of events, either differing in the system or differing in the energy. Three different peripheral bins $0 < N_{\mathrm{ch}}^{\mathrm{rec}} < 5$, $0 < N_{\mathrm{ch}}^{\mathrm{rec}} < 10$ and $0 < N_{\mathrm{ch}}^{\mathrm{rec}} < 20$ are used. The left panels show the results from improved template fits while the right panels show results from ZYAM-based template fits. Both pp and pPb systems do not exhibit considerable dependence on event multiplicity except for the most peripheral events

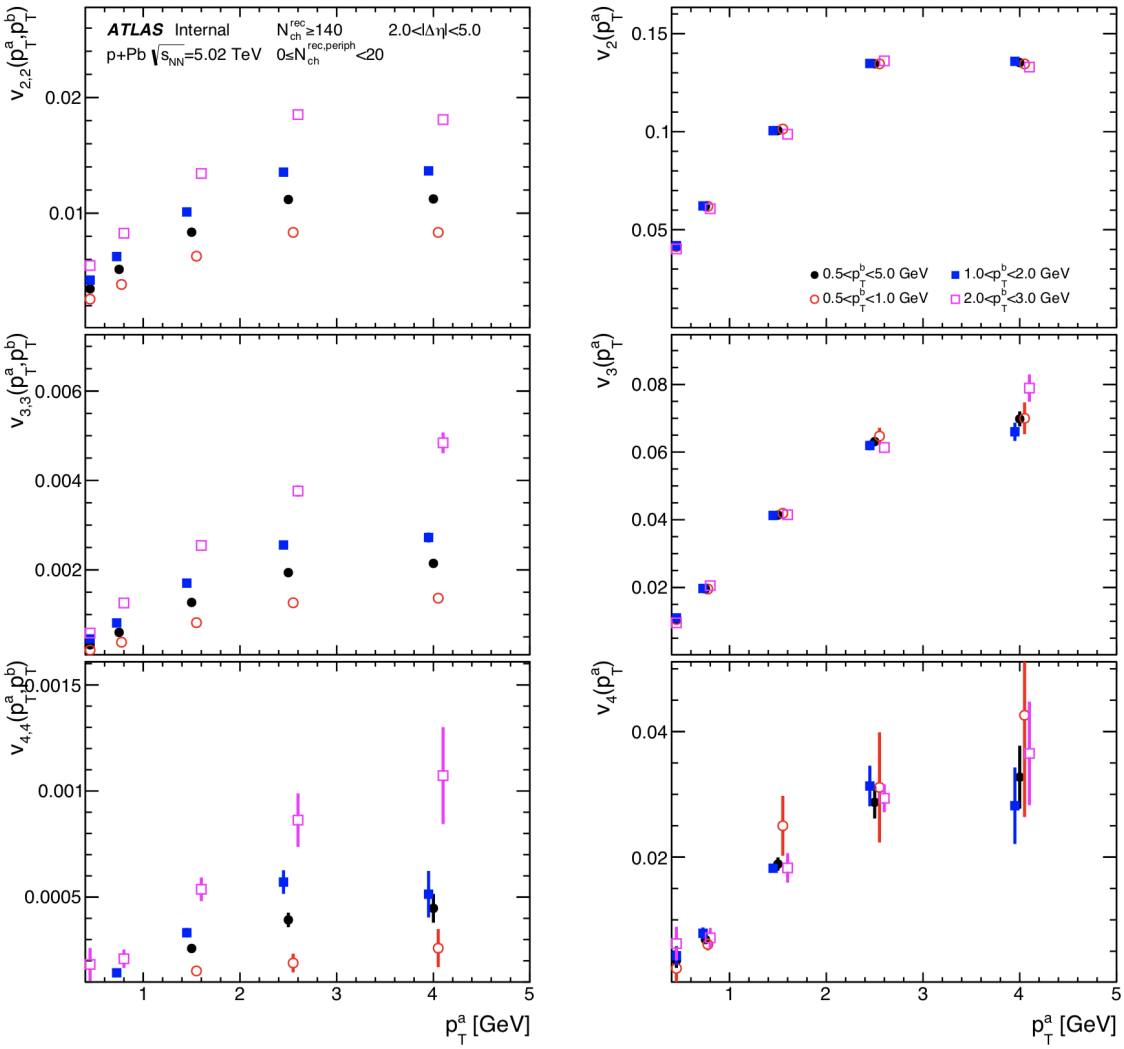

Figure 6.30: Factorization relationship for pPb events at 5.02 TeV is checked as a function of $p_{\mathrm{T}}^{\mathrm{a}}$. $v_{n,n}$ is calculated using different bins for $p_{\mathrm{T}}^{\mathrm{b}}$ for a fixed $p_{\mathrm{T}}^{\mathrm{a}}$. The right panel shows the corresponding v_n values.

that have almost identical multiplicity interval as the peripheral reference. Although v_2 from pPb systems shows a slight increase with $N_{\mathrm{ch}}^{\mathrm{rec}}$, which does not comply with the assumption in the improved template fits, results from different peripheral bins are consistent with each other. On the contrary results from ZYAM-based template fits always show a significant dependence on the peripheral reference. This is especially true in the most peripheral region. As we can see the most peripheral bin $0 < N_{\mathrm{ch}}^{\mathrm{rec}} < 5$ gives the largest v_2 and its v_2 distribution over $N_{\mathrm{ch}}^{\mathrm{rec}}$ is flatter in all of the three cases. When the upper bound of the peripheral bin used for ZYAM-based template fits approaches 0, it should asymptotically give a flat distribution in terms of $N_{\mathrm{ch}}^{\mathrm{rec}}$ which should looks similar to the results from improved template fits. This suggests the assumption made in the ZYAM-based analysis that there is no long-range correlation and thus v_2 is zero in the peripheral reference is not correct. The assumption that v_2 from the peripheral reference has the same value as v_2 from central events is more reasonable.

Analysis from 5.02 TeV pPb, 5.02 TeV pp and 13 TeV pp are compared in Figure 6.32. Only results from improved template fits are included. From top to bottom panels values of v_2, v_3 and v_4 are presented. In the left panels Fourier harmonics are plotted as a function of $N_{\mathrm{ch}}^{\mathrm{rec}}$. In the right panels they are plotted as a function of $p_{\mathrm{T}}^{\mathrm{a}}$. The p_{T} interval used for both particles is (0.5,5) GeV. v_3 and v_4 from pp events at 5.02 TeV are not included in the figure because of the large statistical errors measured in this p_{T} interval which lead to no meaningful results. v_2, v_3 and v_4 from pPb systems show a monotonic increase with the event multiplicity while all harmonics from pp systems do not show a significant dependence on $N_{\mathrm{ch}}^{\mathrm{rec}}$. As for the p_{T} dependence, v_2 from pPb and pp systems show similar trends. They both increase with $p_{\mathrm{T}}^{\mathrm{a}}$, reach their maxima around 3 GeV and then decrease. pPb gives higher values and has a more rapid increase and decrease in p_{T} compared to the pp case. The ratio of pPb to pp maxima is calculated to be 1.51. For a direct comparison pp v_2 is rescaled by this

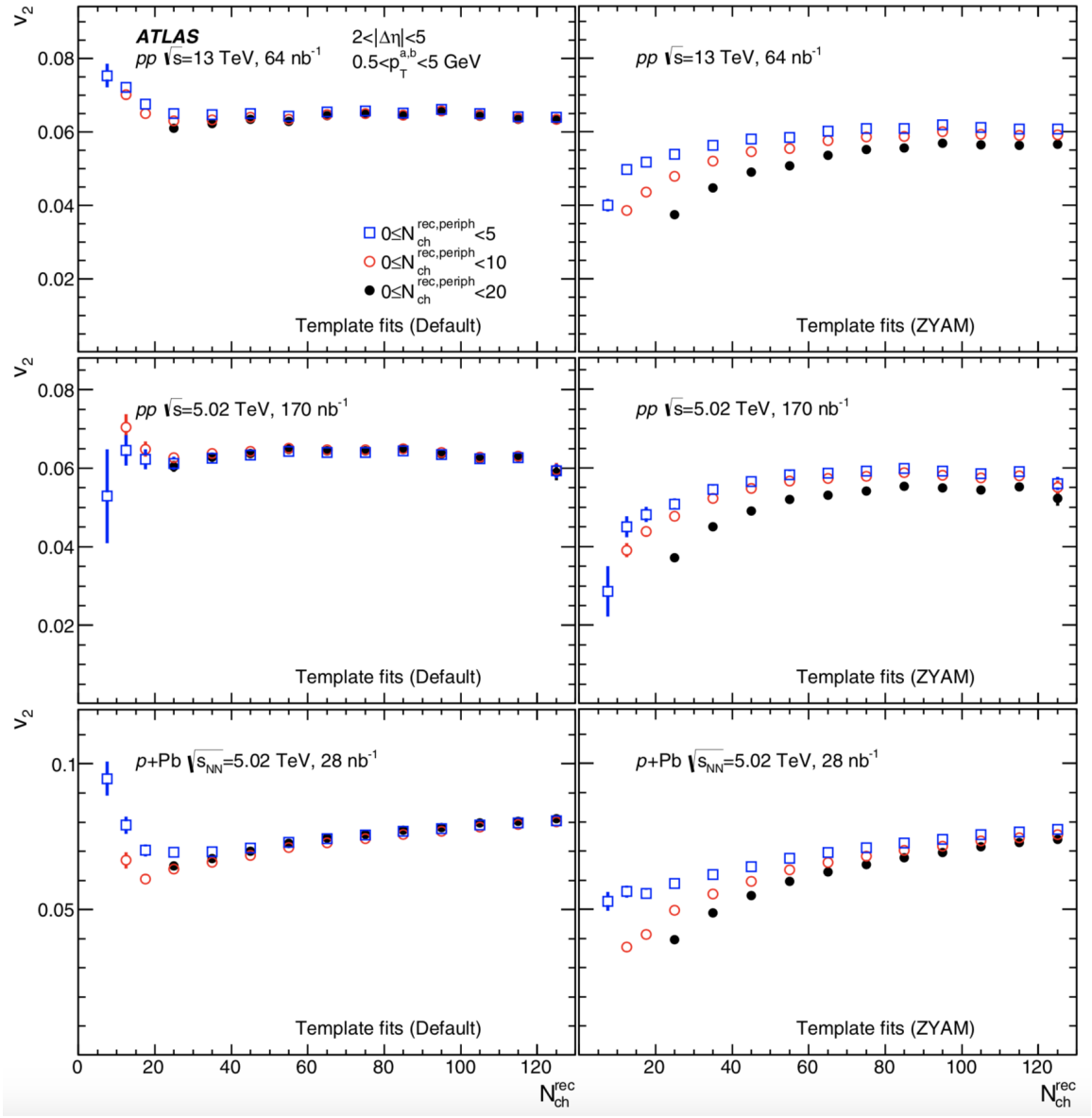

Figure 6.31: This figure shows the dependence of v_2 on the choice of the peripheral reference. Three peripheral bins are used: $0 < N_{\mathrm{ch}}^{\mathrm{rec}} < 5$, $0 < N_{\mathrm{ch}}^{\mathrm{rec}} < 10$ and $0 < N_{\mathrm{ch}}^{\mathrm{rec}} < 20$. The left panels show the results from improved template fits while the right panels show the results from ZYAM-based fits. The error bars in the figure indicate statistical uncertainties.

number to match the maximum of pPb in Figure 6.33. Results from the two systems match quite well up to 4 GeV. At high p_{T} pp v_2 decreases more rapidly because of the multiplicity-dependent distortion of the shape in the away-side dijet correlation which is not considered in the model of template fitting method. v_3 and v_4 from both pp and pPb systems increase with $p_{\mathrm{T}}^{\mathrm{a}}$ in Figure 6.32. pPb values increase more rapidly at low p_{T} but unlike the case in v_2 they reach similar values as pp at high p_{T}.

The p_{T} interval (1,5) GeV is used for both particles in Figure 6.34. v_3 and v_4 from the pp events at 5.02 TeV are now included with meaningful values. pp events at these two energies yield similar values from v_2 to v_4. They converge with the value from pPb at low $N_{\mathrm{ch}}^{\mathrm{rec}}$ in all three panels. A simple explanation for this focuses on the collision geometry. Event multiplicity is closely related to the number of participants. In the ultra-peripheral pPb collision proton only interacts with the most outside nucleon in the lead ion. In this case the nucleon-nucleus collision is more like a nucleon-nucleon collision. The azimuthal anisotropies of single particle distribution in these two systems thus exhibit similar values.

Studies on the correlation of Fourier harmonics and event-plane angles for different flows in Pb+Pb events indicate that the initial elliptic geometry of the overlapping nuclei has a quadratic contribution to the quadrangular flow. Except for the most central events where the quadrangular flow mainly results from the initial state fluctuation, this elliptical properties of the initial geometry should dominate the $\cos(4\phi)$ modulation. This suggests $v^4 \sim v_2^2$ in Pb+Pb. Figure 6.35 shows the v^4/v_2^2 scaling for pp at 13 TeV and pPb at 5.02 TeV. The p_{T} interval is (0.5,5) GeV. Although v_2 and v_4 from pPb systems both increase with $N_{\mathrm{ch}}^{\mathrm{rec}}$, v^4/v_2^2 shows a very weak dependence on event multiplicity. This unchanged ratio suggests the existence of the quadratic contribution of the initial elliptic geometry to the quadrangular flow even in pPb systems. Ratio in pp events is nearly 50% larger than pPb events, which means if the idea of the collective flow is applicable in pp system, this quadratic

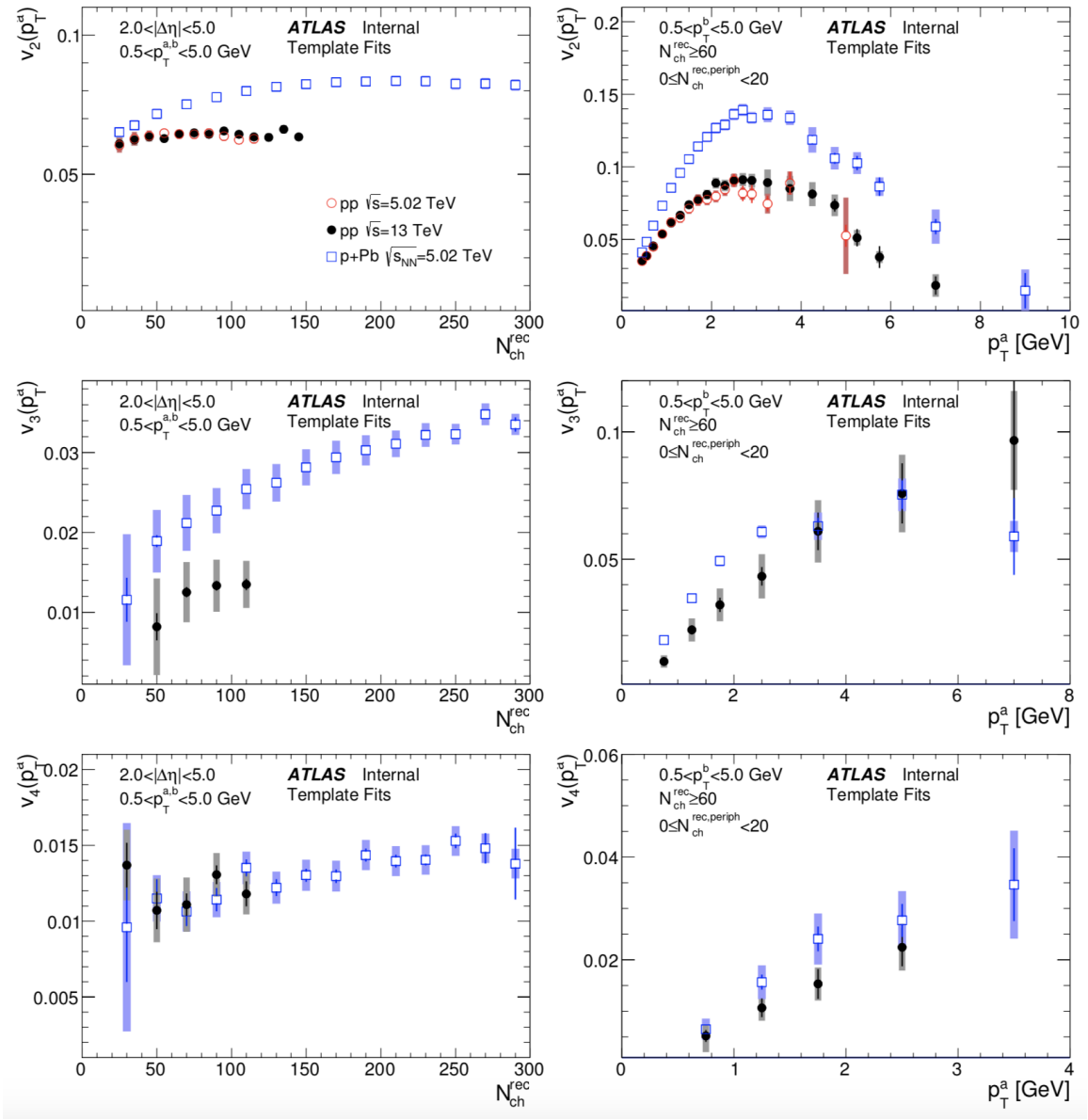

Figure 6.32: Dependence of v_n on $N_{\mathrm{ch}}^{\mathrm{rec}}$ on the left panels and $p_{\mathrm{T}}^{\mathrm{a}}$ on the right panels. Both pp events at 13 TeV and pPb events at 5.02 TeV are presented. p_{T} interval used for both particles is (0.5,5) GeV. The error bars and shaded bands in the figure indicate statistical and systematic uncertainties respectively.

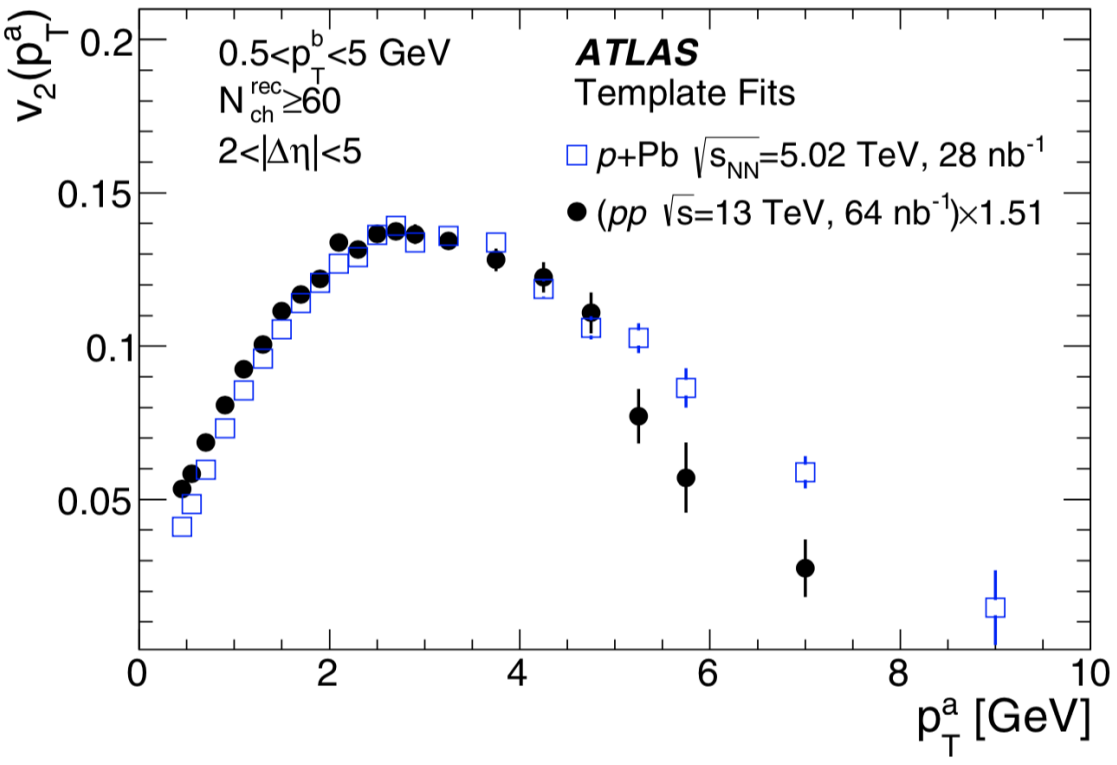

Figure 6.33: Comparison of the shapes of v_2 between pp events at 13 TeV and pPb events at 5.02 TeV. pp distribution has been scaled up by a factor of 1.51 to match its maximum to the pPb distribution. The error bars in the figure indicate statistical uncertainties.

contribution from initial geometry is 50% larger than pPb systems. A more general comparison is to measure the ratio of v^n to $v_2^{n/2}$. A case of $n = 3$ is illustrated in the right panel of Figure 6.36. p_{T} bin of (1,5) GeV is used. Ratios for pp and pPb systems are closer when $n = 3$.

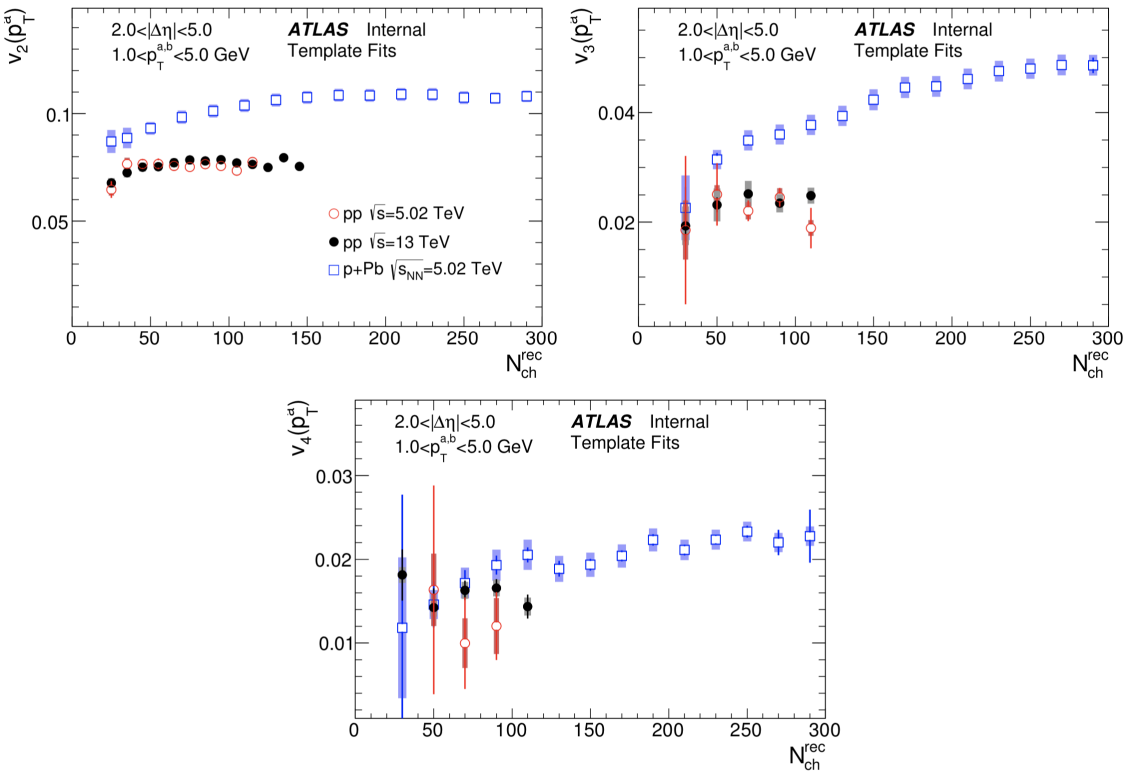

Figure 6.34: Dependence of v_n on $N_{\mathrm{ch}}^{\mathrm{rec}}$. pp events at 13 TeV, pp events at 5 TeV and pPb events at 5.02 TeV are presented. p_{T} interval used for both particles is (1,5) GeV. The error bars and shaded bands in the figure indicate statistical and systematic uncertainties respectively.

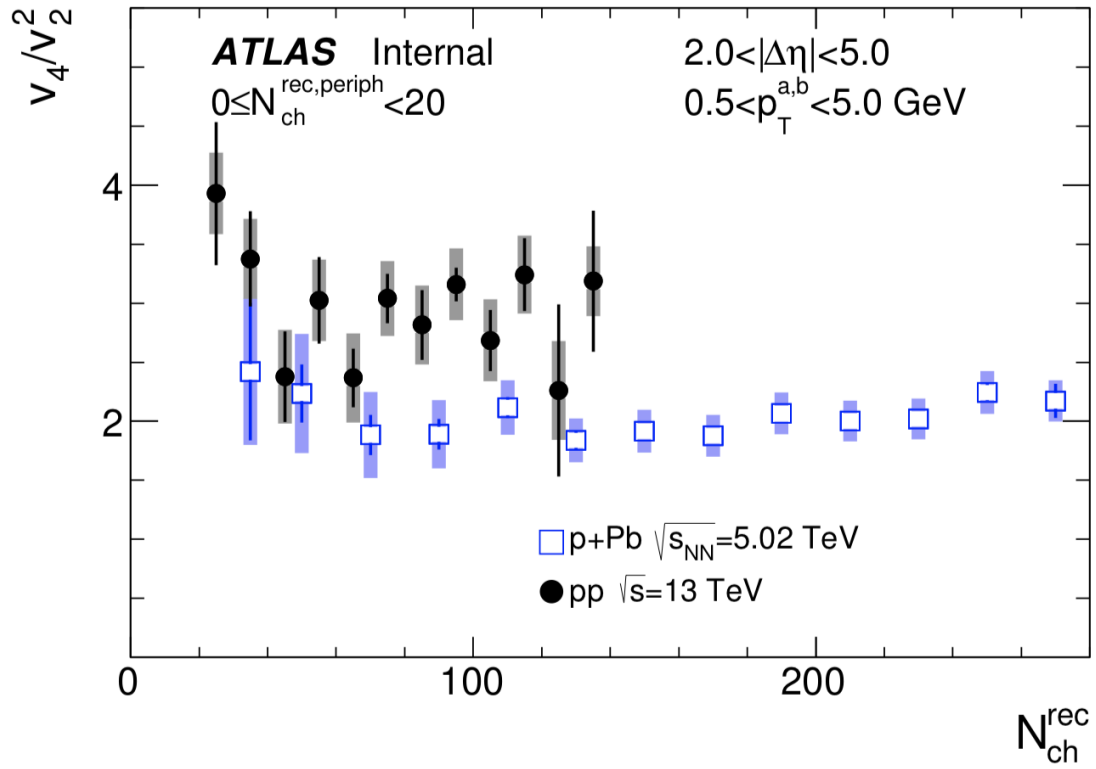

Figure 6.35: Ratios of v_4 to v_2^2 as a function of $N_{\mathrm{ch}}^{\mathrm{rec}}$. Results from both pp events at 13 TeV and pPb events at 5.02 TeV are presented. The error bars and shaded bands in the figure indicate statistical and systematic uncertainties respectively.

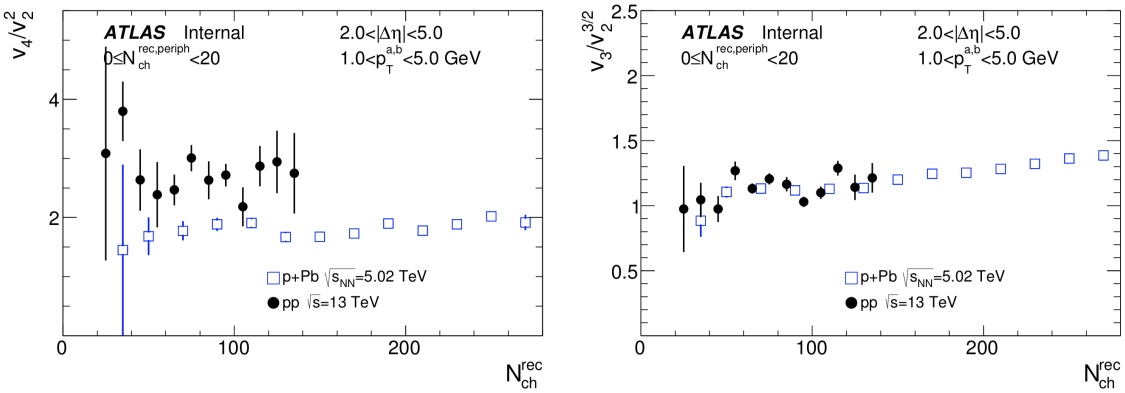

Figure 6.36: Ratios of v_n to v_2^n as a function of $N_{\mathrm{ch}}^{\mathrm{rec}}$ when $n = 4$ in the left panel and $n = 3$ in the right panel. Results from both pp events at 13 TeV and pPb events at 5.02 TeV are presented. The error bars in the figure indicate statistical uncertainties.

Chapter 7

Results of proton-lead events at $\sqrt{s}$ = 8.16 TeV

7.1 $\mathrm{ch}^{\mathrm{trk}} - \mathrm{ch}^{\mathrm{trk}}$ correlation measurement

7.1.1 Results of $\mathrm{ch}^{\mathrm{trk}} - \mathrm{ch}^{\mathrm{trk}}$ correlations in pPb collisions at $\sqrt{s}$ = 8.16 TeV

Figure 7.1 shows the two dimensional two-particle correlation as a function of relative azimuthal angle $\Delta\phi$ and pseudorapidity separation $\Delta\eta$. Each panel corresponds to a certain multiplicity bin. At high multiplicity the near-side ridge structure at $\Delta\phi = 0$ along the $\Delta\eta$ axis becomes prominent. Figure 7.2 shows the projection of two dimensional correlation onto $\Delta\phi$ axis at large $|\Delta\eta|$, $|\Delta\eta| > 2$. It has been normalized to a mean value of 1. The correlation structure at $\Delta\phi = 0$ changes from a concave-up shape to an obvious peak as the multiplicity increases. The red line represents Fourier fits up to the 4th order harmonics. Figure 7.3 demonstrates the per-trigger yields which are defined as the yields of associated particles per trigger particle. A template fitting analysis is done in Figure 7.4. Like the previous pPb events at 5.02

TeV, long range correlations obtained here are much larger than pp events due to the large collective behavior in pPb collisions. As we can see at high multiplicity, the size of the ridge correlation represented by the blue dashed line is comparable to the size of the away-side jet correlation.

The dependence of Fourier harmonics on $N_{\rm ch}^{\rm rec}$ is presented in Figure 7.5. Results from $v_{2,2}$ to $v_{4,4}$ are shown in three different panels. Four different methods, improved template fits, ZYAM-based template fits, direct Fourier transform and peripheral subtraction are implemented here. As we have discussed in the previous pPb results at 5.02 TeV, peripheral subtraction gives the same values of Fourier harmonics as the ZYAM-based template fits. The only difference between these two is how to determine the scale factor for the ZYAMed peripheral reference. Also like the case in the 5.02 TeV, direct Fourier transform leads to similar values to improved template fits in $v_{2,2}$ and $v_{4,4}$ except that there is a rapid decrease in the Fourier transform result of $v_{2,2}$ at low multiplicity region. This comes from the significant contribution of hard component in peripheral collisions. $v_{2,2}$ increases with multiplicity when $N_{\rm ch}^{\rm rec} < 150$ and saturates at high multiplicity, which is probably because of the colliding geometry of pPb events, while $v_{3,3}$ and $v_{4,4}$ increase monotonically with $N_{\rm ch}^{\rm rec}$.

Figure 7.6 checks the factorization of $v_{n,n}$ in terms of $N_{\rm ch}^{\rm rec}$. Each row corresponds to a different Fourier harmonic. The $|\Delta\eta|$ cut implemented here is $|\Delta\eta| > 1$ (not $|\Delta\eta| > 2$ used in the previous analysis). Unlike the previous analysis, here we fix the value of associated particle (particle b) and change the $p_{\rm T}$ ranges for trigger particle (particle a). Although $v_{n,n}$ values from different bins of $p_{\rm T}^{\rm a}$ can vary by a large factor in the left panels, results of v_n match quite well on the right. Figure 7.7 checks whether factorization still holds true in terms of $p_{\rm T}^{\rm b}$. Different from the results obtained in 5.02 TeV there is a decrease in $v_{2,2}$ after its maximum. Both $v_{3,3}$ and $v_{4,4}$ no longer increase with $p_{\rm T}$ monotonically at high $p_{\rm T}$, showing a downward trend when $p_{\rm T}^{\rm b} > 4$ GeV. Factorization holds until $p_{\rm T}^{\rm b} \sim 5$ GeV.

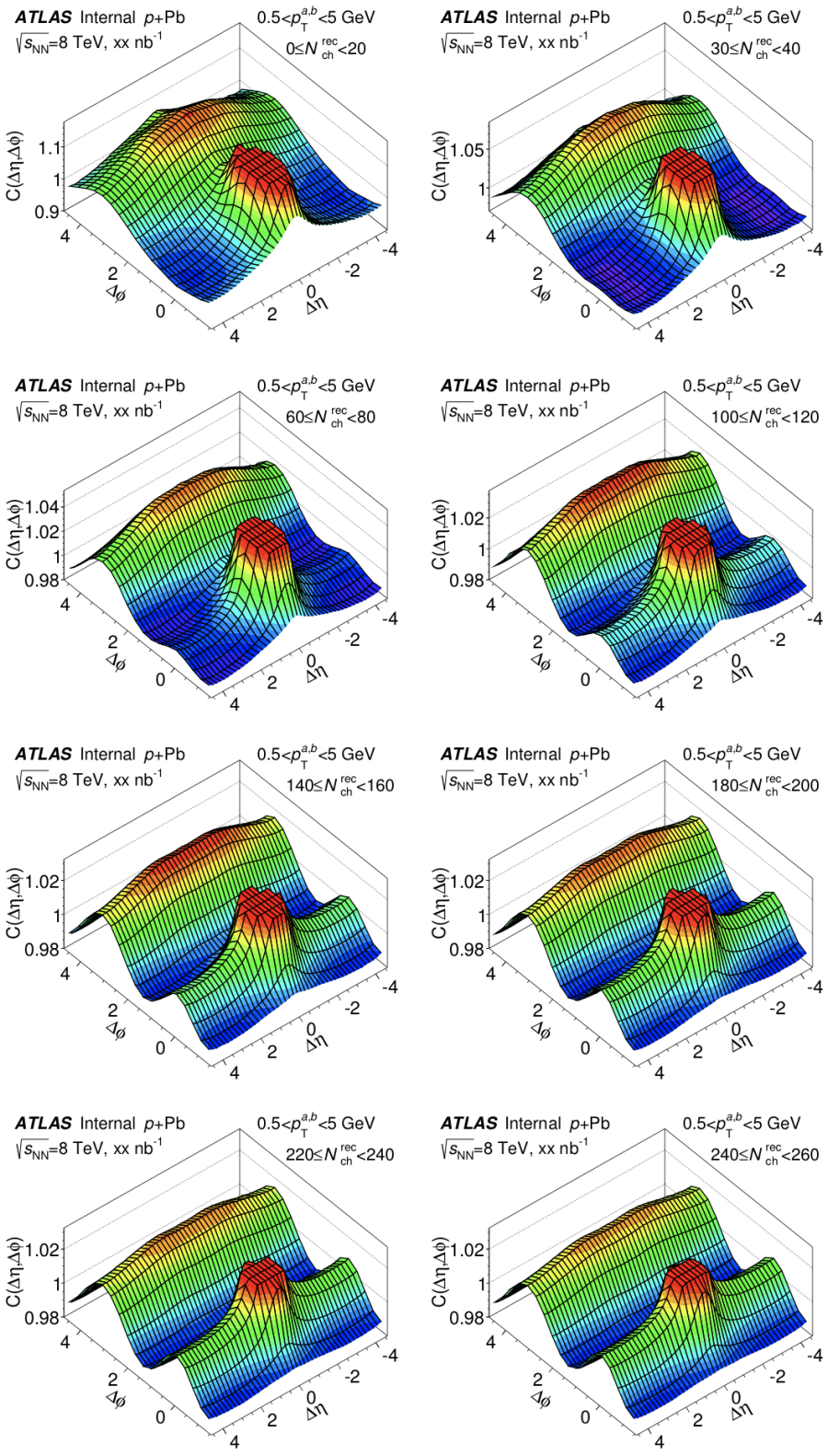

Figure 7.1: Two dimensional $\mathrm{ch}^{\mathrm{trk}} - \mathrm{ch}^{\mathrm{trk}}$ correlation function for pPb events at 8.16 TeV. Each panel is a different multiplicity bin. The large jet correlation at $\Delta\phi = \Delta\eta = 0$ has been truncated.

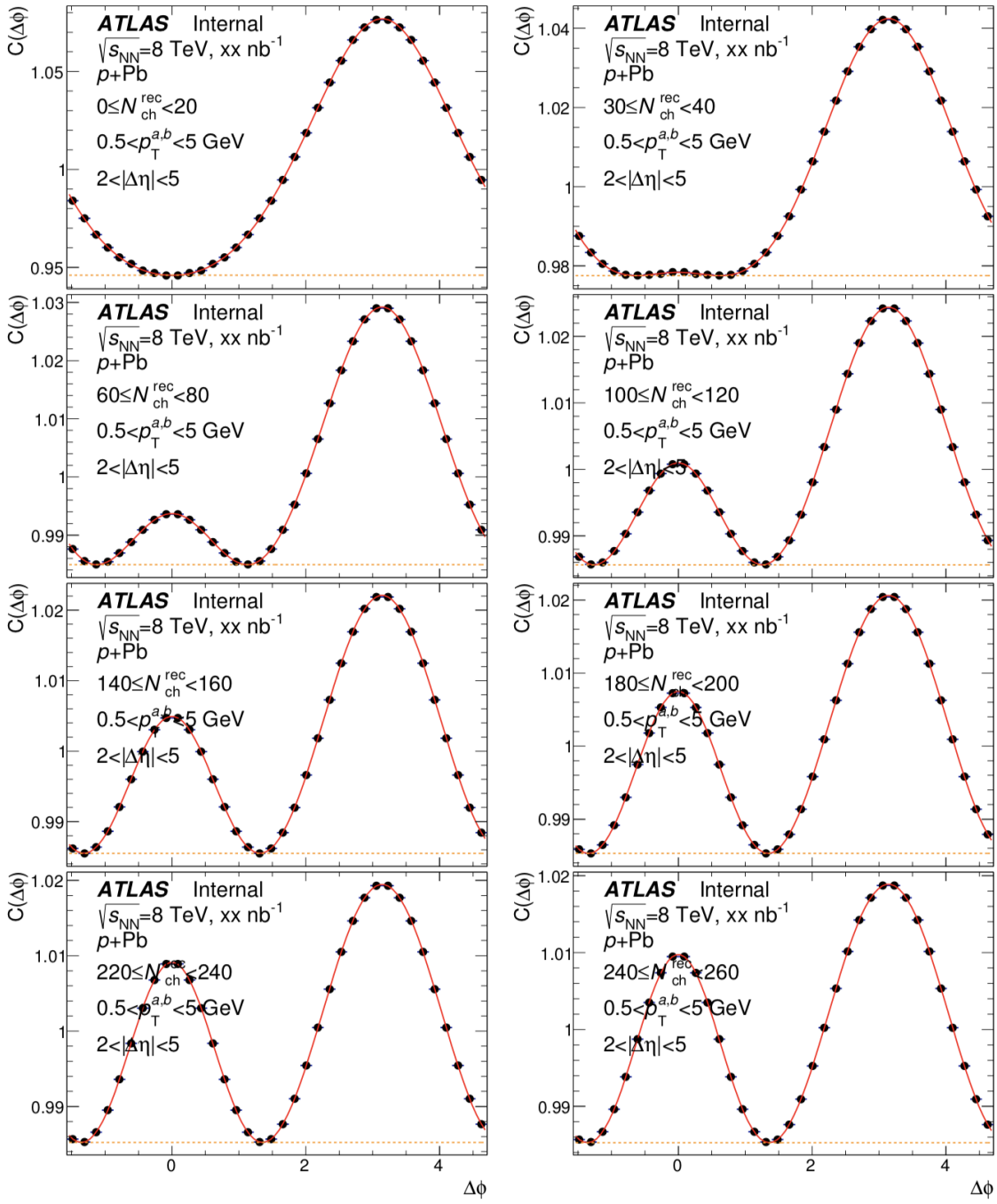

Figure 7.2: One dimensional $\mathrm{ch}^{\mathrm{trk}} - \mathrm{ch}^{\mathrm{trk}}$ correlation function for pPb events at 8.16 TeV. A cut $|\Delta\eta| > 2$ is implemented to exclude the near side jet correlation. Each panel is a different multiplicity bin. The red line represents a Fourier fit up to the 5th order harmonics.

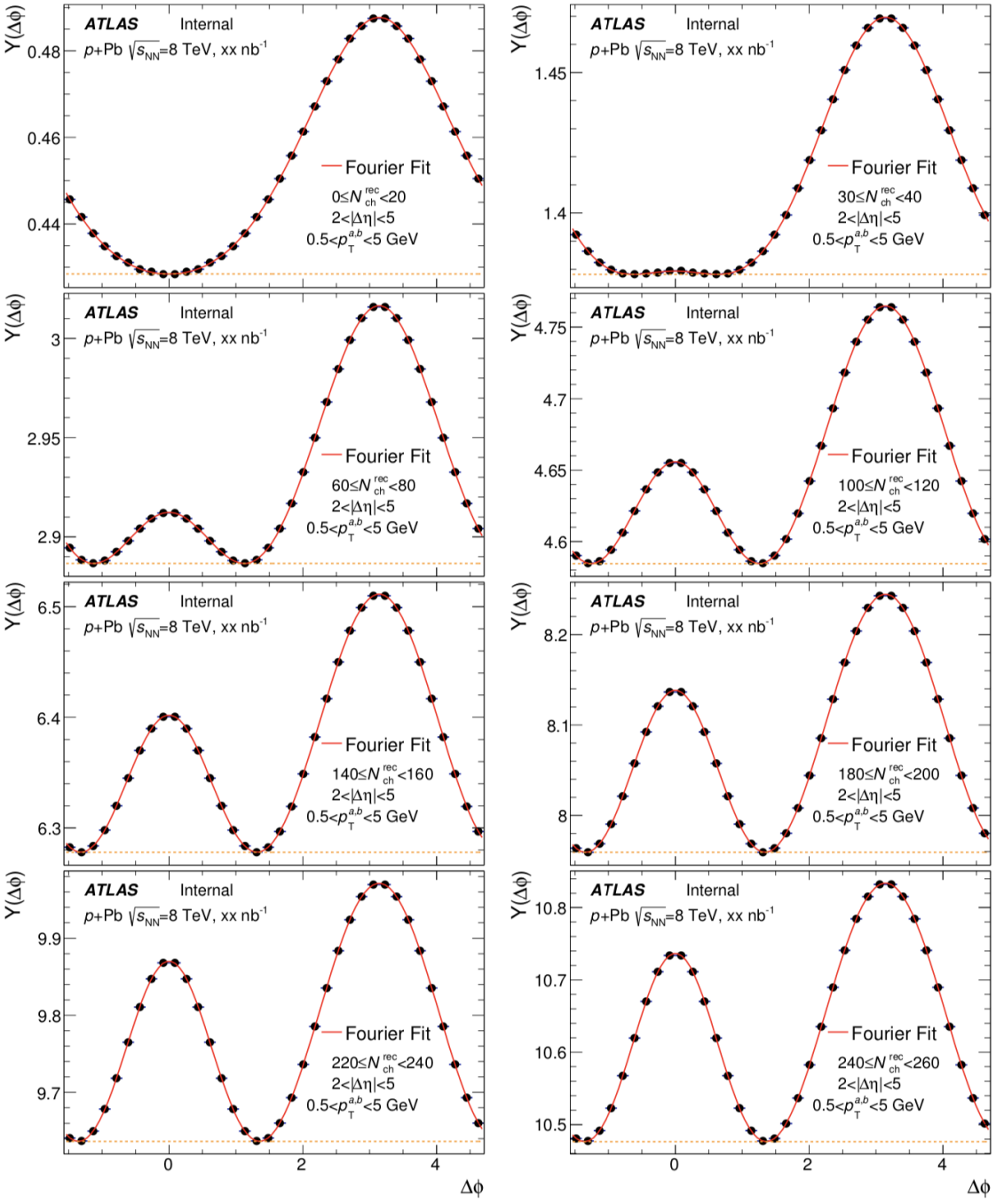

Figure 7.3: Per-trigger yields for pPb events at 8.16 TeV. Each panel is a different multiplicity bin. The red line represents a Fourier fit up to the 5th order harmonics. The yellow dashed line represents the minimum value of the Fourier fits.

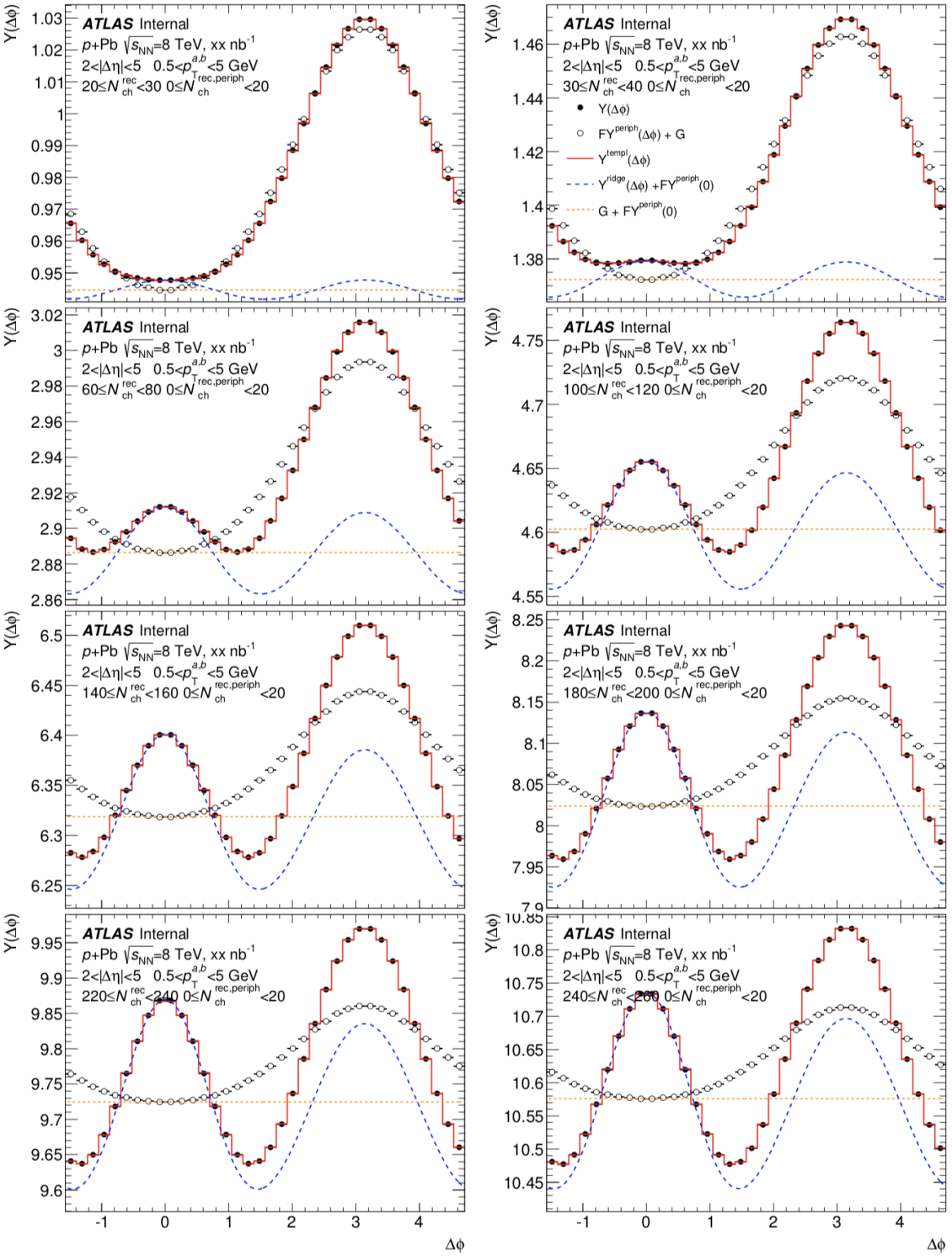

Figure 7.4: Improved template fits for pPb events at 8.16 TeV. The template fits include Fourier harmonics up to the 4th order. Each panel is a different multiplicity bin. The peripheral bin used here is $0 < N_{\mathrm{ch}}^{\mathrm{rec}} < 20$.

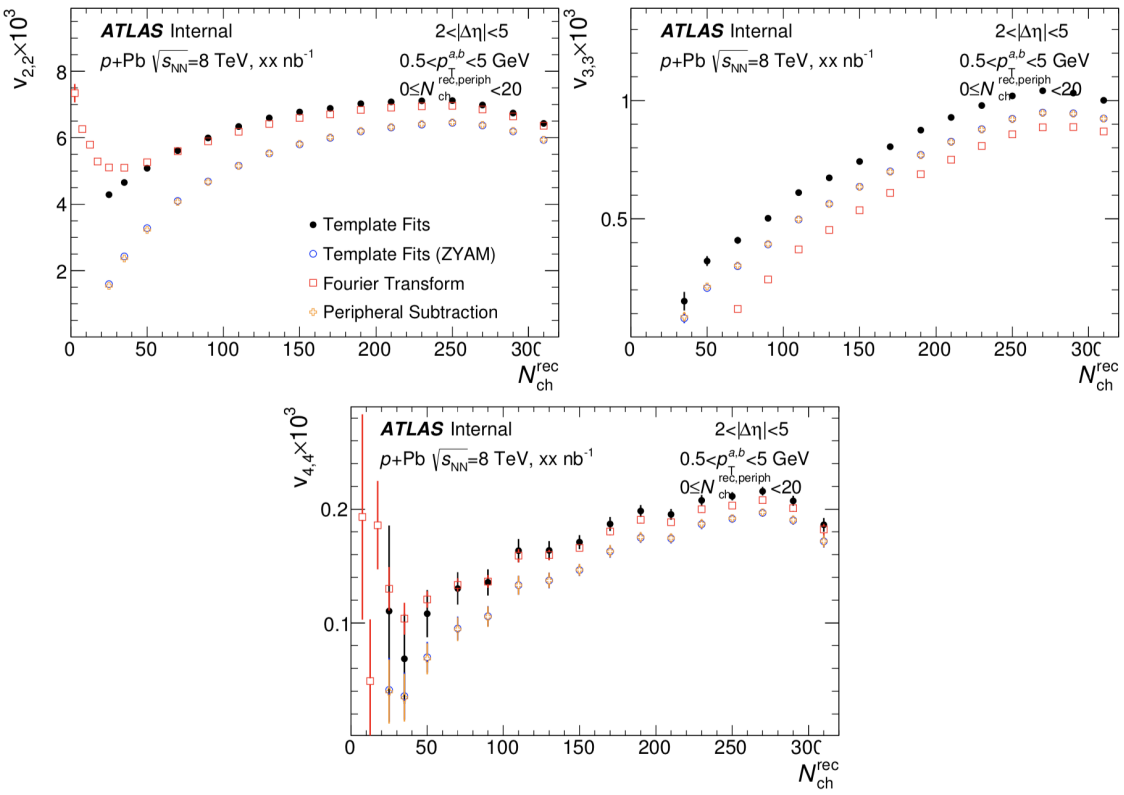

Figure 7.5: Measurement of $v_{2,2}$, $v_{3,3}$ and $v_{4,4}$ from (improved) template fits, template fits (ZYAM), Fourier transform and peripheral subtraction for pPb events at 8.16 TeV. Graphs are plotted as a function of event multiplicity. Both particles are chosen in (0.5,5) GeV.

It is expected that correlation between particles from jets should have a large dependence on $|\Delta\eta|$. Therefore checking the $|\Delta\eta|$ dependence of the long-range correlation can help understanding the origin of this structure. Figure 7.8 shows results from both improved template fits and Fourier transform. Region of $|\Delta\eta| < 1$ is excluded to get rid of the near-side jet correlation centered at $\Delta\eta = \Delta\phi = 0$. Each $|\Delta\eta|$ bin represents the integration limits for the 1D correlation function. Results from template fits indicated by the black dots show a very weak dependence on the pseudorapidity separation. This suggests the cosine modulation extracted from the template fits is truly the long-range correlation, not related to jets. The red circles representing the Fourier transform results have only a slight decline compared to the template-fit graph. This is due to the dijet peak on the away side. Over this p_{T} and

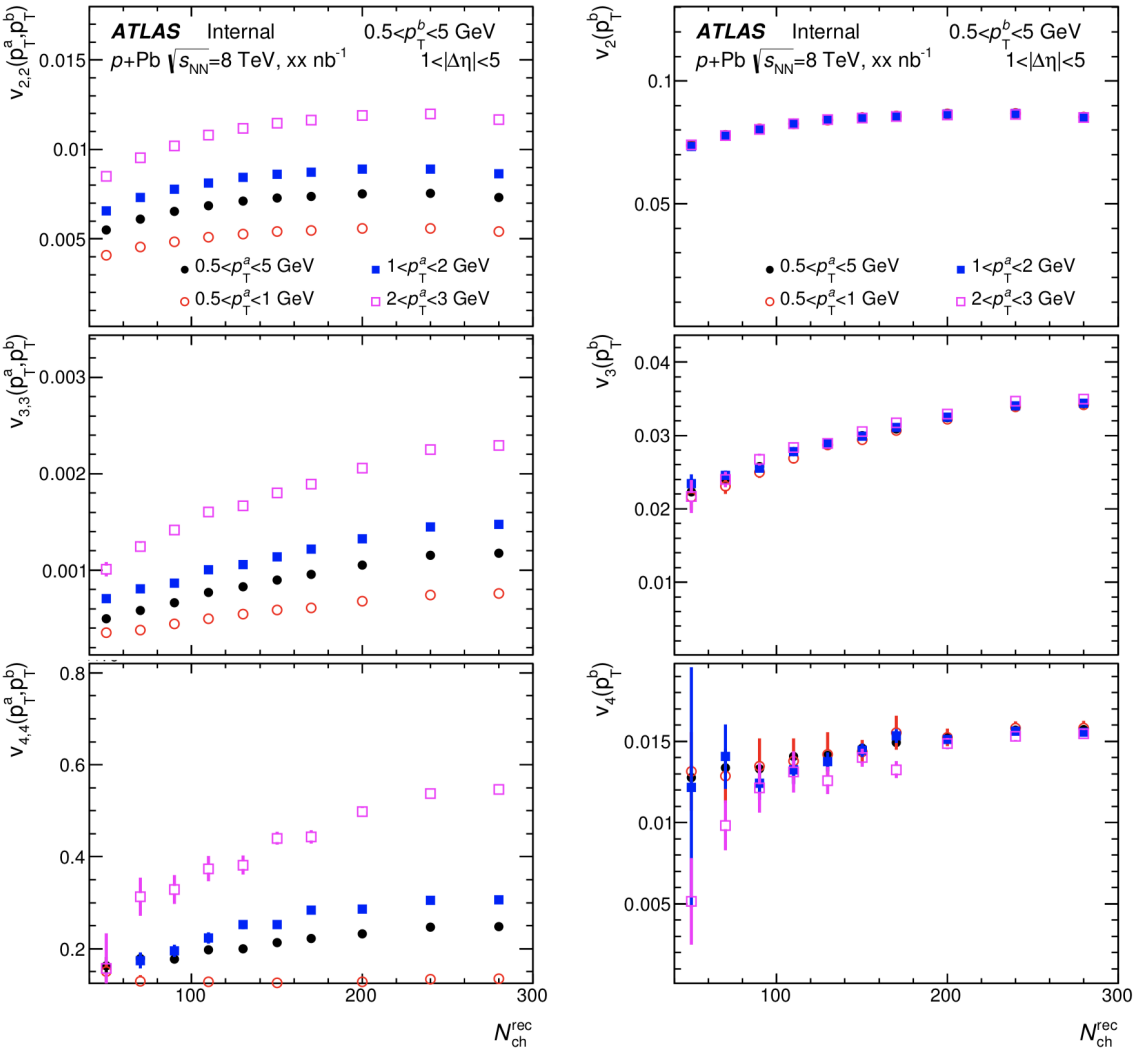

Figure 7.6: Factorization relationship for pPb events at 8.16 TeV is checked as a function of $N_{\mathrm{ch}}^{\mathrm{rec}}$. $v_{n,n}$ is calculated using different bins for $p_{\mathrm{T}}^{\mathrm{a}}$ for a fixed $p_{\mathrm{T}}^{\mathrm{b}}$. The right panel shows the corresponding v_n values.

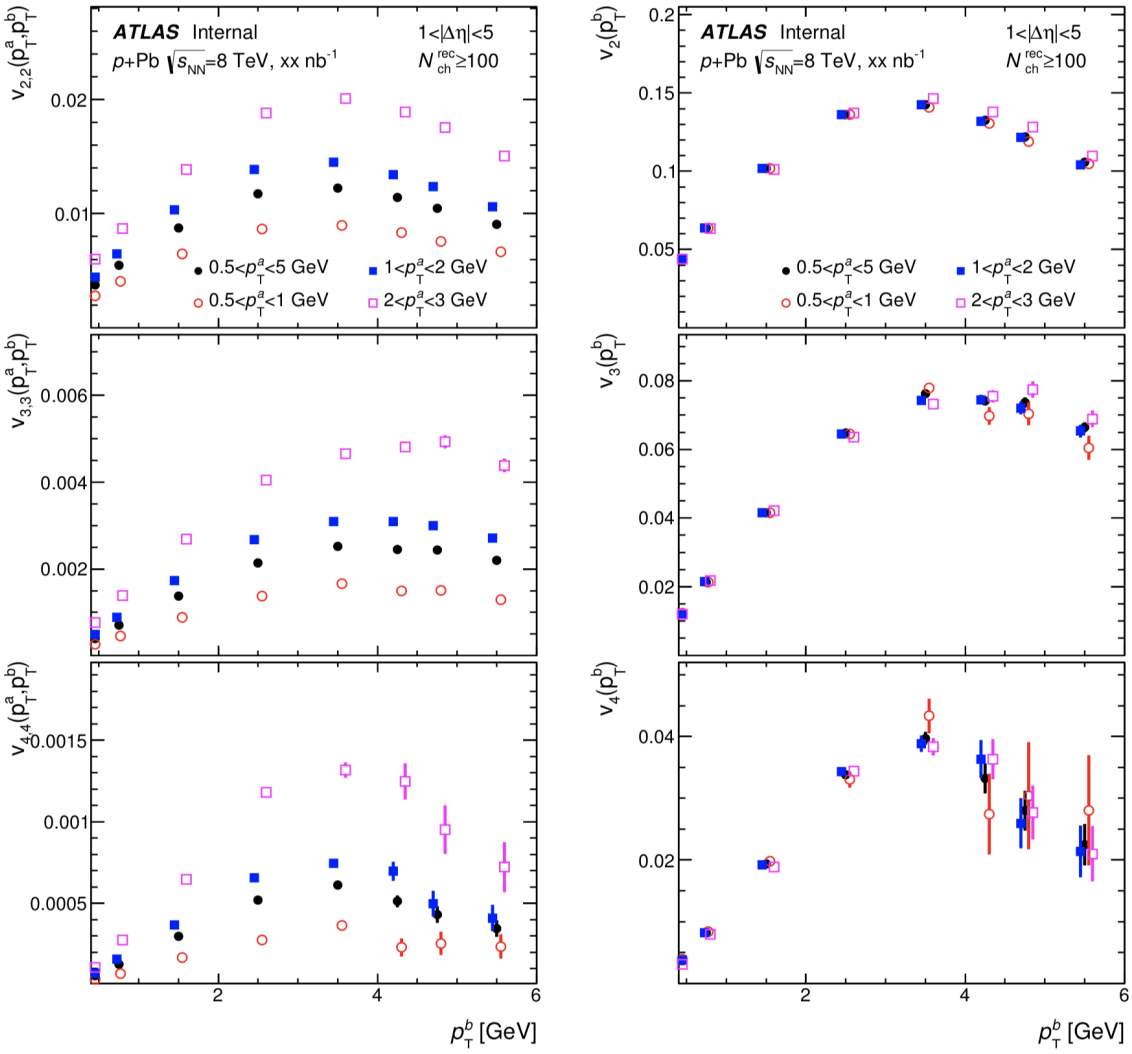

Figure 7.7: Factorization relationship for pPb events at 8.16 TeV is checked as a function of $p_{\mathrm{T}}^{\mathrm{b}}$. $v_{n,n}$ is calculated using different bins for $p_{\mathrm{T}}^{\mathrm{a}}$ for a fixed $p_{\mathrm{T}}^{\mathrm{b}}$. The right panel shows the corresponding v_n values.

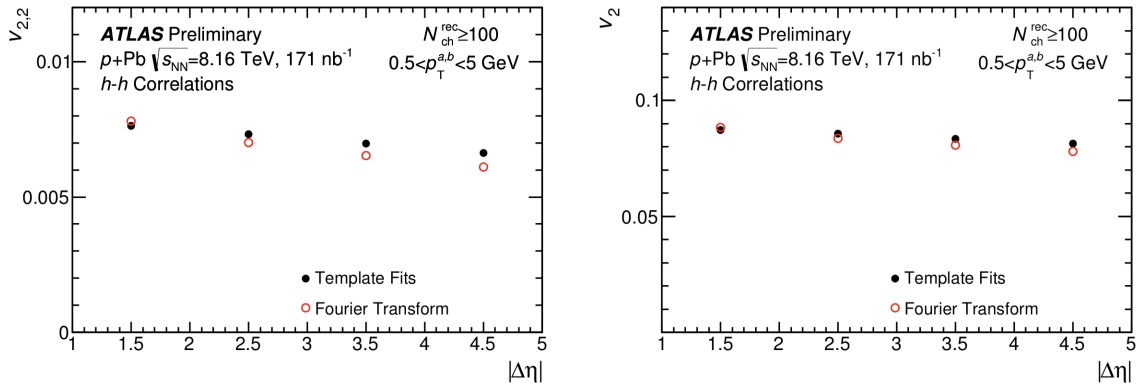

Figure 7.8: This figure shows the dependence of v_2 on $|\Delta\eta|$. Results from both template fits (black dots) and Fourier transform (red circle) are shown. Only a weak dependence on $|\Delta\eta|$ is observed for both methods.

multiplicity interval, the dijet contribution does not have a big impact on $v_{2,2}$.

7.1.2 Comparison with pPb collisions at $\sqrt{s} = 5.02$ TeV

Studies of dependence on the collision energy have been performed in Pb+Pb events. Previous sections in this thesis have also made the comparison between pp systems of different energies. Results have shown that the behavior of Fourier harmonics is independent of $\sqrt{s}$ in pp. A direct and interesting analysis at this point is therefore to extend this comparison to pPb systems. Figure 7.9 illustrates the $N_{\rm ch}^{\rm rec}$ dependence of v_2 from both the previous 5.02 TeV and the current 8.16 TeV pPb events. Peripheral bin is chosen to be $0 < N_{\rm ch}^{\rm rec} < 40$ for this comparison. The ratio of 5.02 TeV results to 8.16 TeV results is plotted in the right panels. Two histograms match quite well over the whole $N_{\rm ch}^{\rm rec}$ range. Similar panels for v_3 and v_4 are shown in Figure 7.10 and Figure 7.11 respectively.

7.2 ch$^{\rm trk}$-muon correlation measurement

Two-particle correlation analysis can be extended to particles of different species. At this stage one particle from the pair is still a charged track. The other particle,

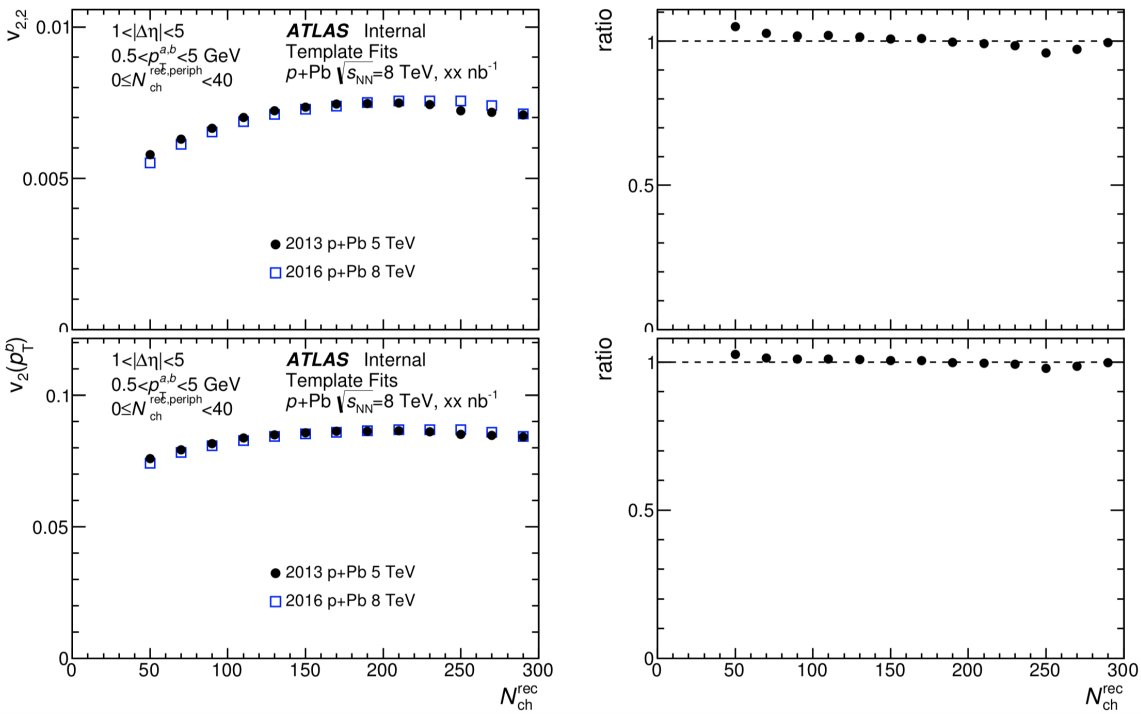

Figure 7.9: Comparison of $v_{2,2}$ and v_2 between the present 8.16 TeV analysis and the previous 5.02 TeV analysis. The peripheral bin $0 < N_{\mathrm{ch}}^{\mathrm{rec}} < 40$ is used as the reference. The ratio of the 5.02 TeV results to the 8.16 TeV results is plotted in the right panels.

however, is chosen to be a muon from the heavy flavor decay. Studying of the ch$^{\mathrm{trk}}$-muon correlation can give us knowledge of the long-range correlation related to heavy flavor quarks. HF muons can be regarded as prompt muons since contributions from other sources of prompt muons, such as muons from electroweak bosons and light mesons, are negligible at this low p_{T} region. As discussed in the previous chapter prompt muons can be discriminated from background muons through the following momentum imbalance

$$\frac{\Delta p}{p_{\mathrm{ID}}} = \frac{p_{\mathrm{ID}} - p_{\mathrm{MS}} - p_{\mathrm{param}}(p_{\mathrm{MS}}, \eta, \phi)}{p_{\mathrm{ID}}} \tag{7.1}$$

Background muons here include non-prompt muons from in-flight kaon or pion decays, muons decayed from particles produced in hadronic showers and mis-associations of tracks from the inner detector and muon spectrometer. A cut $\frac{\Delta p}{p_{\mathrm{ID}}} < 0$ is implemented

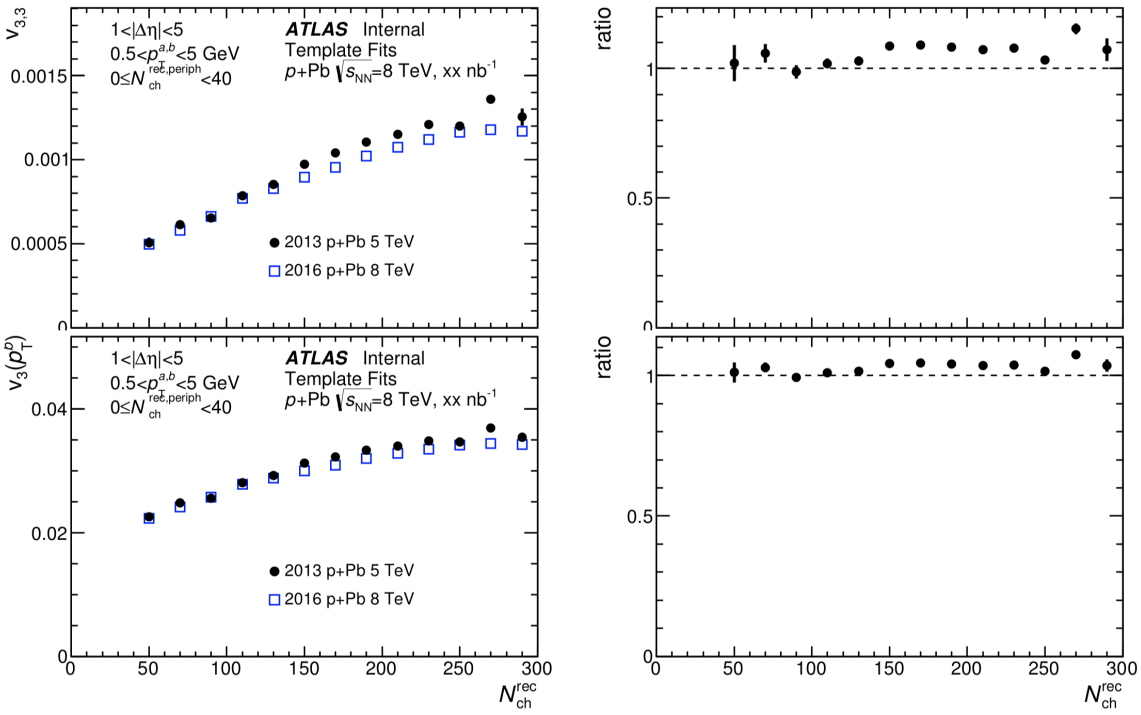

Figure 7.10: Same as Figure 7.9 but for $v_{3,3}$ and v_3.

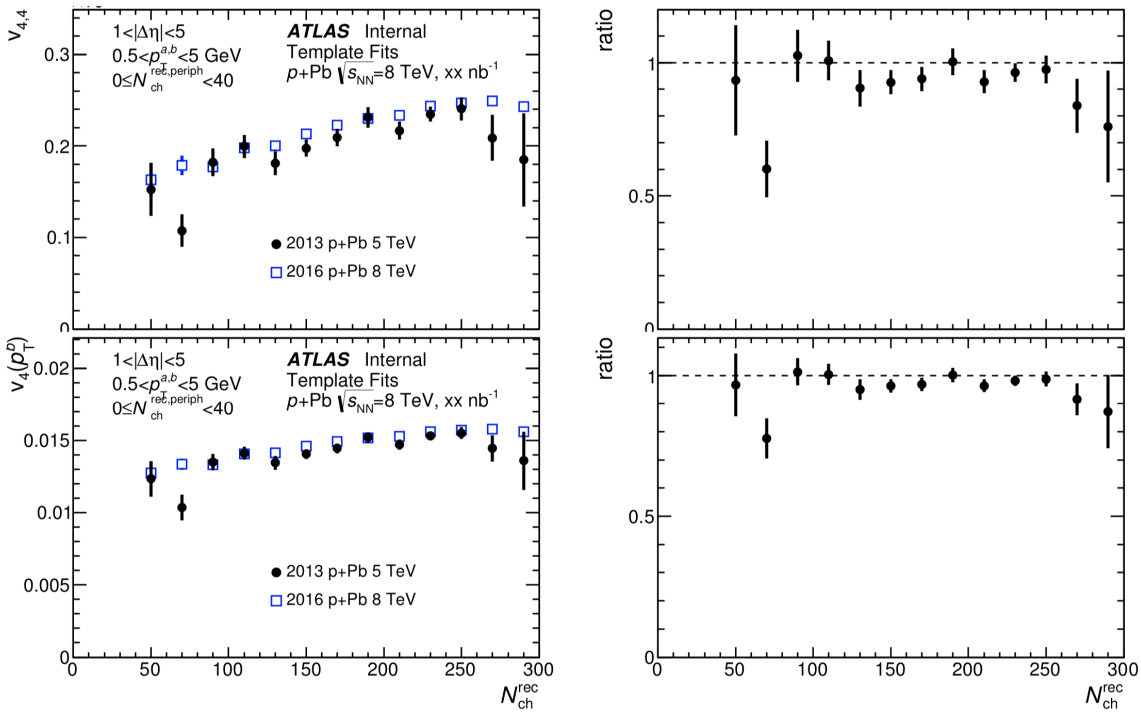

Figure 7.11: Same as Figure 7.9 but for $v_{4,4}$ and v_4.

to reject more than 50% of the background muons. Only less than half of the background muons are left in the analysis. This systematic uncertainties resulted from the remaining background can be estimated by the difference between results with this cut and without this cut.

2D $\mathrm{ch}^{\mathrm{trk}}$-muon correlation functions are presented in Figure 7.12. In this analysis charged hadron is always the trigger particle (i.e. particle a) and HF muon is always the associated particle (i.e. particle b). A broader bin $4 < p_{\mathrm{T}}^{\mu} < 6$ is used for muons to increase the statistics of these plots. Since we further require a reconstructed muon with $p_{\mathrm{T}}^{\mu} > 4$ GeV in the event selection, the statistics may not be sufficient if we use a narrow bin for the correlation function. Although the ridge is small compared to $\mathrm{ch}^{\mathrm{trk}}$-$\mathrm{ch}^{\mathrm{trk}}$ correlation, it is still visible in the highest multiplicity bin. Figure 7.13 shows the 1D correlation functions of the same p_{T}^{μ} ranges. A broader $|\Delta\eta|$ cut $1 < |\Delta\eta| < 5$ is used to increase the statistics. The red line represents Fourier fits up to the 5th order harmonics and the yellow dotted line indicates the minimum value of these fits. Figure 7.14 illustrates improved template fits of the correlation function. A larger peripheral bin $0 < N_{\mathrm{ch}}^{\mathrm{rec}} < 40$ is used here to give sufficient statistics in the peripheral reference. Although two particles in this analysis are not of the same kind, the cosine modulation still exists over the full $2\pi\Delta\phi$ range.

$v_{2,2}$ of the $h - \mu$ correlation is shown in the left panel of Figure 7.15. Results of $h - h$ correlation are plotted in the same panel for comparison. The right panel shows the corresponding v_2. $\mathrm{ch}^{\mathrm{trk}}$ v_2 is calculated as the square root of the $h - h$ $v_{2,2}$ values in the left panel. While muon v_2 is computed by the $h - \mu$ $v_{2,2}$ divided by the $\mathrm{ch}^{\mathrm{trk}}$ v_2 calculated just now. A more detailed result is shown in Figure 7.16. Each row corresponds to a different p_{T}^{μ} bin. From top to bottom bins of $4 < p_{\mathrm{T}}^{\mu} < 6$ GeV, $4 < p_{\mathrm{T}}^{\mu} < 4.5$ GeV, $4.5 < p_{\mathrm{T}}^{\mu} < 5$ GeV and $5 < p_{\mathrm{T}}^{\mu} < 6$ GeV are used. The right panels illustrate the ratios of $h - \mu$ results to $h - h$ results. It is clear that muon v_2 is considerably small and exhibits a very weak dependence on $N_{\mathrm{ch}}^{\mathrm{rec}}$ compared

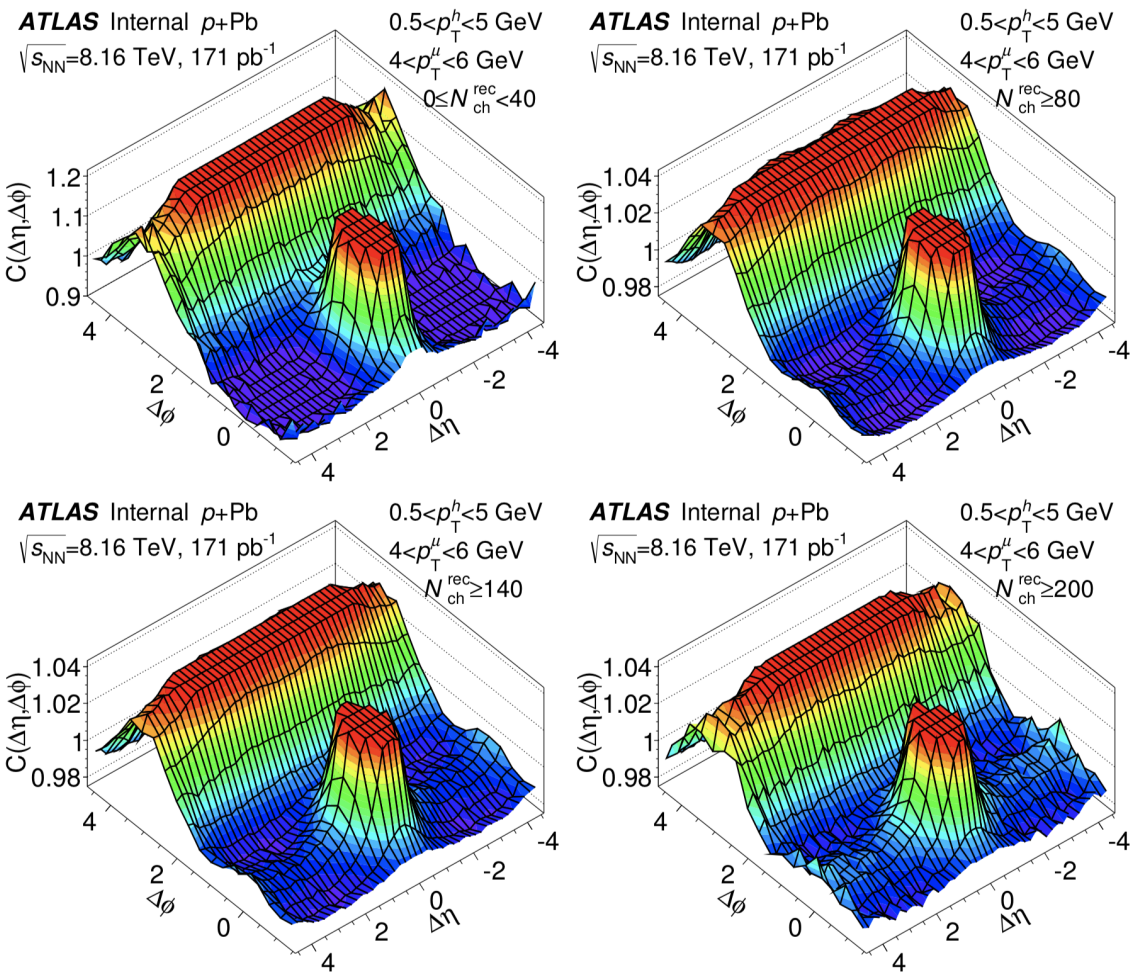

Figure 7.12: Two dimensional ch$^{\text{trk}}$-muon correlation function for pPb events at 8.16 TeV. Each panel is a different multiplicity bin. The large jet correlation at $\Delta\phi = \Delta\eta = 0$ has been truncated.

with ch$^{\text{trk}}$ v_2. There are large statistical errors at the two ends of this multiplicity interval. At low multiplicity the multiplicity bin used for the correlation function is almost identical to the peripheral bin leading to large statistical errors during the template fitting procedure. At high multiplicity the statistics may not be sufficient for the correlation function and thus significant statistical uncertainties obtained from template fits. Figure 7.17 shows similar results of $v_{3,3}$.

The factorization of $h - \mu$ $v_{2,2}$ is checked in Figure 7.18 as a function of $N_{\text{ch}}^{\text{rec}}$. In order to obtain the dependence of muon v_2 on the choice of hadron-p_{T} bin, four

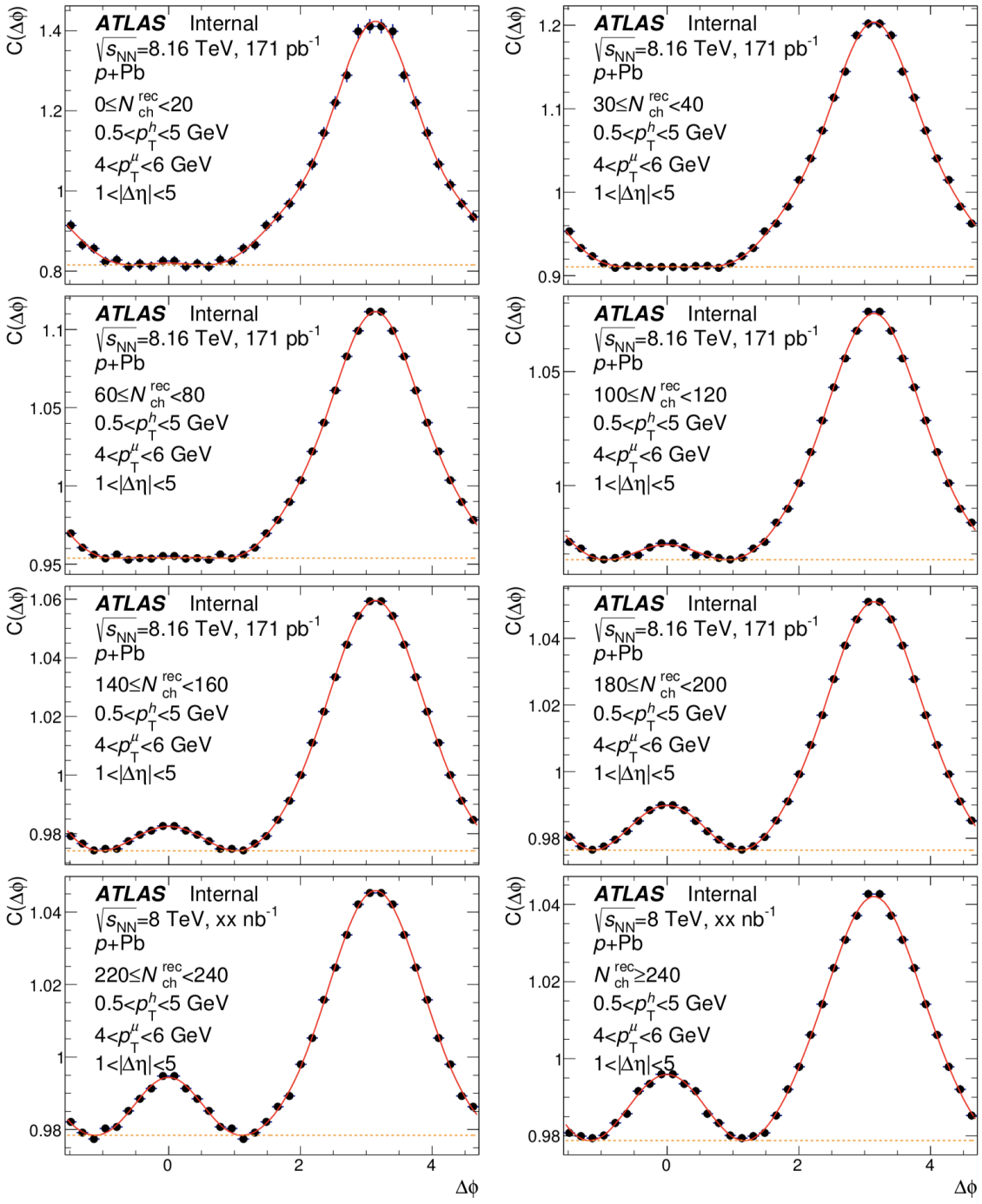

Figure 7.13: One dimensional ch$^{\text{trk}}$-muon correlation function for pPb events at 8.16 TeV. A cut $|\Delta\eta| > 1$ is implemented to exclude the near side jet correlation. Each panel is a different multiplicity bin. The red line represents a Fourier fit up to the 5th order harmonics.

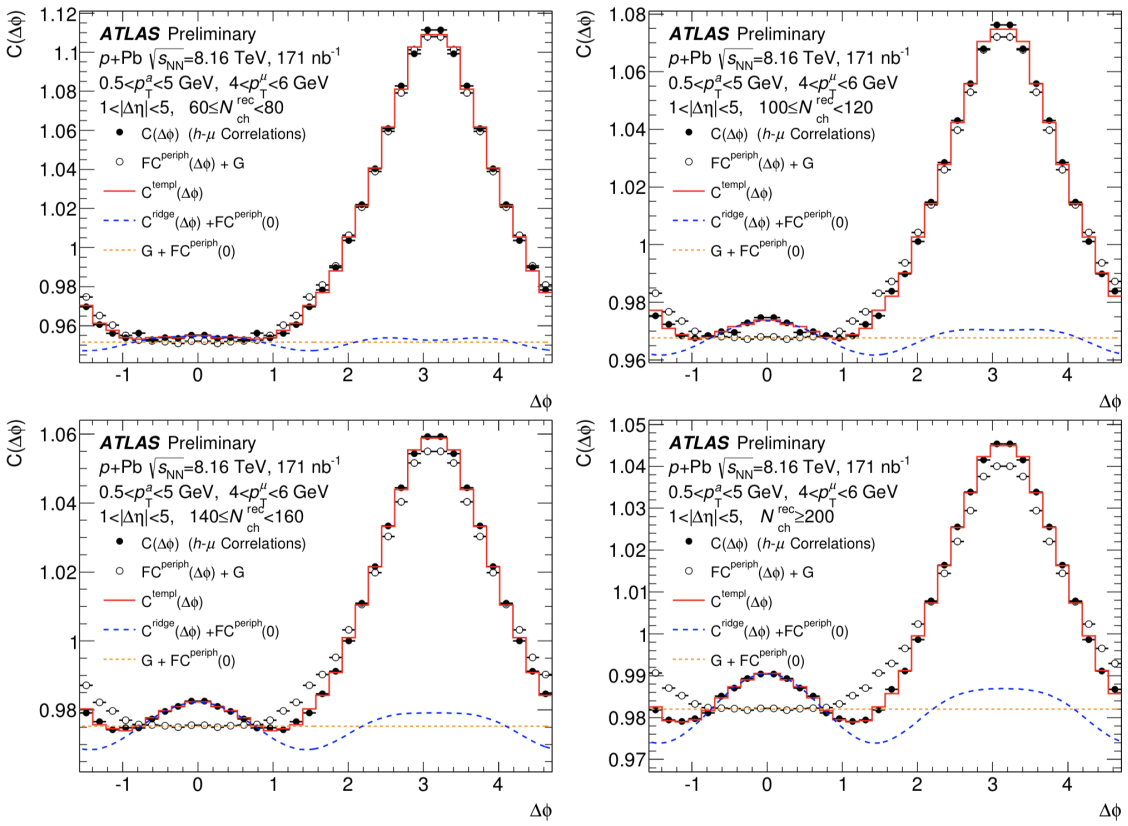

Figure 7.14: Improved template fits of ch$^{\mathrm{trk}}$-muon correlation for pPb events at 8.16 TeV. The template fits include Fourier harmonics up to the 4th order. Each panel is a different multiplicity bin. The peripheral bin used here is $0 < N_{\mathrm{ch}}^{\mathrm{rec}} < 40$.

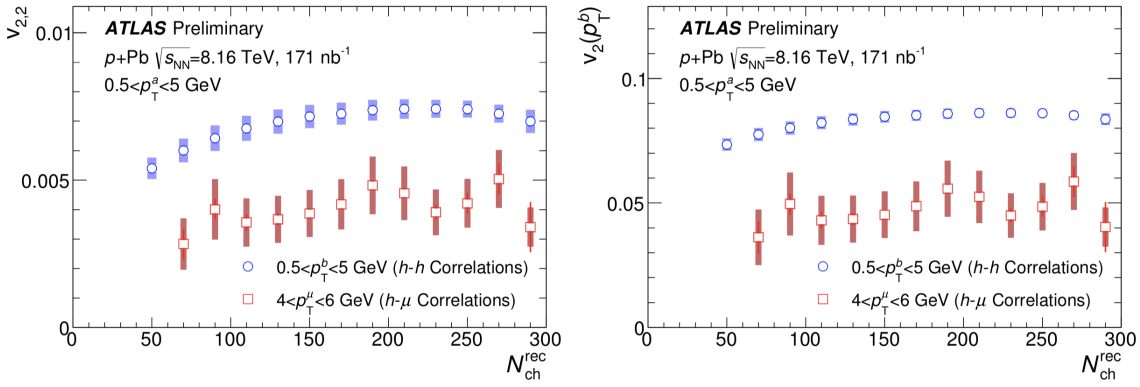

Figure 7.15: The left panel shows the $N_{\mathrm{ch}}^{\mathrm{rec}}$ dependence of $v_{2,2}$ for both ch$^{\mathrm{trk}}$-ch$^{\mathrm{trk}}$ and ch$^{\mathrm{trk}}$-muon correlations. The right panel shows the corresponding ch$^{\mathrm{trk}}$ v_2 and muon v_2. The error bars and shaded bands indicate statistical and systematic uncertainties respectively.

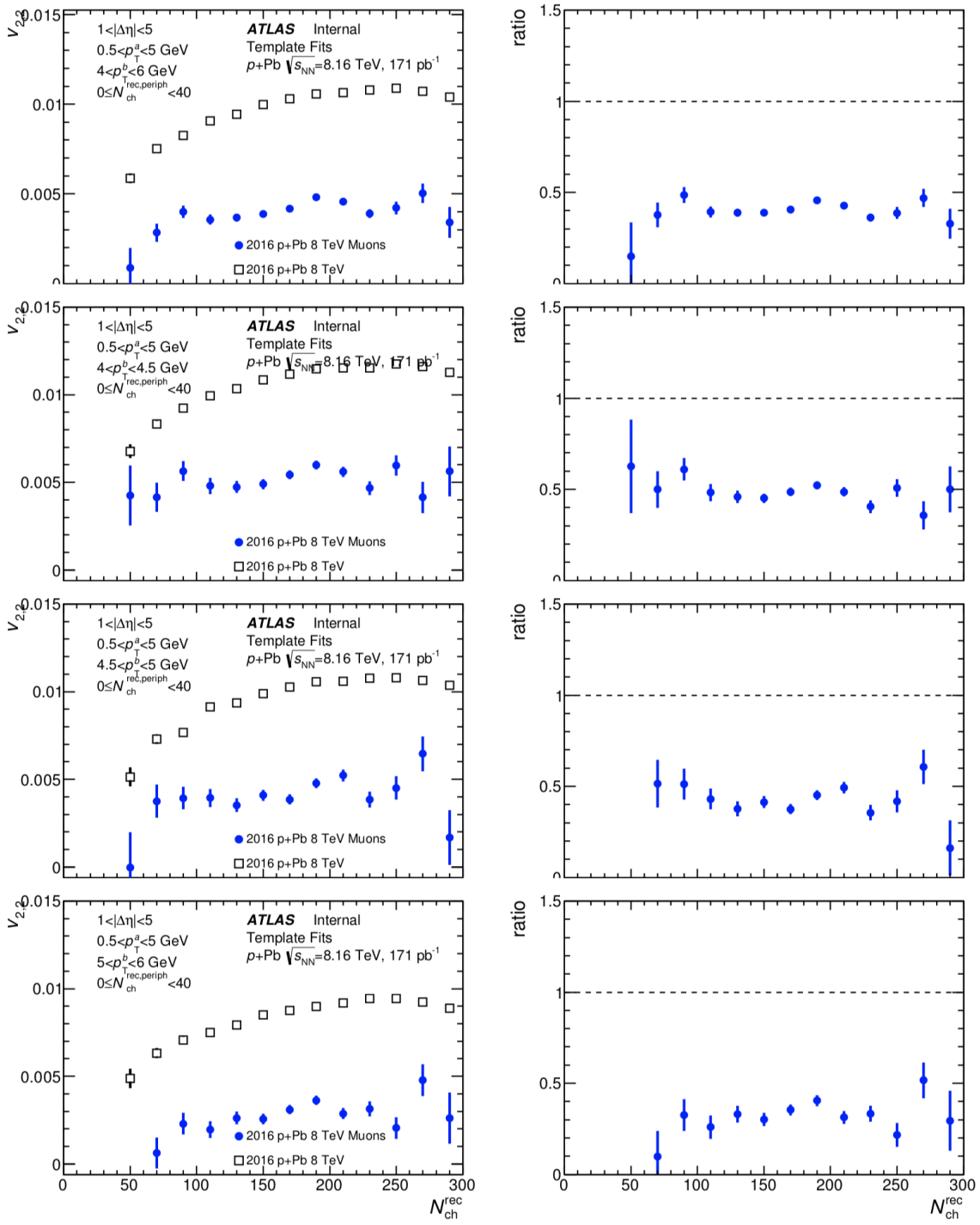

Figure 7.16: The left panels show the $N_{\mathrm{ch}}^{\mathrm{rec}}$ dependence of $v_{2,2}$ for both ch$^{\mathrm{trk}}$-ch$^{\mathrm{trk}}$ and ch$^{\mathrm{trk}}$-muon correlations. From top to bottom different bins for p_{T}^{μ} are used. The right panels show the corresponding ratios of ch$^{\mathrm{trk}}$-muon results to ch$^{\mathrm{trk}}$-ch$^{\mathrm{trk}}$ results. The error bars in the figure indicate statistical uncertainties.

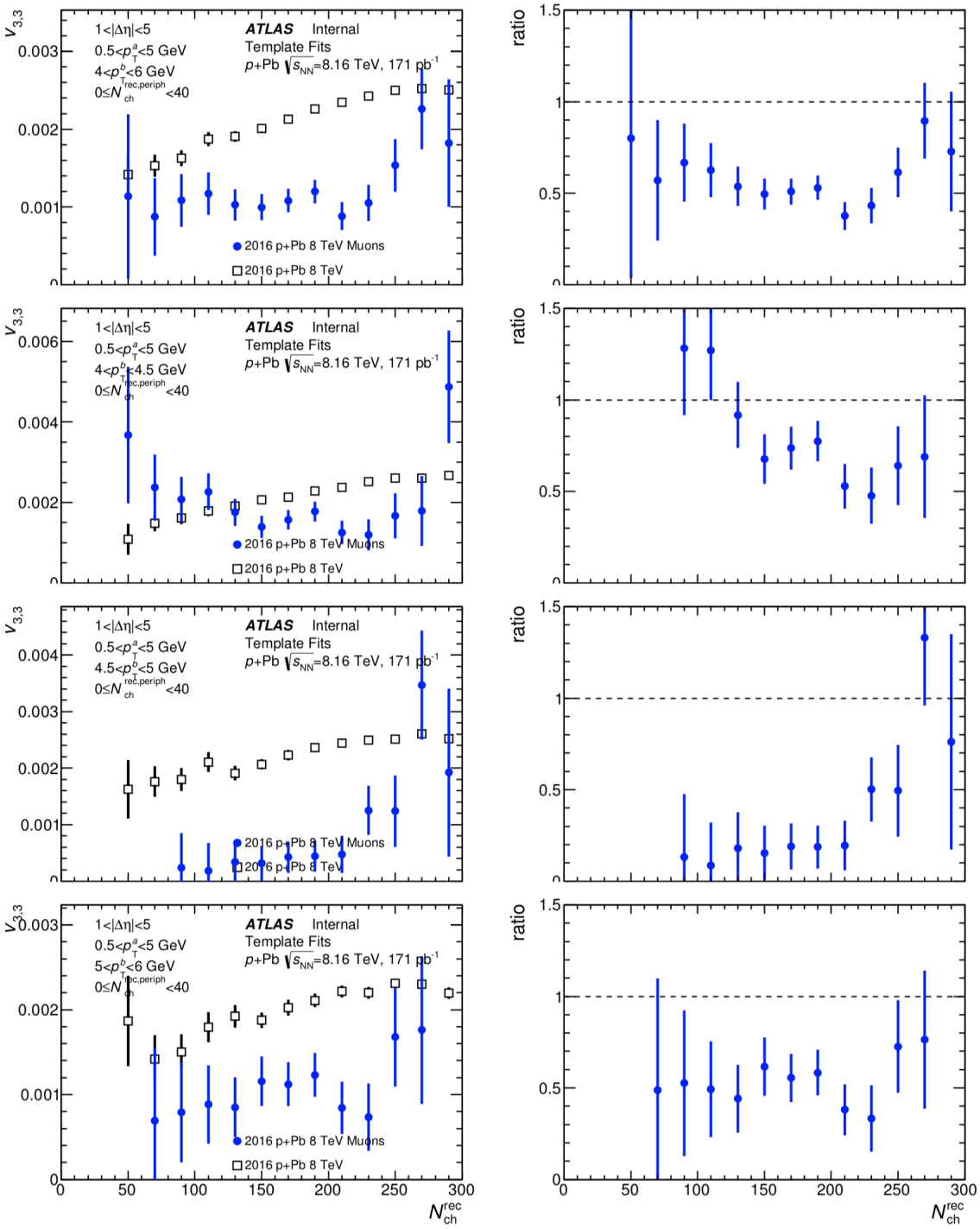

Figure 7.17: Same as Figure 7.16 but for $v_{3,3}$.

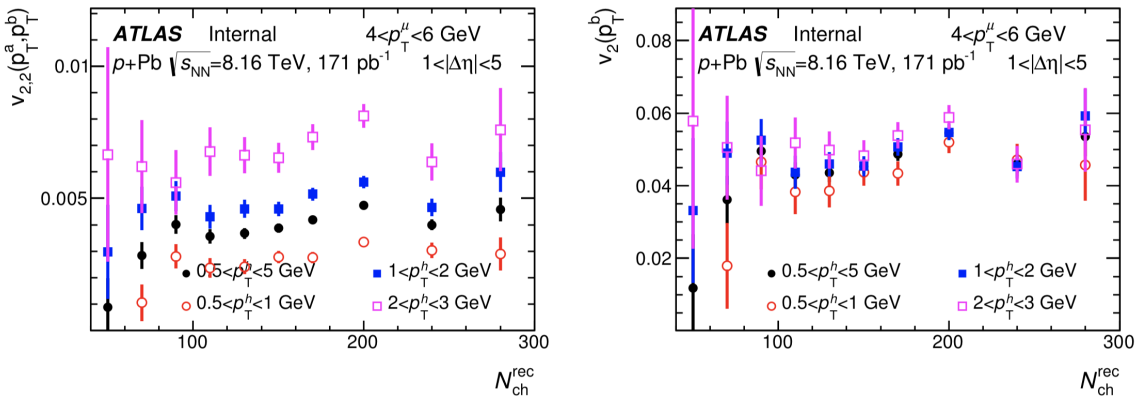

Figure 7.18: Factorization relationship of ch$^{\text{trk}}$-muon correlations for pPb events at 8.16 TeV is checked as a function of $N_{\text{ch}}^{\text{rec}}$. $v_{n,n}$ is calculated using different bins of p_{T}^{a} for a fixed p_{T}^{μ}. The right panel shows the corresponding muon v_n values.

different bins for hadron-p_{T} are used: $0.5 < p_{\text{T}}^{h} < 5$ GeV, $0.5 < p_{\text{T}}^{h} < 1$ GeV, $1 < p_{\text{T}}^{h} < 2$ GeV and $2 < p_{\text{T}}^{h} < 3$ GeV while muon-p_{T} bin is fixed at $4 < p_{\text{T}}^{\mu} < 6$ GeV. The right panel shows the corresponding $v_2(p_{\text{T}}^{\mu})$ which are calculated from the $v_{2,2}$ in the left panel divided by the hadron v_2 obtained in the previous ch$^{\text{trk}}$ – ch$^{\text{trk}}$ correlation measurement. Since all results are consistent with each other, factorization works quite well.

Figure 7.19 shows the p_{T} dependence of muon v_2 from 4 to 8 GeV. A large multiplicity bin $N_{\text{ch}}^{\text{rec}} > 100$ is used to increase the statistics. The result indicates that muon v_2 is a decreasing function of muon-p_{T} over this range. As with the case of ch$^{\text{trk}}$ – ch$^{\text{trk}}$ correlation, $|\Delta\eta|$ dependence of v_2 from template fits and Fourier transform is also studied in Figure 7.20. Results from template fits show a very weak dependence on $|\Delta\eta|$, which suggests Fourier harmonics extracted from this method reflect the genuine long-range correlation. This is because correlation between particles from jets should have a strong dependence on $|\Delta\eta|$. However Fourier transform gives a decreasing v_2 as $|\Delta\eta|$ increases. This means dijet contribution in $h-\mu$ correlations is considerably large compared to $h-h$ correlations and results in a strong bias in the Fourier transform results. This is because HF muons have a larger

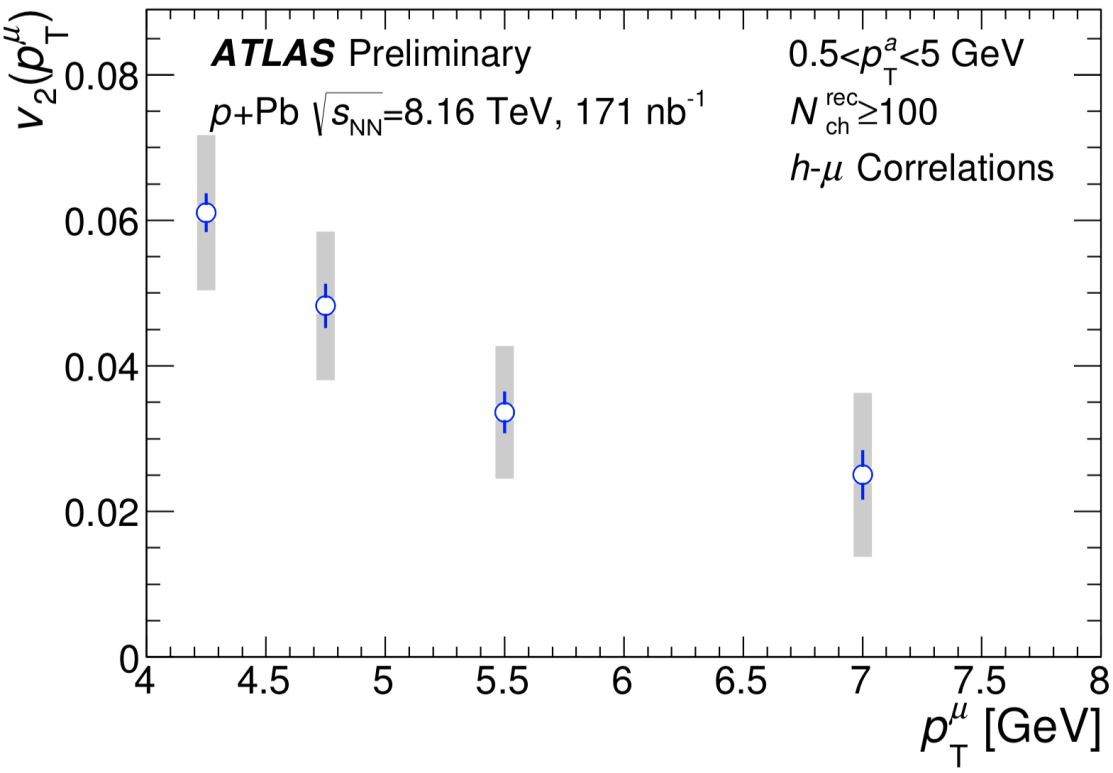

Figure 7.19: p_{T} dependence of muon v_2 over the range $4 < p_{\mathrm{T}} < 8$ GeV is shown in the figure.

p_{T} than charged tracks, which results in a significant dijet contribution. Another reason is probably that the production of muons comes from harder processes than that for charged hadrons. However, when $|\Delta\eta|$ increases, contribution from dijet component becomes negligible at large pseudorapidity separation.

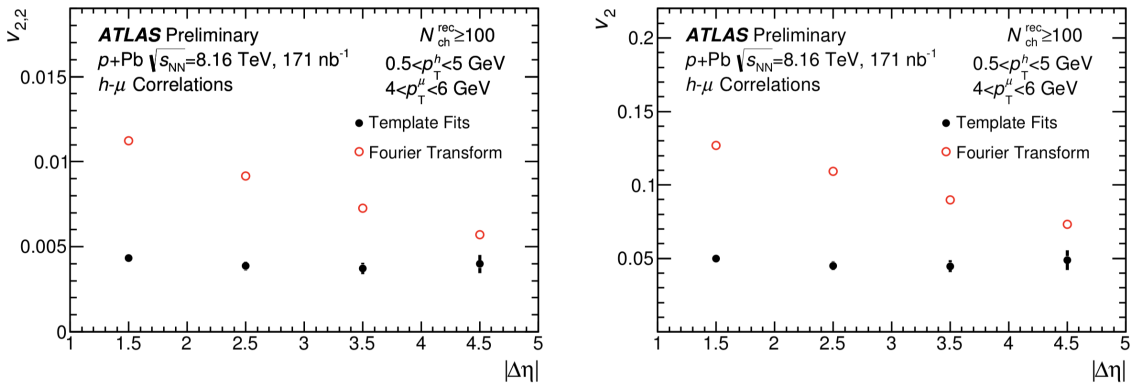

Figure 7.20: This figure shows the dependence of muon v_2 on $|\Delta\eta|$. Results from both template fits (black dots) and Fourier transform (red circle) are shown. The dependence on $|\Delta\eta|$ is weak for template fitting method but strong for Fourier transform.

Chapter 8

Results of XeXe events at $\sqrt{s_{\mathrm{NN}}} = 5.44$ TeV

8.1 Two-particle correlation measurement

2D two-particle correlation functions for XeXe events at 5.44 TeV are illustrated in Figure 8.1. Both particles are selected in the p_{T} range (2,3) GeV. Each panel corresponds to a different centrality bin. The most central collision is shown in the top left panel with centrality (0-5)% and the most peripheral collision is shown in the bottom right panel with centrality (75-80)%. The plots in the last row have large statistical fluctuations due to the insufficient statistics.

The corresponding 1D 2PCs are shown in Figure 8.2. An identical range of y-axis is used in these plots for an easy comparison for correlation functions at different centralities. The red curves indicate the Fourier fits up to the 6th order harmonics. The shape of the away-side enhancement is clearly changing from a broad distribution in central events to a peaking structure in peripheral events. The near-side peak in the long-range correlation is the smallest in the most central collisions and increases towards the mid-central region. It reaches its maximum around 50% centrality and

then decreases with the events going peripheral. This almost follows the same trend that $v_{2,2}$ shows in the following discussion and is different from the features observed in the previous pp and pPb systems where long-range correlation always increases with multiplicity monotonically. In order to give a better understanding of the change in the shape of the correlation function, modulations of individual terms in the Fourier decomposition are shown in Figure 8.3. The black dotted line represents $v_{1,1}$ contribution while the red, blue, pink, orange and green curves indicate $v_{2,2}$, $v_{3,3}$, $v_{4,4}$, $v_{5,5}$ and $v_{6,6}$ harmonics respectively. In the top left panel $v_{2,2}$ and $v_{3,3}$ are comparable. All harmonics ($n \geq 2$) exhibit large modulations while the influence from $v_{1,1}$ is negligible. This suggests in central collisions dijet contribution can be neglected and harmonics from direct Fourier transform reflect the genuine long-range correlation. In the mid-central region near-side and away-side peaks have similar sizes and $v_{2,2}$ becomes dominant in the correlation function. In peripheral events there is s significant contribution from dijet component resulting in a large negative $v_{1,1}$ term. This is especially true at higher p_{T}. All harmonics ($n \geq 2$) except $v_{2,2}$ are small. Harmonics obtained from direct Fourier transform are biased. The dijet component must be removed. Thus template fitting procedure should be implemented.

8.2 Template fit analysis

8.2.1 Results from template fits

In this section template fitting method will be used to extract the long-range correlation $v_{n,n}$ from two particle correlation functions. Template fitting results will be compared to Fourier $v_{n,n}$ to see how much jet contribution can influence the results. Both XeXe and pp peripheral reference are used in this section. The default XeXe reference is 80-90%. The default pp reference is $0 < \mathrm{N}_{\mathrm{ch}}^{\mathrm{rec}} < 20$ using the 5.02 TeV pp data. The default p_{T} interval in this section is $0.5 < p_{\mathrm{T}}^{\mathrm{a,b}} < 5$ GeV.

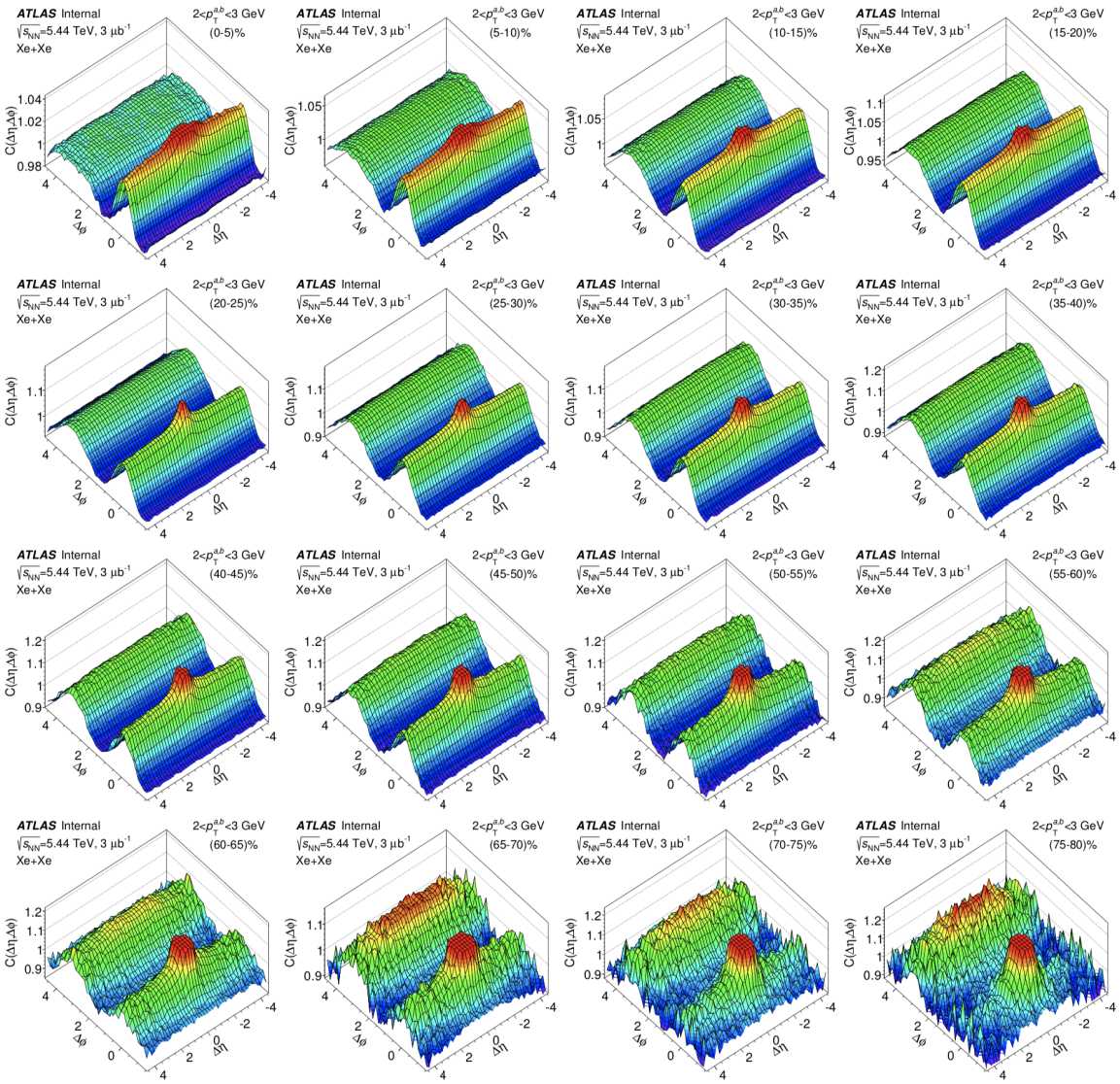

Figure 8.1: 2D two-particle correlation functions for XeXe events at 5.44 TeV. Each panel corresponds to a different centrality bin. Both particles are chosen from the p_{T} interval (2,3) GeV. The short-range jet correlation at $\Delta\phi = \Delta\eta = 0$ has been truncated.

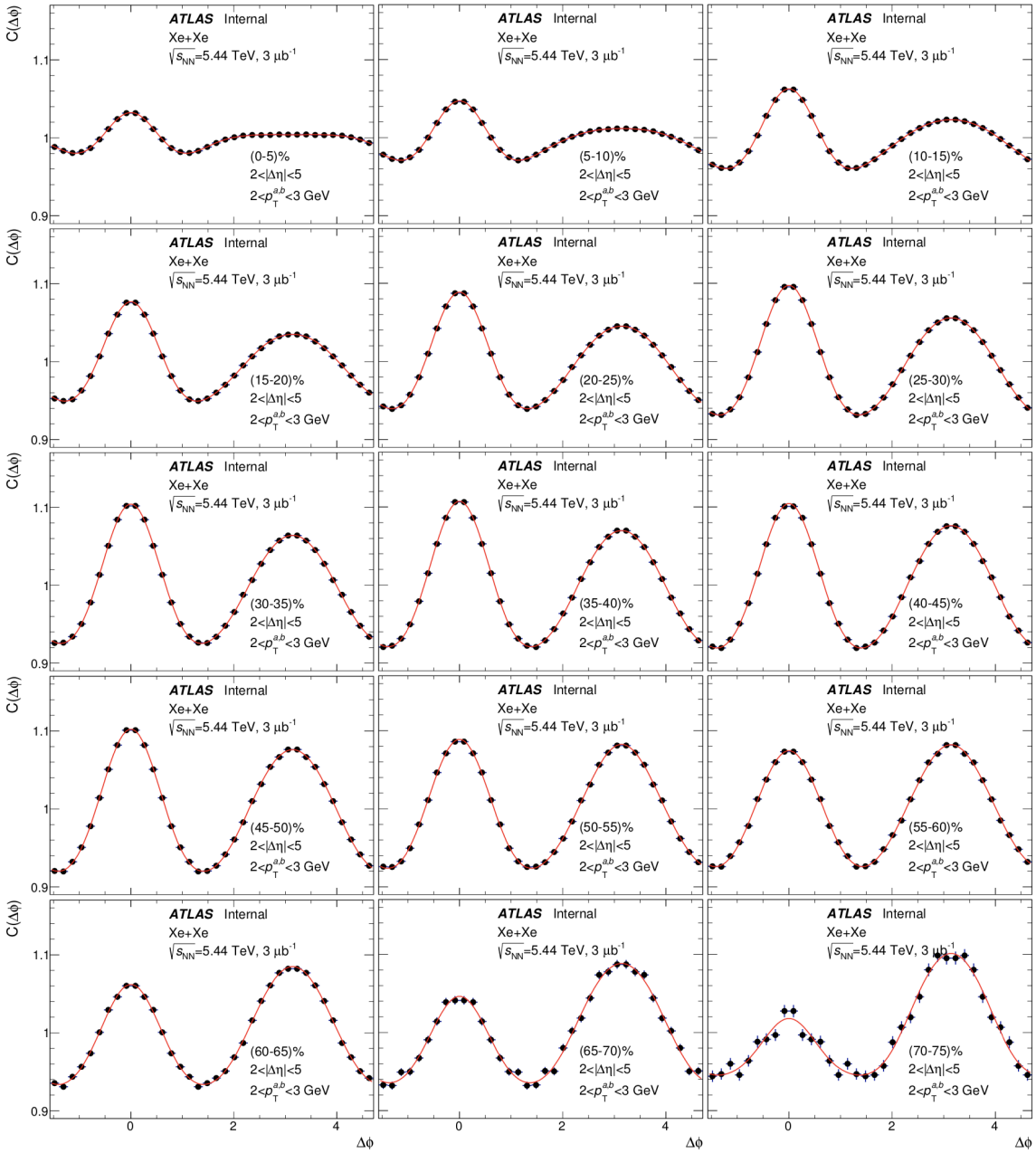

Figure 8.2: 1D two-particle correlation functions for XeXe events at 5.44 TeV. A pseudorapidity cut $|\Delta\eta| > 2$ is implemented. Each panel corresponds to a different centrality bin. Both particles are chosen from the p_{T} interval (2,3) GeV. The red curve represents the Fourier fits up to the 6th order harmonics.

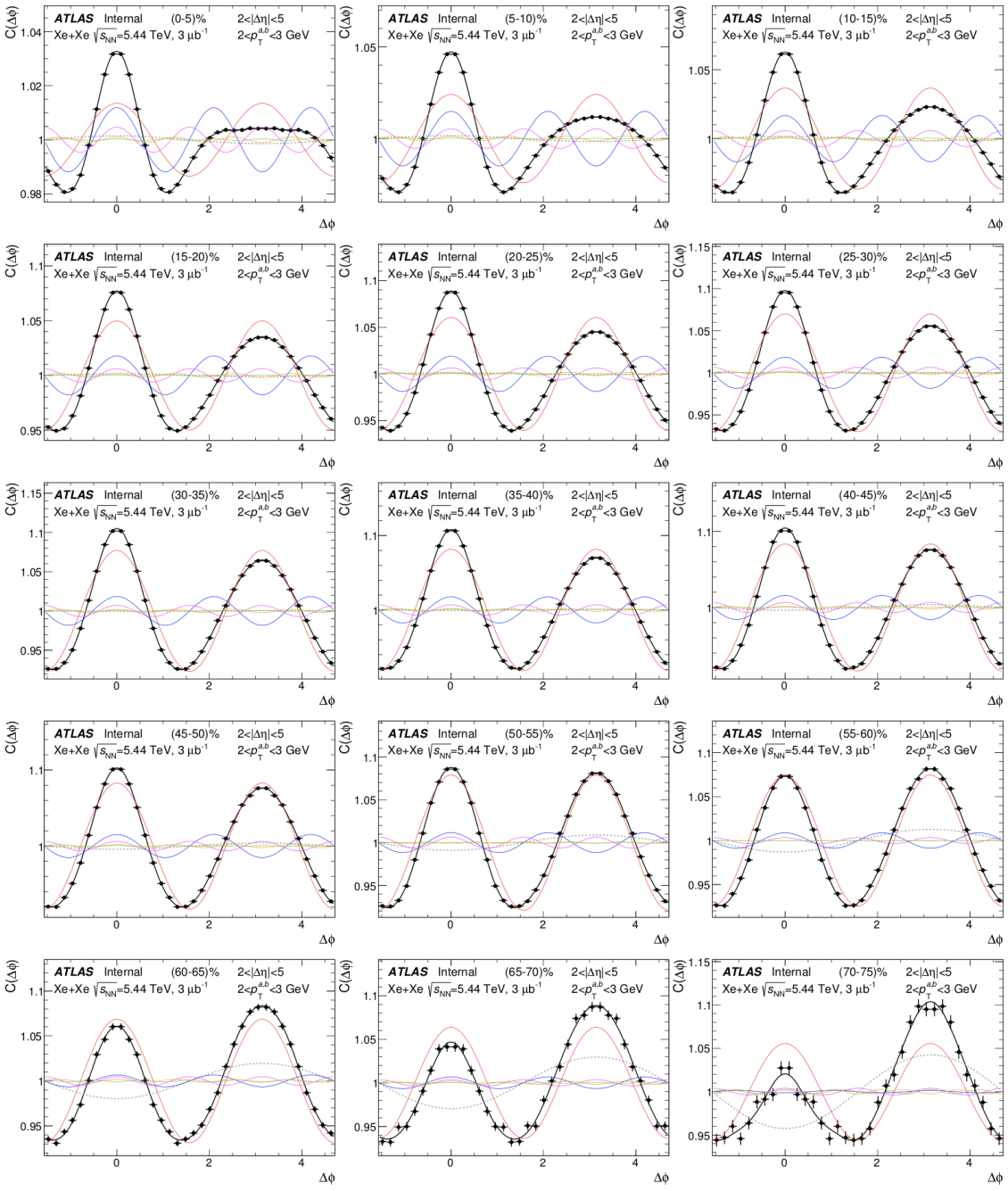

Figure 8.3: 1D two-particle correlation functions for XeXe events at 5.44 TeV. A pseudorapidity cut $|\Delta\eta| > 2$ is implemented. Individual contribution from each Fourier term is demonstrated in the figure with different colors.

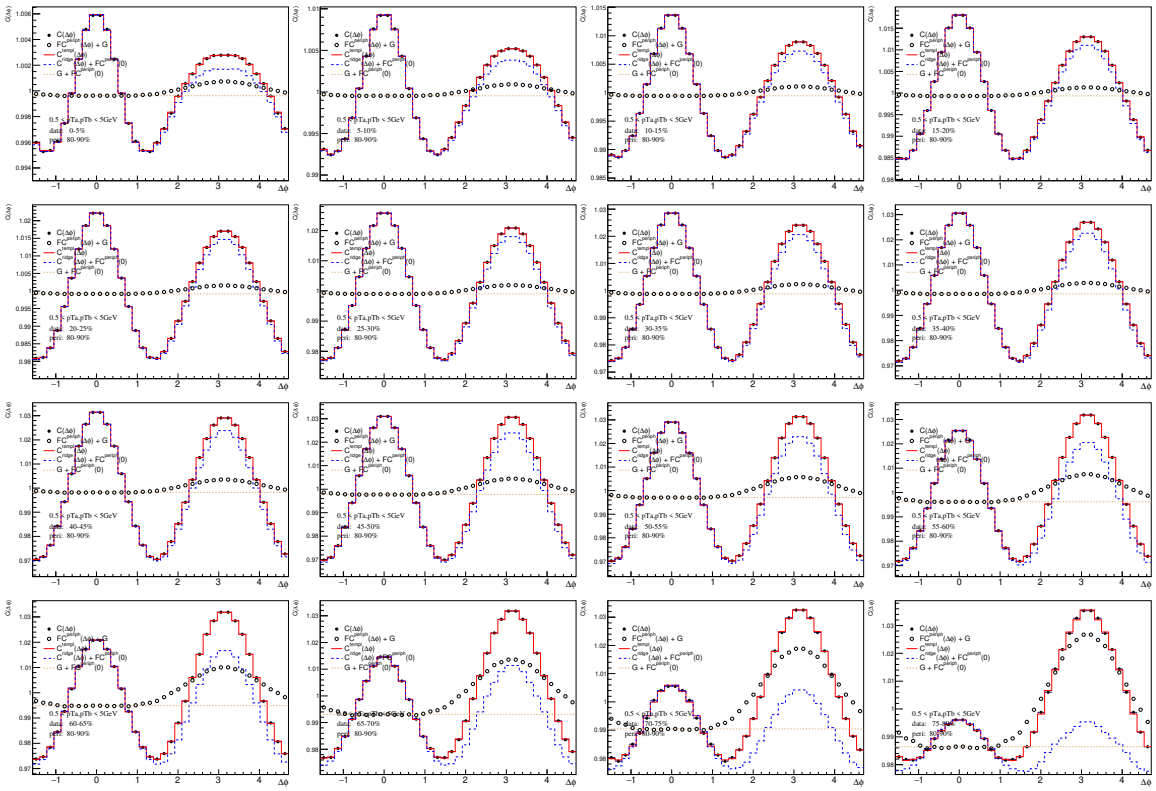

Figure 8.4: Template fits of XeXe events at $\sqrt{s_{\rm NN}} = 5.44$ TeV. Each panel is a different centrality bin. The plots are for $0.5 < p_{\rm T}^{\rm a,b} < 5$ GeV. XeXe events within the centrality range 80-90% are used as the reference.

Template fitting plots for each centrality bin using XeXe and *pp* references are shown in Figure 8.4 and Figure 8.5 respectively. Different panels correspond to different centrality bins. The away-side jet contribution becomes dominant as the centrality goes from 0 to 80%. Figure 8.6 shows the single particle harmonics obtained from different methods. The left panel uses XeXe events as the peripheral reference. The right panel uses *pp* as the reference. Results from three different methods, (improved) template fits, template fits with ZYAM procedure and Fourier decomposition are shown in the figures. When *pp* reference is used, differences among the three methods become smaller, suggesting *pp* is a better reference than XeXe. This makes sense since the long-range correlation observed in *pp* events is much smaller than XeXe. Thus *pp* can give a better estimate of the dijet contribution. Since *pp* reference gives better

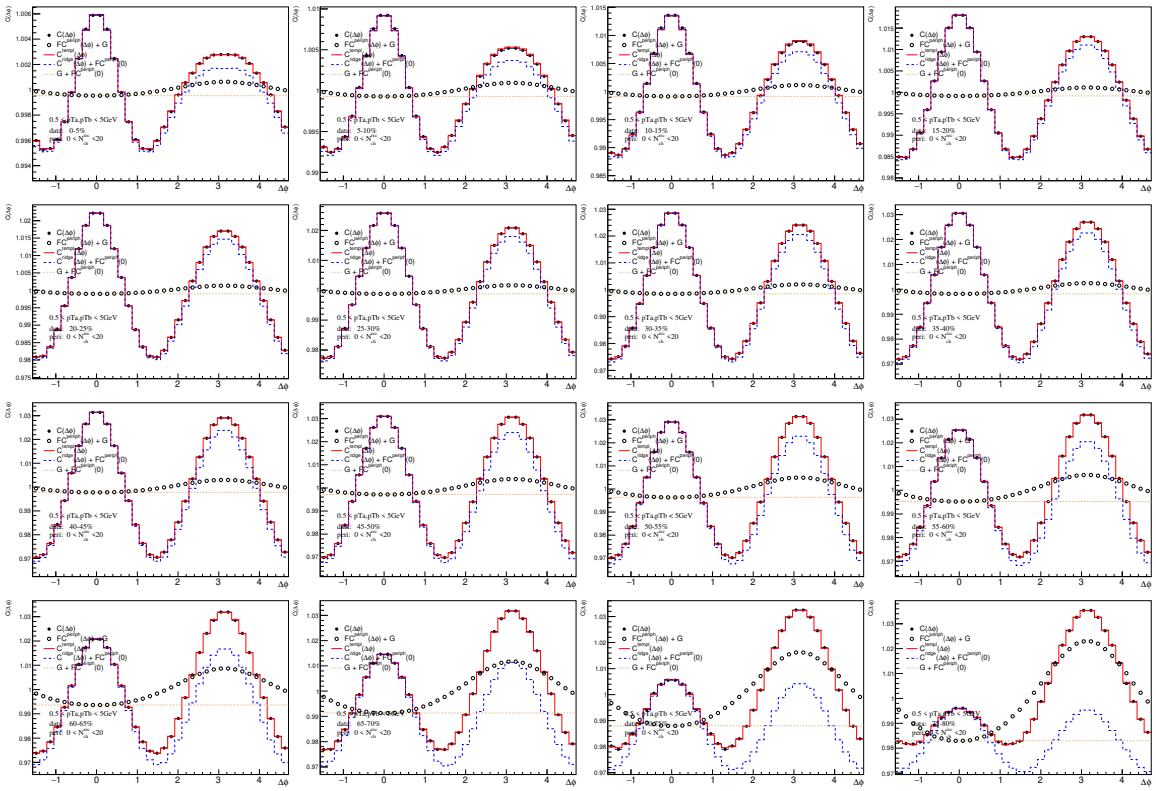

Figure 8.5: Template fits of XeXe events at $\sqrt{s_{\rm NN}} = 5.44$ TeV. Each panel is a different centrality bin. The plots are for $0.5 < p_{\rm T}^{\rm a,b} < 5$ GeV. *pp* events within the multiplicity range $0 < {\rm N}_{\rm ch}^{\rm rec} < 20$ are used as the reference.

results, we will always use *pp* events as the peripheral reference in the following analysis of this section.

In order to check whether the results from the fits are sensitive to the *pp* reference, we compare the centrality dependences given by three different *pp* references ($0 < {\rm N}_{\rm ch}^{\rm rec} < 10$, $0 < {\rm N}_{\rm ch}^{\rm rec} < 20$ and $0 < {\rm N}_{\rm ch}^{\rm rec} < 30$). The results are shown in Figure 8.7. Figure 8.8 and Figure 8.9 show the corresponding ratios of no-ZYAM and ZYAM-based results. It can be seen that when a more peripheral reference is used, the resulted v_2 becomes bigger in ZYAM-based template fits and smaller in improved template fits. However, v_3 always becomes smaller if a more peripheral reference is used.

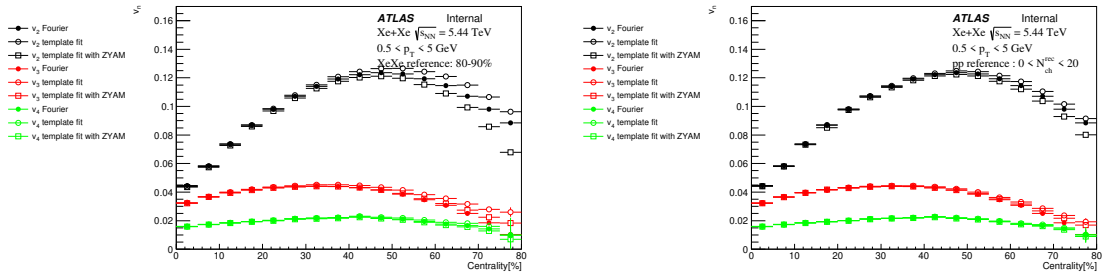

Figure 8.6: Comparison of template-fit v_n and Fourier-v_n of XeXe events at $\sqrt{s_{\mathrm{NN}}}$ = 5.44 TeV. The plots are for $0.5 < p_{\mathrm{T}}^{\mathrm{a,b}} < 5$ GeV. In the left panel, XeXe events within the centrality range 80-90% are used as the reference. In the right panel, pp events within the multiplicity range $0 < \mathrm{N}_{\mathrm{ch}}^{\mathrm{rec}} < 20$ are used as the reference.

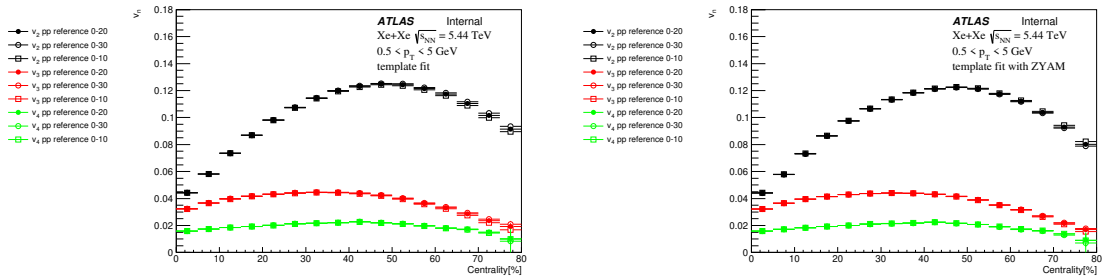

Figure 8.7: Camparisons of v_n in XeXe events at $\sqrt{s_{\mathrm{NN}}}$ = 5.44 TeV using different multiplicity intervals as the pp reference. The results are plotted as a function of centrality. The left panel is the result without the ZYAM procedure. The right panel is the ZYAM-based result.

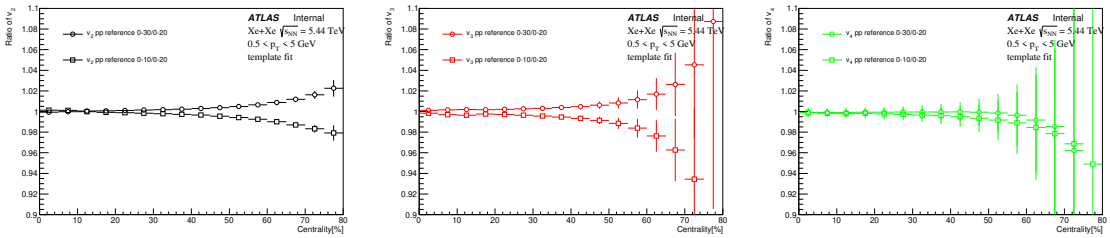

Figure 8.8: Ratios of v_n from improved template fits using different pp references in XeXe events at $\sqrt{s_{\mathrm{NN}}}$ = 5.44 TeV . The plots are for $0.5 < p_{\mathrm{T}}^{\mathrm{a,b}} < 5$ GeV. The multiplicity interval in the denominator is $0 < \mathrm{N}_{\mathrm{ch}}^{\mathrm{rec}} < 20$.

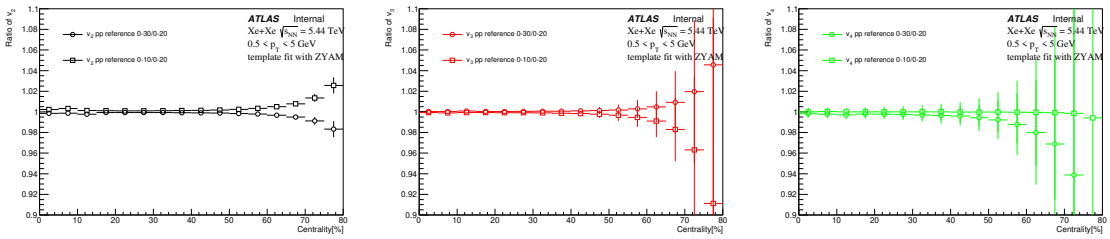

Figure 8.9: Ratios of ZYAM-based v_n from fits using different pp references in XeXe events at $\sqrt{s_{\rm NN}} = 5.44$ TeV . The plots are for $0.5 < p_{\rm T}^{\rm a,b} < 5$ GeV. The multiplicity interval in the denominator is $0 < {\rm N}_{\rm ch}^{\rm rec} < 20$.

8.2.2 Comparison with v_n from different methods

Figure 8.10 is a collection of template fitting plots in $p_{\rm T}$ interval $2 < p_{\rm T}^{\rm a,b} < 5$ GeV. As we can see in this $p_{\rm T}$ interval the away-side jet component determined by the fits in the most central bins becomes negative. This suggests the template fitting method we used before does not work well in the most central region since negative dijet contribution is not physical. Since dijet contribution is pretty small compared to the dominant flow in central XeXe events, template fits cannot give a good estimate of the away-side jet component. In this analysis, we will fix the scale factor of the peripheral reference (which is a fitting parameter of the template fitting method) to 0 once it becomes negative to avoid negative dijet component. This means we will use Fourier $v_{n,n}$ instead of template-fit $v_{n,n}$ in these cases. This fitting convention will always be used in the following analysis of this section.

Figure 8.11 shows the comparison of the old template fitting plots and the fitting plots using the convention mentioned above. In the upper plots, the away-side jet component becomes negative when centrality becomes less than 30%. In the bottom plots, the away-side jet component is above or equal to 0 to avoid negative dijet contribution. We will use the fits in the bottom to replace the upper ones in the following analysis.

Figure 8.12 shows single particle harmonics v_n obtained from different methods using the fitting convention discussed above. The left panel is the same as the right

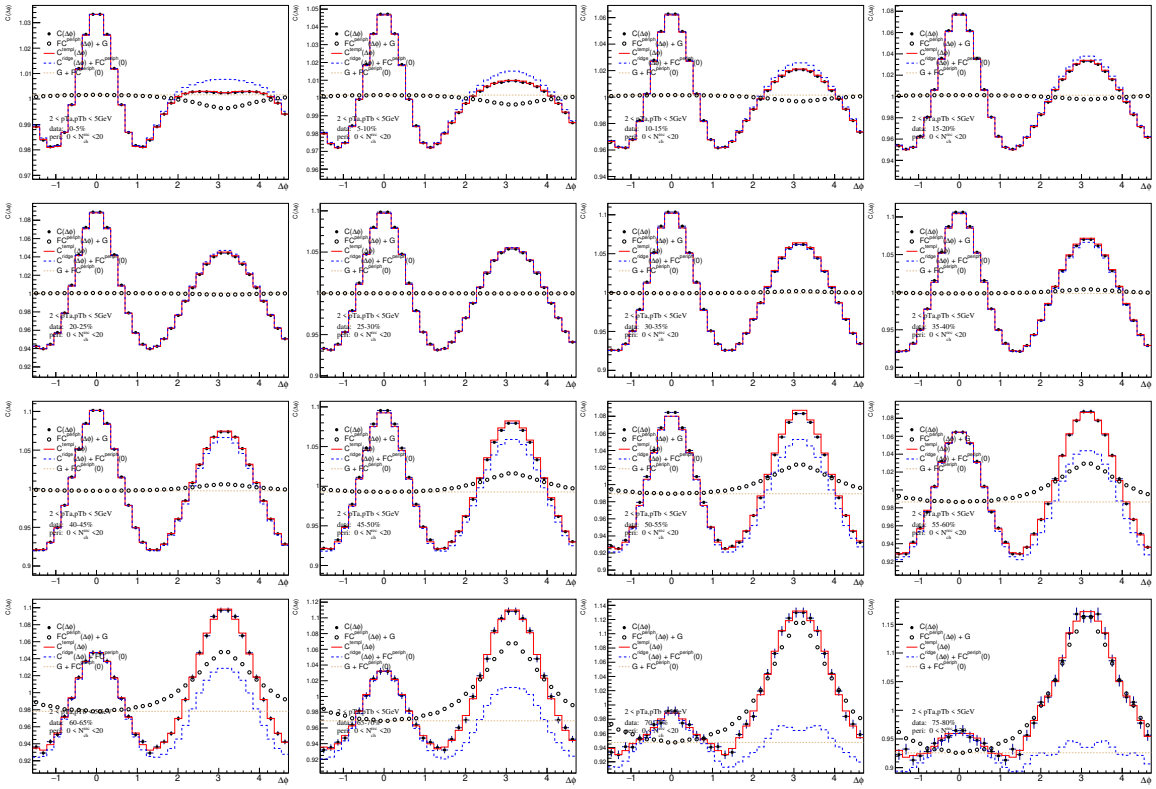

Figure 8.10: Template fits of XeXe events at $\sqrt{s_{\rm NN}} = 5.44$ TeV. Each panel is a different centrality bin. The plots are for $2 < p_{\rm T}^{\rm a,b} < 5$ GeV. pp events within the multiplicity range $0 < {\rm N}_{\rm ch}^{\rm rec} < 20$ are used as the reference.

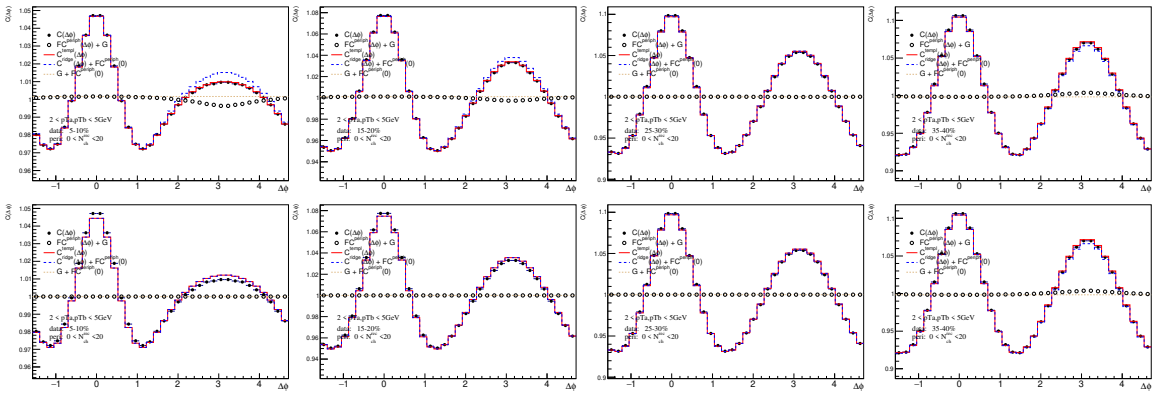

Figure 8.11: The upper plots are old template fits. The bottom ones are fits with scale factor fixed to 0 when the fits give negative scale factors. The plots are for $0.5 < p_{\rm T}^{\rm a,b} < 5$ GeV. pp events within the multiplicity range $0 < {\rm N}_{\rm ch}^{\rm rec} < 20$ are used as the reference.

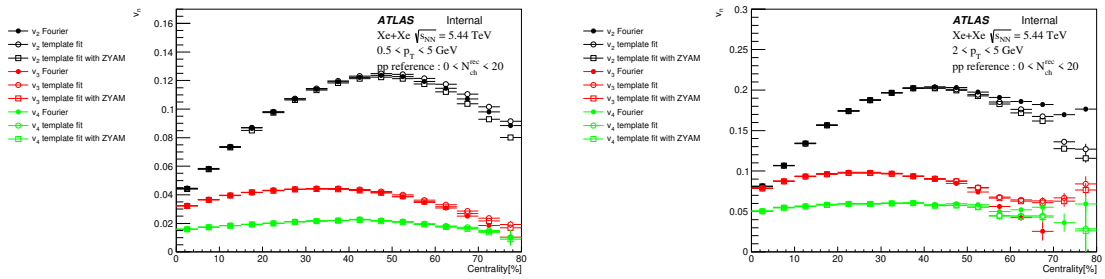

Figure 8.12: Camparisons of v_n in XeXe events at $\sqrt{s_{\mathrm{NN}}} = 5.44$ TeV obtained from different methods. The results are plotted as a function of centrality. The left panel is for $0.5 < p_{\mathrm{T}}^{\mathrm{a,b}} < 5$ GeV. The right panel is for $2 < p_{\mathrm{T}}^{\mathrm{a,b}} < 5$ GeV. For template fitting results, pp events within the multiplicity range $0 < \mathrm{N}_{\mathrm{ch}}^{\mathrm{rec}} < 20$ are used as the reference.

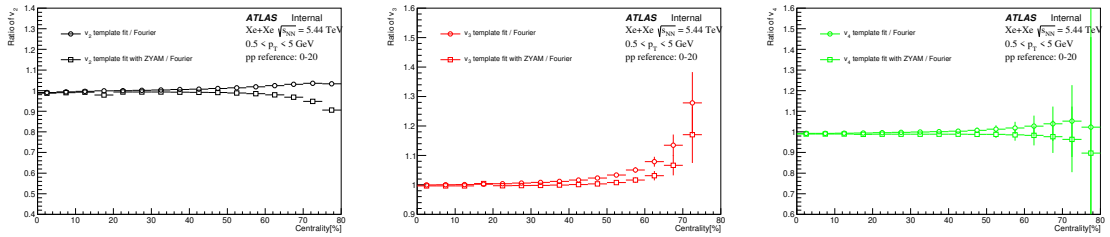

Figure 8.13: Ratios of v_n from template fits to Fourier v_n in XeXe events at $\sqrt{s_{\mathrm{NN}}}$ = 5.44 TeV. The plots are for $0.5 < p_{\mathrm{T}}^{\mathrm{a,b}} < 5$ GeV. pp events within the multiplicity range $0 < \mathrm{N}_{\mathrm{ch}}^{\mathrm{rec}} < 20$ are used as the reference.

panel in Figure 8.6. The right panel is for a different p_{T} interval $2 < p_{\mathrm{T}}^{\mathrm{a,b}} < 5$ GeV. Generally the p_{T} interval $2 < p_{\mathrm{T}}^{\mathrm{a,b}} < 5$ GeV gives larger v_n values than interval $0.5 < p_{\mathrm{T}}^{\mathrm{a,b}} < 5$ GeV. Figure 8.13 and Figure 8.14 show the ratios of template-fit v_n to Fourier v_n. Ratios of v_2, v_3 and v_4 are shown in three different panels. Since part of the pedestal in the peripheral reference is removed through ZYAM procedure, template fitting without ZYAM gives bigger v_n values than ZYAM-based fits. Both template fits with and without ZYAM give bigger v_3 compared to Fourier decomposition. This is expected because dijet contribution always gives a negative Fourier v_3. In $0.5 < p_{\mathrm{T}}^{\mathrm{a,b}} < 5$ GeV, fits with no ZYAM give the biggest v_2 and v_4 values among the three methods while ZYAM-based fits give the smallest v_2 and v_4. In $2 < p_{\mathrm{T}}^{\mathrm{a,b}} < 5$ GeV, v_2 and v_4 from Frourier decomposition becomes the biggest in these three methods.

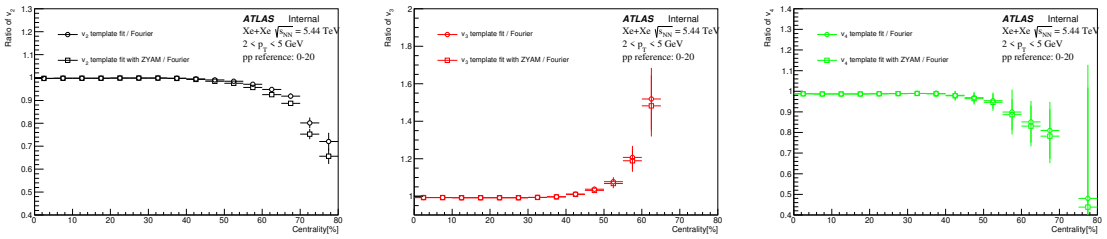

Figure 8.14: Ratios of v_n from template fits to Fourier v_n in XeXe events at $\sqrt{s_{\rm NN}}$ = 5.44 TeV . The plots are for $2 < p_{\rm T}^{\rm a,b} < 5$ GeV. pp events within the multiplicity range $0 < {\rm N}_{\rm ch}^{\rm rec} < 20$ are used as the reference.

8.2.3 Comparison with PbPb events at 5.02 TeV

Figure 8.15 shows template fitting plots for PbPb events at $\sqrt{s_{\rm NN}}$ = 5.02 TeV. Its centrality dependence is shown in Figure 8.16. Figure 8.17 shows the ratios of template-fit v_n to Fourier v_n. The comparison of XeXe and PbPb v_n is shown in Figure 8.18. The same pp reference is used for both XeXe and PbPb events here. The left and right panels are for fits without and with ZYAM procedure respectively. Ratios of XeXe to PbPb are plotted in Figure 8.19. Ratios for v_2 and v_4 are almost flat in the two panels while ratios for v_3 decrease with centrality slightly.

8.2.4 $p_{\rm T}$ dependence

A comparison of template fits for different $p_{\rm T}$ intervals is shown in Figure 8.20. $p_{\rm T}^{\rm a}$ is fixed in (0.5,5) GeV while $p_{\rm T}^{\rm b}$ changes from 0.5 GeV to 6 GeV. It can be seen that the away-side dijet contribution increases with the value of $p_{\rm T}^{\rm b}$. Figure 8.21 demonstrates the centrality dependence of the Fourier harmonics in different $p_{\rm T}^{\rm a,b}$ bins. From left to right $p_{\rm T}$ bins used are the same as the $p_{\rm T}^{\rm b}$ interval used in the above template fits. In the top panels the black, red and green legends represent v_2, v_3 and v_4 respectively. Different legend styles indicate different methods used to extract these harmonics. It is easy to see that all methods give the largest v_2 in the intermediate $p_{\rm T}$ range and smaller v_2 at low and high $p_{\rm T}$ values. In central collisions v_2 is comparable to v_3 while

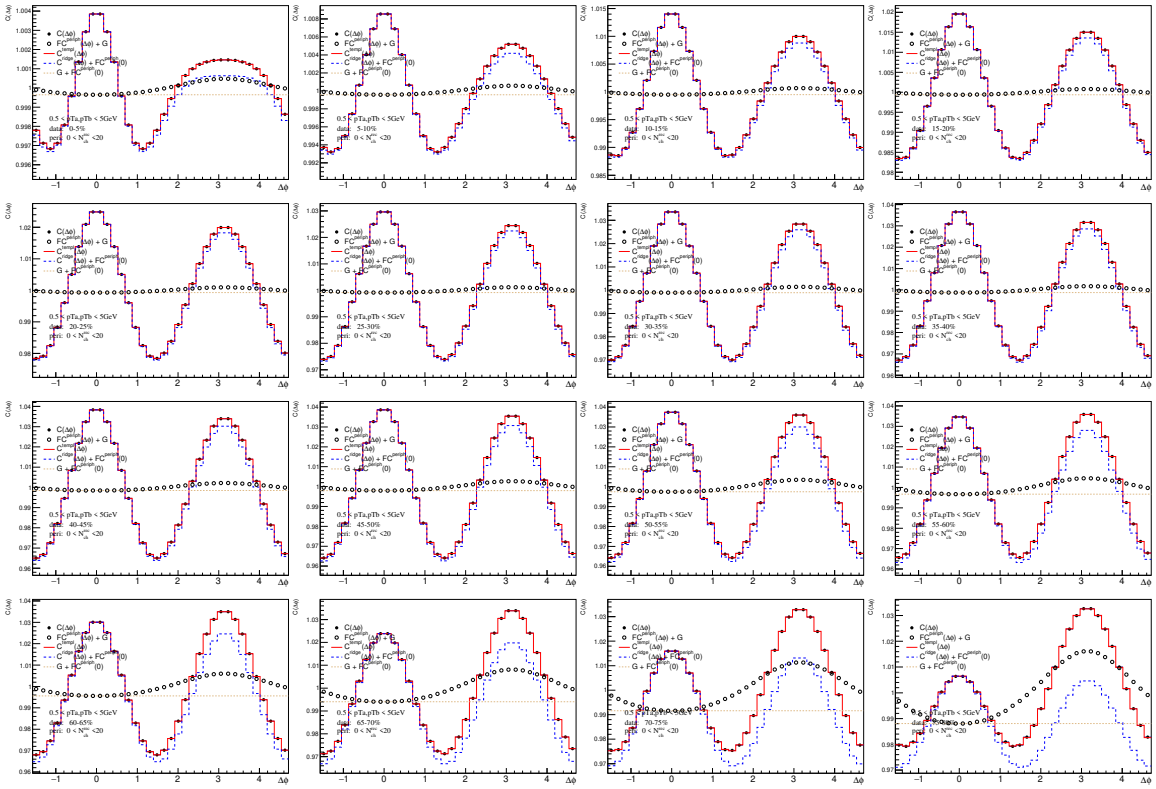

Figure 8.15: Template fits of PbPb events at $\sqrt{s_{\rm NN}} = 5.02$ TeV. Each panel is a different centrality bin. The plots are for $0.5 < p_{\rm T}^{\rm a,b} < 5$ GeV. *pp* events within the multiplicity range $0 < {\rm N}_{\rm ch}^{\rm rec} < 20$ are used as the reference.

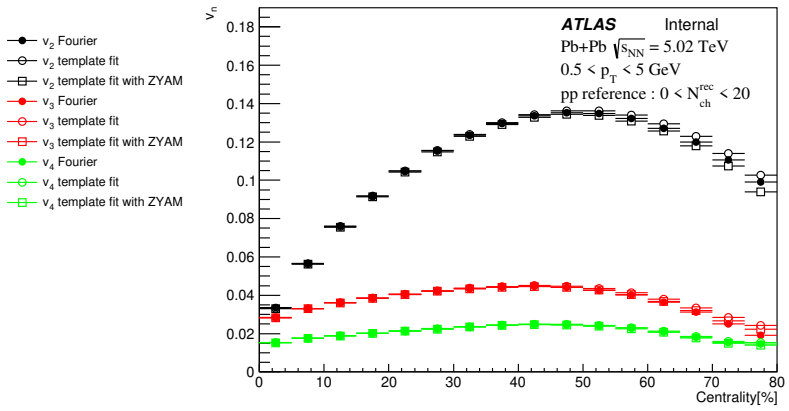

Figure 8.16: Camparisons of v_n in PbPb events at $\sqrt{s_{\rm NN}} = 5.02$ TeV obtained from different methods. The results are plotted as a function of centrality. The plots are for $0.5 < p_{\rm T}^{\rm a,b} < 5$ GeV. For template fitting results, pp events within the multiplicity range $0 < {\rm N}_{\rm ch}^{\rm rec} < 20$ are used as the reference.

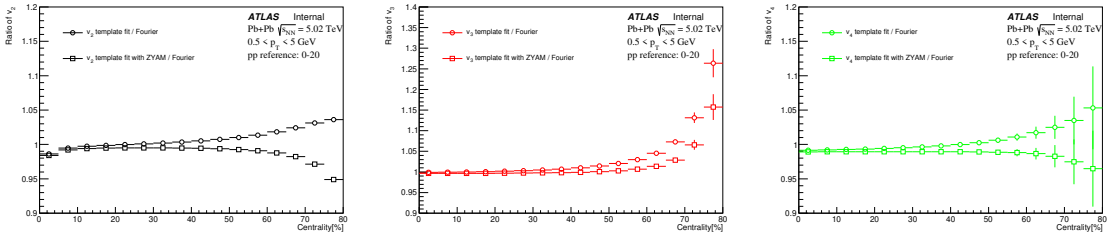

Figure 8.17: Ratios of v_n from template fits to Fourier v_n in PbPb events at $\sqrt{s_{\mathrm{NN}}}$ = 5.02 TeV. The plots are for $0.5 < p_{\mathrm{T}}^{\mathrm{a,b}} < 5$ GeV. *pp* events within the multiplicity range $0 < \mathrm{N}_{\mathrm{ch}}^{\mathrm{rec}} < 20$ are used as the reference.

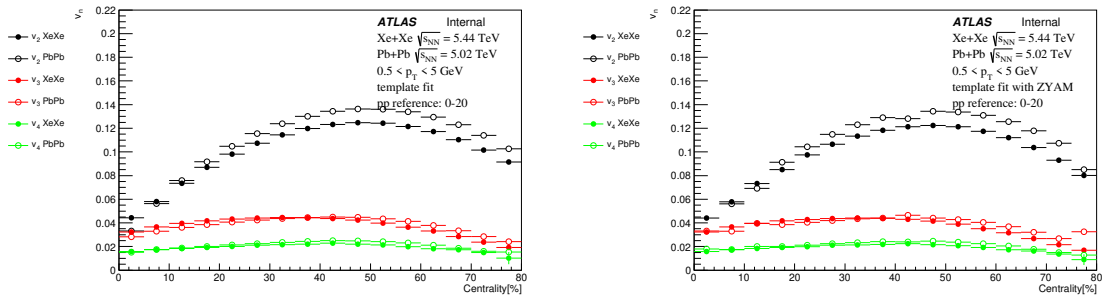

Figure 8.18: Comparisons of v_n between the present XeXe measurements and PbPb measurements at $\sqrt{s_{\mathrm{NN}}}$ = 5.02 TeV. The left panel shows template fitting results without ZYAM procedure. The right panel shows results with ZYAM procedure on the reference. The plots are for $0.5 < p_{\mathrm{T}}^{\mathrm{a,b}} < 5$ GeV. *pp* events within the multiplicity range $0 < \mathrm{N}_{\mathrm{ch}}^{\mathrm{rec}} < 20$ are used as the reference for template fits.

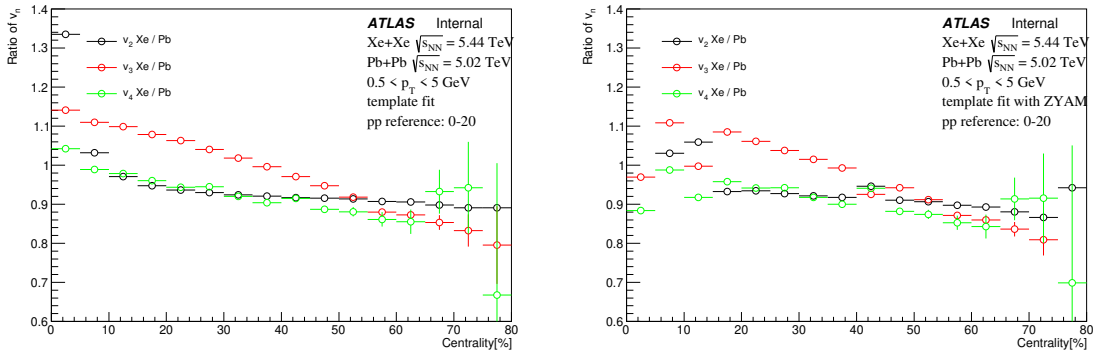

Figure 8.19: The corresponding ratios of v_n from XeXe measurements to PbPb measurements. The left panel shows the ratios from template fits without ZYAM procedure. The right panel shows the ratios from template fits with ZYAM procedure. The plots are for $0.5 < p_{\mathrm{T}}^{\mathrm{a,b}} < 5$ GeV. *pp* events within the multiplicity range $0 < \mathrm{N}_{\mathrm{ch}}^{\mathrm{rec}} < 20$ are used as the reference for template fits.

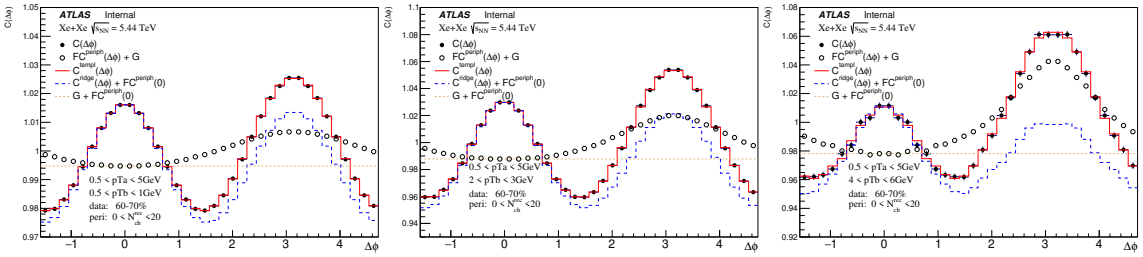

Figure 8.20: Template fits of correlation functions in XeXe events at 5.44 TeV. Events are chosen in the 60–70% centrality interval and (0.5,5) GeV $p_{\mathrm{T}}^{\mathrm{a}}$ interval. From left to right three panels correspond to different $p_{\mathrm{T}}^{\mathrm{b}}$ intervals (0.5,1) GeV, (2,3) GeV and (4,6) GeV respectively.

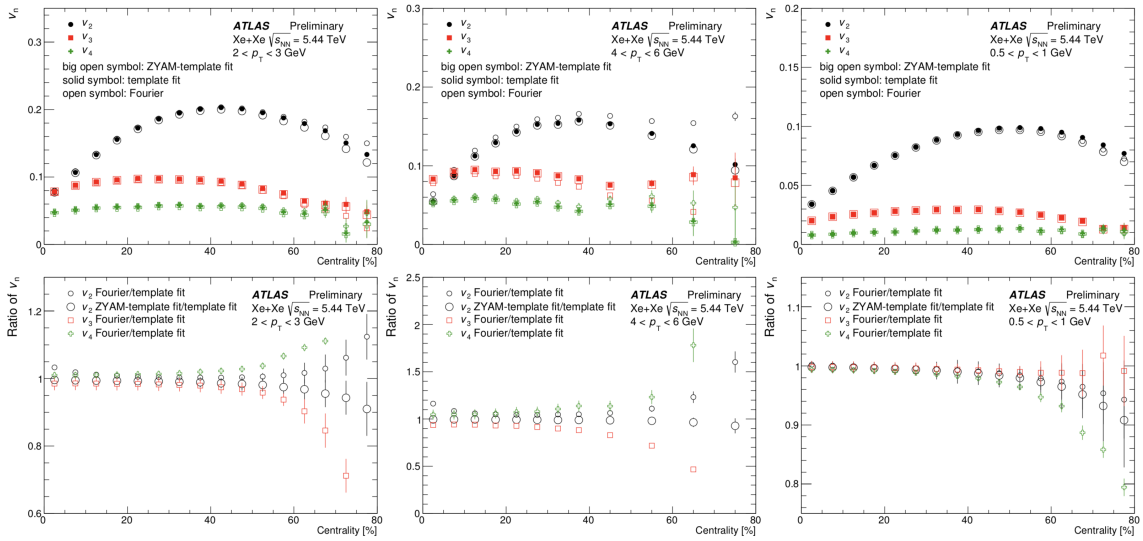

Figure 8.21: The top panels compare the centrality dependence from three different methods for v_2, v_3 and v_4. From left to right p_{T} ranges of (0.5,1) GeV, (2,3) GeV and (4,6) GeV are used respectively. The bottom panels show the ratios of v_n obtained from other methods to the template-fit v_n.

in mid-central and peripheral collisions v_2 is dominant over other harmonics. Three methods give almost identical values at the most central collisions. Their results begin to differ from each other when centrality goes above 50%. The corresponding ratios are shown in the bottom panels. Since ratios of v_n from ZYAM-based template fits to improved template fits should give identical results for all n by construction, only ratio of v_2 is plotted in the figure.

The p_{T} dependence of single particle harmonics in XeXe events is also studied

directly. Figure 8.22 is the comparison of p_{T} dependences among different methods. From top to bottom each row shows results in a different centrality interval with a width of 5%. Left panels are showing p_{T} dependence, while right ones are the corresponding ratios. Figure 8.23, 8.24, 8.25 are the comparisons of p_{T} dependence among different centrality intervals. v_2, v_3 and v_4 are shown from top to bottom panels in this figure. Each histogram represents a certain centrality bin. Different centrality bins are included in the left and right panels. The result shows that v_n increases rapidly until 2-4 GeV and then gradually decreases. By comparing histograms from different centrality bins it is easy to see that v_2 always has its maximum value in the mid-centrality region.

8.3 Systematic uncertainties from peripheral reference variations

Figure 8.26 to Figure 8.35 demonstrate the variations arising from different peripheral bins chosen. Particle a is fixed at (0.5,5) GeV p_{T} interval. Each figure corresponds to a different bin of $p_{\mathrm{T}}^{\mathrm{b}}$ from (0.5,0.6) GeV to (8.0,10.0) GeV. The left panels include centrality dependence of v_n from different peripheral references. The right panels show the ratios between different graphs in the corresponding left panel. The red line estimates the systematic uncertainties that result from the choice of the peripheral bin. For v_2 and v_3 centrality dependence of these uncertainties usually looks similar. The systematic error below 50% centrality is mostly a small constant around 1% or 2%. Above 50% the uncertainty increases dramatically. This means in peripheral events errors from the choice of the peripheral bin can be extremely large while in central and mid-central events these errors can be assumed to be a constant. For v_4 and v_5 the systematic errors have large values even in central and mid-central collisions.

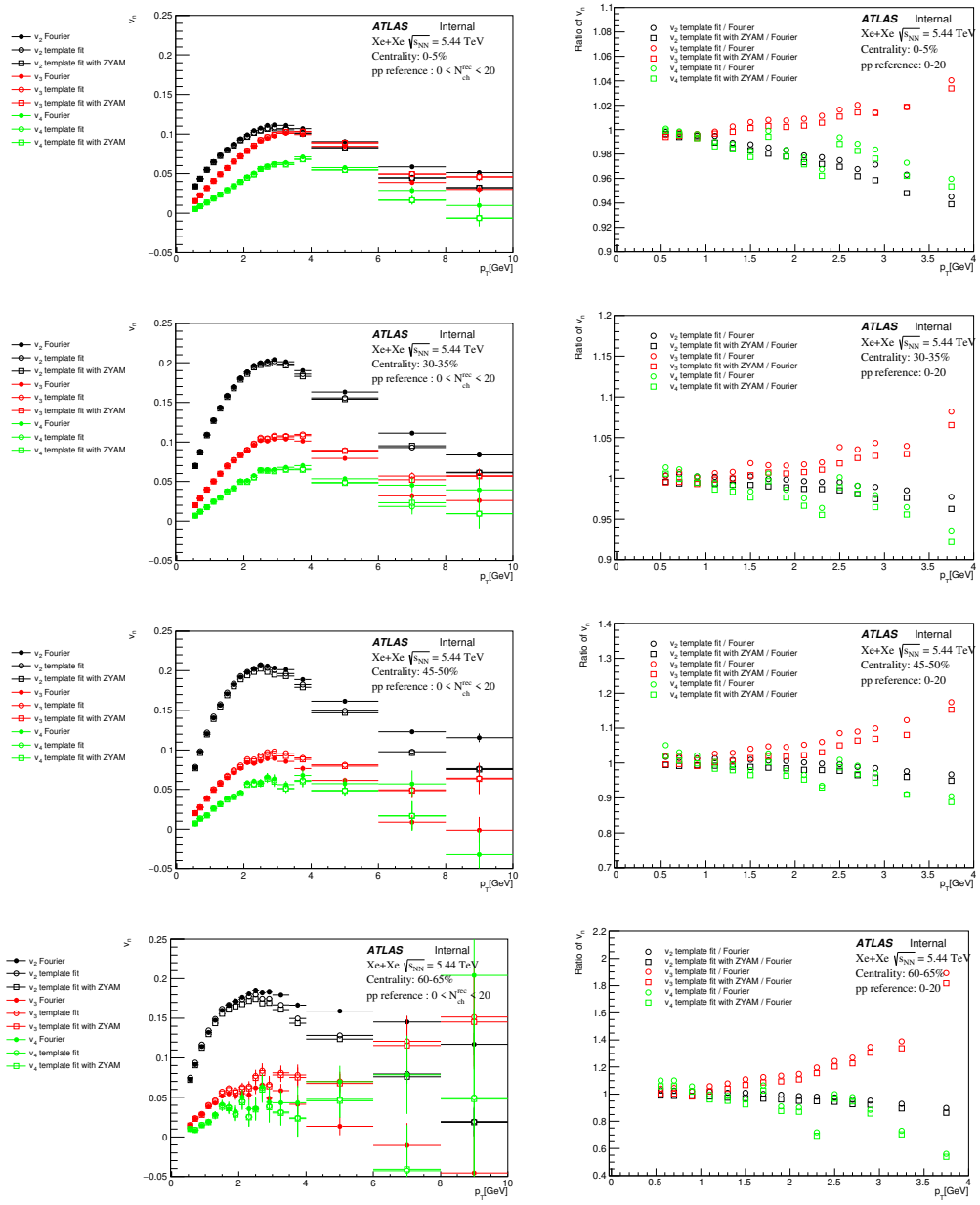

Figure 8.22: Camparisons of v_n in XeXe events at $\sqrt{s_{\rm NN}} = 5.44$ TeV obtained from different methods. The results are plotted as a function of $p_{\rm T}$. The left panels are the $p_{\rm T}$ dependence. The right panels are the ratios of template-fit v_n to Fourier v_n . To make the histograms clear, the error bars in the right panels are ignored. From top to bottom panels, different centrality intervals are used: 0-5%, 30-35%, 45-50% and 60-65%. For template fitting results, *pp* events within the multiplicity range $0 < {\rm N}_{\rm ch}^{\rm rec} < 20$ are used as the reference.

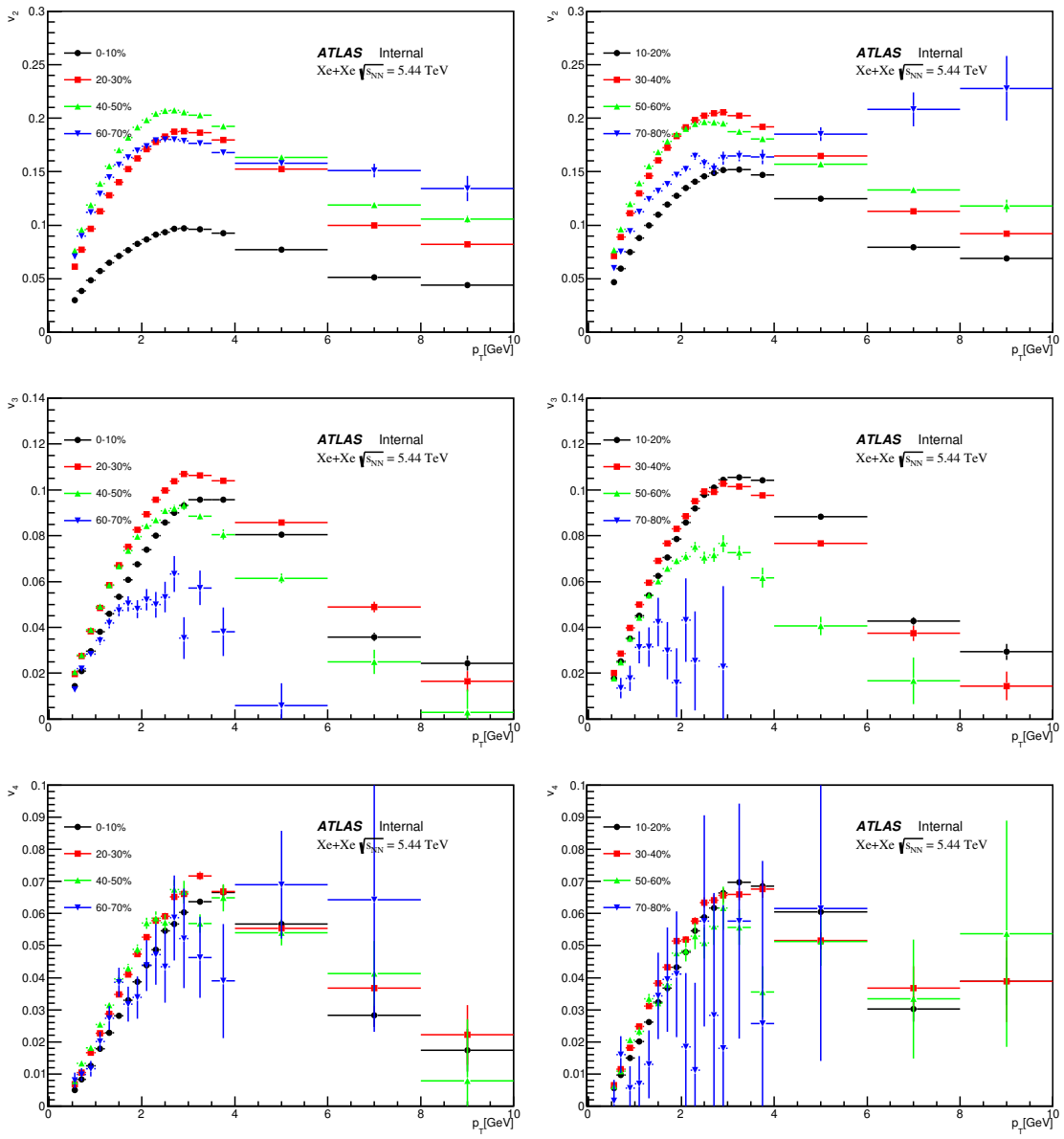

Figure 8.23: pT dependence of Fourier v_n from XeXe measurements at $\sqrt{s_{\mathrm{NN}}}$ = 5.44 TeV.

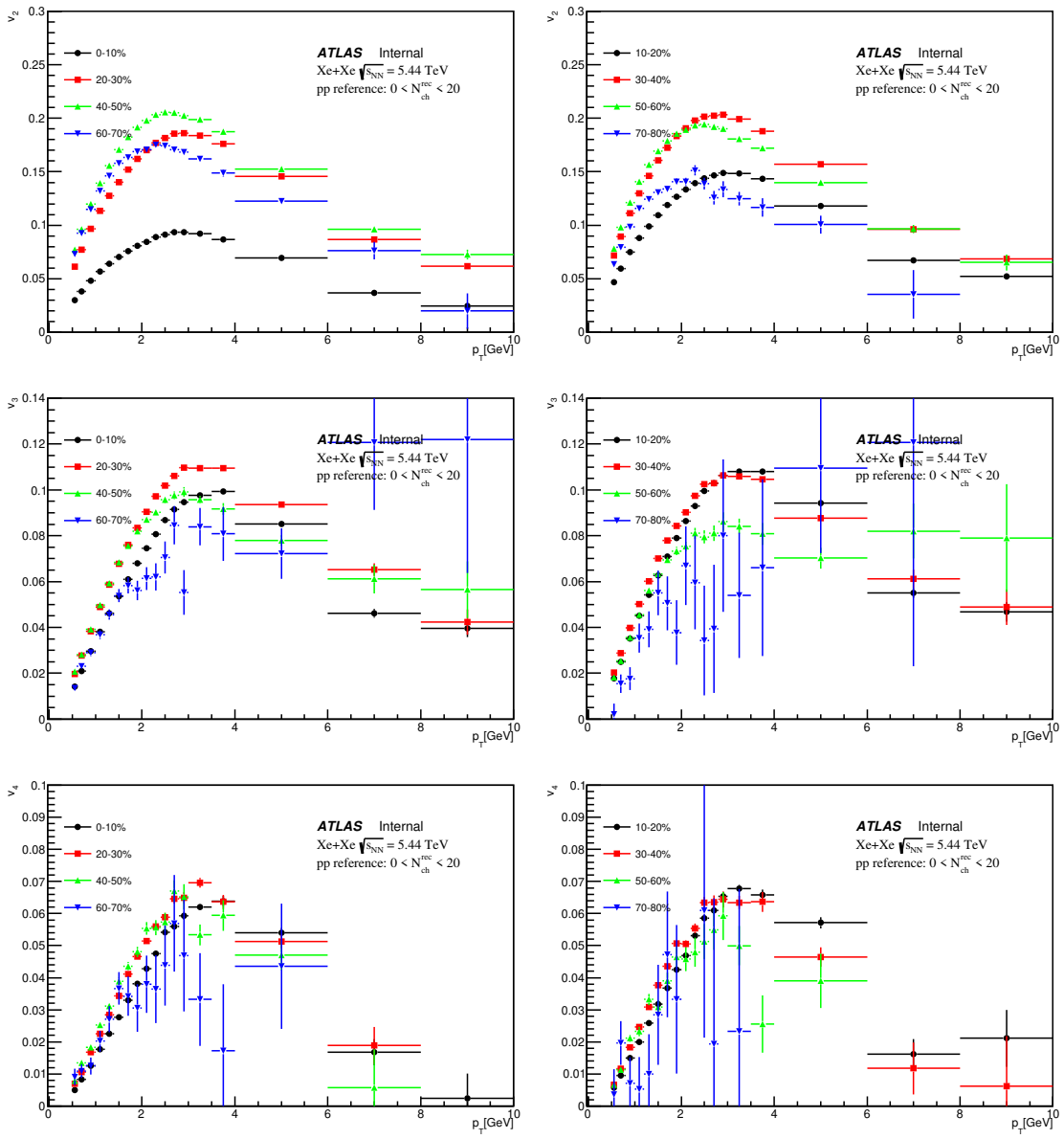

Figure 8.24: pT dependence of template-fit v_n from XeXe measurements at $\sqrt{s_{\mathrm{NN}}} = 5.44$ TeV.

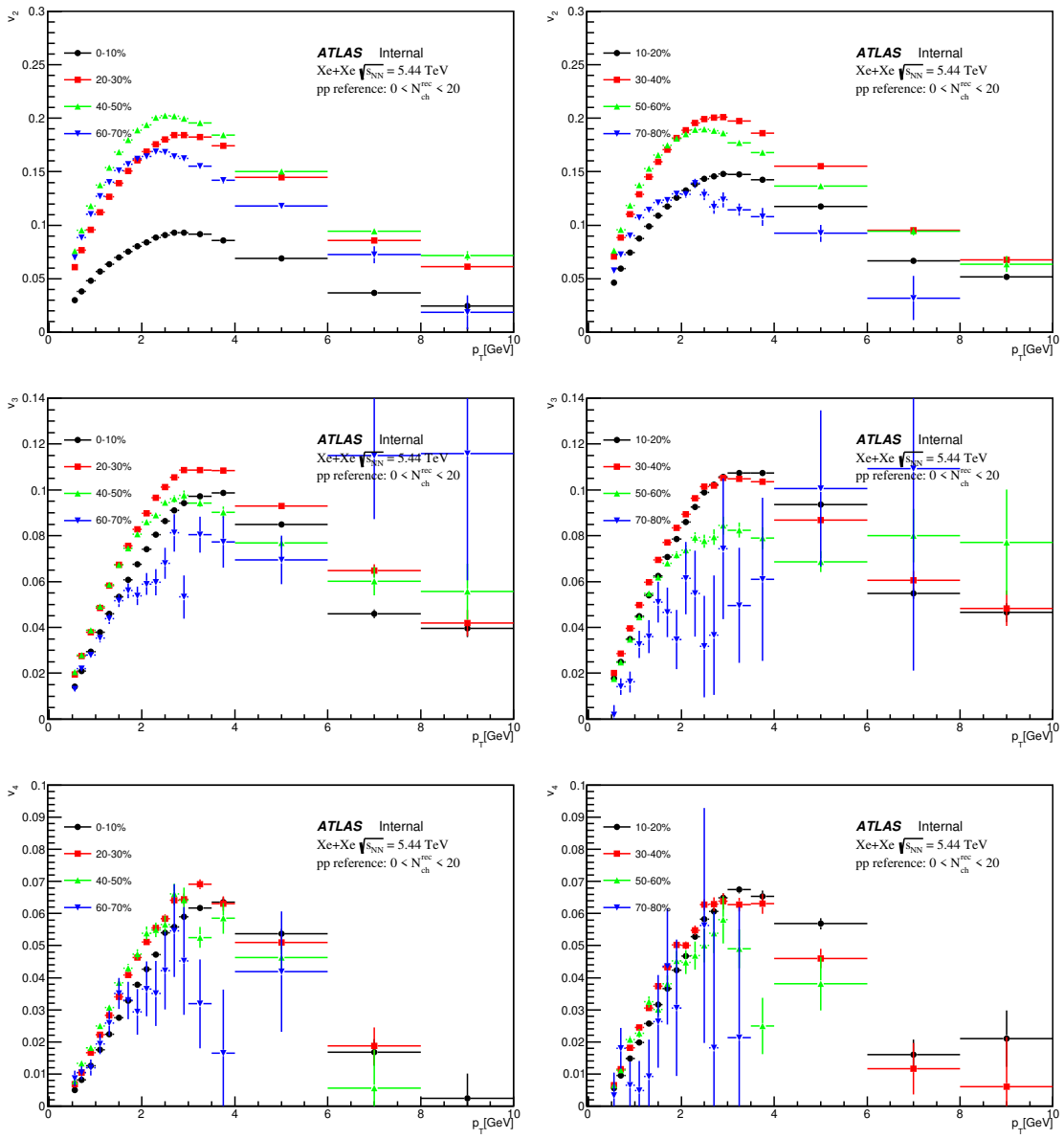

Figure 8.25: pT dependence of ZYAM-based template-fit v_n from XeXe measurements at $\sqrt{s_{\mathrm{NN}}} = 5.44$ TeV.

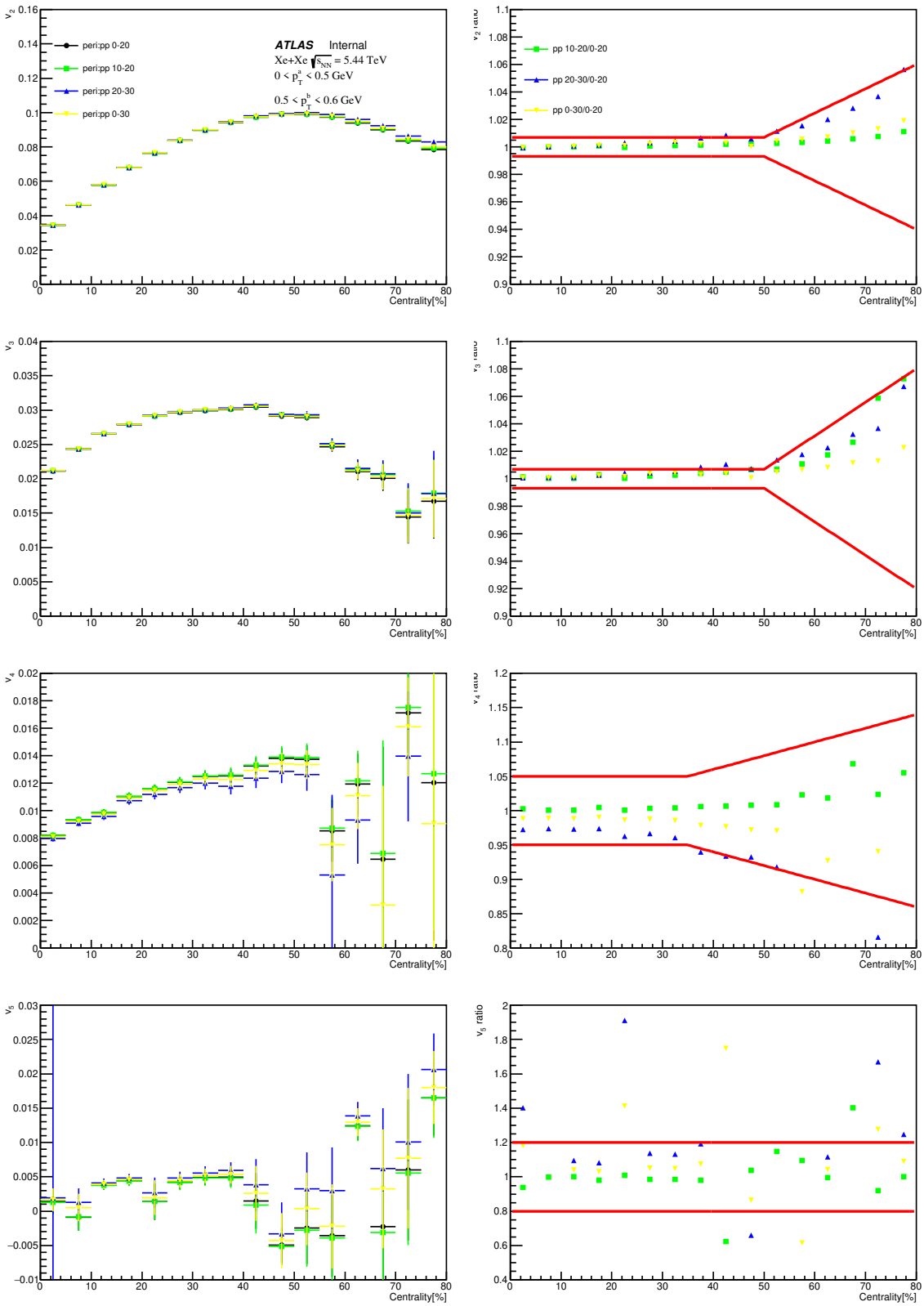

Figure 8.26: Comparison of v_n obtained using different peripheral references. From top to bottom each row shows a different harmonic. The plots are for 0.5-0.6 GeV p_{T} interval. The red lines represent the systematic uncertainty.

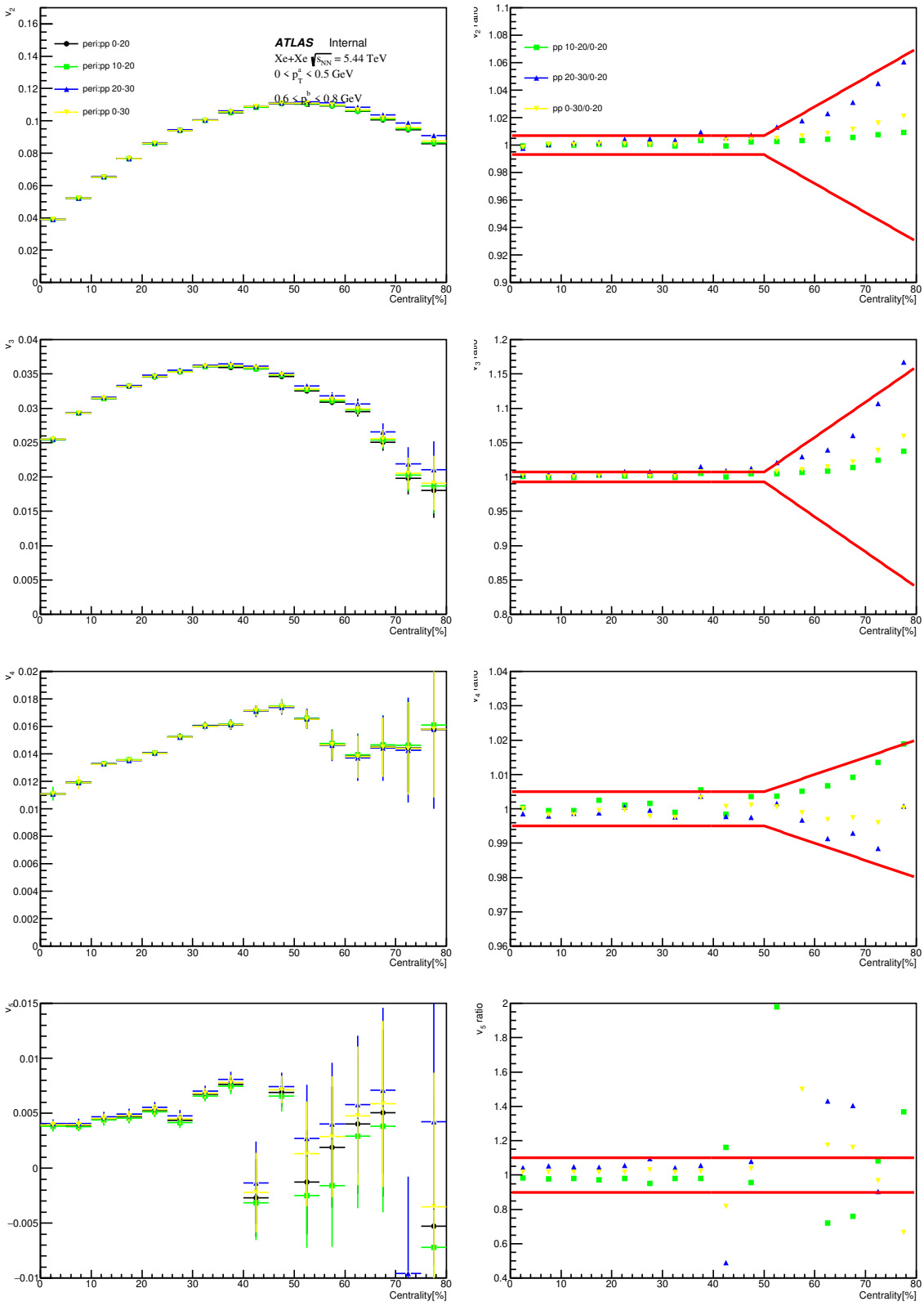

Figure 8.27: Same as Figure 8.26, but for 0.6-0.8 GeV p_{T} interval.

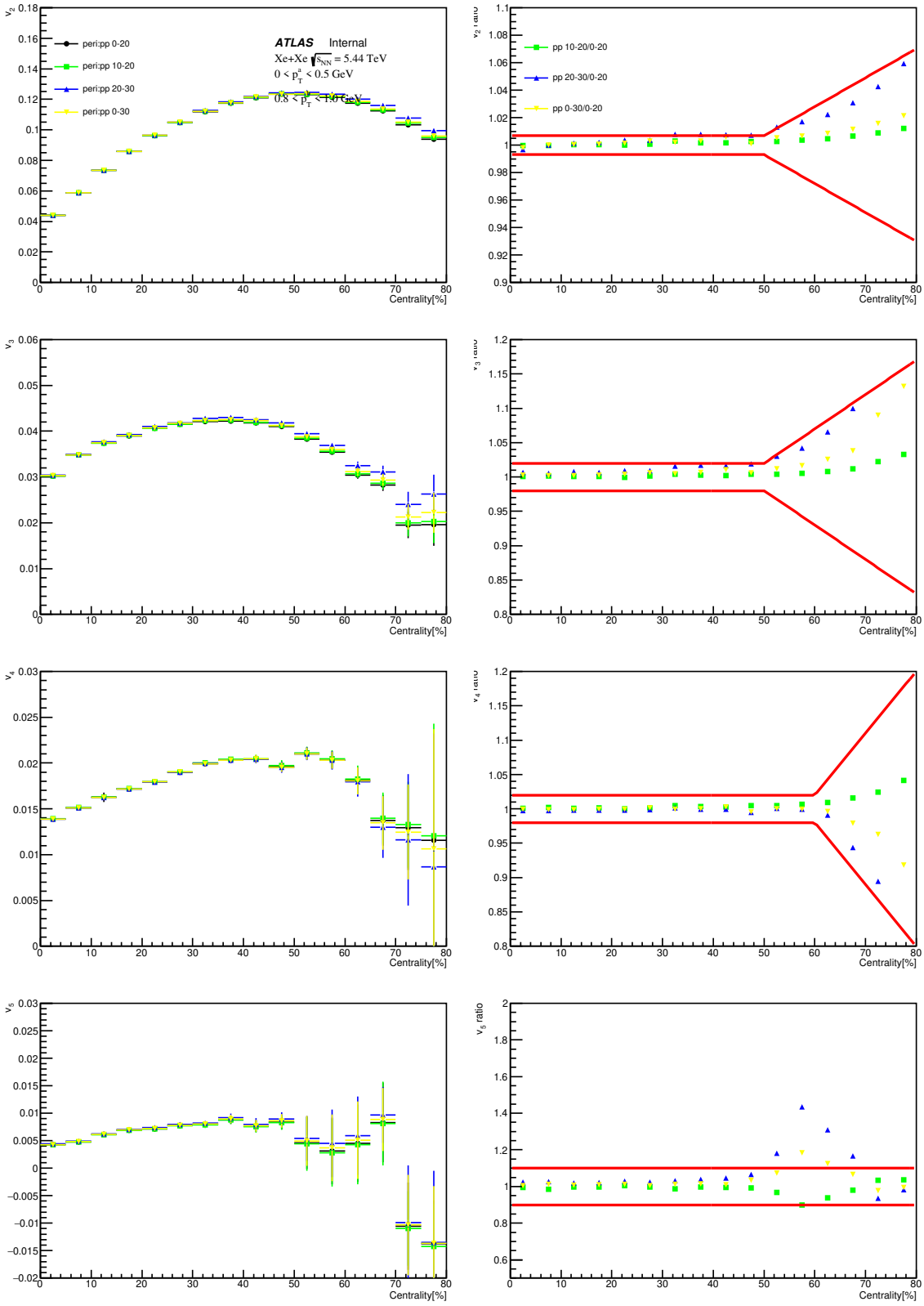

Figure 8.28: Same as Figure 8.26, but for 0.8-1.0 GeV p_{T} interval.

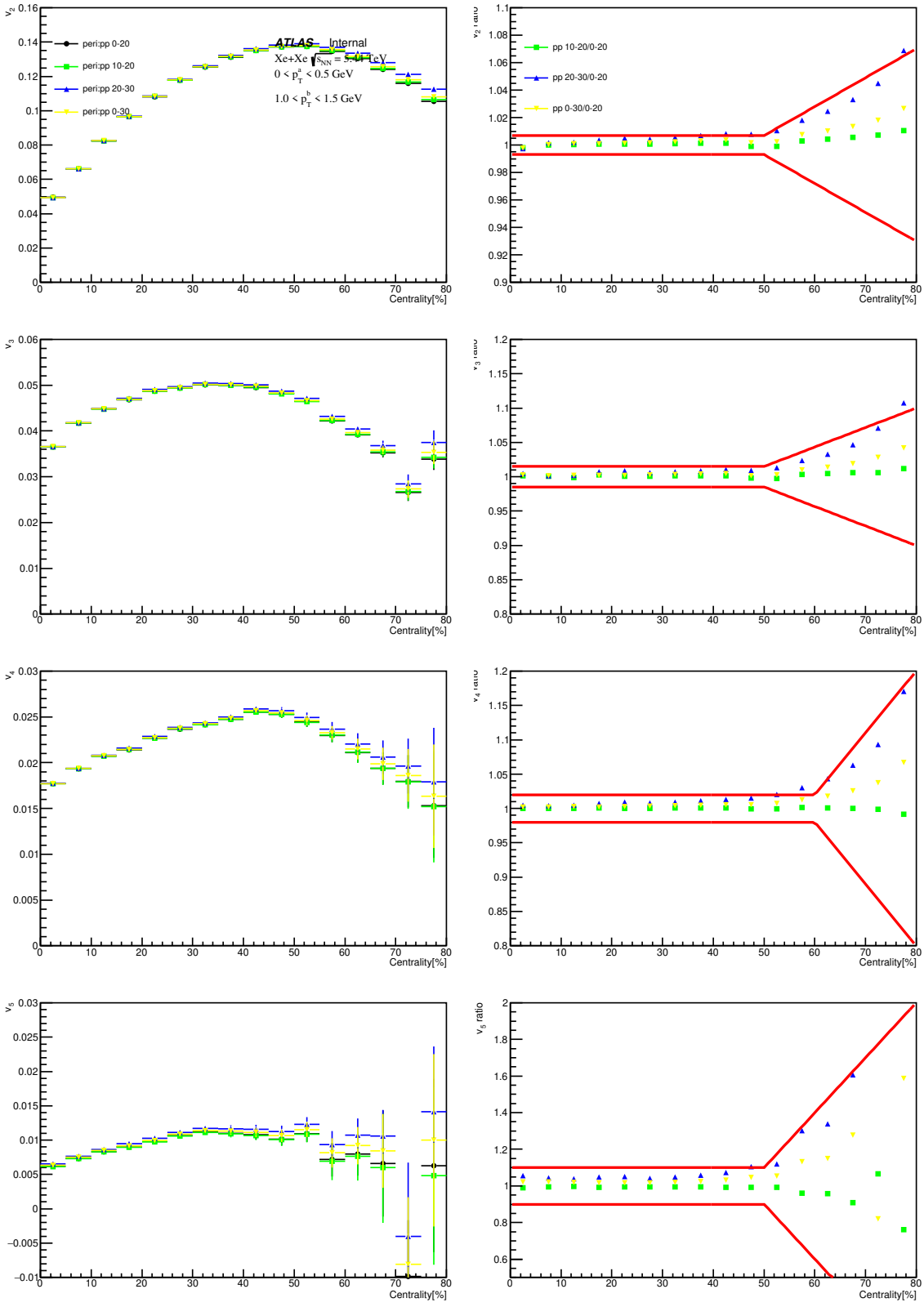

Figure 8.29: Same as Figure 8.26, but for 1.0-1.5 GeV p_{T} interval.

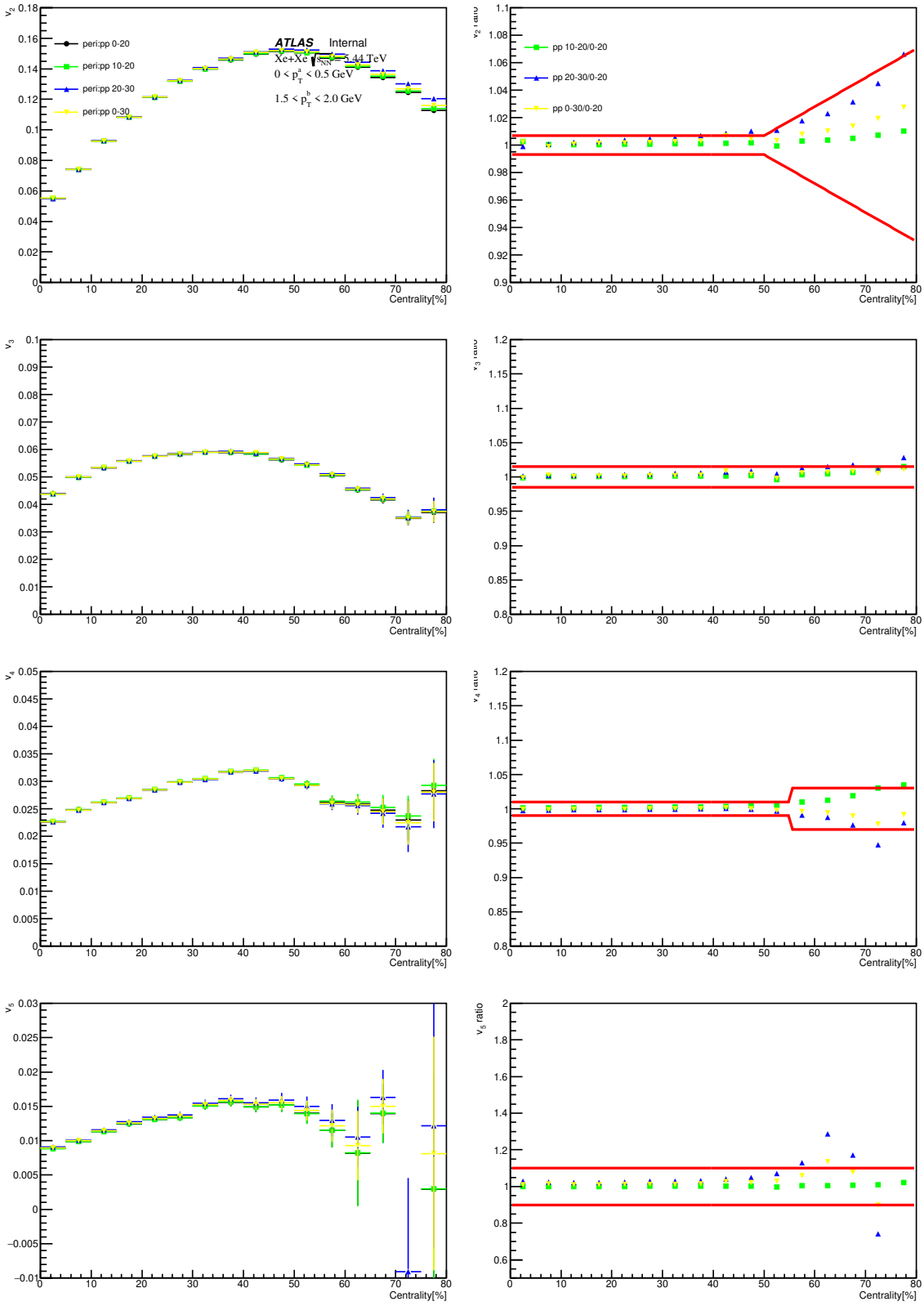

Figure 8.30: Same as Figure 8.26, but for 1.5-2.0 GeV p_{T} interval.

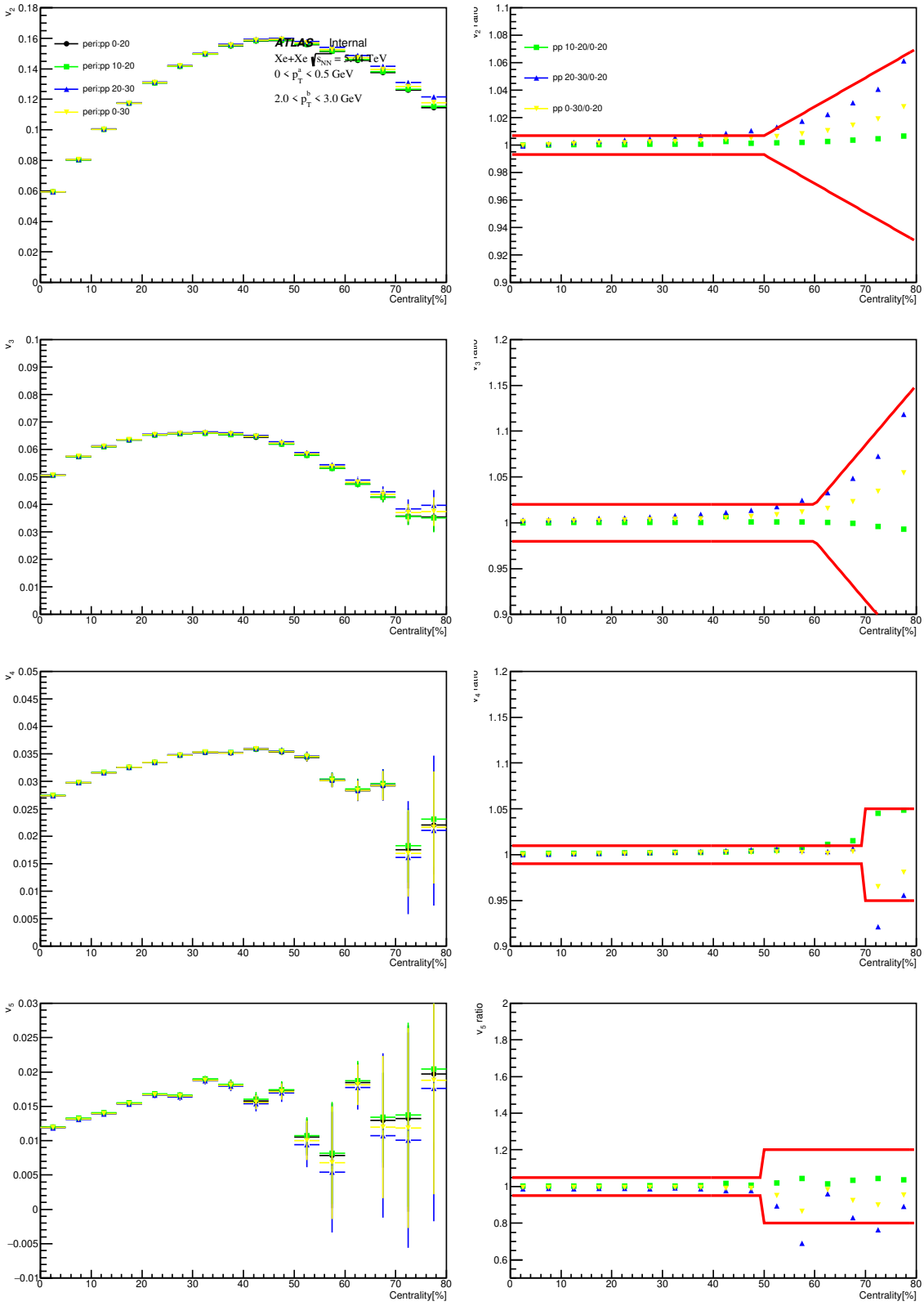

Figure 8.31: Same as Figure 8.26, but for 2.0-3.0 GeV p_{T} interval.

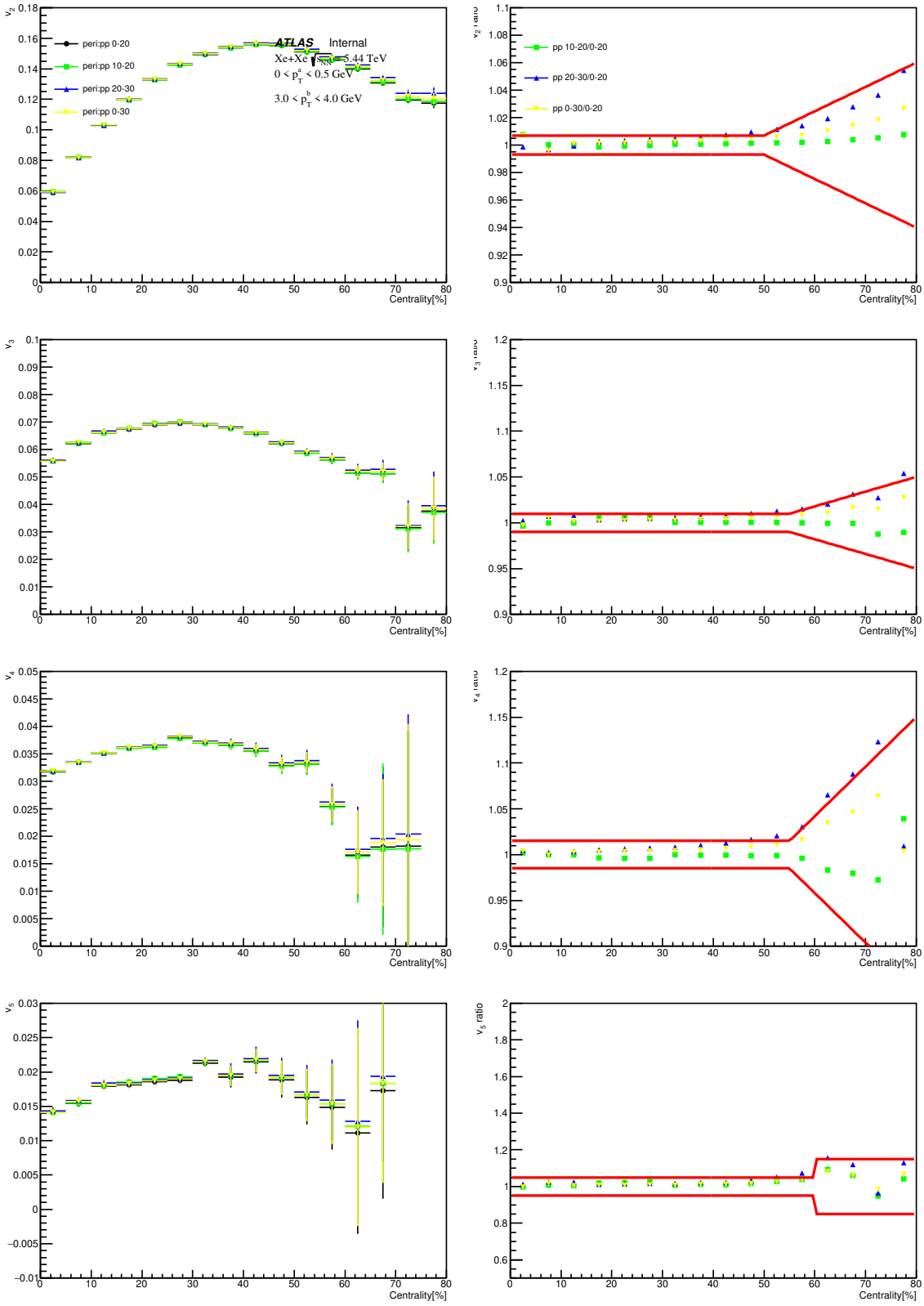

Figure 8.32: Same as Figure 8.26, but for 3.0-4.0 GeV p_{T} interval.

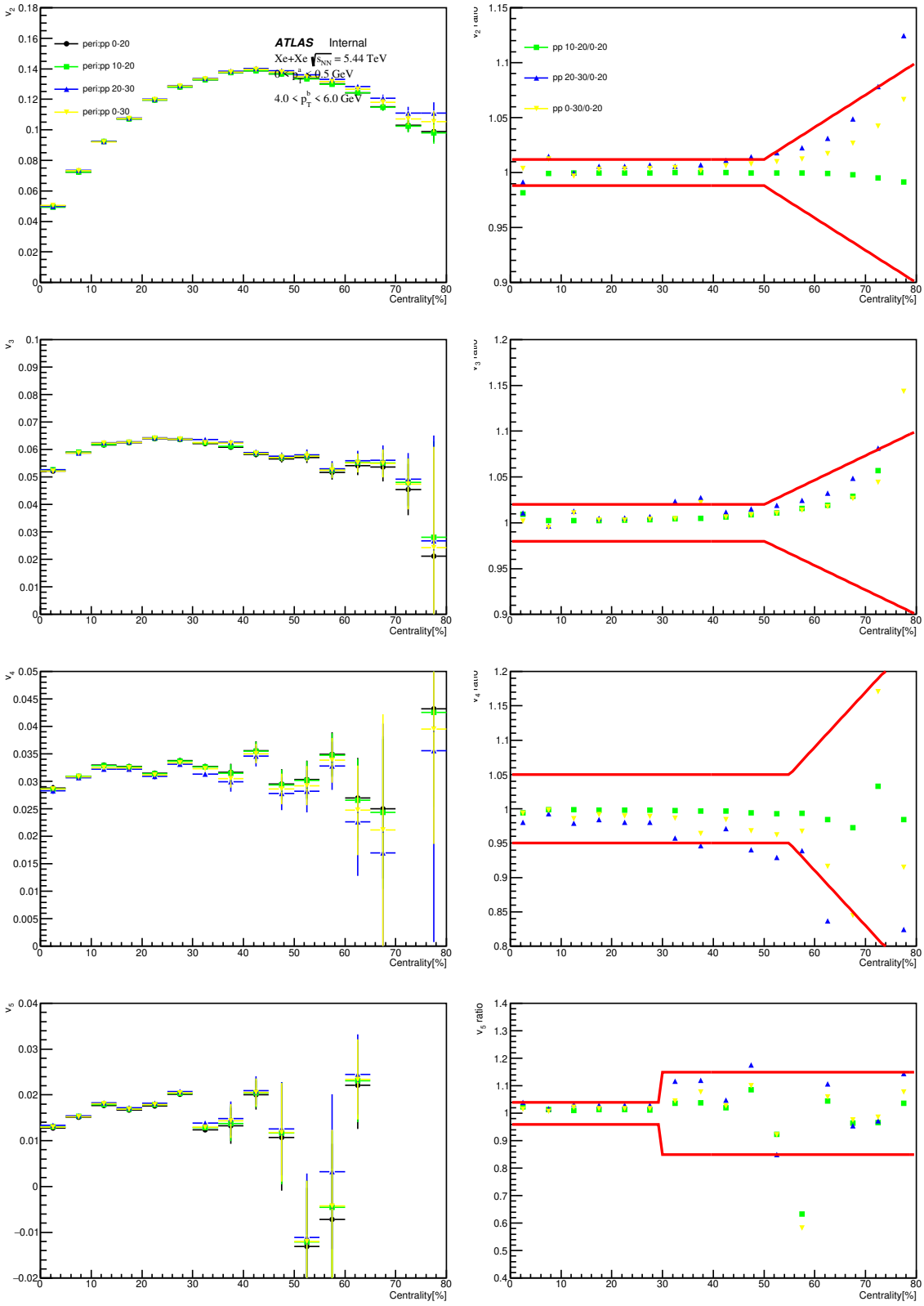

Figure 8.33: Same as Figure 8.26, but for 4.0-6.0 GeV p_{T} interval.

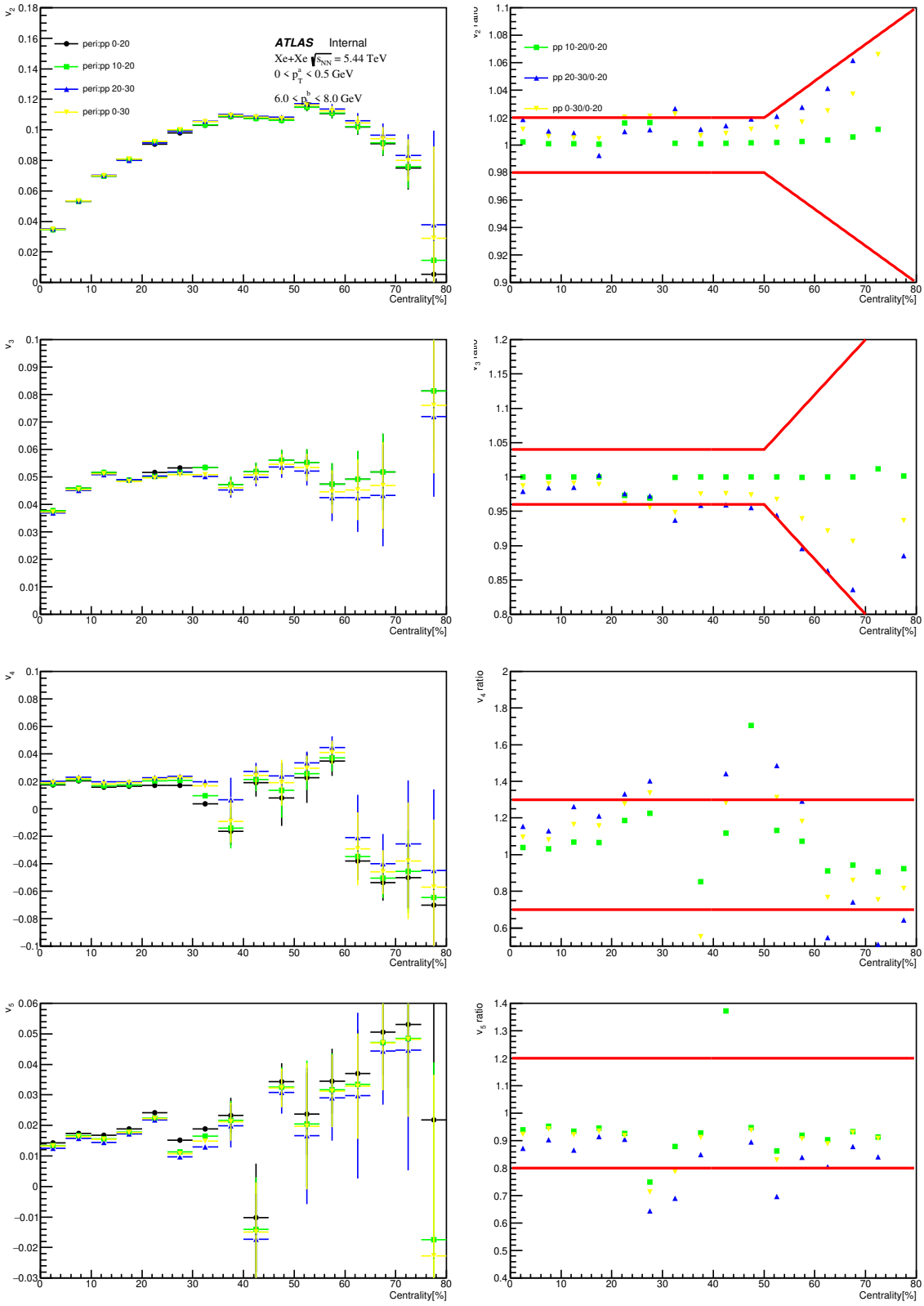

Figure 8.34: Same as Figure 8.26, but for 6.0-8.0 GeV p_{T} interval.

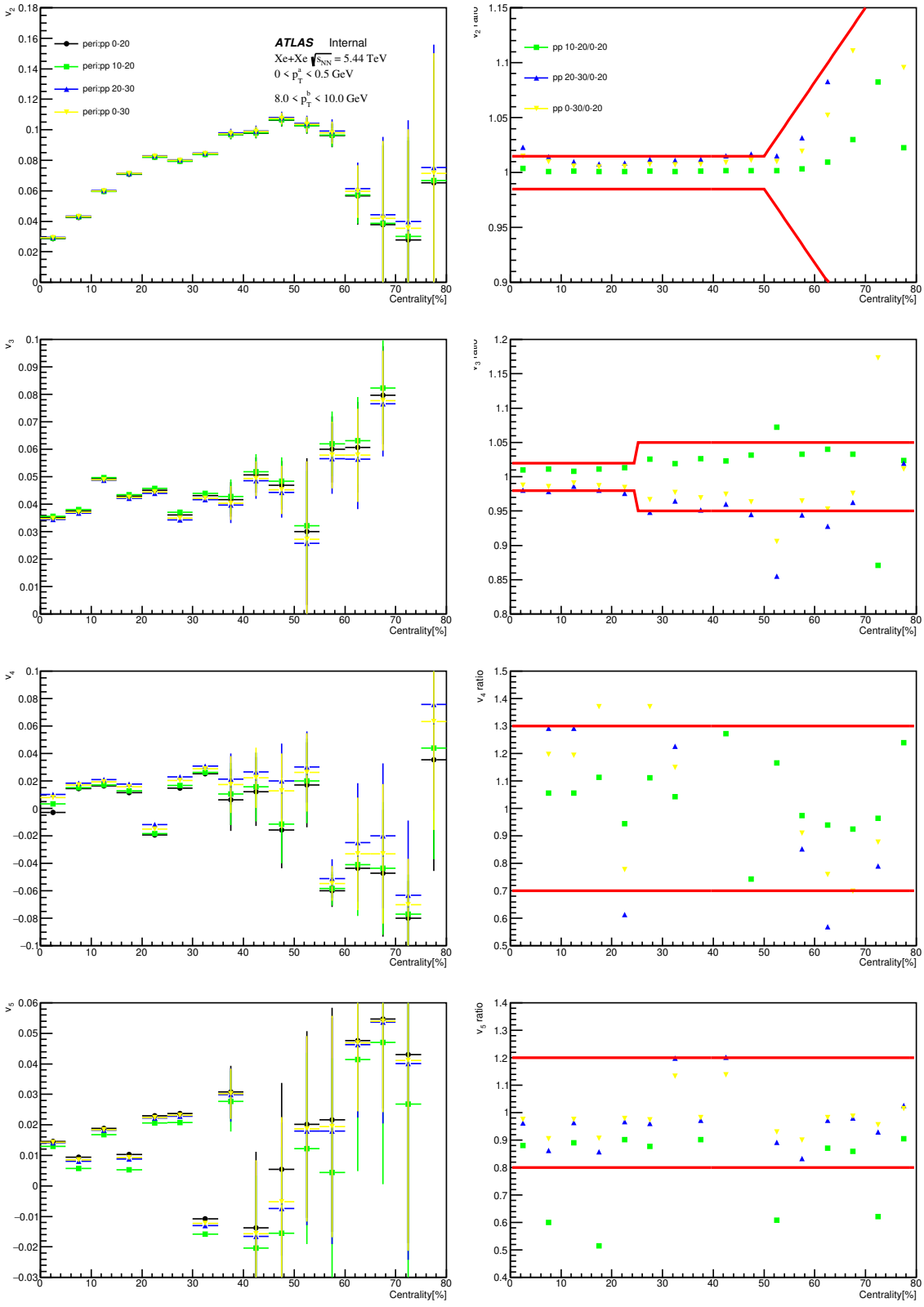

Figure 8.35: Same as Figure 8.26, but for 8.0-10.0 GeV p_{T} interval.

Chapter 9

Long-range correlation measurement in small systems at CMS and ALICE

9.1 pp and pPb measurement

This chapter briefly discusses the measurement of the previous dataset by other collaborations in LHC. This section focuses on 13 TeV pp, 5 and 8 TeV pPb measurement by CMS and ALICE as well as their comparison with 2.76 TeV PbPb results. CMS basically uses the same rescaled peripheral subtraction method as discussed in Chapter 3.2.2. Therefore their results of single particle flows decline to 0 by construction and are smaller than the true v_n values especially in the peripheral region. Figure 9.1 shows the two dimensional two-particle correlation functions from CMS measurement [49]. The first row is for unidentified hadron correlations. The second row and the third row use K^0_s and $\Lambda/\overline{\Lambda}$ as trigger particles respectively correlated with charged unidentified hadrons as associated particles. Figure 9.2 demonstrates the azimuthal dependence of per-trigger yields after ZYAM procedure. Upper plots represent long

range correlations for central and peripheral events. Bottom ones are short-minus-long range correlations for central and peripheral events. The scale factor for the peripheral event class is determined by the ratio of short-minus-long range yields in central events to peripheral events. A rescaled peripheral pre-trigger yield after the ZYAM procedure is subtracted from the central yield. The remaining part represents the correlation from soft particles and can be decomposed into Fourier series.

Figure 9.3 shows the v_2 and v_3 values after the peripheral subtraction. Similar to what we have observed in the ATLAS measurement, pp v_2 shows only weak dependence on the collisions energy. Distributions of v_2 from three different systems have similar trends. They all decrease to zero in the peripheral region by construction and become saturated in the mid-central region. However v_2 signal from PbPb is larger than that in pPb, and v_2 in pPb is larger than that in pp. The three distributions seems only differ by a scale factor. Figure 9.4 illustrates the p_{T} dependence of v_2 and v_2^{sub}. The former is the second order flow obtained before the peripheral subtraction, while the latter is the one after the peripheral subtraction. It's interesting to see that the second order harmonics before the subtraction have the p_{T} dependence that are independent of the system collision energy. While v_2 after the peripheral subtraction behave quite similar to the ATLAS measurement: all the distributions increase rapidly in the low-p_{T} region until 2-4 GeV then gradually decrease, which is also consistent with the trend observed in the previous pPb and PbPb measurement.

CMS also performed the multi-particle cumulant measurement for 13 TeV pp collisions. These results are illustrated in Figure 9.5 [49]. The advantage of cumulant measurement is that when multiple particles (usually larger than four) are correlated, the short-range correlation (i.e.same jet correlation and resonance decays) and away-side dijet peak are automatically suppressed. $v_2\{n\}$ calculated from n particle correlations can approximately represent the single particle elliptic flow without using any model to separate the flow contribution from non-flow contribution in the correlation

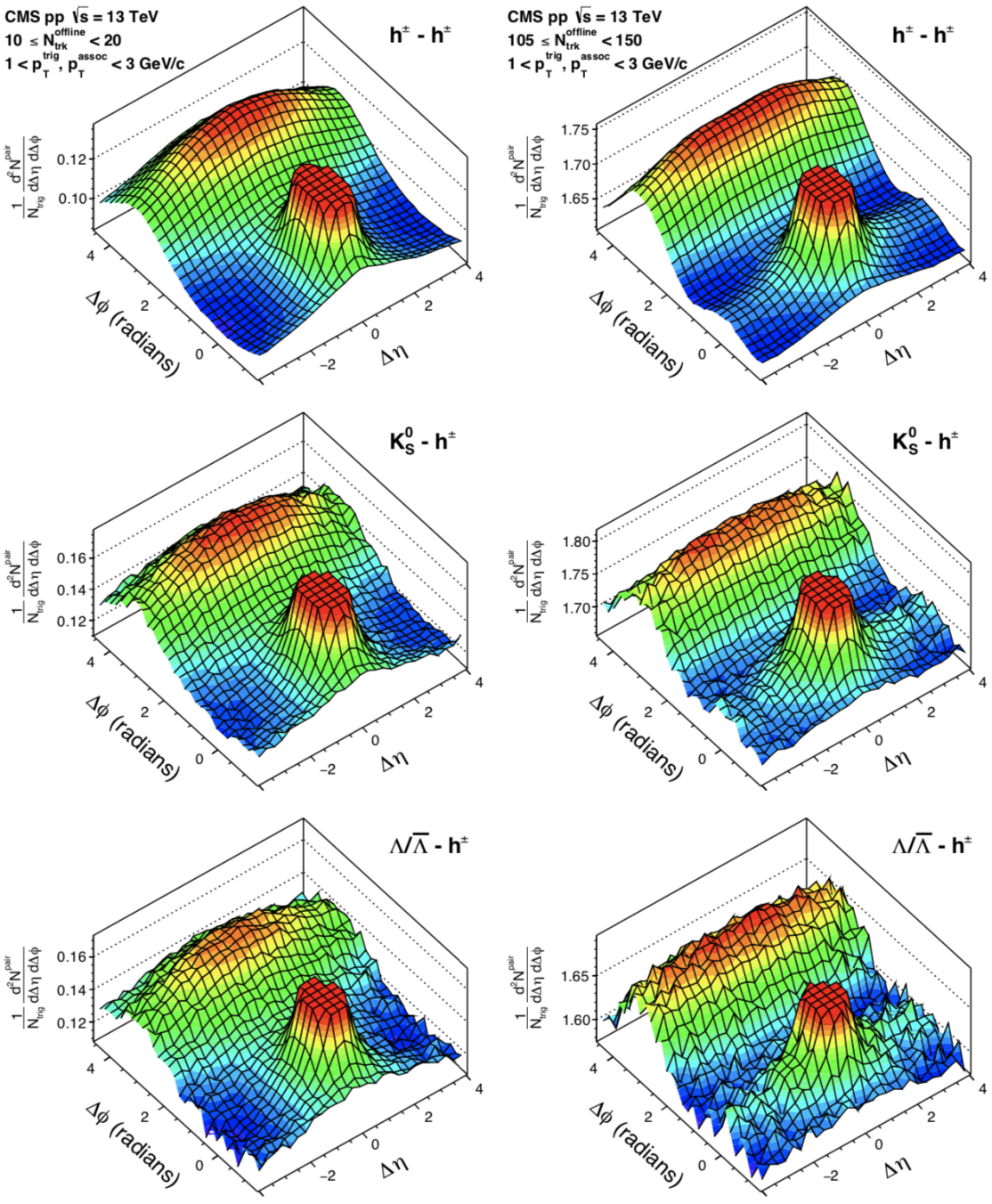

Figure 9.1: Measurement of two dimensional two-particle correlations at CMS for pp events at 13 TeV. The first row is for unidentified hadrons. The second row and the third row use K^0_s and $\Lambda/\overline{\Lambda}$ as trigger particles respectively.

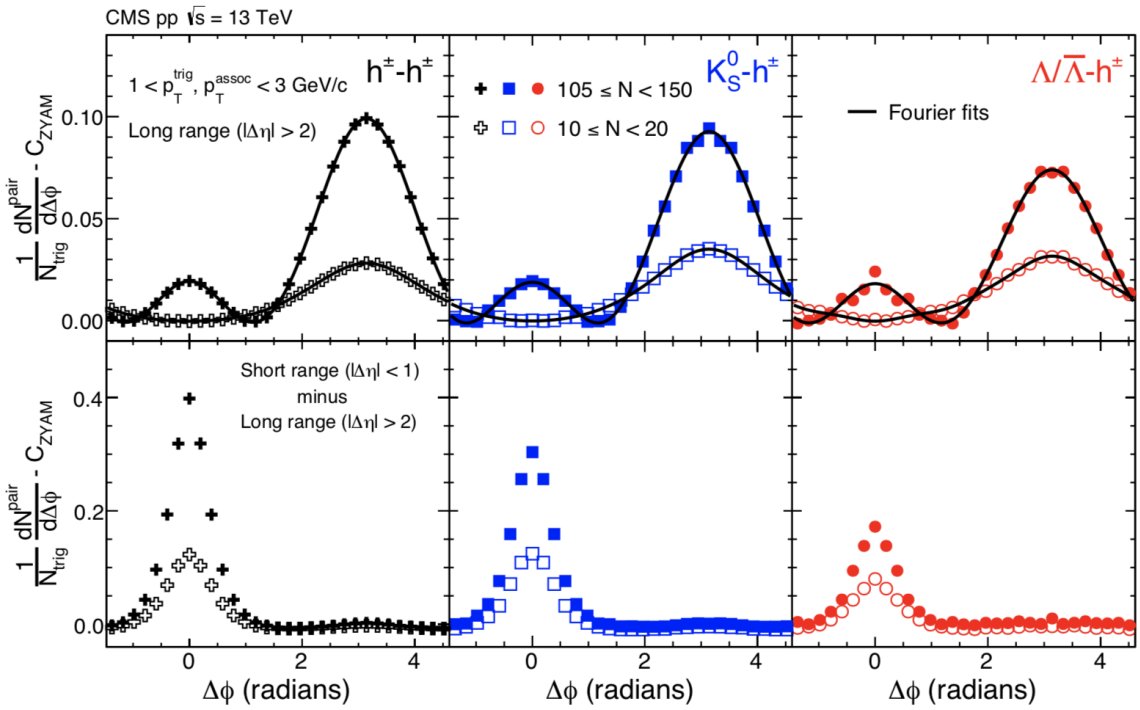

Figure 9.2: The upper panels represents the long range correlations for central and peripheral events. The bottom panels are short-minus-long range correlations for central and peripheral events.

functions. Therefore this is a model-independent result. Four-, six- and eight-particle cumulants are used to compute their corresponding v_2. LYZ represents the Lee-Yang Zeros method. $v_2\{2\}$ after the peripheral subtraction is also included for comparison. As discussed in Chapter 2.4.2, event-by-event flow fluctuations tend to increase $v_2\{2\}$ but to decrease $v_2\{n\}$ ($n \geq 4$). The difference between $v_2\{2\}$ and $v_2\{4\}$ stands for the initial geometry fluctuation. In addition, in the small variance Gaussian limit, $v_2\{4\}$, $v_2\{6\}$ and $v_2\{8\}$ are the same by construction. The equality of those multi-particle second order cumulants is a strong evidence of the collectivity origin for the anisotropic behavior. Small deviations from this equality may come from the non-Gaussian distribution of single particle flow v_2. From the figure, it's easy to see values of $v_2\{4\}$, $v_2\{6\}$ and $v_2\{8\}$ are consistent in all the three systems. $v_2\{2\}$ and $v_2\{4\}$ split in high-multiplicity pPb and PbPb events. However in 13 TeV pp $v_2\{2\}$ gives almost identical result as $v_2\{4\}$. This suggests the initial state event-by-event

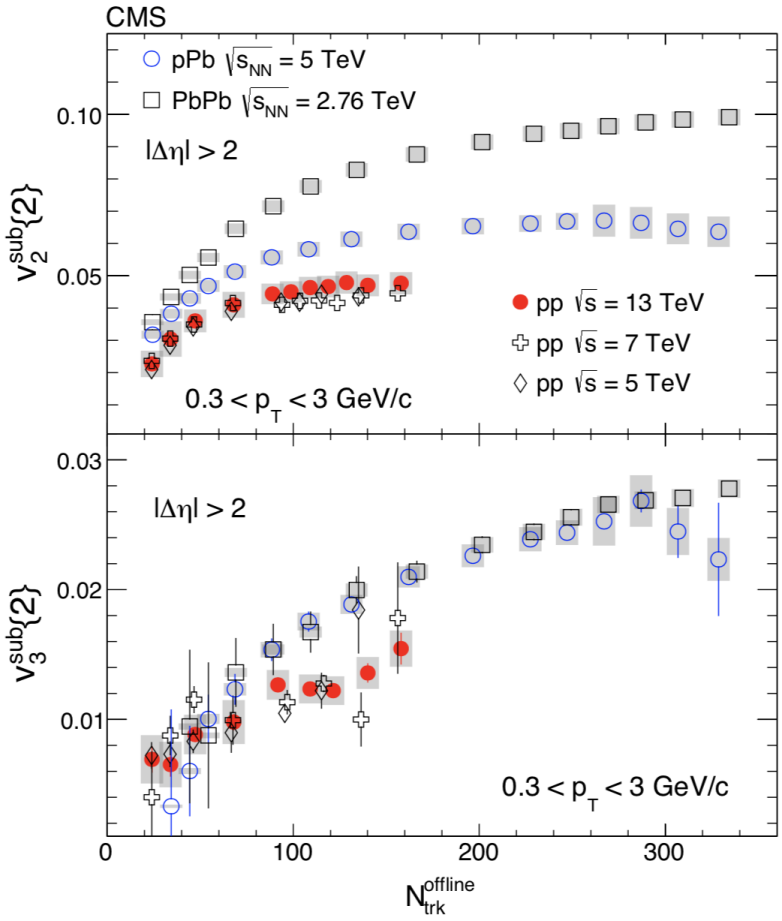

Figure 9.3: Distributions of v_2 and v_3 as a function of event multiplicity after peripheral subtraction for PbPb, pPb and different pp systems.

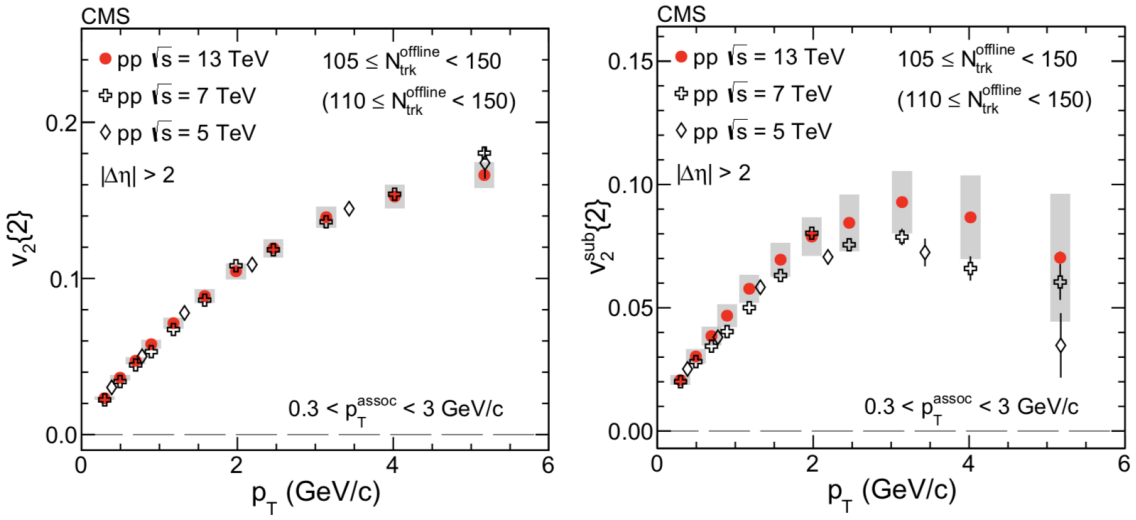

Figure 9.4: Distributions of v_2 as a function of transverse momentum before and after peripheral subtraction for PbPb, pPb and different pp systems.

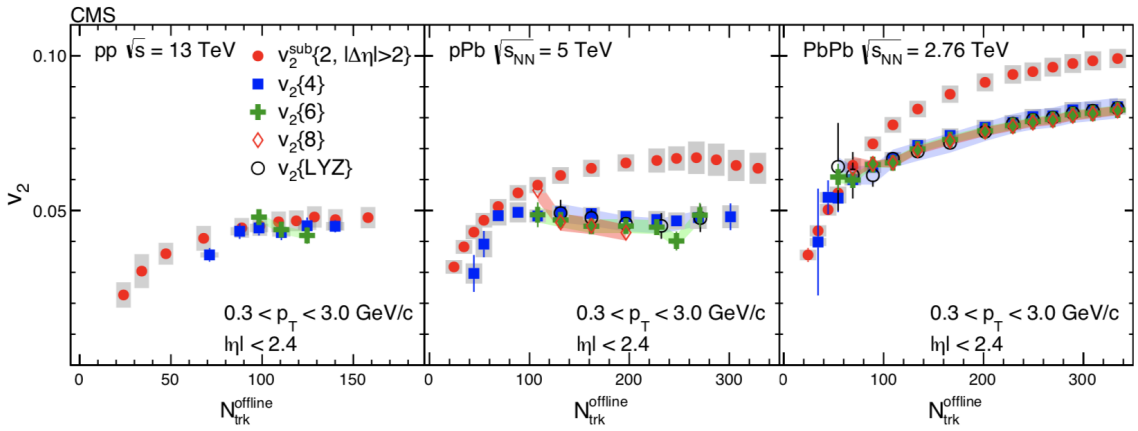

Figure 9.5: Measurement of the second order flows from multi-particle cumulants and the comparison with v_2 values after the peripheral subtraction for PbPb, pPb and pp systems.

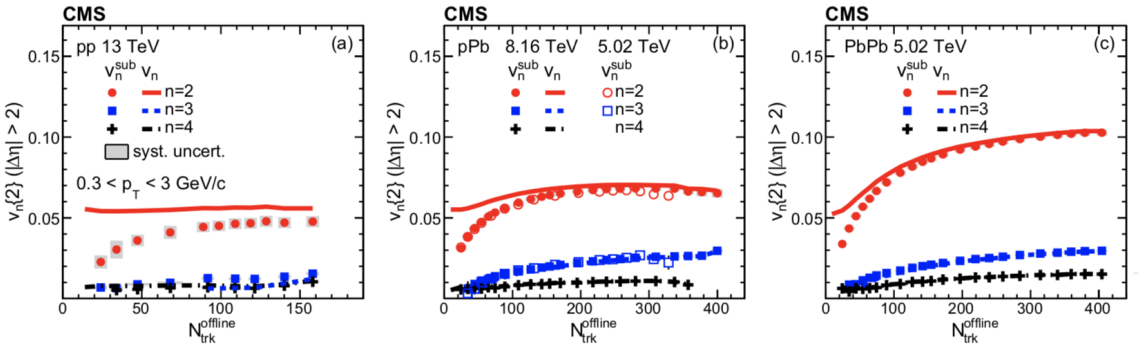

Figure 9.6: Comparison of v_n values before and after the peripheral subtraction for pp, pPb and PbPb systems.

fluctuation is quite small in pp collisions. Due to the low-multiplicity nature of the peripheral pp collision, the multi-particle cumulant analysis can not be performed in such regions. Figure 9.6 demonstrates the distribution of v_n and $v_n^{\rm sub}$ as a function of event multiplicity in four different systems: 13 TeV pp, 5.02 TeV pPb, 8.16 TeV pPb and 5.02 TeV PbPb [50]. The effect of the peripheral subtraction is quite small for pPb and PbPb except for the most peripheral regions. v_2 is dominant among the first three harmonics. All these observations are consistent with the previous ATLAS results.

The muon-hadron correlation analysis for 5.02 TeV pPb is also performed at

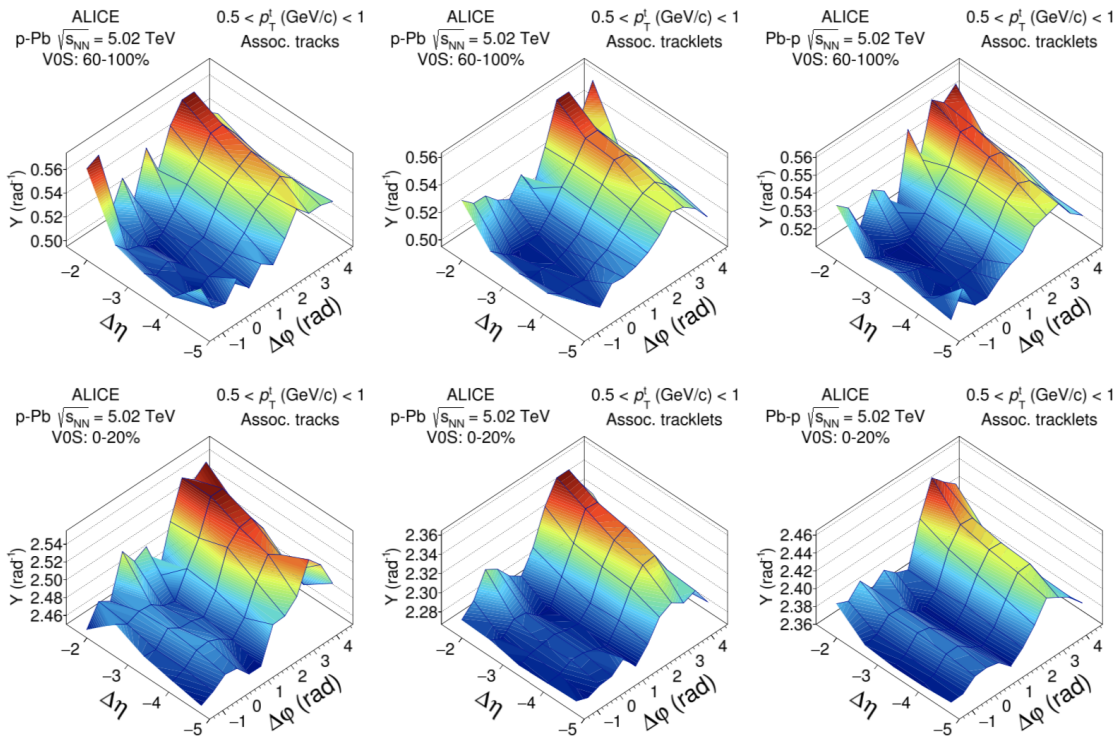

Figure 9.7: Two dimensional two particle correlations for pPb at 5.02 TeV. For pPb configuration, both muon-track and muon-tracklet correlations are included. For Pbp configuration, only muon-tracklet correlation is included.

ALICE [51]. In this measurement muons are chosen to be trigger particles. Both tracks and tracklets constructed by the ALICE detector are used for associated particles. The tracklet candidates are short track segments and built by only the primary vertex plus two layers of Silicon Pixel Detectors (SPD). In Figure 9.7, p-Pb configuration represents the period when the trigger particle muon moves along the proton-going direction. While in Pb-p configuration, the trigger particle muon moves in the Pb-going direction. In p-Pb configuration both muon-track and muon-tracklet correlations are studied, In Pb-p configuration only muon-tracklet correlation is included. Comparing the upper row with the bottom row in Figure 9.7, it is clear that the near-side ridge structure emerges in central collisions.

The method ALICE uses to extract the flow component in the long range is basically the same as the peripheral subtraction described in Chapter 3.2.1. In Figure

9.8 the peripheral event class 60-100% is subtracted from the central event class 0-20%. The remaining correlation structures are plotted in the upper panels and their $\Delta\phi$ projections are illustrated in the bottom. It is obvious that for all the three cases the away-side enhancements are still larger than the near-side ones. This is because the scale factor equal to 1 is assumed in this peripheral subtraction. When Y_{sub} is decomposed into Fourier series, the first order harmonic is used to account for this residual jet correlation on the away side. $v_{n,n}$ is calculated by $a_n/(a_0 + b)$, where b is the pedestal in the peripheral event class. It is determined by the integral around the minimum point of the peripheral correlation function. Equivalently a fit with a functional form of a Gaussian plus a constant can be applied to the long-range peripheral correlation to estimate b. $v_{n,n}$ can also be computed using the central event pedestal B, $v_{n,n} = a_n/B$. To determine B, a second-order polynomial fit is performed around the minimum point of the central event correlations. These two alternative ways are used to estimate the systematic uncertainties in this analysis.

Figure 9.9 demonstrates the p_{T} dependence of muon-v_2 for both muon-track and muon-tracklet correlations in pPb configuration. v_2 increases with p_{T} up to 1-2 GeV and then decreases. The decline beyond 2 GeV is similar to what we have observed in the ATLAS results. Results from muon-track and muon-tracklet correlations agree with each other. Since tracks and tracklets typically have different p_{T} ranges, this agreement suggests factorization relationship holds quite well for this analysis.

9.2 XeXe measurement

XeXe measurement at 5.44 TeV is also performed by CMS and ALICE. They use the direct Fourier transform for two particle correlations to measure flow coefficients v_n. This means no away-side jet contribution is subtracted from the correlation function. Figure 9.10 shows the distributions of v_2 as a function of p_{T} in different

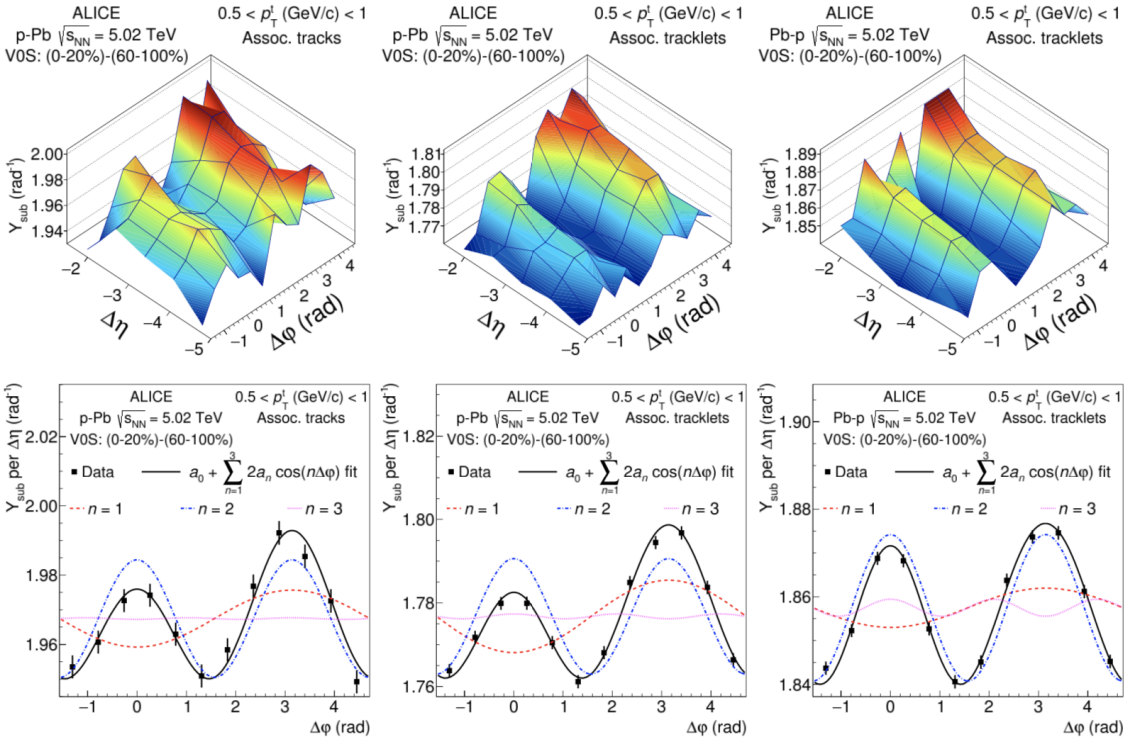

Figure 9.8: Two particle correlation functions for pPb at 5.02 TeV after the subtraction of peripheral events. The upper panels are 2D plots. The bottom ones are 1D projection onto the $\Delta\phi$ axis.

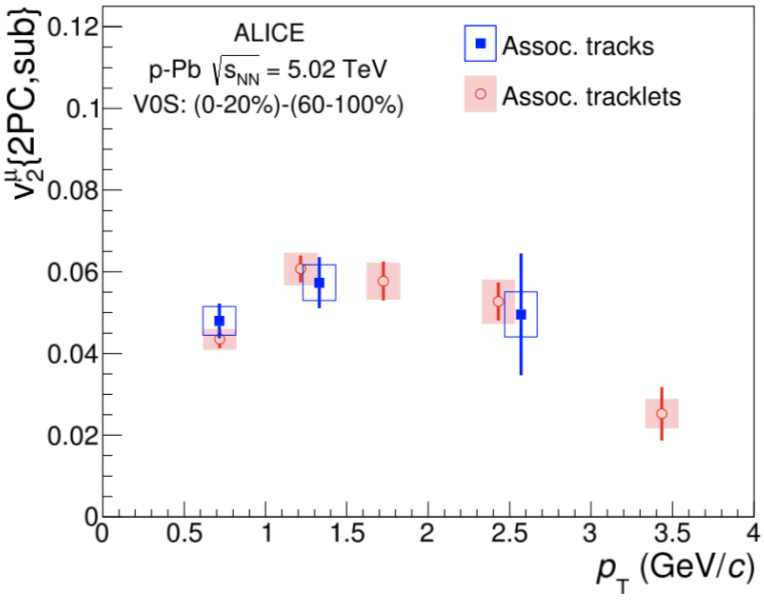

Figure 9.9: Muon-v_2 vs p_{T} for both muon-track and muon-tracklet correlations in pPb configuration.

centrality bins [52]. Three different methods are used to calculate XeXe v_2, the scalar product (SP) technique, the two particle correlation method and the cumulant method. The SP method and the two particle correlation method give nearly the same results. The small difference between them may come from different $\Delta\eta$ regions for SP ($|\Delta\eta| > 3$) and two particle correlations ($|\Delta\eta| > 2$). Results from different multi-particle cumulants agree with each other suggesting the collective origin for XeXe flows. All cumulant results are smaller than the two particle correlation result. The difference is a measure of the initial state fluctuations. Figure 9.11 demonstrates the ratios of XeXe v_n to PbPb v_n. Ratios for all harmonics are greater than 1 in the most central events, especially for v_2. This is due to the non-spherical shape of the Xe nucleus. This deformed shape will increase the eccentricity of the overlap region in central collisions leading to a larger v_2 value than PbPb collision. All these ratios gradually decrease as centrality percentage increases until the most peripheral region where all v_n ratios become smaller than 1. This is the same trend as what we have observed in the previous ATLAS results.

Figure 9.12 shows the ALICE measurement of 5.44 TeV XeXe with values of v_2, v_3 and v_4 included [53]. Cumulant method is also included for the measurement of v_2. Similar to the previous CMS measurement, these results agree with each other and are smaller than two-particle correlation results. The bottom panel shows the ratio $v_2\{4\}/v_2\{2\}$ for both the data and prediction. The red solid line stands for a hydrodynamic calculation using $\eta/s = 0.047$ and an initial condition model called TRENTo. For both the data and model prediction, $v_2\{4\}/v_2\{2\}$ decreases in central events since initial state fluctuations play a more important role than hydrodynamic expansion in this region. Curves of eccentricity ratio and elliptic flow ratio from initial condition model and hydrodynamic model are not exactly the same, but generally follow the same trend.

Figure 9.13 represents the centrality dependence of Xe and Pb v_n as well as their

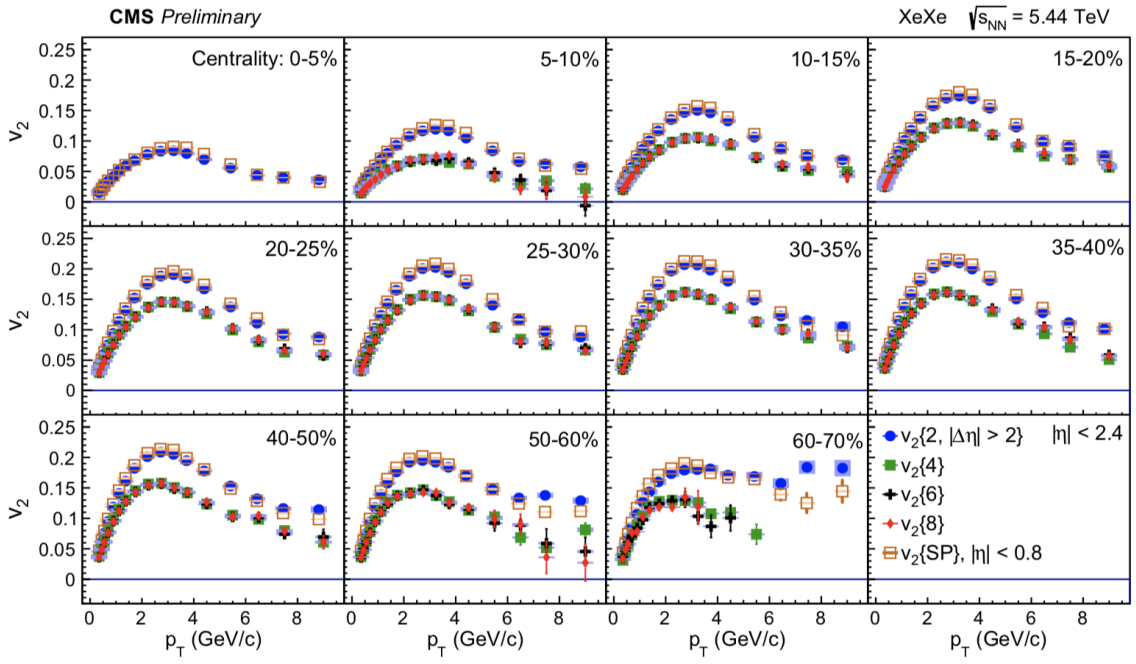

Figure 9.10: Distributions of v_2 as a function of p_{T} in different centrality bins for XeXe at 5.44 TeV by CMS.

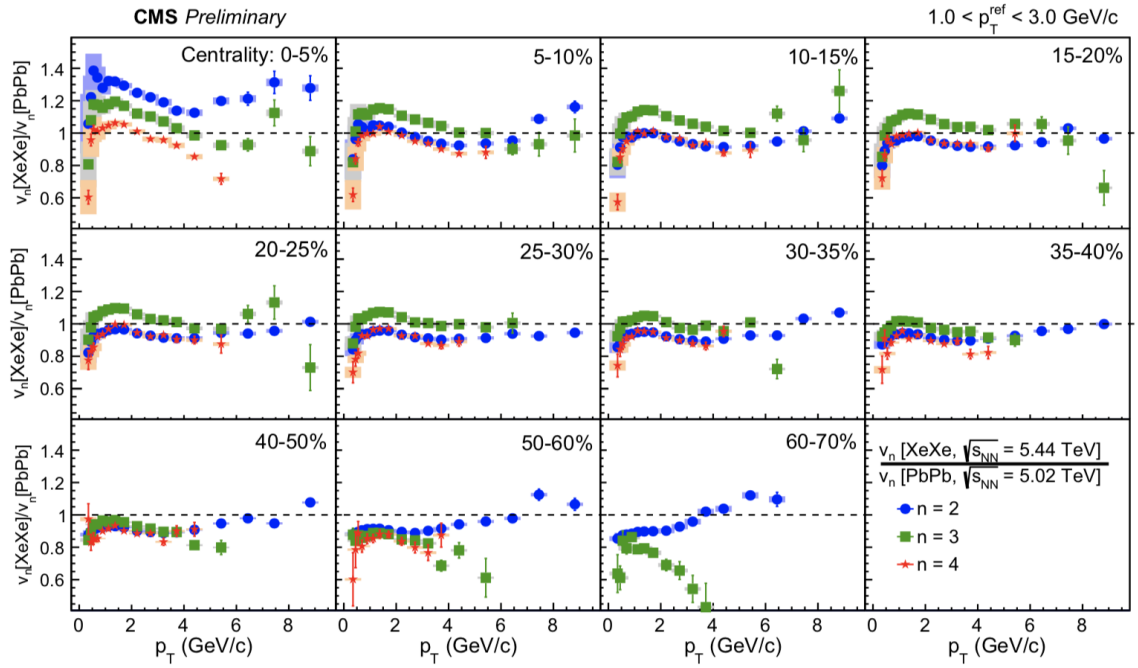

Figure 9.11: Ratios of XeXe v_n to PbPb v_n as a function of p_{T} in different centrality bins for XeXe at 5.44 TeV by CMS.

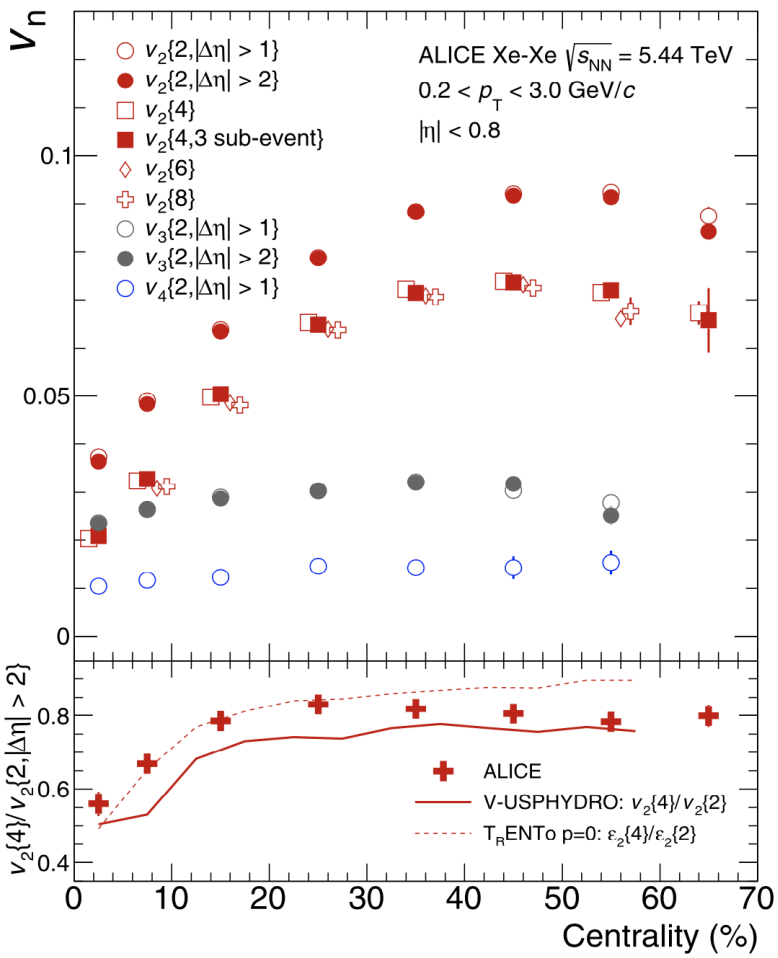

Figure 9.12: The top panel represents the distributions of v_n as a function of centrality for XeXe at 5.44 TeV. The bottom panel is the ratio $v_2\{4\}/v_2\{2\}$. Hydrodynamic calculation is also included for comparison.

ratios in the bottom. This is quite similar to our ATLAS result. In central events XeXe v_2 is much larger than PbPb v_2 due to the non-spherical shape of the Xe nucleus discussed before. Figure 9.14 and Figure 9.15 show the distributions of v_2 and v_3 as a function of p_T in different centrality bins respectively. Only two particle correlation result $v_2\{2\}$ in the long range is included. The same distribution has been observed in the previous CMS measurement.

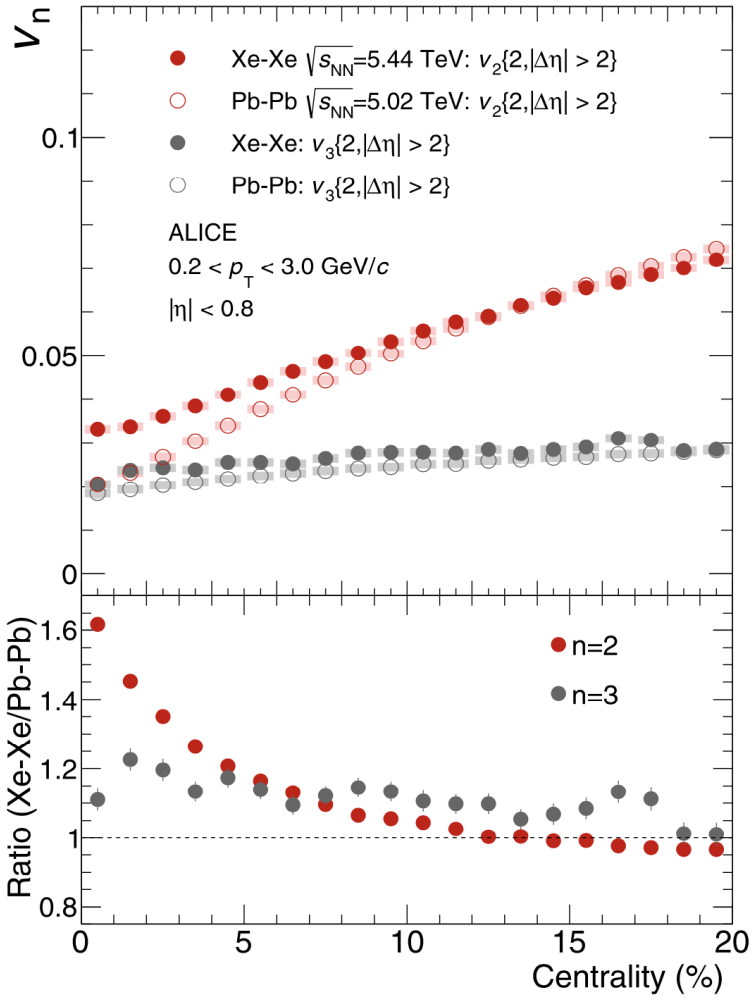

Figure 9.13: Comparison of XeXe v_n and PbPb v_n with their ratios plotted in the bottom panel as a function of centrality.

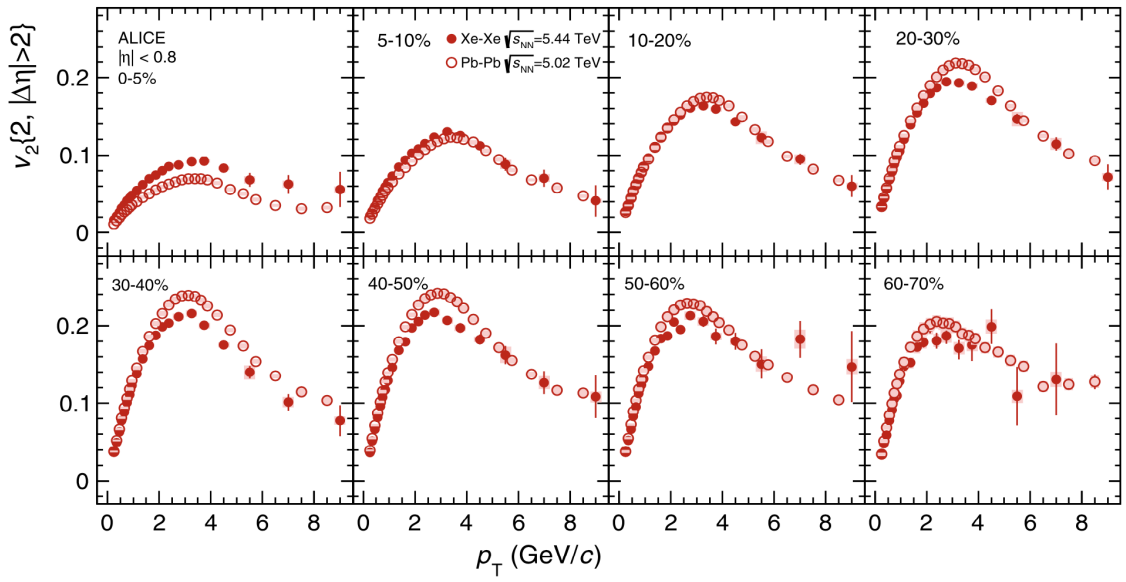

Figure 9.14: Distributions of v_2 as a function of p_{T} in different centrality bins for XeXe at 5.44 TeV by ALICE.

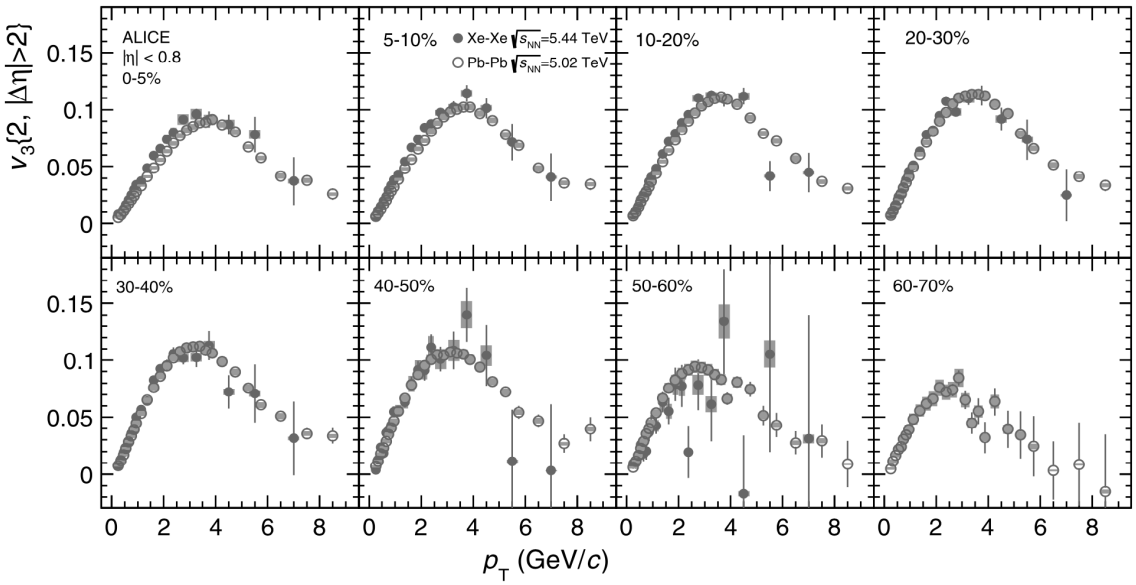

Figure 9.15: Distributions of v_3 as a function of p_{T} in different centrality bins for XeXe at 5.44 TeV by ALICE.

Chapter 10

Conclusion

During a heavy ion collision, a large amount of energy is deposited into a small space region. A hot and dense medium called quark-gluon plasma is formed after the interaction. The evolution of this strongly-coupled matter can be well described by viscous hydrodynamics. The experimental observation of the anisotropic flows in AA systems suggests QGP has almost the smallest viscosity of all fluids in nature. Similar behavior is also observed in small systems, such as pp, pPb at LHC and dAu at RHIC, where the creation of the hot and dense medium is not expected previously. Different analysis methods and models are used to extract the anisotropic flows from the experimental data. Multiple theoretical calculations have also been performed in order to explain the origin of the small system collectivity. This thesis has mainly discussed the recent measurement of flow correlations in small systems, the related theoretical background of quark-gluon plasma and also the associated analysis methods to extract anisotropic flows.

The final particle azimuthal anisotropy after a collision can be quantified by flow harmonics v_n. Two-particle correlation analysis is implemented in the long range to extract the single particle flow harmonics. 2D two-paricle correlations are constructed as a function of $\Delta\phi$ and $\Delta\eta$. It can be projected onto $\Delta\phi$ axis by the integration over

the long range $2 < |\Delta\eta| < 5$. A new analysis method for anisotropic flows based on template fitting is introduced in this thesis. It assumes the correlation function can be decomposed into two terms. The first one is a soft component, which is the flow term, represented by a cos modulation. The second term is a dijet component on the away side whose shape can be determined from peripheral events. The contribution of this dijet component can be estimated and subtracted from the correlation function to obtain the flow modulation.

We first present the pp analysis at $\sqrt{s} = 5.02$ and 13 TeV as well as the pPb analysis at $\sqrt{s} = 8.16$ TeV. The measurement is performed at $0.5 < p_{\mathrm{T}}^{a,b} < 5$ GeV. $v_{2,2}$, $v_{3,3}$ and $v_{4,4}$ are obtained using three different methods: ZYAM-based template fits, improved template fits and direct Fourier transform. ZYAM-based template fits give smaller v_n values than improved template fits especially in peripheral collisions. Their distributions are studied as a function of both $N_{\mathrm{ch}}^{\mathrm{rec}}$ and $E_{\mathrm{T}}^{\mathrm{FCal}}$. Results show that pp v_2 from improved template fitting method is multiplicity and energy independent, while v_2 from ZYAM-based fits increases slowly with event multiplicity. pPb v_2 always increases with the multiplicity regardless of the method to use. To estimate systematic errors and accuracy of the template fitting results, different peripheral references are used for comparison. v_2 from pp events are also investigated using opposite-charge pair and same-charge pair correlations seperately. They both give the same results as the combined-charge pair correlation. Factorization relationship is studied as a function of both $N_{\mathrm{ch}}^{\mathrm{rec}}$ and p_{T}. The consistence of distributions from different p_{T} intervals of "associated" particles suggests that the long-range correlation may truly come from the single particle distributions. $|\Delta\eta|$ dependence is also investigated for a better understanding of the "ridge" structure. $|\Delta\eta| < 1$ is excluded to get rid of the near-side jet peak.

We also studied the muon-hadron and hadron-hadron correlations at 8.16 TeV pPb collisions. The measurement is performed at hadron p_{T} range $0.5 < p_{\mathrm{T}} < 5$

GeV and muon p_{T} range $4 < p_{\mathrm{T}}^{\mu} < 6$ GeV. In both analysis multiplicity and p_{T} dependence of v_n are studied as before. Their factorization relations are verified. In muon-hadron analysis, a momentum imbalance cut $\Delta p/p < 0$ is implemented to select only prompt muons. Muon-v_2 is relative small compared to the corresponding hadron-v_2 from template fitting method. The p_{T} dependence of muon-v_2, which is a decreasing function of muon-p_{T}, is also studied. Template fitting results from both muon-hadron and hadron-hadron correlations are studied as a function of $|\Delta\eta|$. It seems that there is not a significant $|\Delta\eta|$ dependence from template fits in both cases. Direct Fourier transform is also plotted for comparison. The two methods give close values in hadron-hadron correlations, while in muon-hadron correlation results from Fourier transform are larger. This gives a decreasing function of $|\Delta\eta|$. Different peripheral bins are used for the template fitting method to estimate the systematic errors.

At last we examine XeXe collisions at $\sqrt{s_{\mathrm{NN}}} = 5.44$ TeV. p_{T} interval $0.5 < p_{\mathrm{T}} < 5$ GeV is used. We choose either pp low multiplicity bins or XeXe high centrality bins as the reference to remove the dijet component. Results from different peripheral references are compared. Three different methods ZYAM-based template fitting, improved template fitting and direct Fourier transform are used to extract flow harmonics v_2, v_3 and v_4 from correlation functions. Centrality dependence of flow harmonics is studied in different p_{T} bins. XeXe results are compared with PbPb events at the same energy. Flow harmonics are mostly close for the two sets of data, except that PbPb usually gives higher values in peripheral collisions, while XeXe gives higher values in central events. PbPb events have larger values than XeXe in v_2 for the most cases. p_{T} dependence for different centrality bins using various methods is also studied. Results show that v_n increases rapidly until 2-4 GeV and then gradually decreases. It reaches its maximum value in the mid-centrality region. Systematic errors arising from different peripheral references are studied in different

p_{T} intervals. The errors are estimated as a function of centrality in different p_{T} bins.

Similar measurements at CMS and ALICE have also been discussed and compared with the previous ATLAS results. 13 TeV pp, 5.02 TeV pPb and 8.16 TeV pPb measurements are performed at CMS. The comparison between different systems has been shown, which is similar to the ATLAS comparison mentioned in previous chapters. Muon-hadron correlation for 5.02 TeV pPb is observed at ALICE. The results are compared with ATLAS 8.16 TeV pPb muon-hadron correlation analysis. XeXe measurement in CMS and ALICE are also briefly discussed.

In general anisotropic flows in pp, pPb and PbPb systems share similar properties. Factorization to single particle flows works pretty well and different cumulant flows agree with each other in small systems. These observations may suggest some degrees of the collectivity do exist in small systems. To study the origin of this collective behavior, theoretical calculation is also performed. Hydrodynamic calculation matches the dAu measurement better than pPb measurement. Jet-medium interaction represented by R_{AA} is not observed in pPb. This may also be an indication that the collectivity in small systems may not be driven by exactly the same source as in AA systems. Now we understand collectivity is the phenomenon of multi-particle rapidity correlations, which is not only observed in AA systems, but also exists in small systems. It is not implying a specific physical explanation. In AA systems, collectivity arises from initial geometry fluctuation and hydrodynamic expansion. It is the hydrodynamic collectivity. However in small systems, especially in pp, collectivity may come from other physical mechanism, which needs to be answered.

Bibliography

[1] S. Borsanyi and others, *Transition temperature and the equation of state from lattice QCD, Wuppertal-Budapest results*, J.Phys.Conf.Ser. **316** (2011) p. 012020, arXiv: 1109.5032 [hep-lat].

[2] F. Karsch, E. Laermann and A. Peikert, *The Pressure in 2, 2+1 and 3 Flavour QCD*, Phys. Lett. B **478** (2000) p. 447, arXiv: hep-lat/0002003 [hep-lat].

[3] Z. Fodor and S.D. Katz, *Critical point of QCD at finite T and μ, lattice results for physical quark masses*, JHEP **04** (2004) p. 050, arXiv: hep-lat/0402006 [hep-lat].

[4] T.D. Lee, G.C. Wick, *Vacuum Stability and Vacuum Excitation in a Spin 0 Field Theory*, Phys.Rev. D **9** (1974) p. 2291.

[5] J.C. Collins, M.J. Perry, *Superdense Matter: Neutrons Or Asymptotically Free Quarks?* Phys.Rev.Lett. **34** (1975) p. 1353.

[6] STAR Collaboration (John Adams et al.), *Particle type dependence of azimuthal anisotropy and nuclear modification of particle production in Au + Au collisions at $\sqrt{s_{\mathrm{NN}}}$ = 200 GeV*, Phys.Rev.Lett. **92** (2004) p. 052302, arXiv: nucl-ex/0306007 [nucl-ex].

[7] J.L. Nagle and W.A. Zajc, *Small System Collectivity in Relativistic Hadron and Nuclear Collisions*, Annual Review of Nuclear and Particle Science **68** (2018) p. 211, arXiv: 1801.03477 [nucl-ex].

[8] I. Grabowska-Bold, B. Cole, J. Jia, S. Mohapatra, P. Steinberg, and X. Tu, *Measurement of the long–range pseudorapidity correlations in $\sqrt{s_{\mathrm{NN}}}$ = 2.76 TeV, 13 TeV and 8 TeV proton-proton collisions with the ATLAS detector*, ATL-COM-PHYS-2015-563, 2015, URL: https://cds.cern.ch/record/2026567.

[9] ATLAS Collaboration,
Observation of Long-Range Elliptic Azimuthal Anisotropies in $\sqrt{s} = 13$ and 2.76 TeV pp Collisions with the ATLAS Detector,
Phys. Rev. Lett. **116** (2016) p. 172301, arXiv: 1509.04776 [hep-ex].

[10] I. Grabowska-Bold, B. Cole, J. Jia, S. Mohapatra, and X. Tu,
Measurement of the long–range pseudorapidity correlations in $\sqrt{s_{\mathrm{NN}}} = 5.02$ TeV and 13 TeV proton-proton collisions and in $\sqrt{s_{\mathrm{NN}}} = 5.02$ TeV proton-lead collisions with the ATLAS detector, ATL-COM-PHYS-2016-095, 2016, URL: https://cds.cern.ch/record/2128610.

[11] ATLAS Collaboration, *Measurements of long-range azimuthal anisotropies and associated Fourier coefficients for pp collisions at $\sqrt{s} = 5.02$ and 13 TeV and p+Pb collisions at $\sqrt{s_{\mathrm{NN}}} = 5.02$ TeV with the ATLAS detector*,
Phys. Rev. C **96** (2017) p. 024908, arXiv: 1609.06213 [hep-ex].

[12] B. Cole, S. Mohapatra, and X. Tu, *Measurement of the long–range pseudorapidity correlations between muon and charged-particles in $\sqrt{s_{\mathrm{NN}}} =$ 8.16 TeV proton-lead collisions with the ATLAS detector*,
ATL-COM-PHYS-2016-1793, 2016,
URL: https://cds.cern.ch/record/2239123.

[13] ATLAS Collaboration, *Measurement of the long–range pseudorapidity correlations between muons and charged particles in $\sqrt{s_{\mathrm{NN}}} = 8.16$ TeV proton-lead collisions with the ATLAS detector*, ATLAS-CONF-2017-006, 2017, URL: https://cds.cern.ch/record/2244808.

[14] ATLAS Collaboration,
Measurement of the azimuthal anisotropy of charged particle production in Xe+Xe collisions at $\sqrt{s_{\mathrm{NN}}} = 5.44$ TeV with the ATLAS detector,
ATL-COM-PHYS-2017-1806, 2017,
URL: https://cds.cern.ch/record/2298472.

[15] ATLAS Collaboration,
Measurement of the azimuthal anisotropy of charged particle production in Xe+Xe collisions at $\sqrt{s_{\mathrm{NN}}} = 5.44$ TeV with the ATLAS detector,
ATLAS-CONF-2018-011, 2018,
URL: https://cds.cern.ch/record/2318870.

[16] C. Patrignani et al. (Particle Data Group), *Review of Particle Physics*,
Chin. Phys. C **40** (2016).

[17] A. Laschka, N.Kaiser, and W. Weise,
Quark-antiquark potential to order 1/m and heavy quark masses,
Phys.Rev.D **83** (2011) p. 094002, arXiv: 1102.0945 [hep-ph].

[18] M. L. Miller, K. Reygers, S. J. Sanders, P. Steinberg,
Glauber Modeling in High Energy Nuclear Collisions,
Ann.Rev.Nucl.Part.Sci. **57** (2007) p. 205,
arXiv: nucl-ex/0701025 [nucl-ex].

[19] P. Shukla,
Glauber model for heavy ion collisions from low energies to high energies (),
arXiv: nucl-th/0112039 [nucl-th].

[20] N. A. Gromov, *QCD Development in the Early Universe*,
Physics of Atomic Nuclei **80** (2017) 377–382.

[21] Raimond Snellings, *Elliptic Flow: A Brief Review*,
New J.Phys. **13** (2011) p. 055008, arXiv: 1102.3010 [nucl-ex].

[22] Martin Spousta, *Elliptic flow phenomenon at ATLAS* (),
arXiv: 1406.5541 [nucl-ex].

[23] Alice Ohlson, *Calculating Jet v_n and the Event Plane in the Presence of a Jet*,
Phys. Rev. C **87** (2013) p. 034909, arXiv: 1205.1172 [nucl-ex].

[24] ATLAS Collaboration,
Measurement of the azimuthal anisotropy for charged particle production in $\sqrt{s_{\mathrm{NN}}}$ = 2.76 TeV lead-lead collisions with the ATLAS detector,
Phys.Rev. C **86** (2012) p. 387, arXiv: 1104.3038 [hep-ex].

[25] ATLAS Collaboration,
Measurement of the azimuthal anisotropy of charged particles produced in $\sqrt{s_{\mathrm{NN}}}$ = 5.02 TeV Pb+Pb collisions with the ATLAS detector,
Eur. Phys. J. C **78** (2018) p. 997, arXiv: 1808.03951 [nucl-ex].

[26] ATLAS Collaboration,
Measurement of the distributions of event-by-event flow harmonics in lead–lead collisions at $\sqrt{s_{\mathrm{NN}}}$ = 2.76 TeV with the ATLAS detector at the LHC,
JHEP **11** (2013) p. 183, arXiv: 1305.2942 [hep-ex].

[27] B.Alver, G.Roland,
Collision geometry fluctuations and triangular flow in heavy-ion collisions,
Phys.Rev.C **81** (2010) p. 054905.

[28] W. Israel, J.M. Stewart,
Transient relativistic thermodynamics and kinetic theory,
Annals Phys. **118** (1979) p. 341.

[29] J. Ollitrault, *Relativistic hydrodynamics for heavy-ion collisions*, Eur.J.Phys. **29** (2008) p. 275, arXiv: 0708.2433 [nucl-th].

[30] Wit Busza, Krishna Rajagopal, Wilke van der Schee, *Heavy Ion Collisions The Big Picture, and the Big Questions*, Annual Review of Nuclear and Particle Science **68** (2018).

[31] H. Niemi, K. J. Eskola, R. Paatelainen, *Event-by-event fluctuations in perturbative QCD + saturation + hydro model: pinning down QCD matter shear viscosity in ultrarelativistic heavy-ion collisions*, Phys. Rev. C **93** (2016) p. 024907.

[32] Jonah E. Bernhard, J. Scott Moreland, Steffen A. Bass, Jia Liu, Ulrich Heinz, *Applying Bayesian parameter estimation to relativistic heavy-ion collisions: simultaneous characterization of the initial state and quark-gluon plasma medium*, Phys. Rev. C **94** (2016) p. 024907.

[33] Piotr Bozek, *Collective flow in p-Pb and d-Pb collisions at TeV energies*, Phys. Rev. C **85** (2012) p. 014911.

[34] ATLAS Collaboration, *Observation of Associated Near Side and Away Side Long Range Correlations in 5.02 TeV ProtonLead Collisions with the ATLAS Detector*, Phys. Rev. Lett. **110** (2013) p. 182302.

[35] PHENIX collaboration, *Quadrupole Anisotropy in Dihadron Azimuthal Correlations in Central d+Au Collisions at* $\sqrt{s_{\mathrm{NN}}}$ *=200 GeV*, Phys. Rev. Lett. **111** (2013) p. 212301.

[36] ATLAS Collaboration, *Measurement of long-range pseudorapidity correlations and azimuthal harmonics in* $\sqrt{s_{\mathrm{NN}}}$ *= 5.02 TeV proton-lead collisions with the ATLAS detector*, Phys. Lett. B **725** (2013) p. 60, arXiv: 1409.1792 [hep-ex].

[37] Xilin Zhang, Jinfeng Liao, *Jet Quenching and Its Azimuthal Anisotropy in AA and possibly High Multiplicity pA and dA Collisions* (2013), URL: https://arxiv.org/abs/1311.5463.

[38] CMS Collaboration, *Charged-particle nuclear modification factors in PbPb and pPb collisions at* $\sqrt{s_{\mathrm{NN}}}$ *= 5.02 TeV*, JHEP **04** (2017) p. 039.

[39] B. Cole, L. Havener, D. Perepelitsa, W. Kozanecki, *Luminosity calibration for February 2013 s = 2.76 TeV pp measurements*, ATL-COM-DAPR-2014-009, 2014, URL: https://cds.cern.ch/record/1747966.

[40] ATLAS Collaboration, *Measurement with the ATLAS detector of multi-particle azimuthal correlations in p+Pb collisions at* $\sqrt{s_{\mathrm{NN}}}$ *= 5.02 TeV*, Phys. Rev. C **90** (2014) p. 044906, arXiv: 1303.2084 [hep-ex].

[41] ATLAS Collaboration, *The ATLAS Experiment at the CERN Large Hadron Collider*, JINST **3** (2008) S08003.

[42] ATLAS Collaboration, *Performance of the ATLAS Track Reconstruction Algorithms in Dense Environments in LHC Run 2*, Eur. Phys. J. C **77** (2017) p. 673, arXiv: 1704.07983 [hep-ex].

[43] T. Cornelissen, M. Elsing, I. Gavrilenko, W. Liebig, E. Moyse, and A. Salzburger, *The new ATLAS track reconstruction (NEWT)*, J.Phys.Conf.Ser. **119** (2008) p. 032014.

[44] V. Lacuesta, *Track and vertex reconstruction in the ATLAS experiment*, JINST **8** (2013) p. C02035.

[45] ATLAS Collaboration, *Muon reconstruction performance of the ATLAS detector in proton–proton collision data at* $\sqrt{s}$ *=13 TeV*, Eur. Phys. J. C **76** (2016) p. 292, arXiv: 1603.05598 [hep-ex].

[46] H. Herde on behalf of the ATLAS Collaboration, *Muon reconstruction performance in ATLAS at Run-2*, PoS EPS-HEP **2015** (2015) p. 285.

[47] N. Ko hler, *ATLAS Muon Reconstruction Performance in LHC Run 2*, ATL-PHYS-PROC-2015-186, 2015, URL: https://cds.cern.ch/record/2113434.

[48] Y. Chen, *The production of heavy flavor in lead-lead collisions at* $\sqrt{s_{\mathrm{NN}}}$ *= 2.76 TeV with the ATLAS detector at the LHC*, ATL-COM-PHYS-2012-418, 2012, URL: https://cds.cern.ch/record/1441150.

[49] CMS Collaboration, *Evidence for collectivity in pp collisions at the LHC*, Phys. Lett. B **765** (2017) p. 193.

[50] CMS Collaboration, *Flow and correlation phenomena measurements in pp, pPb and PbPb collisions at CMS*, EPJ Web Conf. **172** (2018) p. 05005.

[51] ALICE Collaboration, *Forward-central two-particle correlations in p-Pb collisions at* $\sqrt{s_{\mathrm{NN}}}$ *= 5.02 TeV*, Phys. Lett. B **753** (2016) p. 126.

[52] Milan Stojanovic, CMS collaboration, *Measurement of anisotropic flow in XeXe collisions at 5.44 TeV with the CMS experiment*, Nuclear Physics A **982** (2019) 395–398, URL: https://www.sciencedirect.com/science/article/pii/S0375947418302756.

[53] ALICE Collaboration, *Anisotropic flow in Xe-Xe collisions at* $\sqrt{s_{\mathrm{NN}}} = 5.44$ *TeV* (2018), URL: https://arxiv.org/abs/1805.01832.